A Comparison of System Architectures for Wireless Links in the Terahertz Band

Von der Fakultät für Informatik, Elektrotechnik und Informationstechnik der Universität Stuttgart zur Erlangung der Würde eines Doktor-Ingenieurs (Dr.-Ing.) genehmigte Abhandlung

Vorgelegt von

Iulia Dan

geboren in Bukarest, Rumänien

Hauptberichter:	**Prof. Dr. Ing. Ingmar Kallfass**
Mitberichter:	**Prof. Dr. Ing. Thomas Kürner**

Tag der mündlichen Prüfung: 25.07.2022

Institut für Robuste Leistungshalbleitersysteme der Universität Stuttgart

2022

Executive Summary

Research in the field of ultra-fast wireless transmissions with operation frequencies above $200\,\mathrm{GHz}$ has been fueled by the continuously growing demand for wireless data. Predictions for the up-coming years show that the conventional wireless communication systems currently available will not be able to satisfy this demand. The beginning of this thesis gives an overview of available technologies that can satisfy this demand and what has been achieved so far employing them. It continues by portraying the essential aspects of a communication system and treats in detail the discussion about the possible architecture terahertz communication systems can have.

The direct-conversion approach has been so far predominant for the few wireless links reported above 200 GHz. This thesis shows two 300 GHz links employing this architecture and presents methods of analyzing the performance of the wireless transmission. The first link uses only active electronic components which are based on monolithic microwave integrated circuits developed using a III-V compound semiconductor technology. The link achieves a transmission data rate of 64 Gbps. The second link employs a photonics-based uni-traveling-carrier diode transmitter and an active electronic receiver, similar to the one from the previous link. 100 Gbps can be achieved in this case. Complex modulation formats up to 64-QAM can be successfully demodulated. The transmission of complex modulation formats is a must for terahartz communication systems. Furthermore, this link exceeds the state of the art in wireless transmission at these frequencies in terms of transmitted bandwidth, which is 54 GHz. An optimized electronic receiver chip is designed and presented in this thesis. The employment of this receiver could significantly improve the performance of the wireless link.

The second architecture discussed in this thesis is very common in conventional radio links, but was never used before for terahertz communication systems. The development of wireless transmission systems above 60 GHz in the frame of 5G offers the perfect IF system for the superheterodyne approach, making this architecture a promising candidate for easy integration in a communication network. A proof-of-concept experiment is shown using the wireless link designed for direct-conversion. Although the setup is far from ideal, the experiment shows a fast transmission with 64 Gbps. Using this architecture multichannel transmission is demonstrated employing 64-QAM modulation and channel data rates of above 10 Gbps. The successful transmission of aggregated channels shows one of the biggest advantages of this architecture.

Finally, this thesis presents a fully integrated transmitter and receiver chipset based on the same 35 nm gate-length InGaAs metamorphic high-electron-mobility transistor technology which can be used in a superheterodyne system. The IF frequency ranges from 75 to above 91 GHz. To the best of the author's knowledge this is the first chipset for THz communication to operate at such high IF frequencies. This chipset represents the missing piece of the previous wireless transmission experiment. Packaging these chips into modules and integrating them with commercially available IF systems will bring 300 GHz communication networks a step closer to the status of application-ready.

Zusammenfassung

Die kontinuierliche wachsende Nachfrage nach höheren Datenraten treibt seit mehr als zwei Dekaden die Forschung der ultraschnellen drahtlosen Übertragungen mit Trägerfrequenzen über $200\,\mathrm{GHz}$. Die Prognosen für die nächsten Jahre zeigen, dass die derzeit verfügbaren herkömmlichen drahtlosen Kommunikationssysteme diesen steigenden Bedarf nicht decken können. Der erste Teil der vorliegenden Disseration gibt einen Überblick über verschiedene Technologien, die diesen Anspruch erfüllen können und welche Ergenisse bisher mit ihrem Einsatz erzielt wurden. Des Weiteren beschriebt diese Arbeit die wesentlichen Komponenten eines Multi-Gigabit-Funkkommunikationssystems und vergleicht ausführlich die möglichen Architekturen die dafür in Frage kommen.

Für die wenigen drahtlosen Übertragung die jenseits von 200 GHz erfolgreich getestet wurden, wurden bisher ausschließlich Homodynempfänger eingesetzt. Diese Arbeit zeigt zwei 300 GHz Funksysteme, die diese Architektur verwenden und stellt die Methoden für die Untersuchung der Übertragungsqualität der drahtlosen Verbindung vor. Der erste Link besteht aus rein elektrischen Komponenten, die auf monolithischen integrierten Millimeterwellenschaltungen basieren und unter Verwendung einer III-V-Verbindungshalbleitertechnologie entwickelt wurden. Der Link erreicht eine Übertragungsdatenrate von 64 Gbps. Der zweite Link verwendet einen photonischen Transmiter und einen aktiven elektronischen Empfänger, ähnlich dem aus dem vorherigen Link.In diesem Fall liegt die maximale Datenrate bei 100 Gbps und sogar komplexe Modulationsformate bis 64-QAM können erfolgreich demoduliert werden, was für Terahartz-Kommunikationssysteme von zentraler Bedeutung ist. Darüber hinaus übertrifft diese übertragung den Stand der Technik hinsichtlich der Übertragenen Bandbreite von 54 GHz. In einem weiteren Kapitel dieser Arbeit wird eine optimiertere elektronische Empfängerschaltung vorgestellt. Der Einsatz dieses Empfängers könnte die Übertragungsqualität der drahtlosen Verbindung erheblich verbessern.

Die zweite Architektur die in dieser Arbeit diskutiert wird ist in konventionellen Funkstrecken sehr verbreitet, wurde aber noch nie für Terahertz-Kommunikationssysteme verwendet. Die Entwicklung drahtloser Übertragungssysteme über 60 GHz im Rahmen von 5G bietet das perfekte ZF-System für den Superheterodyn-Ansatz und macht diese Architektur zu einem vielversprechenden Kandidaten für die einfache Integration in einem Kommunikationsnetzwerk. Für eine Machbarkeitsstudie wurde ein System verwendet, das zwar auf Homodynempfang ausgelegt ist, aber durch leichte Anpassungen auch für Heterodynempfang verwendet werden kann. Obwohl die Übertragung nicht unter idealen Bedingungen durchgeführt wurde, konnte im Experiment eine schnelle Datenübertragung mit 64 Gbps erzielt werden. Unter Verwendung dieser Architektur wird eine Mehrkanalübertragung mit 64-QAM-Modulation und Kanaldatenraten von über 10 Gbps demonstriert. Die erfolgreiche Übertragung aggregierter Kanäle zeigt einen der größten Vorteile dieser Architektur.

Das abschließende Kapitel stellt eine vollständig integrierte Sender-und Empfängerschaltung vor, die mit der gleichen 35 nm Gate-Länge InGaAs metamorphern High-Electron-Mobility Transistor Technology gefertigt wurden. Dieses Frontend ist nun im Gegensatz zum System

der Machbarkeitsstudie eigens für ein Superheterodyn-Funksystem entworfen. Der nutzbare ZF-Frequenzbereich liebgt bei 75 bis über 91 GHz. Nach bestem Wissen der Autorin ist dies das erste Frontend für THz-Kommunikation, das bei so hohen ZF-Frequenzen arbeitet. Dieser Frontend stellt die logische Weiterentwicklung der Machbarkeitsstudie zur drahtlosen Übertragungen mittels Homodynansatzes dar. In Modulen integriert und in Verbindung mit handelsübliche ZF-Systeme werden diese Schaltungen 300 GHz Kommunikationsnetze der Anwendungsreife einen Schritt näher bringen.

Contents

List of Abbreviations and Symbols

Abbreviations

5G 5th generation cellular systems

ADC analog-to-digital converter

Au gold

AWG arbitrary waveform generator

AWGN additive white Gaussian noise

BCB benzocyclobutene

BER bit-erorr-rate

BiCMOS bipolar complementary metal-oxide-semiconductor

BPSK Binary phase shift keying

BW bandwidth

CMOS complementary metal-oxide-semiconductor

CPW coplanar waveguide

CPWG grounded coplanar waveguide

DAC digital to analog converter

DSB double side band

EDFA erbium-doped fiber amplifier

EVM error vector magnitude

FDM frequency-domain multiplexing

FEC forward error correction codes

FET field effect transistor

FSPL free-space path loss

GaAs Galium Arsenide

GaN Galium Nitride

GSG ground-signal-ground

HBT heterojunction bipolar transistor

HD high definition

HEMT high electron mobility transistor

IAF Fraunhofer Institute for Applied Solid State Physics (IAF)

IF intermediate frequency

IQ in-phase and quadrature

InP Indium Phosphide

LNA low-noise amplifier

LO local oscillator

LSB lower side band

mHEMT metamorphic high electron mobility transistor

MIM metal-insulator-metal

MIMO multiple input multiple output

MOSFET metal oxide semiconductor field effect transistor

MMIC milimeterwave monolithic integrated circuit

mmW milimeterwave

NiCr nickel-chrome

PAM pulse amplitude modulation

pHEMT pseudomorphic high electron mobility transistor

PRBS pseudo random binary sequences

PTFE polytetrafluoroethylene

QAM quadrature amplitude modulation

QCL quantum cascade laser

QPSK Quadrature phase shift keying

RR radio regulations

RTD resonant tunneling diode

RF radio frequency

Si Silicon

SiGe Silicon Germanium

SiN Sillicon Nitride

SISO single input single output

SNR signal-to-noise ratio

SSB single side band

THz terahertz

USB upper side band

UTC-PD uni-traveling-carrier photo diode

via vertical interconnect access

VNA vector network analyzer

WPAN wireless personal area networks

Symbols

f_{max} maximum frequency of oscillation

f_{t} transit frequency

$J_{\mathrm{D,max}}$ Maximum drain current reffered to gate width

$V_{\mathrm{GS,th}}$ Gate-source threshold voltage

$V_{\mathrm{DS,Bon}}$ on-state drain-source breakdown voltage

$V_{\mathrm{DS,Boff}}$ off-state drain-source breakdown voltage

$g_{\mathrm{m,max}}$ transconductance reffered to gate width

List of Figures

List of Tables

1 Wireless Communication in the Low THz Range

The terahertz (THz) regime is defined as the part of the electromagnetic spectrum that lies between the microwave and optical frequencies. The boundaries between far infrared, terahertz and microwaves are fairly arbitrary and are being employed in a different manner depending on the field of research and operation. In radio frequency (RF) engineering the THz range starts at $100\,\mathrm{GHz}$ and ends at $3\,\mathrm{THz}$ and milimeterwave (mmW) signals have frequencies between 30 and $300\,\mathrm{GHz}$. The THz radiation has some uniquely attractive qualities and finds applications in various research fields starting with already established sensing and imaging to emerging fields like wireless communication. THz radiation is not dangerous for human tissue thanks to its non-ionizing properties. It also stimulates different molecular and electronic motions in many materials. This means that THz radiation can be used to identify hidden objects [SSH+16], check for defects in different materials [ZRG+20] and even detect cancerous tissue in the human body [ESVBB19]. Although this is not new, starting from the mid 20th century researchers have been investigating this promising frequency spectrum, the past two decades have seen the most intense research towards the goal of turning laboratory experiments into real-world applications. Especially the progress of THz technology made in radio astronomy and space science is noticeable and this is due to the operation in a near-vacuum environment. Terrestrial THz applications have to deal with a dense atmosphere, which absorbs, refracts and scatters THz signals, not to mention the influence of different weather conditions like rain, fog and snow. This represents one of the main challenges applications like wireless communication and radar using THz technologies have to face.

For wireless links operating in the previously mentioned THz range transmission loss is accounted for principally by the free-space path loss (FSPL)[1], describing the loss in signal strength of an electromagnetic wave propagating along a line-of-sight path with no obstacles blocking or reflecting the signal. In addition to this, the effects of atmospheric attenuation become more and more significant due to the interaction of the electromagnetic radiation with the atmosphere [MP05]. When the THz signal travels through the atmosphere it is absorbed by molecules of oxygen, water vapor, and other gaseous atmospheric constituents. This absorption is not constant over the frequency spectrum, showing absorption maximas, generating the so-called atmospheric attenuation windows. Below $400\,\mathrm{GHz}$ there are five such windows [RMG11]. The largest one, with a bandwidth of $120\,\mathrm{GHz}$ is located between 200 and $325\,\mathrm{GHz}$. Furthermore, in this frequency range, the atmospheric attenuation under fair weather conditions stays well below $10\,\mathrm{dB/km}$. Hence, this frequency range is the perfect compromise between the challenge of high attenuation and advantage of high available

[1] The attenuation due to the dissipation of the radiated energy between a transmitter and receiver is given by Friis transmission formula [Cou] as free-space loss $(c/4\pi fr)^2$, where c is the speed of light, f is the frequency of the electromagnetic wave and r is the distance between transmitter and receiver.

bandwidth. This is also the reason why the term THz communication refers to the frequency range around $300\,\mathrm{GHz}$.

After the atmospheric attenuation the next big challenge in developing application-ready THz communication systems is the lack of appropriate THz sources. The requirements on these sources are hard to meet: they have to generate a high power at very high frequencies, they have to be efficient and have small dimensions. Generally speaking there are three types of THz sources:

- vacuum electronic devices including travelling-wave tubes [SJB+06] and gyrotrons [SI10], [ISO+08]
- solid state electronic devices including frequency multipliers based on high-frequency transistors [SL00]
- laser and photonic devices including quantum cascade laser (QCL) [Wil07] and opto-electronic RF generators [MBN+95]

All these types of devices have advantages and disadvantages. What they have in common is the very low conversion efficiency, typically less than $1\,\%$ [A14]. As a comparison, an RF power amplifier in a typical smartphone operates at around $50\,\%$ efficiency [HAR10]. For communication and radar applications all of the above mentioned requirements are a must. But most importantly the dimensions play a crucial role. This is the reason why vacuum devices and most lasers are out of question for these applications, despite their highest average power among all THz sources. This leaves solid-state devices followed by photonic devices as the best sources for THz communication. Low efficiency combined with small device sizes leads to another challenge: high power and current densities. This requires an elaborated technology using the right materials to minimize the internal power dissipation and an adequate cooling method.

1.1 The need for multi-gigabit wireless communication

The need for higher wireless data rates and capacities overwhelms the challenges the THz gap poses. According to Edholm's Law, presented by J. H. Yoakum in 2004 [Web07], data rates of cellular, wireless and wire systems increase exponentially. This law predicts that the bandwidth and data rates double every 18 months, which has been proven true since the 1970s [Che04]. Fig. 1.1 shows the evolution of the data rates for cellular and wireless systems for the past 30 years. Due to the logarithmic scale of the y-axis representing the data rate in Gbps, it is obvious that the increase is exponential like stated by Edholm's Law [Web07]. The same law also states, that the continuous growth is strongly dependent on society's demand for ever-higher data rates, and this will one day be satisfied. As a consequence, this could also be the end of wireline systems. When wireless will be able to reach some fundamental limits, like the number of pixels per second the human eye can process, all communication systems will be completely wire-free. In 2020 wired (fiber-optic) communications such as Ethernet with capabilities of $100\,\mathrm{Gbps}$ are very common [P80]. A look at Fig. 1.1 reveals that once beyond-5G technologies, based on THz communication systems, can be commercialized the end of Edholm's Law will be achieved.

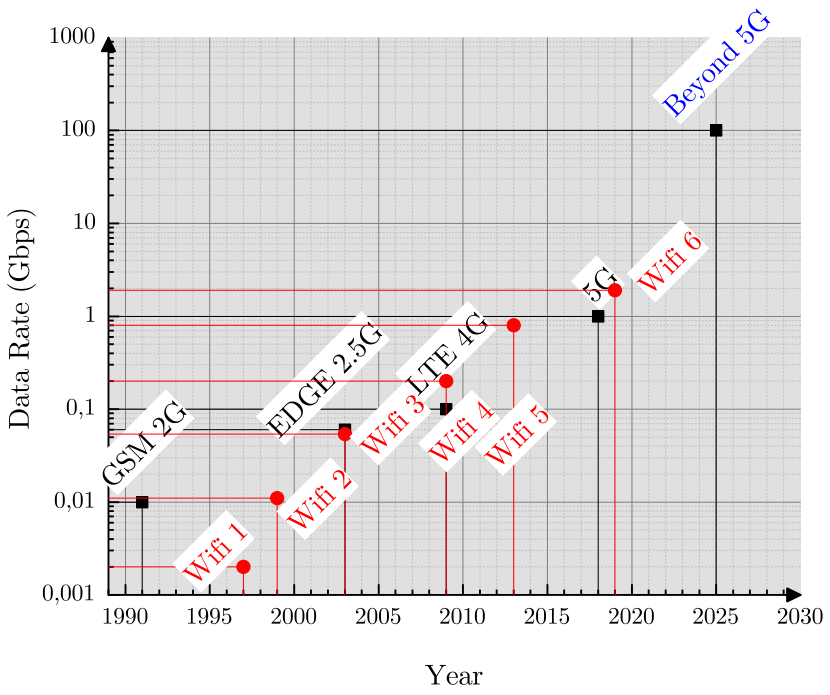

Figure 1.1: Oveview and forcast of the data rate evolution for cellular and fixed wireless services.

Another indicator of the continuous growing demand for wireless data rates are the data traffic reports conducted by several network and communication technology providers. Ericsson is a constant observer of the trends in the mobile industry and publishes regularly a mobility report where the situation of mobile data traffic is assessed and past predictions are corrected if needed. Their latest report [Erib] shows that a global event, the COVID-19 pandemic, has strongly influenced the growth of wireless data traffic in a lot of sectors. The lockdown restrictions in many countries caused significant digital behavioral changes. The critical role a stable functioning high data rate wireless network (mobile networks as well as fixed wireless networks like WiFi) has become more obvious than ever. The increased data consumption was due to the usage of a variety of apps for remote-working, streaming, education and e-learning, remote health consultation and last but not least social shared experiences. The probability that this new digital behaviors will remain after the crisis is high. The following are just a few of many imaginable scenarios:

- Contact-free interactions will drive the demand for automated drone deliveries or driverless cars
- Remote working will become a standard for many professions
- Online health care consultants will become a growing addition to conventional hospitals and practices
- Augmented and virtual reality applications will transform travel and social experiences

This increases the requirements for wireless networks and pushes the demand that was predicted before the pandemic even further. In addition, many new devices will require a wireless connection, not just smartphones and tablets. In the mobility report from November

2019 [Eric] the prediction for global 5th generation cellular systems (5G) subscription was 2.6 billion. This number was corrected in the report from June 2020 to 2.8 billion [Erib]. Although the pandemic has caused big regional differences in the consolidation of the 5G network, for example delays in spectrum licensing, 5G is expected to be the fastest deployed mobile communication technology in history. Furthermore, not only the mobile data traffic is predicted to continuously increase. By the end of 2020 $25\,\%$ of the world's mobile network data traffic is predicted to be supported by fixed wireless access, like WiFi. This would represent a threefold increase in comparison to the end of 2019.

Next to the severe spectrum shortage the acceleration of future digital applications caused by the pandemic points out that mmW bands will play a significant role in 5G and beyond-5G communication systems. An example that sustains this statement, that becomes reality with each day that passes is the transition of backbone networks from copper and fiber to mmW wireless connections. E-band is considered essential for the backhaul in 5G networks [Eria]. A backhaul link using a MIMO[2] E-band link reached a data rate of $139\,\mathrm{Gbps}$ in April 2019 in Athens, Greece over a distance of $1.5\,\mathrm{km}$, proving that this technology is ripe for commercialization [Eria]. Such mmW systems can and will complement optical fiber especially in urban environments[3]. They also offer an exciting opportunity for circuit, antenna and communication systems at even higher frequencies. In order to enable higher capacities in both traditional spectrum and E-band, access to wider bandwidths is important. E-band is just the beginning of a trend to exploit further attenuation windows, which will deliver unprecedented data rates, allowing new applications to emerge. Shorter wavelengths lead to smaller dimensions of antennas. In addition, advances in low-power complementary metal-oxide-semiconductor (CMOS) RF circuits enable large numbers of miniaturized antennas to be placed in ever smaller components. This can be used to form very high gain, electrically steerable arrays [DES+04, DENB05]. At frequencies of around $300\,\mathrm{GHz}$, the planar antenna size is in the order of sub-millimeters, and the beam-forming antenna array will be in a range of a few millimeters. These miniature antennas are integrable with communication terminals and equipments at low cost [KON11].

Technological innovation is often fueled by federal authorities and international spectrum regulators groups. In 2018 the first THz standard was published by the IEEE P802.15 working group for wireless personal area networks (WPAN) [IEE17]. It uses the band 252 to $321\,\mathrm{GHz}$ and it is based on the 2016 version of the radio regulations (RR) [Cona], where the use of the band above $275\,\mathrm{GHz}$ is ruled by footnote 5.565 requiring that passive services such as earth exploration satellite services and radio astronomy have to be protected from harmful interference by any active service, such as THz communications. This implies that sharing studies have to be conducted. As a general rule, the usage of the frequency area between 252 to $321\,\mathrm{GHz}$ is allowed given that the passive services of earth exploration satellite services and radio astronomy are not negatively affected by the radiation of the active links [Conb]. A study conducted already in 2010 [ITU] calculates the minimum distance at which no interference occurs for radio astronomy telescopes under extreme conditions. At $300\,\mathrm{GHz}$ THz transmitters have to be placed at least $50\,\mathrm{km}$ away from radio telescopes. This is normally not an issue since radio telescope are mostly located at isolated sites far from human

[2]MIMO is a well established antenna technology for enhancing spectral efficiency in a communication link. It is widely used at lower frequencies in cellular services and WiFi.

[3]The cost for providing fiber connection in urban environments is very high [Kra17] and since in this area the density of cells has to be very high, mmW links prove to be more cost-effective.

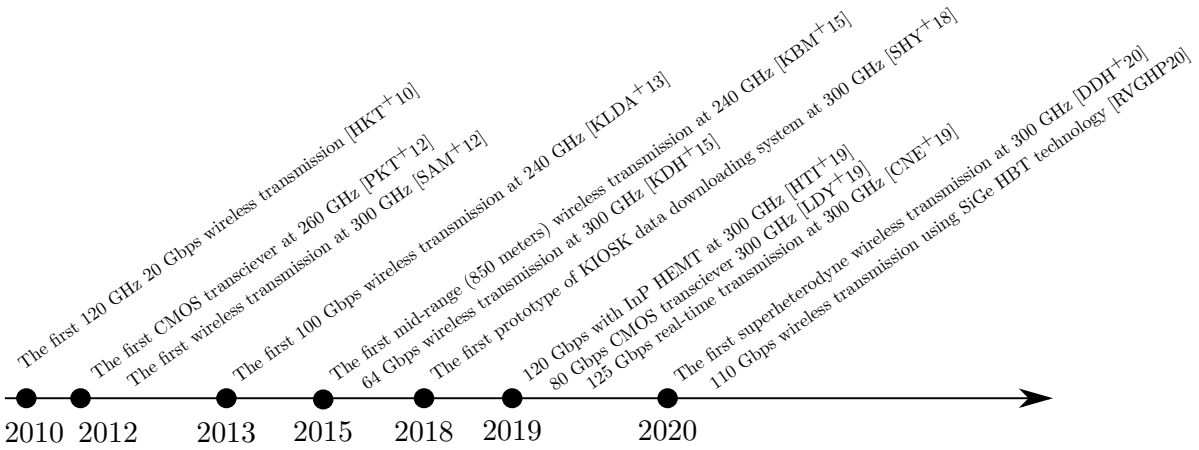

Figure 1.2: Timeline of the milestones relevant for the progress of THz communication up to now.

settlements in which THz communication will most probably be used. This leads to the fact, that radio astronomy and active THz services for communications will be able to share the THz-band.

The first THz standard validates the fact that the frequency range beyond $275\,\mathrm{GHz}$ represents an attractive research area and has the potential for commercial development. Its level of maturity is demonstrated by the manifold of projects and prototypes that operate in this frequency range. There is a variety of studies made available in the literature which give a good and complete overview of the progress and history of THz technologies for communication purposes starting with [FM10] in 2010, continuing with [KON11, SN11, NC15] just to name a few and concluding with the latest survey [EAS+20] which reviews devices, channel models as well as possible applications related to THz communication.

Fig. 1.2 shows the milestones timeline relevant for the progress of THz communication, proving that THz research is moving from an emerging to a more mature field, where an obvious technological step forward occurs within the last five years. One of the first successful demonstration of wireless links operating at frequencies in the low THz region is developed by NTT in Japan [HKM+04, HKT+06, HYK+09, HKT+10, THTK10]. The aim of the system is to transmit a large volume of digital data over a higher distance, around $1\,\mathrm{km}$. During the Beijing Olympic Games in 2008 the system is utilized by Fuji Television Network Inc. to transmit high definition (HD) video signal from a studio to the broadcasting center. In 2012 the first CMOS transciever is reported by [PKT+12]. Using this fully integrated $260\,\mathrm{GHz}$ chip, which operates beyond the device's cut-off frequency, a short range wireless transmission at a data rate of $10\,\mathrm{Gbps}$ over $10\,\mathrm{mm}$ is conducted. The first $300\,\mathrm{GHz}$ wireless transmission occurs in 2012 [SAM+12] and is realized using a uni-traveling-carrier photo diode (UTC-PD) transmitter and a Schottky barrier diode detector. A data rate of $24\,\mathrm{Gbps}$ is reached at a transmission distance of $50\,\mathrm{cm}$. An important milestone in the development of THz communication represents the transmission experiment reported by [KLDA+13] in 2013. For the first time $100\,\mathrm{Gbps}$ is achieved. This experiment uses a photonic transmitter and an active electronic milimeterwave monolithic integrated circuit (MMIC) based receiver and manages to successfully transmit and demodulate data over a distance of $20\,\mathrm{m}$. The system operates at a center frequency of around $240\,\mathrm{GHz}$. This transmission will continue to be state of the art for the next 6 years. Using the same technology for the receiver and, in comparison to the previous experiments, an active electronic transmitter,

the first mid-range wireless transmission is realized in 2015 [KBM+15]. The distance the point-to-point link was covering is $850\,\mathrm{m}$. In the same year a $300\,\mathrm{GHz}$ transmission with a data rate of $64\,\mathrm{Gbps}$ is reported [KDR+15]. In 2018 the first 'application-ready' prototype of a $300\,\mathrm{GHz}$ communication system is presented in [SHY18]. The authors of this work present the development of a KIOSK data downloading system designed for 'touch-and-go' implementation. The prototype is validated with the help of an instant data transfer. In 2019 the $100\,\mathrm{Gbps}$ milestone is reached and overcome for a $300\,\mathrm{GHz}$ all electronic front-end based on InP high electron mobility transistor (HEMT) [HTI+19]. The same year Lee et. al reports on a CMOS transceiver capable of wireless data rates up to $80\,\mathrm{Gbps}$ at a center frequency of $300\,\mathrm{GHz}$ [LDY+19]. Among the newest successes for THz communication can be counted the real-time transmission with a data rate of $125\,\mathrm{Gbps}$ [CNE+19], the $110\,\mathrm{Gbps}$ reached using the SiGe heterojunction bipolar transistor (HBT) technology [RVGHP20] and last but not least the first superheterodyne transmission in the $300\,\mathrm{GHz}$ band reported also in this thesis in chapter 6.

As can be seen in the timeline pictured in Fig. 1.2 there are a variety of technologies suitable for THz communication and they will be briefly described in the following section.

1.2 Technologies for THz wireless communication

The significant growth of wireless data traffic has fueled the research of different THz communication systems, mostly in the fourth and largest mentioned attenuation window, located between 200 and $325\,\mathrm{GHz}$. Nevertheless, a lot of research is still to be made and the best suited technology for next-generation THz communication systems is still to be determined.

1.2.1 Photonic based transmitters and receivers

From the state-of-the-art perspective it seems that purely photonic sources and detectors are not the best choice. There are many types of photonic sources, which have been used in THz communication applications including QCL and non-linear optical mixing sources and ultrafast laser-driven pulsed sources. All these sources have strong and weak points. For example, QCLs achieve very high output powers, above $100\,\mathrm{mW}$ above $1\,\mathrm{THz}$, but require cryogenic cooling [LLW17]. Pulsed non-linear mixing sources on the other hand do not require cooling but have no tunability and rely on very high optical intensities to generate THz pulse streams with low average power, in the range of a couple of microwatts [SA11]. The downside of all these sources is that they are not easily integratable into complex digital electronic systems, which makes them less appealing for THz communication systems.

A **resonant tunneling diode (RTD)** is a photonic device based on the quantum mechanical tunneling principle, in which at certain energy levels electrons pass through some resonant states [Sae13]. They are suited for THz communication transmitters because the output power is easily modulated by the bias voltage and oscillations can be controlled either by electrical or optical signals. High speed direct modulation up to $30\,\mathrm{GHz}$ has been achieved [IKO+15]. [OHSA17] reports on a wireless transmission at 500 and $800\,\mathrm{GHz}$ in which RTD oscillators with different frequencies and polarizations are integrated in one chip. A data rate of $56\,\mathrm{Gbps}$ is achieved at a distance of $20\,\mathrm{cm}$. The size of these devices proves to be very

advantageous, since it is possible to integrate multiple oscillators on a single chip, enabling multi-channel transmission. Despite this advantage, the low output power of this technology is a major bottleneck, thus, other technologies have been gaining interest in the research community.

Photonics technologies gained the attention of broadcasters who wanted to transmit high-definition TV data after the success of the first $120\,\mathrm{GHz}$ wireless link [TKH+13], which used the photonic transmitter reported in [NHR+]. They have broadband characteristics and are able to transmit complex modulation introduced from optical coherent network technologies [NDR16]. Most of the devices are based on the optical-to-THz and THz-to-optical conversion using nonlinear optical materials, photoconductors and photodiodes. The last mentioned type of devices, photodiodes, offer the ability of high speed processing and high saturation output power. The combination of a photodiode and an optical amplifier eliminates the need of an electronic amplifier and extends the bandwidth of the system [4] [II20]. **UTC-PD** are a promising example of a photonic device for THz communication. They offer bandwidths of up to $150\,\mathrm{GHz}$ [SMA+98] proving to be perfect candidates in communication systems like presented in [YJH+16], where a $160\,\mathrm{Gbps}$ wireless transmission is demonstrated. Due to this fact, a UTC-PD will be used as a transmitter in a transmission experiment presented in this thesis in chapter 4. The biggest challenge photonic technologies face is integrating the bulky devices with electronic circuits.

1.2.2 Solid-state electronics

As opposed to photonics, the advances in semiconductor technologies and their manufacturing lead to compact devices. Critical for reaching THz operational frequencies for integrated circuits are transistors with sufficiently high maximum frequency of oscillation ($f_{\max}$). The main approaches in developing high speed transistors include both transistor gate scaling for parasitic reduction as well as epitaxial material enhancement for improved electron transport properties.

A technology that has advanced quickly in the last decade is the **CMOS** technology. High level of integration, small form factor and a high potential for low costs are just a few advantages this technology has to offer. At lower frequencies, this is the technology of choice for microprocessors, microcontrollers and memory chips, but also for highly integrated transceivers for cellular networks and many other types of communication systems. This is actually the technology that introduced digital signal processing in wireless communication [KBA]. Thanks to aggressive technology downscaling CMOS transcievers offer reasonable RF performance. Already at the beginning of the century, in 2006, the scaling of a $65\,\mathrm{nm}$ CMOS process reached a power gain frequency of $420\,\mathrm{GHz}$ [PAC+06]. The big disadvantage of this technology is that the output power is restricted by the decreasing breakdown voltage of the devices. To overcome this difficulty CMOS signal sources utilize device nonlinearities and harmonic generation. For short-range applications like chip-to-chip communication transceivers as presented in [MHAA15] and [PKT+12] can be very successful. Both publications report on fully integrated 40 and $65\,\mathrm{nm}$ CMOS transceivers at 210 and $260\,\mathrm{GHz}$, that can transmit

[4] Even in the existing highest speed fiber-optic transmission systems the operation speed of optical receivers has been limited by electronic circuits

data with a data rate of around $10\,\mathrm{Gbps}$ over a couple of cm. Recently, a single-chip $40\,\mathrm{nm}$ CMOS transceiver capable of data rates up to $80\,\mathrm{Gbps}$ was presented in [LHY+19a].

Although the CMOS technology is not yet mature for frequencies in the low THz range the possibility of co-integration with digital circuitry is a constant motivation for further research.

Another Si-based technology suitable for THz communication applications is **Silicon Germanium (SiGe) HBT**. The HBT transistor uses different materials for the emitter and the base region, creating a heterojunction which limits the injection of holes from the base into the emitter. This leads to a high doping density in the base and to an increase in gain at the cost of reducing the base resistance. In comparison to conventional bipolar transistors, HBTs have the advantage of higher cut-off frequency, higher voltage handling capability and reduced capacitive coupling with the substrate [Hou00]. In the case of the SiGe HBT the material used for the base is Silicon (Si). This technology offers higher transit frequency (f_t) and a higher f_max than CMOS technology, recently reaching $505\,\mathrm{GHz}$ and $720\,\mathrm{GHz}$ respectively [HRB+16, SBd+16]. In addition, it can leverage the compatibility with CMOS, enabling the design of complex mixed-signal circuits.

In comparison to CMOS, due to the scaling related deterioration of f_max [VTD+13], the speed of SiGe HBT is predicted to improve with further transistor scaling. [SRC+16] shows that operating frequencies in the range of $1\,\mathrm{THz}$ are expected in the future. One of the biggest challenges that this technology is facing is the unfavorable environment for antenna and passive integration, due to the technology stack of the foundry-level silicon technology [HGJP19]. The design of on-chip antennas is strongly affected by multimode propagation issues, like surface waves, [SSYH15]. This is the reason why backside radiating on-chip antennas with an auxiliary silicon lens are widely used in systems employing this technology [RVGHP19, RGHP19b, RGHP18, RVGS+18]. In one of the most recent demonstrations [RVGHP20] presents a wireless multiple input multiple output (MIMO) link using a SiGe HBT front-end capable of transmitting $110\,\mathrm{Gbps}$ over a distance of $2\,\mathrm{m}$. This successful experiment confirms that SiGe HBT is regarded as a bridging technology, showing similar integration capabilities as CMOS and offering an alternative to the more expensive III-V MMICs.

Efforts have been made also in the development of the SiGe HBT and its integration in a bipolar complementary metal-oxide-semiconductor (BiCMOS) technology [RHF12]. BiCMOS technology is not a competition for CMOS, but a complement, being the default choice for RF applications for which large digital densities are not necessary [CLR+18]. The SiGe BiCMOS technology achieves an f_t and f_max of 300 and $500\,\mathrm{GHz}$ [HBB+10, BAB+15]. Although these devices have a better achievable output power and hence promise a more relaxed link budget than CMOS transceivers, the experiments reported so far using this type of solid state electronics are mostly in the short range area or even under wafer-probing conditions, due to the lack of an appropriate package. [FSCE17] presents a transceiver chipset operating at $190\,\mathrm{GHz}$ which can transmit data with speeds up to $50\,\mathrm{Gbps}$ over $6\,\mathrm{mm}$. In [**?**] and in [EML+20] the operation frequency of the transceiver is increased to $240\,\mathrm{GHz}$, as well as the transmission distance to $15\,\mathrm{cm}$.

Compared to Si technologies in **III-V compound semiconductors** the carriers are injected with a higher velocity, thanks to their higher energy and due to superior mobility and are best suited for circuits operating in the low THz range. Devices based on III-V semiconductors are historically the enabling constituents for wireless communication systems based on solid-state

electronics in the low THz range. The first transistor that operated above $1\,\mathrm{THz}$ was an Indium Phosphide (InP) HEMT [LMD+07]. These devices meet all the requirements such a wireless THz system has: a high output power, high linearity and low noise capabilities. Low RF noise transistors are the key components of microwave receivers in communication and radar systems. They are mostly based on Galium Arsenide (GaAs) pseudomorphic high electron mobility transistor (pHEMT) and mHEMT or on InP HEMTs. For low phase noise oscillators, MMICs based on III-V compound semiconductors HBTs show promising features [WS04]. When it comes to power applications, Galium Nitride (GaN) devices are being developed and represent a fierce competition for GaAs and InP because of their superior power handling capabilities [Ino21, Sch20, CKC+20].

Wireless communication systems using exclusively solid-state electronics or only in the receiver have been very successful due to III-V compound semiconductors, starting with the first $100\,\mathrm{Gbps}$ wireless transmission in the low THz range in 2013 [KLDA+13] and ending with the newest achievement, $120\,\mathrm{Gbps}$ over a distance of around $10\,\mathrm{m}$ reported in [HNT+19, HTM+20]. The transceiver employed in this experiment uses InP HEMT with f_t and f_max of 300 and $700\,\mathrm{GHz}$ respectively. Another suited III-V compound semiconductor technology for THz transmitters and receivers is the GaAs mHEMT, which was used in a numerous of successful wireless experiments [KLDA+13, KBM+15, BMA+14, CNE+19]. Since this is also the technology of choice for all the electronic integrated circuits presented in this thesis, it will be described in more detail in the following section.

Table 1.1 offers an overview of the available solid-state technologies described above including the state-of-the art transmission experiment employing that kind of technology. As can be seen compound semiconductor technologies dominate this research field. Especially, the InGaAs mHEMT was used for many frontends that achieved state-of-the-art results in terms of distance, data rate, frequency and last but not least architecture. The last mentioned work in the table, [DDH+20], is part of this thesis and will be presented in detail in chapter 6.

Table 1.1: Available solid-state technologies and state-of-the art wireless transmissions employing that technology for both transmitter and receiver.

Technology	**State-of-the-art transmissions**					
	f_t / f_max in GHz	Distance in m	Data Rate in Gbps	Frequency in GHz	Year	Reference
$40\,\mathrm{nm}$ CMOS	n.a./ 280	0.03	80	265	2019	[LHY+19b]
$130\,\mathrm{nm}$ SiGe HBT	350 / 550	1	110	230	2020	[RVGHP20]
$130\,\mathrm{nm}$ SiGe:C BiCMOS	300 / 500	0.15	7.8	240	2019	[EML+20]
$80\,\mathrm{nm}$ InP HEMT	300 / 700	9.8	120	296	2020	[HTM+20]
$35\,\mathrm{nm}$ InGaAs mHEMT	515 / 1000	850	64	240	2015	[KBM+15]
$35\,\mathrm{nm}$ InGaAs mHEMT	515 / 1000	40	96	240	2015	[KBM+15]
$35\,\mathrm{nm}$ InGaAs mHEMT	515 / 1000	1	64	300	2015	[KDR+15]
$35\,\mathrm{nm}$ InGaAs mHEMT	515/ 1000	10	56	300	2019	[DDH+20]*

*the first superheterodyne architecture employed in a THz communication link

1.2.3 InGaAs 35 nm mHEMT

The semiconductor process used for the MMICs designed and presented in this work is the $35\,\mathrm{nm}$ mHEMT process developed at IAF. A HEMT is a field-effect transistor incorporating a junction between two materials with different band gaps as the channel instead of a doped region, as is generally the case for a metal oxide semiconductor field effect transistor (MOSFET). At IAF the molecular beam epitaxy growth of the metamorphic structures is done on $100\,\mathrm{mm}$ semi-insulating GaAs substrate wafers. A $1.1\,\mu\mathrm{m}$ thick InAlGaAs buffer layer transforms the lattice constant from the GaAs to the InP value. The active devices are defined by a two-step electron beam litography and are encapsulated in benzocyclobutene (BCB) to reduce parasitic capacitances. A detailed description of the front-end-of-line process is given in [LTD+13]. The gate is defined with two separate electron beam lithography layers. To suppress substrate modes the wafers are thinned down to $50\,\mu\mathrm{m}$, through-substrate vertical interconnect access (via) are dry-etched and the wafers are gold-plated on the back side. The back-end-of-line process includes nickel-chrome (NiCr) thin film resistors and an $80\,\mathrm{nm}$ thick chemical vapor deposition Sillicon Nitride (SiN) layer used for on-wafer metal-insulator-metal (MIM) capacitors. Three metal layers are available for the design of coplanar waveguide (CPW) transmission lines. The electron beam evaporated gold (Au)-based first and second metal layers are defined in a lift-off process. MET3 is a $2.7\,\mu\mathrm{m}$ thick plated Au layer in air bridge technology. The electrical transistor parameters of a transistor with two fingers and a gate width of $10\,\mu\mathrm{m}$ are listed in Table 1.2.

Fig. 1.3 shows the cross section and available layers of the front side process. The image is not to scale. The process allows the use of air bridges. These are connected using the third metal layer on the top with an air gap of $16\,\mu\mathrm{m}$. To prevent the air bridges from collapsing they need contacts to the other metal layers with the ground plane on the bottom. For suppressing substrate modes and to ensure a good ground connection, vias can be placed through the substrate to connect the top metal layer with the ground plane on the bottom.

Coplanar Waveguide Transmission Lines. Transmission lines can be realized using coplanar waveguides or thin-film microstrip lines both available in the $35\,\mathrm{nm}$ mHEMT process developed at IAF. Microstrip lines are constructed by layouting the signal line on the MET2 layer with a solid ground plane on the MET1 layer underneath. Microstrip lines have the advantage that the ground plane is not cut by the signal trace. The ground plane on the

Table 1.2: Key electrical parameters of the $35\,\mathrm{nm}$ mHEMT process developed at IAF for a transistor with two fingers and a gate width of $10\,\mu\mathrm{m}$ [LTM+08].

Parameter	Value	Description
$J_{\mathrm{D,max}}$	$1600\,\mathrm{mAmm^{-1}}$	Maximum gain current per gate width
$V_{\mathrm{GS,th}}$	$-300\,\mathrm{mV}$	Gate-source threshold voltage
$V_{\mathrm{DS,Bon}}$	$1.5\,\mathrm{V}$	On-state drain-source breakdown voltage
$V_{\mathrm{DS,Boff}}$	$2\,\mathrm{V}$	Off-state drain-source breakdown voltage
$g_{\mathrm{m,max}}$	$2500\,\mathrm{mSmm^{-1}}$	Maximum achievable transconductance per gate width
f_{t}	$515\,\mathrm{GHz}$	Transit frequency
f_{max}	$>1000\,\mathrm{GHz}$	Maximum oscillation frequency

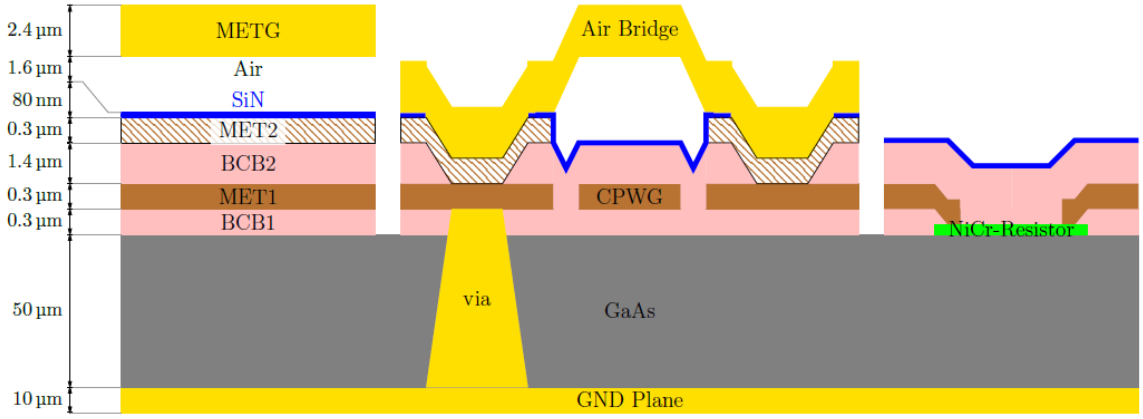

Figure 1.3: Cross section and available layers of the front side $35\,\mathrm{nm}$ mHEMT process developed at IAF.

MET1 layer stays solid. This eliminates the need for air bridges over the signal trace. In this work transmission lines based on coplanar waveguides will be exclusively used. In the M45 process grounded coplanar waveguide (CPWG) structures are designed on the MET1 layer with a fixed ground-to-ground spacing of $14\,\mu\mathrm{m}$. Fig. 1.3 also shows a sketch of a CPWG. Table 1.3 lists the inner conductor width for specific commonly used wave impedances.

Table 1.3: Conductor widths at commonly used wave impedances..

Wave impedance in Ω	**Inner Width in μm**
40	10
50	7.4
70	3.6

Airbridges and Vias. Typically a ground plane on the MET1 layer covers the whole chip. This plane is cut by the signal tracks of CPWGs and transistors. The separate segments of the plane are connected to the continuous ground plane on the backside of the chip through vias. These vias also shorten wave modes that can occur inside the substrate. Due to their length through the substrate, their big size of $17 \cdot 17 \mu m^2$ and a minimum via-to-via spacing of $30\,\mu\mathrm{m}$, vias are not sufficient in order to suppress unwanted slot-line modes on CPWG structures. As shown in Fig. 1.3 air bridges can be placed across the ground planes of a CPWG. This shortens the slot line modes. However, the field distribution for the CPWG mode also changes. Thus, the wave impedance of a line with an air bridge is slightly mismatched.

Capacitors. Capacitors are created as MIM between the METG layer and the underlying metal layers. In order to achieve high capacity per area, the METG layer is directly applied onto the SiN layer. Capacitors are the preferred way to route DC supplies. This way the ground plane on the MET1 layer is not cut. Furthermore, the routing of the tracks as capacitors ensures a good RF short on DC connections.

Resistors. A NiCr layer, located directly on the GaAs substrate is used to realize resistors. Fig. 1.3 shows a NiCr resistor with contacts to the MET1 layer.

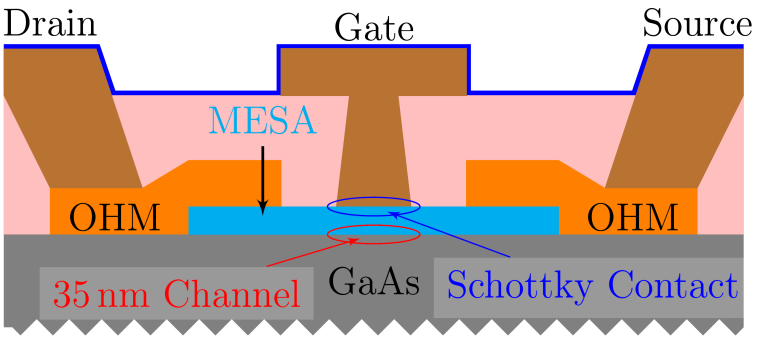

Figure 1.4: Cross section of a $35\,\mathrm{nm}$ mHEMT transistor with one finger.

Transistors. In the $35\,\mathrm{nm}$ mHEMT process transistors with a fixed gate length of $35\,\mathrm{nm}$, a variable gate width and a different number of fingers are available. Fig. 1.4 shows the cross-section of a single gate-finger. The transistor channel is located at the interface plane of the GaAs substrate with the mesa layer. A so called electron gas forms at the interface of both layers. This electron gas consists of unbound electrons with a very high mobility, which allows the mHEMT to achieve high operating frequencies [LTM+08]. Because the channel is conductive by default, the transistor is a depletion type field effect transistor (FET). In order to pinch off the transistor, a negative gate-source voltage must be applied. This pinches of the channel under the gate finger.

In contrast to a MOSFET, the gate is not isolated through an insulator like an oxide. The junction between the metal terminal of the gate and the underlying mesa layer forms a Schottky barrier. This contact isolates the gate and the transistor channel for negative gate-source voltages. Positive gate-source voltages are only applicable up to the threshold voltage of the Schottky contact. If the threshold voltage is exceeded, current flows into the gate and the isolation between gate and channel is lost.

Fig. 1.5 shows the simulated set of output current, I_D, versus drain source voltage, V_DS for different gate voltages for a transistor with two fingers and a gate width of $10\,\mu\mathrm{m}$. Up to a voltage of $0.2\,\mathrm{V}$ the transistor is in its linear operation area. Beyond this voltage the transistor operates in saturation. The on-state breakdown voltage of the transistor, on-state drain-source breakdown voltage ($V_\mathrm{DS,Bon}$), is as stated in Table 1.2 $1.5\,\mathrm{V}$. For safety reasons the maximum drain source voltage, V_DS, applied to transistors will be $1\,\mathrm{V}$.

1.3 Thesis outline

Given the context of the wireless demand in our society and the prediction for ever growing data rates the goal of this thesis can be determined. Two types of architectures that can be employed in THz communication systems for beyond 5G networks are examined. The common zero-IF or direct conversion approach has been the architecture of choice for all wireless transmission experiments employing THz technologies until now. The second architecture is the new superheterodyne approach, never used before in THz links. For each architecture a wireless front end composed of one transmitter and one receiver is designed. Wireless data transmissions are conducted, the quality of the data transfer is investigated and main impairments are identified. The main goal is to investigate which of the two architectures

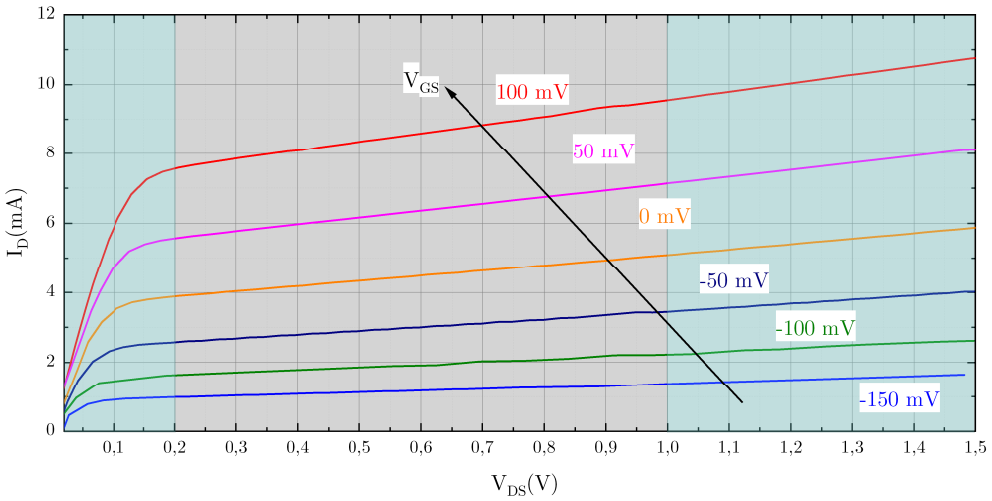

Figure 1.5: Simulated output characteristic of a two finger $35\,\mathrm{nm}$ mHEMT transistor with a gate width of $10\,\mu\mathrm{m}$. The model does not consider breakdown.

offers more advantages and is more likely to be used for future ultra-fast communication systems. The present work is organized as follows:

Chapter 2 describes the main components of a THz wireless communication system. Impairments and ways of evaluating the quality of a wireless transmission are discussed. Furthermore, the differences between the two types of architectures are treated.

Chapter 3, Chapter 4 and Chapter 5 handle the first type of architecture: the direct conversion approach. In **Chapter 3** both the transmitter and the receiver are based on solid-state electronics, employing the $35\,\mathrm{nm}$ mHEMT process developed at IAF. The focus of this chapter is on methods of evaluating the performance of the transmission and the optimal configuration of the THz wireless link. **Chapter 4** presents a $300\,\mathrm{GHz}$ wireless transmission using a photonic transmitter and an electronic receiver. The comparison between all electronic and hybrid links is another goal of this thesis.

In **Chapter 5** an optimized active electronic receiver is presented. The goal of this receiver is to be employed in a similar transmission experiment, as the one presented in Chapter 4, combining photonic and electronic technologies to reach a high data rate and a system compatible with the standards needed for beyond-5G communication networks.

Chapter 6 and Chapter 7 present the new superheterodyne approach. In **Chapter 6** the proof-of-concept for this new architecture is demonstrated based on the zero-IF frontend presented in Chapter 4. Finally, in **Chapter 7** a new transmit-receive chipset is presented designed specifically for superheterodyne operation.

The tremendous potential of THz links has led to considerable interest in both industry and academia, with a growing belief that THz bands will play a significant role in beyond 5G cellular systems [BHL+14]. THz links are anticipated to revolutionize the communications research, academia and industry communities, changing the way of accessing information replacing and transforming traditional applications.

2 Essential Aspects of a THz Wireless Link

Wireless communication is one of the biggest successes of technological progress made in the last two decades. For a long time it was associated with cellular telephony but in the last years wireless communication networks have extended to a manifold of application, growing further each year. The ultimate performance limits of wireless systems are determined by the quality of each component. This chapter describes the general structure of a transceiver, the various blocks in a transmitter and receiver as well as signal processing aspects crucial for the wireless transmission. The task of designing a future wireless communication network involves finding the perfect trade-off between hardware and software performance.

Fig. 2.1 presents a simplified diagram of a wireless transmission system. In general, the goal of such a transmission is to transmit information from an analog source to an analog sink over a certain propagation channel. The source could be, for example, a microphone or a camera and the sink could be a screen. There are many examples where the source and the sink are already digital in which case the first two steps can be omitted. In general a wireless link can be divided into three components: the signal processing hardware including the information source and sink, the wireless frontend including the transmitter and the receiver and the propagation channel.

The information source is an analog signal that is converted into a digital one by the analog-to-digital converter (ADC), which converts the signal into a stream of digital data at a certain sampling rate and resolution denoting the number of bits per sample. The source codes help reduce redundancy in the source signal and thus reduce the amount of transmitted data and required bandwidth. This is where encryption takes place to protect sensitive data. The channel coder helps increase the transmission quality by reducing transmission errors. They use information about the statistics of error sources in the channel like noise power or interference statistics to design codes that are well suited for certain types of channels. The baseband modulator assigns the gross data bits to complex transmit symbols in the baseband. Spectral properties, intersymbol interference, peak-to-average ratio, and other properties of the transmit signal are determined by this step. The transmitted symbols at this point are in oversampled form and discrete in time and amplitude. The digital to analog converter (DAC) translates this signal in discrete amplitude voltages corresponding to the real and imaginary part of the transmitted symbols. This signal is applied to the up-converter, which is part of the transmitter, and is converted here to a passband signal by mixing it with the local oscillator (LO) signal. The transmitted signal is, in general, filtered and amplified.

The propagation channel attenuates the signal and leads to delay and frequency dispersion. Here additive white Gaussian noise (AWGN) and co-channel interference are the most influential factors. The signal then travels through a very similar path as in the transmitter, but in the other direction. In the receiver a low-noise amplifier (LNA) is required to reduce the noise in the subsequent stages. The receiver ADC converts the analog received signal into

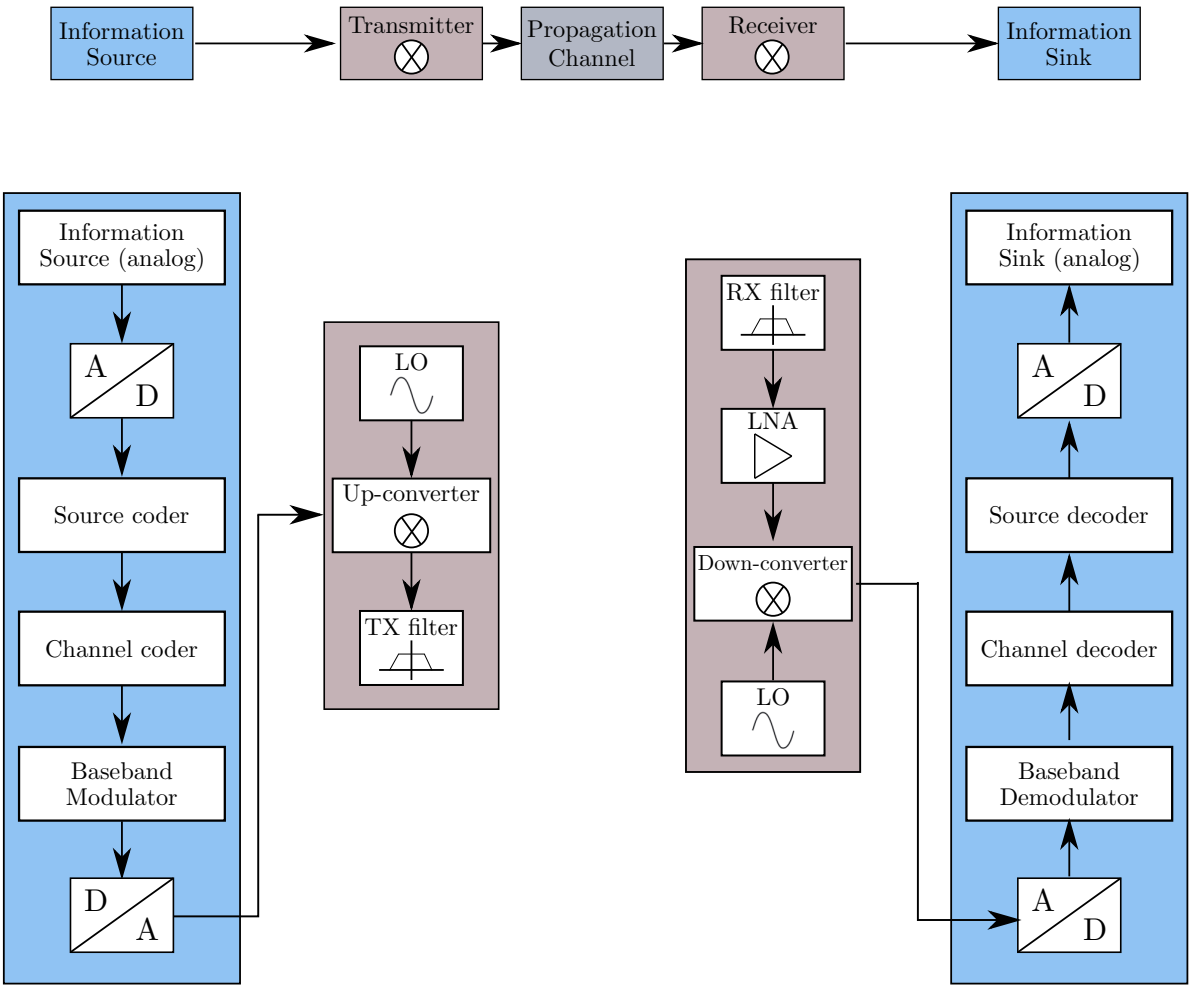

Figure 2.1: General block diagram of a wireless link.

discrete amplitude values. The baseband demodulator can include further signal processing like equalization.

This is the general description of a wireless link, and it applies also for the links described in this thesis, designed for future generations of wireless networks. In the cases presented in this work the signal processing hardware including the information source and sink is provided by commercially available waveform generator and oscilloscopes which integrate all the components graphically presented in Fig. 2.1.

2.1 Modulation formats

Each bit of the data stream that reaches the baseband modulator in the transmitters signal processing hardware is mapped to a certain signal waveform, which is called digital modulation. The wireless propagation channel is an analog medium. Thus, this step cannot be spared. The number of bits mapped to a single analog waveform depends on the type of modulation. The most simple modulation is binary amplitude modulation, where a $+1$-bit value is mapped to a specific amplitude and 0-bit value to another amplitude. If the assumption is made that a symbol has K bits, a number of $\mathrm{M} = 2^{\mathrm{k}}$ waveforms are necessary to fully map this symbol.

Different modulation formats differ in the waveforms that are transmitted, and in the way the mapping is achieved.

To mathematically describe different modulation formats a bandpass signal, $\mathrm{s_{BP}(t)}$, is defined in relation to the complex baseband (low-pass), $\mathrm{s_{LP}(t)}$, representation as:

$$s_{\mathrm{BP}}(t) = \mathrm{Re}\{s_{\mathrm{LP}}(t)\exp[j2\pi f_{\mathrm{c}}t]\}. \tag{2.1}$$

For pulse amplitude modulation (PAM) formats a basis pulse, $g(t)$ is multiplied with a modulation coefficient c_{i}:

$$s_{\mathrm{LP}}(t) = \sum_{i=-\infty}^{\infty} c_{\mathrm{i}} g(t - \mathrm{i}T_{\mathrm{S}}) \tag{2.2}$$

where T_{S} is the duration of a symbol. This means the analog waveform of the transmitted signal is a series of time-shifted basis pules.

Different PAM formats differ in how the data bits b are mapped to the modulation coefficients c. The assumption that the basis pulses are normalized to unit average power leads to:

$$\int_{-\infty}^{\infty} |g(t)|^2 dt = \int_{-\infty}^{\infty} |G(f)|^2 df = T. \tag{2.3}$$

The most simple pulse is a rectangular pulse with a duration of T defined by the equation:

$$g_{\mathrm{R}}(t,T) = \begin{cases} 1, & \text{if } 0 < t < T \\ 0, & \text{otherwise} \end{cases} \tag{2.4}$$

which can be transformed in frequency domain to:

$$G_{\mathrm{R}}(f,T) = T\mathrm{sinc}(\pi f T)\exp(-j\pi f T), \tag{2.5}$$

where $\mathrm{sinc}(x) = \sin(x)/x$.

The disadvantage of this pulse is that the spectrum extends over a large bandwidth. The first sidelobes are only $13\,\mathrm{dB}$ weaker than the maximum. This leads to a large adjacent channel interference and to a decrease of the spectral efficiency of a system. This is the reason why pulses with stronger roll-offs in the frequency domain are required. Among them, the Nyguist pulse is one of the most common. They fulfill the Nyguist criterion and do not lead to intersymbol interference [Mol10]. The raised cosine pulse is a good example of Nyguist pulses and has a roll-off that follows a sinusoidal shape. The roll-off factor, α, is the parameter showing the steepness of spectral decay. The pulse has the following time domain definition:

$$G_{\mathrm{N0}}(f,\alpha,T) = \begin{cases} 1, & 0 \le |2\pi f| \le (1-\alpha)\frac{\pi}{T} \\ \frac{1}{2}\cdot\Big(1 - \sin\Big(\frac{T}{2\alpha}(|2\pi f| - \frac{\pi}{T})\Big)\Big), & (1-\alpha)\frac{\pi}{T} \le |2\pi f| \le (1+\alpha)\frac{\pi}{T} \\ 0, & (1+\alpha)\frac{\pi}{T} \le |2\pi f| \end{cases} \tag{2.6}$$

The spectrum of the raised cosine pulse is

$$G_{\mathrm{N}}(f,\alpha,T) = \frac{T}{\sqrt{1-\frac{\alpha}{4}}} \cdot G_{\mathrm{N0}}(f,\alpha,T)\exp(-j\pi f T_{\mathrm{S}}). \tag{2.7}$$

A root-raised cosine filter denotes a filter where both the transmitter pulse spectrum and the receiver filter spectrum are the square root of a raised cosine spectrum.

The constellation diagram represents the analog transmit symbol as vectors (points) in a finite-dimensional space. It is one of the most useful tools in the performance assessment of wireless transmissions, providing a graphical representation of signals that allows an intuitive and uniform treatment of different modulation formats. It displays the signal as a two-dimensional xy-plane scatter diagram in the complex plane at symbol sampling instant.

Binary phase shift keying (BPSK) modulation is the simplest modulation method where the carrier phase is shifted by $\pm\pi/2$, depending on whether a $+1$ or a -1 is sent. BPSK can be viewed either as a phase modulation or as PAM. In the first case, the data stream influences the phase of the transmit signal. Depending on the data bit, b_{i}, the phase of the transmitted signal is $\pi/2$ or $-\pi/2$. In the more popular interpretation, as a PAM the basis pulses are rectangular pulses with amplitude 1, so that

$$s_{\mathrm{BP}}(t) = \sqrt{2E_{\mathrm{B}}/T_{\mathrm{B}}}P_{\mathrm{D}}(t)\cos\Big(2\pi f_{\mathrm{c}}t + \frac{\pi}{2}\Big) \tag{2.8}$$

where

$$P_{\mathrm{D}}(t) = \sum_{i=-\infty}^{\infty} b_{\mathrm{i}}g(t-iT) = b_{\mathrm{i}} * g(t) \tag{2.9}$$

and

$$g(t) = g_{\mathrm{r}}(t, T_{\mathrm{B}}). \tag{2.10}$$

In equivalent baseband, the complex modulation symbols are $\pm j$:

$$c_i = j \cdot b_i \tag{2.11}$$

so that the real part of the signal is

$$\mathrm{Re}s_{\mathrm{LP}}(t) = 0 \tag{2.12}$$

and the imaginary part is

$$\mathrm{Im}s_{\mathrm{LP}}(t) = \sqrt{\frac{2E_{\mathrm{B}}}{T_{\mathrm{B}}}}P_{\mathrm{D}}(t). \tag{2.13}$$

Due to the unfiltered rectangular basis pulse, the envelope has a constant amplitude, except at times $t = iT_{\mathrm{B}}$, and it has a low bandwidth efficiency. This parameter can be improved by using a filter with a higher roll-off factor.

Quadrature phase shift keying (QPSK)-modulated signals are PAM where the signal carries $1\,\mathrm{bit}$ per symbol interval on both the in-phase and quadrature-phase component. The original data stream is split in two streams, $b1_i$ and $b2_i$, each of which has a data rate, R_{S}, that is

half of the original data stream, R_{B}. Considering a QPSK signal with a rectangular pulse $g(t) = g_{\mathrm{R}}(t, T_{\mathrm{S}})$, the signal contains the following two sequences:

$$\begin{aligned} P1_{\mathrm{D}}(t) &= \sum_{i=-\infty}^{\infty} b1_i g(t - iT_{\mathrm{S}}) = b1_i * g(t) \\ P2_{\mathrm{D}}(t) &= \sum_{i=-\infty}^{\infty} b2_i g(t - iT_{\mathrm{S}}) = b2_i * g(t) \end{aligned} \tag{2.14}$$

The bandpass signal results in

$$S_{\mathrm{BP}}(t) = \sqrt{E_{\mathrm{B}}/T_{\mathrm{B}}}[P1_{\mathrm{D}}(t)\cos(2\pi f_c t) - P2_{\mathrm{D}}(t)\sin(2\pi f_c t)] \tag{2.15}$$

and the baseband signal in

$$s_{\mathrm{LP}}(t) = [P1_{\mathrm{D}}(t) + jP2_{\mathrm{D}}(t)]\sqrt{E_{\mathrm{B}}/T_{\mathrm{B}}}. \tag{2.16}$$

The spectral efficiency of QPSK is twice the efficiency of BPSK, due to the in-phase and quadrature-phase components. As in the case of BPSK, the usage of a filter with a higher roll-off factor leads to improvements in efficiency and is recommended.

Higher order modulation formats transmit more information in each symbol interval, resulting in a higher spectral efficiency, but being more sensitive to noise and interference. Higher order quadrature amplitude modulation (QAM) transmit multiple bits in the in-phase and the quadrature-phase component, by sending a signal with positive and negative polarity and multiple amplitude levels on each component. The mathematical representation is the same as for QPSK, just that in the pulse sequences of Eq. 2.14 not only the levels ± 1 are allowed but $2m - 1 - \sqrt{M}$, with $m = 1, \cdots, \sqrt{M}$ with M being the number of bits for each modulation format. The disadvantage of higher order QAM is the strong variations of output power, which requires the usage of very linear transmitters and receivers. Fig. 2.2 shows the constellation diagrams of the most common used modulation formats, that will appear in this thesis and are relevant for wireless links in the mmW range: 16-QAM ($M = 4$), 32-QAM ($M = 5$), 64-QAM ($M = 6$) and 256-QAM ($M = 8$).

2.2 Frequency transfer function of a linear system

To characterize a linear and time-invariant system the transfer function can be used. The signal applied at the input of the system can be described in time-domain, $x(t)$. At the output the signal $y(t)$ can be measured and the impulse response, $h(t)$, of the system can be defined. When the input signal is transformed in the frequency domain a frequency transfer function, $H(f)$ of the system can be defined. Fig. 2.3 shows a graphical representation of the above mentioned functions. It is assumed that there is no stored energy at the time the input is applied.

The response of a network to an arbitrary input signal, $x(t)$, is the convolution of $x(t)$ with $h(t)$

$$y(t) = x(t) * h(t) = \int_{-\infty}^{\infty} x(\tau)h(t - \tau)d\tau. \tag{2.17}$$

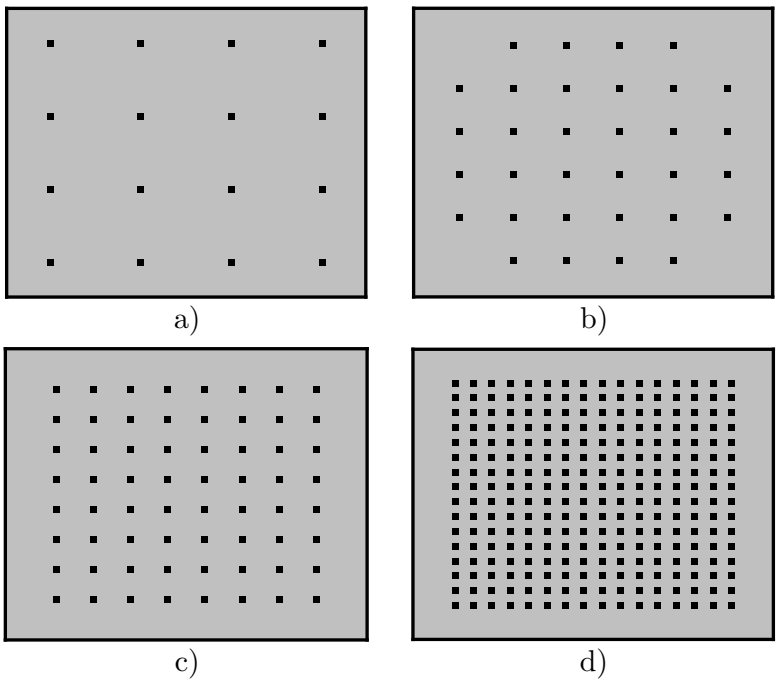

Figure 2.2: Ideal constellation diagram for the most common modulation formats for THz wireless links: a) 16-QAM, b) 32-QAM, c) 64-QAM, d)128-QAM.

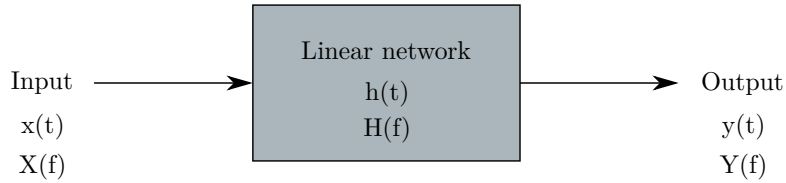

Figure 2.3: The input and output functions of a linear system in time- and frequency-domain..

The system is assumed to be causal, considering the input signal is applied at time $t = 0$ and there is no output signal before this. Hence the output becomes

$$y(t) = \int_0^\infty x(\tau)h(t-\tau)d\tau = \int_0^\infty x(t-\tau)h(t)d\tau \tag{2.18}$$

The output signal in frequency domain is obtained by the Fourier transform of this equation

$$Y(f) = X(f)H(f). \tag{2.19}$$

The frequency transfer function is complex and can be divided into a real and an imaginary part or a magnitude, $|H(f)|$, and a phase response, $\theta(f)$.

$$H(f) = |H(f)|e^{j\theta(f)} \tag{2.20}$$

The frequency transfer function of a linear time-invariant system can be measured with an input signal generated by a network analyzer and an oscilloscope measuring the output. At each step the amplitude and phase at the output are measured.

In the wireless systems presented in this thesis the frequency transfer function represents an important starting point for the characterization of the performance and transmission quality of the link.

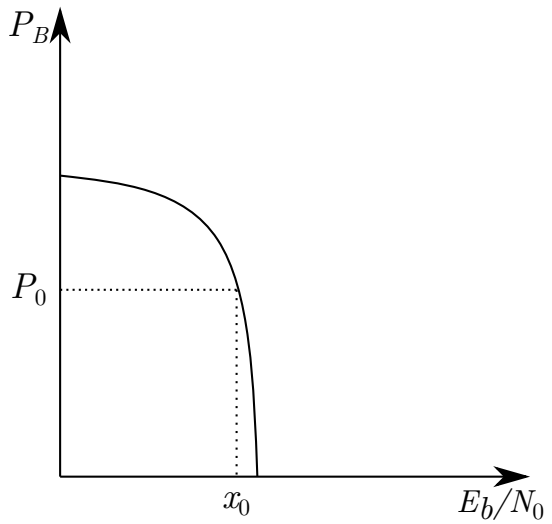

Figure 2.4: General shape of the bit error probability in dependency of E_b/N_0.

2.3 Performance assessment of a wireless transmission

In analog communication the most powerful figure of merit for a wireless transmission is the *average signal power to average noise power ratio* (signal-to-noise ratio (SNR)). In digital communication a normalized version of SNR is often used: E_b/N_0. E_b is the bit energy and is equal to the signal power S multiplied by the duration of a bit, T_b. N_0 is the noise power spectral density and is equal to the noise power N divided by the bandwidth B.

$$\frac{E_b}{N_0} = \frac{S\ T_b}{\frac{N}{B}} = \frac{S}{N}(\frac{B}{R}) \tag{2.21}$$

The bit error rate is the number of bit errors per time unit. The *bit error ratio* is the number of errors divided by the number of transmitted bits and is dimensionless. When infinitely many bits are transmitted this parameter transforms into bit error probability P_B.

Fig. 2.4 shows the dependency of P_B on E_b/N_0. The smaller E_b/N_0 the more efficient is the detection process for a given probability of error. Given the probability of a transmitted signal and the noise vector affecting this signal the probability of the detector making an incorrect decision is also called the probability of symbol error, P_E. Although decisions are made on the basis of symbols P_B is the more convenient system performance figure of merit.

To determine the exact number of errors in a transmitted signal using the bit error rate requires an effort for high order modulation formats. Furthermore, to achieve statistical meaningful results a certain number of bits have to be detected, which directly leads to very long measurement times, especially when the performance seems to be good and very few errors appear [SRI06]. Another method of estimating the quality of the transmission is by evaluating the constellation diagram in combination with an error vector magnitude (EVM) measurement. This method is independent of modulation format and is faster than a BER measurement, since it is based on the comparison between the received symbol and the expected one. Another advantage is that this method gives information about the root cause of the error, since specific non-idealities show a different pattern on the constellation diagram.

Fig. 2.5 shows the graphical representation of an erroneous symbol, s_1', when s_1 is the transmitted and desired received symbol. The EVM is defined as the mean-square error

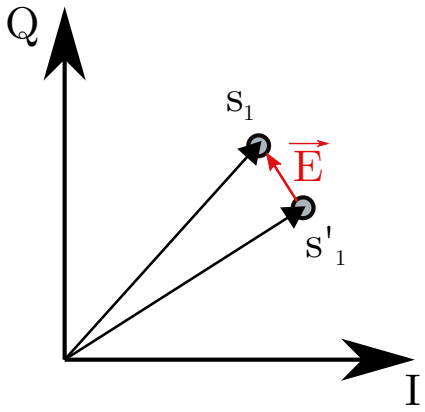

Figure 2.5: Graphical representation of EVM in a constellation diagram

between the samples of the actual and the ideal symbol vectors in the constellation diagram, normalized by the average power of the ideal symbol [Gu05]. EVM is measured in $\%$ and the mathematical definition is:

$$\mathrm{EVM}_{rms} = \sqrt{\frac{\frac{1}{N}\sum_{n=1}^{N}|s_r - s_i|^2}{\frac{1}{N}\sum_{n=1}^{N}|s_1|^2}} = \sqrt{\frac{\frac{1}{N}\sum_{n=1}^{N}|s_r - s_i|^2}{P_{avg}}}, \tag{2.22}$$

where N is the total number of symbols, s_r is the received symbol (s_1' in Fig. 2.5), s_i is the ideal received symbol and $\mathrm{P_{avg}}$ the average symbol power [SRI06].

Very important for the performance assessment of wireless transmission in the mmW range is the availability of dedicated baseband equipment. Data sources, that provide a high-speed data stream for the transmitter and data sinks, which receive the IF signal from the receiver and evaluate the received bits with the transmitted one.

In this thesis the following hardware will be used to asses the performance of the analog wireless links. On the transmitter side, an arbitrary waveform generator (AWG) will be employed. This piece of equipment uses ADCs and DACs to digitally process any wanted waveforms and convert them into an analog signal. On the receiver side, a broadband real-time oscilloscope represents the data sink. The bandwidth of the high-speed ADCs and DACs inside these measurement equipment needs to be in the same range as the wireless system's IF bandwidth. Furthermore, according to the Nyguist-Shannon-Theorem the sampling frequency of these equipment has to be at least twice the highest used frequency. For example, if a wireless system uses a $2\,\mathrm{GHz}$ IF frequency the sampling frequency of the data source and sink has to be at least $4\,\mathrm{GHz}$. The state-of-the-art AWG, at the time of writing this thesis, has a sample rate of $120\,\mathrm{GSa/s}$ combined with a bit resolution of $14\,\mathrm{bits}$ an analog bandwidth of $50\,\mathrm{GHz}$, while the state-of-the-art oscilloscope provides sample rates of $256\,\mathrm{GS/s}$ and an analog bandwidth of $110\,\mathrm{GHz}$ [Keya].

The digital carrier recovery as well as the digital demodulation is performed by a software, which also provides the possibility of using an equalization filter on the received signal. Information about the demodulation process of the software used for this thesis can be found in [Keyb]. An adaptive feed-forward equalizer can be applied to the measurement signal to remove linear errors like group delay, distortion, frequency response errors. Equalization refers to any signal processing or filtering technique that is designed to eliminate or reduce intersymbol interference (ISI).

Figure 2.6: Simplified model of a wireless transmission.

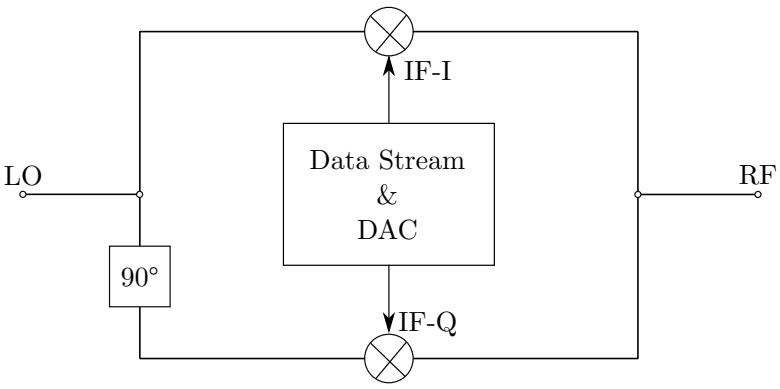

Figure 2.7: Ideal quadrature modulator.

A wireless communication channel can be characterized by an impulse response $h(t)$ and a frequency response $H(f)$, as is described in equation 2.20. $|H(f)|$ must be constant over the signal's bandwidth for an ideal, nondistorting transmission. Furthermore, $\theta(f)$ must be a linear function of frequency, hence the delay must be constant for all spectral components of the signal. Amplitude distortion is the effect of a varying $|H(f)|$ and phase distortion is the effect of a not linear $\theta(f)$ function. In many cases amplitude and phase distortion appear together.

Equalization uses two main processes. The maximum-likelihood sequence estimation (MLSE) measures $h_c(t)$ and provides a mean of adjusting the receiver to the transmission environment. The goal is to provide the detector with a good estimation from the demodulated distorted pulse sequence. The second technique uses filters to compensate the distorted pulses. The detector is presented with a sequence of demodulated samples which are free of effects of ISI. This is the most popular approach and it is used in the software processing tool employed in this thesis. The filters for this technique can be either linear, containing feedforward elements (transversal equalizers) or nonlinear devices that contain both feedforward and feedback elements (decision feedback equalizers). Another important parameter is the automatic nature of their operation which can be either preset or adaptive.

2.4 Most common impairments of a wireless transmission in the THz range

Fig. 2.6 shows the simplified model of a wireless transmission on the basis of which the most common impairments can be defined. The channel is considered to be AWGN. For most wireless links presented in this thesis the modulator and the demodulator are IQ type. The in-phase (IF-I) and quadrature (IF-Q) signals are applied to mixers fed by cosine and sine LO signals, like shown in Fig. 2.7.

The first type of impairments are caused by asymmetry in the I- and Q-path, like different losses in the couplers, in the transistors of the two mixers or a deviation of the ideal $90°$

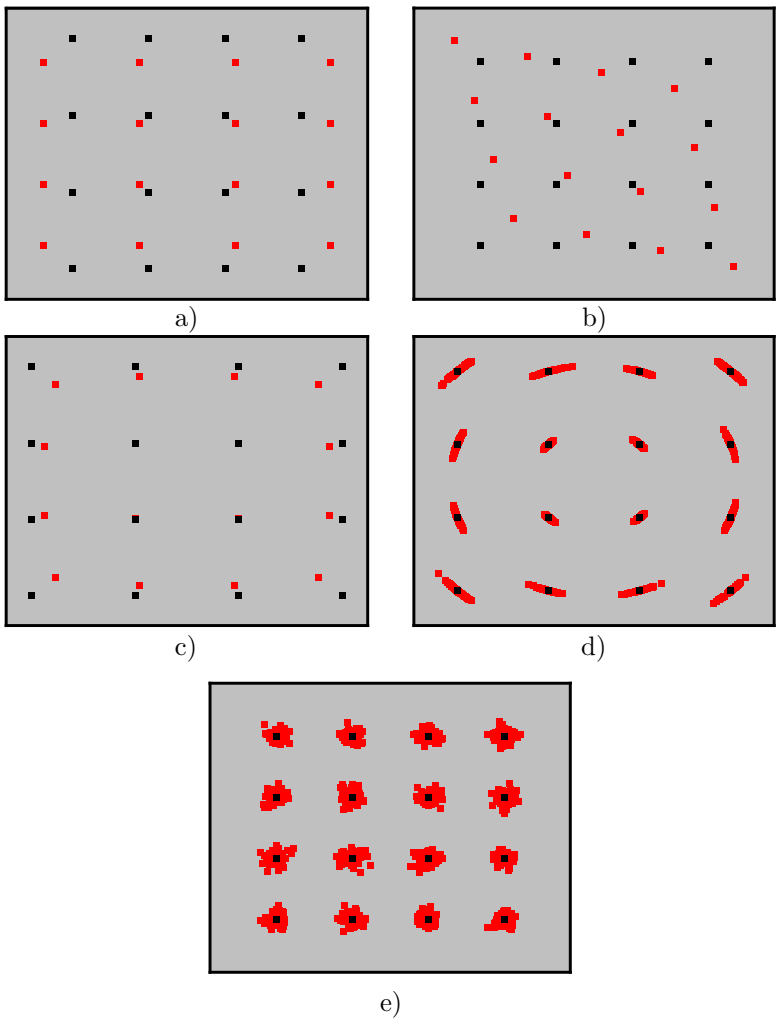

Figure 2.8: Impairments of wireless transmission observed on a 16-QAM constellation diagram. a) Gain imbalance b) Phase imbalance c) Compression d) Phase noise e) Gaussian noise

phase difference between channels. This asymmetry causes IQ-amplitude and phase errors and their effect on the constellation diagram can be seen in Fig. 2.8 a) and b) for the case of a 16-QAM modulated signal. Here the black dots represent the ideal transmitted and demodulated symbol and the red ones represent the actual demodulated symbol, considering only one impairment at a time for simplicity.

When a system is considered linear, the gain is obtained under the assumption that harmonics do not exist. When the signal amplitude increases, the gain begins to vary. If the output is a saturating function of the input, the gain approaches zero for high input levels. In the case of linearity impairments the demodulated signal shows amplitude imbalances in the outer symbols and fewer imbalances for the inner ones, like shown in Fig. 2.8 c). This can be explained by the higher peak power of the outer symbols, which drive the link components into saturation.

The next impairment is introduced by the LO source, an oscillator which is susceptible to noise. The constituent devices of the oscillator inject noise that leads to a random deviation of the generated frequency, while the amplitude remains constant. The LO signal has the following mathematical expression:

$$x_{LO}(t) = A\cos[\omega_{LO}t + \phi_n(t)], \tag{2.23}$$

where A is the amplitude of the signal and $\phi_n(t)$ is the function called phase noise. For an ideal sinusoidal oscillator operating at ω_{LO}, the spectrum is a perfect Dirac impulse, while for an oscillator which takes into account phase noise the spectrum exhibits a skirt around the carrier frequency. Phase noise corrupts the information carried in the carrier. The effect of this impairment on the transmission quality can be observed in Fig. 2.8 d). All symbols have a phase shift, but the outer ones are affected most by this effect. The phase noise generated in the LO source is amplified by the subsequent multiplier stages by a factor of $20\log N$, where N is the multiplication factor.

Fig. 2.8 e) shows the effect of Gaussian noise on the demodulated signal. All symbols are equally affected by this impairment. The term noise refers to unwanted electrical signals. The presence of noise superimposed on a signal deteriorates the transmitted signal and limits the receiver's ability to demodulate correctly. Noise sources that can affect signals in wireless transmissions are switching transients, other electromagnetic signals, the atmosphere, etc. Noise can be eliminated through careful design of the system: filtering, shielding, choice of modulation and selection of transmission location. There is one source of natural noise that cannot be eliminated, thermal or Johnson noise, caused by the thermal motion of electrons. The main characteristic of thermal noise is that its power spectral density is the same for all frequencies of the desired signal. Such noise is also called white noise, similar to the white light, which has equal amount of all frequencies in the visible band of electromagnetic radiation. The effect on the detection process of a channel with AWGN is that the noise affects each symbol independently. Additive means, in this case, that the noise is superimposed or added to the transmitted signal.

2.5 Zero-IF and superheterodyne architectures

Information starts as an analog baseband signal with its lowest frequency close to zero: audio, video, sensors, images, etc. An easy way to transmit this information is to multiply or heterodyne the baseband signal with a carrier signal, $\cos(2\pi f_c t)$. The final signal can be expressed as

$$x_c(t) = x(t)\cos 2\pi f_c t. \tag{2.24}$$

In frequency domain this leads to

$$X_c(f) = \frac{1}{2}[X(f - f_c) + X(f + f_c)] \tag{2.25}$$

This resulting signal has two components, called sidebands. Fig. 2.9 shows the graphic representation of the above equation. The part of the spectrum above f_c is called upper sideband and the part below lower sideband. Mirror images in the negative frequency also appear, but they are not represented here for simplicity. The carrier wave is most commonly referred to as the local oscillator and is much higher in frequency than the upper edge of the baseband signal. In terms of bandwidth a double sideband transmission requires twice the bandwidth compared to the baseband.

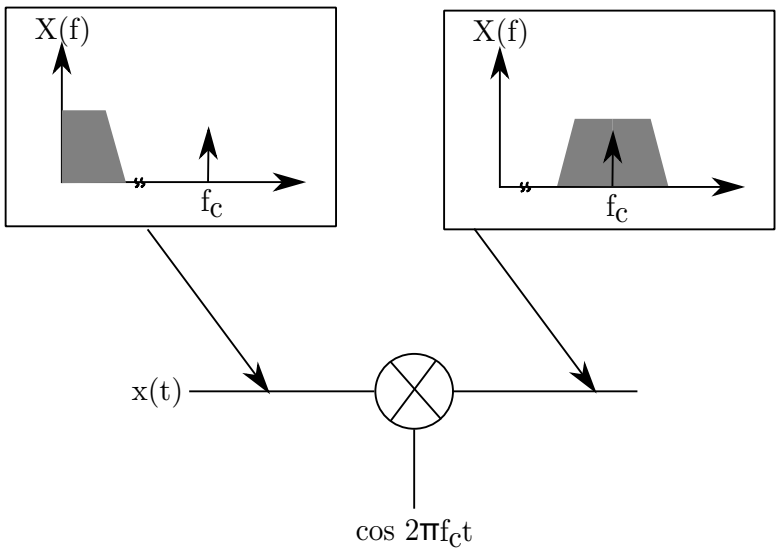

Figure 2.9: Double sideband transmission of a baseband signal.

Bandwidth can be defined in various ways. All definitions attempt to specify a measure of a spectral density defined for all frequencies. The single-sided power spectral density for a signal $x_c(t)$ has the following definition:

$$G_x(f) = T\left(\frac{\sin \pi(f - f_c)T}{\pi(f - f_c)T}\right)^2 \tag{2.26}$$

where T is the pulse duration. This power spectral density characterizes a random pulse sequence and can be represented as in Fig. 2.10. The plot consists of a main lobe and smaller symmetrical sidelobes. The general shape of the plot is valid for most digital modulation formats. However, some modulation formats do not have well-defined lobes.

As depicted in Fig. 2.10 following bandwidth definitions can be used:

- Half-power bandwidth or 3-dB bandwidth (a). Is the bandwidth at which the spectral density has decreased to a value that is $3\,\mathrm{dB}$ below its maximum value.
- Noise equivalent bandwidth (b). This was originally conceived to permit rapid computation of output noise power from an amplifier with a wideband noise input.
- Null-to-null bandwidth (c). This is the most popular measure of bandwidth for digital communication, representing the width of the main spectral lobe, where most of the power is contained. This is applicable for modulation formats that have a defined main lobe.
- Fractional power containment bandwidth (d). This criterion states that the occupied bandwidth is the band that leaves exactly $0.5\,\%$ of the signal power above the upper band limit and exactly $0.5\,\%$ of the signal below the lower band limit. Hence, this band includes $99\,\%$ of the signal power.
- Bounded power spectral density. Is the bandwidth at which the spectral density has decreased to a defined value below its maximum. This value could be 35 or $50\,\mathrm{dB}$.

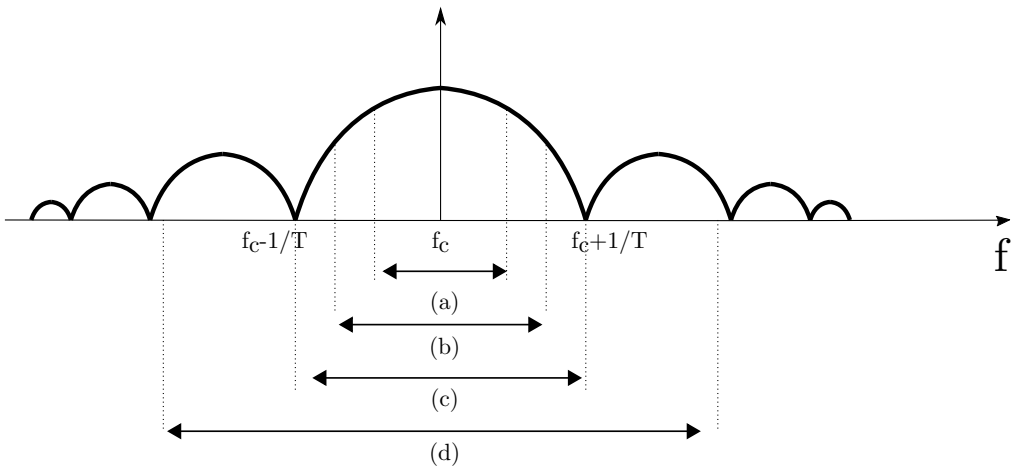

Figure 2.10: Possible bandwidth definitions based on a random pulse sequence and its power spectral density.

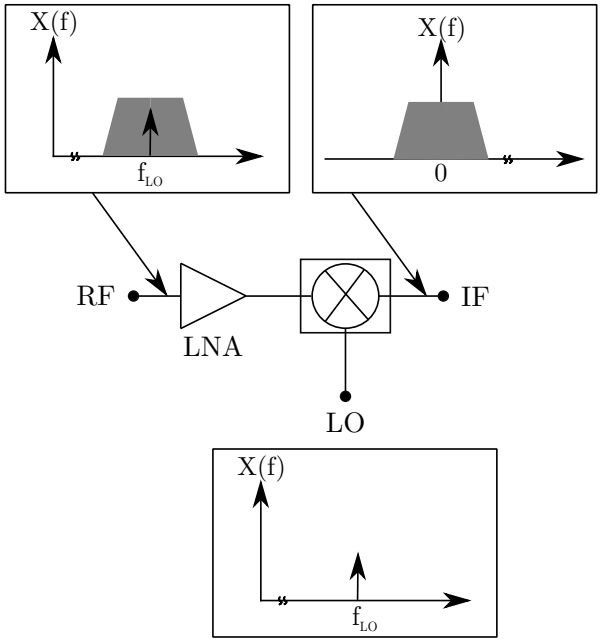

Figure 2.11: Simplified model of a direct-conversion receiver

- Absolute bandwidth. Outside this band the spectrum is zero. For all realizable waveform this is infinite.

In this work bandwidth typically refers to the null-to-null bandwidth, unless stated otherwise.

For wireless transmission systems and transceivers working from the low GHz range to the low THz range different architectures can be employed. In literature they are defined separately for the receiver and the transmitter. There are a variety of approaches for reception because noise issues, interference rejection, and band selectivity are less problematic in transmitters. For the terahertz wireless links presented in this thesis the transmitter and the receiver share the same architecture, hence the nomenclature will be applied to the whole system.

The **direct-conversion architecture** has been up to now the architecture of choice for wireless links operating in the low THz region. This architecture is also called zero-IF.

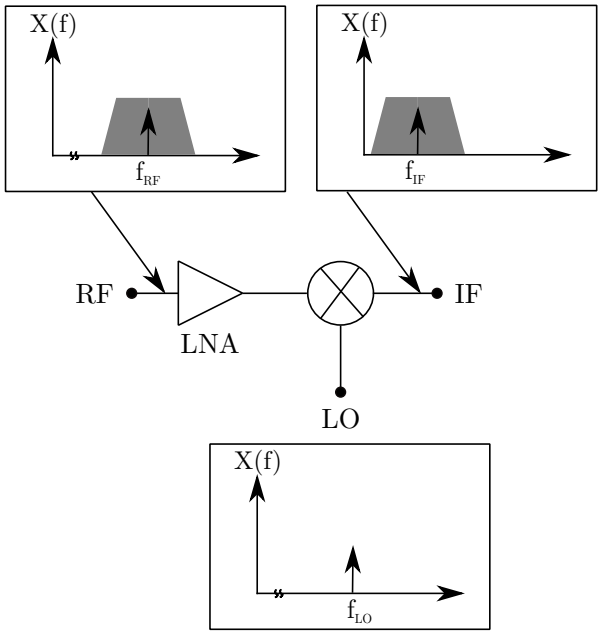

Figure 2.12: Simplified model of a superheterodyne receiver

Fig. 2.11 shows the simplified model of a zero-IF receiver. The LO frequency is equal to the input carrier frequency and the intermediate frequency (IF) is centered around $0\,\mathrm{Hz}$, hence the name zero-IF. The requirement for this architecture is that the mixer in Fig. 2.11 sustains double-sideband transmission, hence must provide quadrature outputs to avoid loss of information.

As opposed to zero-IF in **superheterodyne architecture** the IF has a value higher than zero and the carrier frequency of the RF signal is different than the LO signal. Fig. 2.12 shows the schematic of a superheterodyne receiver, where $\mathrm{f_{IF}} = \mathrm{f_{RF}} - \mathrm{f_{LO}}$.

One of the biggest disadvantages of the superheterodyne approach is the generation of the image. The bands located symmetrically above and below the LO frequency are down-converted to the same frequency. Not only the desired $\mathrm{f_{IF}} = \mathrm{f_{RF}} - \mathrm{f_{LO}}$ is generated but also $\mathrm{f_{IF}} = \mathrm{f_{LO}} - \mathrm{f_{RF}}$, which needs to be filtered out. Depending on the system the image could have an even higher power level than the desired signal causing serious disturbances in other wireless systems. The solution to this problem is the usage of image reject filters, which have a small loss in the band of the signal and a large attenuation outside. Although feasible this solution brings a higher complexity to this otherwise very simple architecture. Despite this complexity and the need for a larger number of external components, heterodyning is the most reliable reception technique in conventional wireless systems in the low GHz range [Raz98].

The biggest advantage of the direct-conversion architecture is that the problem of image frequencies is avoided since $\mathrm{f_{IF}} = 0$. On the other hand, there are a few disadvantages that make this architecture less convenient for usage in wireless systems. Because of finite isolation of the LNA in Fig. 2.11 and Fig. 2.12 there is a certain amount of LO leakage appearing at the input of the LNA. This signal is mixed with the actual LO signal leading to a DC component at the IF output. This is problematic because this DC component gets amplified by the following stages and can lead to an early saturation of the system. Problematic is also the transmission of this leakage to other receivers using the same wireless standard.

Because a zero-IF architecture requires quadrature mixing asymmetries between the I- and Q-path arise. They are mainly caused by the 90° phase shifter and eventual gain and phase errors in the two different paths. Furthermore, the zero-IF architecture is more prone to even-order distortion and flicker noise because the down-converted spectrum extends to zero the $1/\mathrm{f}$ noise of devices substantially corrupts the signal.

The superheterodyne architecture provides a high sensitivity and selectivity. For a long time, the main problem in employing this type of architecture in systems operating in the low THz range was the limitation of the usable bandwidth for data transmission to what is feasible at IF frequency. The disadvantages of the highly selective filters which are difficult to implement in monolithic integrated circuits do not apply with increasing frequency. With the rapid development of 5G wireless systems a solution to the mentioned drawback arises. Wireless transmission systems that operate between 60 and $80\,\mathrm{GHz}$ which are gaining in popularity with each day that passes can serve as the IF system and provide a promising interface for the RF system in Fig. 2.12.

Like previously mentioned the prospect of the highest possible bandwidth made the zero-IF architecture the most promising for wireless links operating in the low THz region. Research in reducing the impact of its disadvantages has been the focus of most groups active in this field. With the development of mmW links in the frame of 5G, a proper IF system for the superheterodyne architecture is given and this scheme can be finally considered for the employment in THz wireless networks. The two architectures are surely not in direct competition and can coexist to supply the technical background for the high data demand future applications will bring.

3 Wireless Transmission Employing Active Electronics based on the Direct-Conversion Approach

The direct-conversion approach offers the advantage of huge available bandwidths which is the reason why this scheme has been employed in most THz wireless links up to now. The following chapter presents a link employing a transmit and receive MMIC chip set based on a $35\,\mathrm{nm}$ mHEMT technology described in section 1.2.3 of this thesis. Both transmitter and receiver employ this transistor technology, hence the wireless system is based on all-active electronics.

3.1 300 GHz transmitter and receiver MMIC chipset

The analog frontend employed in the wireless link has four core blocks: the transmitter and the receiver block, each with an LO generation block. The LO generation module consists of an overall multiplier-by-twelve, a cascade of a multiplier-by-two, followed by a multiplier-by-three and finally a multiplier-by-two. To ensure that enough input power is delivered to the transmitter and the receiver a power amplifier stage is integrated in the LO module. Fig. 3.1 shows the simplified setup of the wireless link with emphasis on the building blocks.

Fig. 3.2 shows the simplified circuit schematic and the chip photograph of the receive MMIC. The chip size is 1 x 4 mm^2. This circuit has been partially described in [1]. The $300\,\mathrm{GHz}$ receiver has an input frequency of the LO of $100\,\mathrm{GHz}$. The transmitter has a similar architecture, integrating the same LO path components and frequency converter with the only difference being the final stage, a power amplifier. The transmitter has the same dimensions and the same LO input frequency as the receiver.

The LO is multiplied by a factor of three in the frequency multiplier. The LO generation is easier at lower frequencies and has a better efficiency. The tripler used for this chip is based on a similar multiplier presented in [LTW+12] and has a single-stage FET amplifier biased under class A condition and driven into saturation by a high input power level. Driving the amplifier stage into compression leads to a trapezoidal output signal, which contains mainly the odd-order harmonics. The unwanted fundamental tone will be filtered out by the output-matching network.

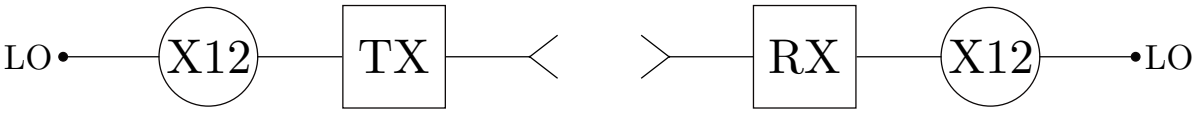

Figure 3.1: Building blocks of the wireless link based on all-active electronics.

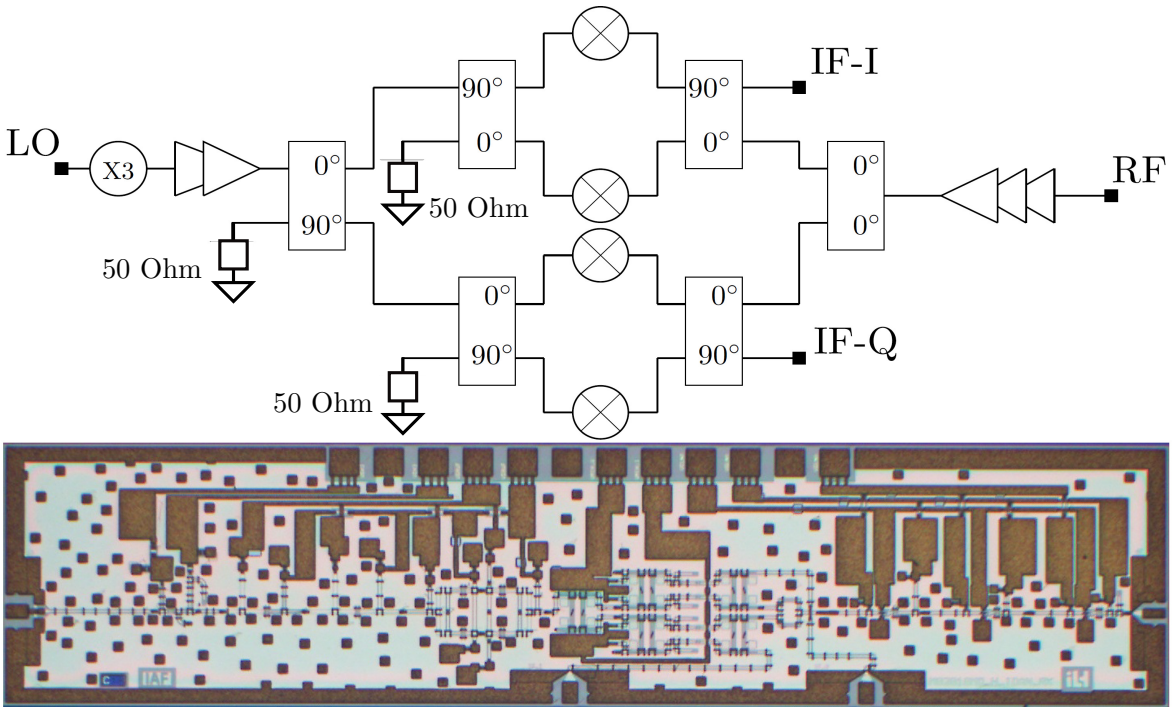

Figure 3.2: Circuit schematic and chip photograph of the $300\,\mathrm{GHz}$ receiver MMIC.

The multiplier has been measured as a stand-alone device and shows an output power at $300\,\mathrm{GHz}$ of $-12\,\mathrm{dBm}$ at $7\,\mathrm{dBm}$ LO input power. Since this power level is not enough for the mixer, a two-stage buffer amplifier is placed after the multiplier. With a gain of the amplifier of $16\,\mathrm{dB}$ the LO power at the mixer input lies at $4\,\mathrm{dBm}$, which is enough to drive the mixer in saturation with respect to the LO power.

The frequency converter is a fundamental single-balanced resistive mixer with in-phase and quadrature channels. The total phase difference generated in the I- and the Q-path of the mixer of $180°$ is responsible for the destructive interference of the LO signals and therefore for the overall LO suppression. The IF signals are fed over the isolated ports of the tandem couplers. The IF signal gets multiplied with the LO signal only in one mixer branch. The mixer in the other path receives no IF signal.

A three-stage cascode LNA provides the RF power and improves the overall signal to noise ratio due to the its low noise figure. At $300\,\mathrm{GHz}$ the amplifier has a measured small-signal gain of $19\,\mathrm{dB}$. No noise measurements for the stand-alone amplifier are available, but similar LNAs built with the same technology have a very low noise figure, around $6\,\mathrm{dB}$, which is one of the lowest published values of any MMIC technology in this frequency range [LTD+13].

The receiver is measured in an on-wafer measurement setup using coplanar probes in the appropriate waveguide bands. Measurements of the conversion gain versus LO input power at $100\,\mathrm{GHz}$ with a fixed RF frequency and power and versus RF frequency are performed. Fig. 3.3 shows the results of the receiver conversion gain under variation of the LO input power at a fix RF power of $-35\,\mathrm{dBm}$ and at an RF frequency of $300.1\,\mathrm{GHz}$. The receiver shows a saturated conversion gain of $-1\,\mathrm{dB}$. No IF amplification is used. The conversion gain results from the gain of the pre-amplifier of $19\,\mathrm{dB}$ and the conversion loss of the mixer of around $-20\,\mathrm{dB}$. To ensure full saturation of the receiver with respect to the LO an input power of $7\,\mathrm{dBm}$ is chosen for further measurements.

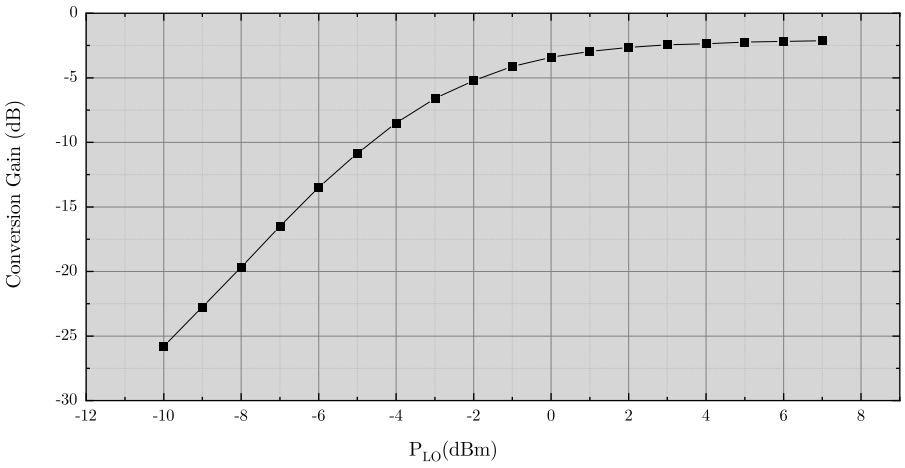

Figure 3.3: Measurement results of the receiver conversion gain under variation of the LO input power at a fix RF power of $-35\,\mathrm{dBm}$ and at an RF frequency of $300.1\,\mathrm{GHz}$.

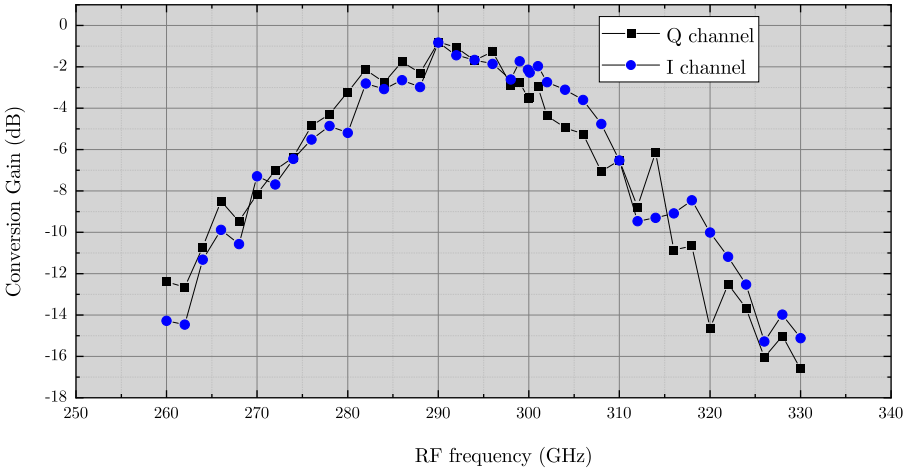

Figure 3.4: Measurement results of the receiver conversion gain under variation of the RF frequency at a fix LO input power of $7\,\mathrm{dBm}$ and at an LO frequency of $100\,\mathrm{GHz}$.

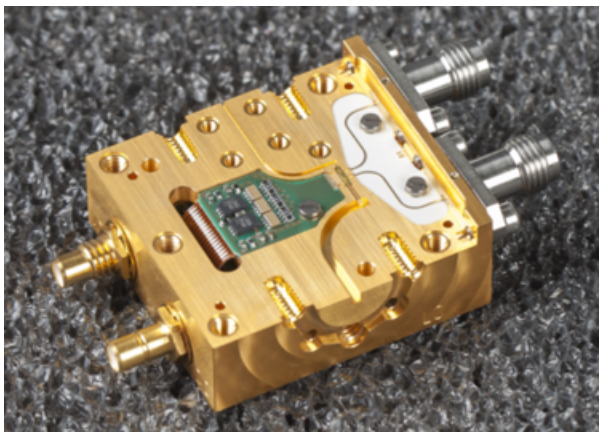

Figure 3.5: Split-block package of the 300 GHz transmitter MMIC fabricated by Fraunhofer IAF.

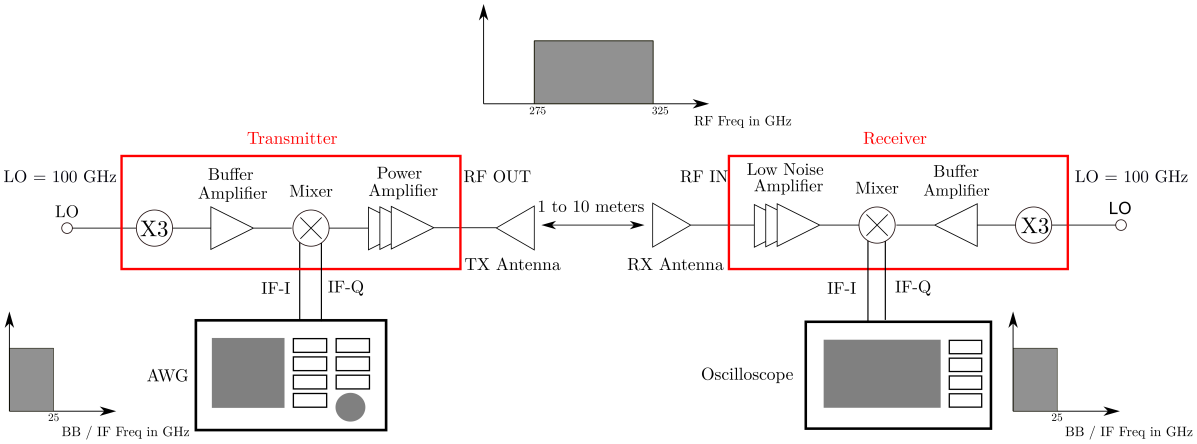

Figure 3.6: Setup of the 300 GHz wireless transmission experiment using the active all electronics based transmitter and receiver.

Fig. 3.4 shows the measurement results of the receiver conversion gain under variation of the RF frequency at a fixed LO input power of $7\,\mathrm{dBm}$ and at an LO frequency of $100\,\mathrm{GHz}$. The MMIC shows a maximum conversion gain of $-1\,\mathrm{dB}$ for both I and Q channel. The RF 3-dB bandwidth is $30\,\mathrm{GHz}$ from 280 to $310\,\mathrm{GHz}$.

Compared to the previous generation of circuits [KDR+15], this MMIC has been improved in terms of frequency operating range for double-sideband operation centred around $300\,\mathrm{GHz}$ and for reduced IQ imbalance. Especially the IQ imbalances influence negatively the transmission quality, measured in terms of EVM [AK15].

Both transmitter and receiver MMICs are packaged in split-block waveguide modules. Fig. 3.5 shows the housing of the transmitter. The MMIC-to-waveguide transition is realized by quartz substrates, thinned down to the thickness of the MMICs. Ultra-short wedge-wedge bond wires connect the MMIC bond pad with the microstrip transmission line on the quartz substrate. The rectangular waveguide mode is coupled by an E-plane probe to the microstrip mode. The I- and Q- signals are provided by V-connectors and a liquid crystal polymer substrate. The LO and RF signals use a rectangular waveguide interface. The packaging technology is developed by Fraunhofer IAF and has been described in detail in various publications like [TLW+17, KDR+15, LTM+08].

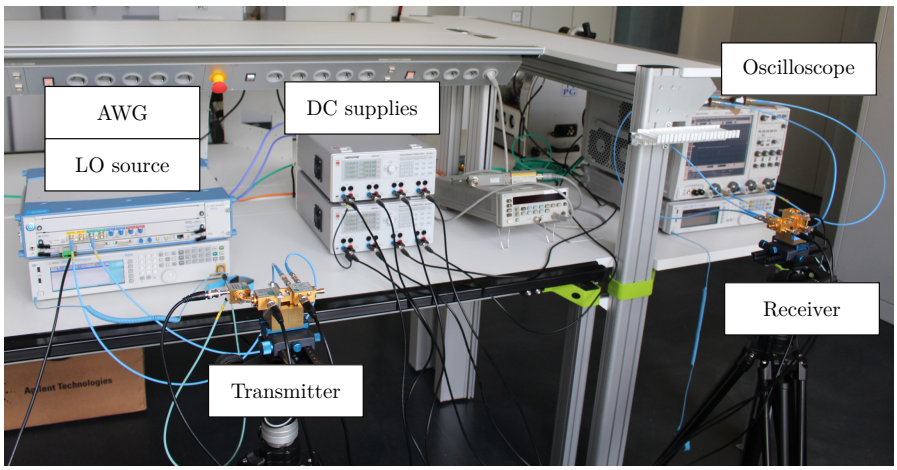

Figure 3.7: Photograph of the 300 GHz 1 meter wireless transmission experiment using the active all electronics based transmitter and receiver.

Fig. 3.6 shows the schematic setup of the $300\,\mathrm{GHz}$ wireless link transmission experiment, including a simplified model of the transmitter and receiver circuit architecture and used hardware. The measurement setup as well as the following measurements are published in [3]. The LO is generated with a Keysight MXG N5183B synthesizer at a frequency of $8.33\,\mathrm{GHz}$ and a variable power. This signal is frequency-multiplied and amplified through the multiplier-by-twelve module as previously described. The input frequency at the LO port of the transmitter and receiver is thereafter $100\,\mathrm{GHz}$. The baseband I and Q signals are created by a state-of-the-art AWG Agilent M9502A with an analog bandwidth of $20\,\mathrm{GHz}$ and a sample rate of $65\,\mathrm{GS/s}$. On the receiver side the signal is amplified by two broadband and phase-matched $22\,\mathrm{dB}$ baseband amplifiers and captured by a real-time oscilloscope DSA-X93204A with an analog bandwidth of $32\,\mathrm{GHz}$ and a sampling rate of $80\,\mathrm{GS/s}$. The transceiver components with attached horn antennas were mounted onto adjustable tripods, for better alignment. Each horn antenna provides an antenna gain $\mathrm{G_{TX,RX}}$ of $24\,\mathrm{dBi}$. Fig. 3.7 shows the photograph of the transmission setup for a distance of $1\,\mathrm{meter}$.

The vector signal analyzer software of the oscilloscope is used to process and evaluate the data. The baseband signals were created using pseudo random binary sequences (PRBS) and mapped into different modulation formats. After modulation the signals are filtered with a simple rectangular pulse.

The first step was to determine the optimal distance and received power $\mathrm{P_{RX}}$ by performing a sensitivity analysis. For this a distance of $0.5\,\mathrm{m}$ was set between TX and RX. In addition, a variable attenuator, which can provide an extra attenuation up to a maximum of $25\,\mathrm{dB}$, was placed after the RX-antenna. The total attenuation, the sum of FSPL and extra attenuation, varies between $76\,\mathrm{dB}$ and $101\,\mathrm{dB}$. A QPSK modulated signal with a symbol rate of $2\,\mathrm{Gbd}$ was sent over the link and the EVM was measured. Since an H-Band power meter was not available, the $\mathrm{P_{RX}}$ could not be measured directly. The $\mathrm{P_{RX}}$ can be calculated using the measured power in the baseband ($\mathrm{P_{IF}}$) and the single tone measurements of the modules which reveal the conversion gain (CG) of the receiver:

$$\mathrm{P_{RX}} = \mathrm{P_{IF}} - \mathrm{CG} \tag{3.1}$$

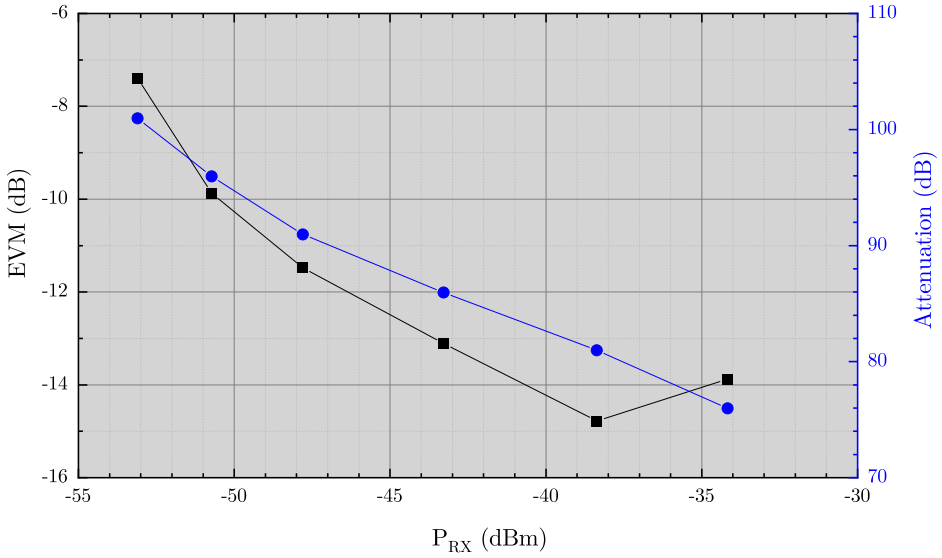

Figure 3.8: Sensitivity analysis of the $300\,\mathrm{GHz}$ link done at different attenuations corresponding to different distances, using a QPSK data signal with $2\,\mathrm{GBd}$ symbol rate.

For example, powers of $-30.4\,\mathrm{dBm}$ and $-28.9\,\mathrm{dBm}$ were measured at the I- and Q-outputs of the RX for a total attenuation of $76\,\mathrm{dB}$, corresponding to a distance of $0.5\,\mathrm{m}$. Considering the QPSK modulation format and the conversion gain the received power is calculated to be $-34.2\,\mathrm{dBm}$. The measurement was repeated for a total attenuation of $81\,\mathrm{dB}$, $86\,\mathrm{dB}$, $91\,\mathrm{dB}$, $96\,\mathrm{dB}$, $101\,\mathrm{dB}$. The result of this analysis can be seen in Fig. 3.8. For low received powers the EVM is poor because of the poor signal to noise ratio. For higher powers the EVM slightly worsens due to non-idealities of the link, like compression, LO phase noise, IQ phase and amplitude imbalances. The optimal received power has been measured to be around $-40\,\mathrm{dBm}$ which corresponds to a distance of $1\,\mathrm{m}$. Accordingly, all the presented measurements were performed with this optimal distance.

For a QPSK modulated signal a symbol rate ($\mathrm{R_s}$) of $32\,\mathrm{GBd}$ results in a data rate of $64\,\mathrm{Gbit/s}$ and for BPSK in a data rate of $32\,\mathrm{Gbit/s}$. Fig. 3.9 shows the recorded EVM for different bandwidths and for QPSK and BPSK modulation formats. The signal quality is dependent on the bandwidth of the wireless link. The RF bandwidth (BW) of a complex modulated signal generated using a rectangular baseband filter is twice the symbol rate of the signal:

$$\mathrm{BW} = 2 \cdot \mathrm{R_s} \tag{3.2}$$

For example, a signal with a symbol rate of $32\,\mathrm{GBd}$ occupies $64\,\mathrm{GHz}$ RF bandwidth.

The measurements presented in [KDR+15] have shown that up to $15\,\mathrm{GHz}$ intermediate frequency, which corresponds to a $30\,\mathrm{GHz}$ RF bandwidth, the output power of the transmitter remains constant. After this frequency $\mathrm{P_{TX}}$ begins to drop. This explains why the EVM worsens starting at a symbol rate of 12 - $14\,\mathrm{GBd}$. The maximal symbol rate at which the signal was successfully demodulated with an EVM value of ca. $-10\,\mathrm{dB}$ corresponds to the maximal data rate transmitted in the experiment $64\,\mathrm{Gbit/s}$.

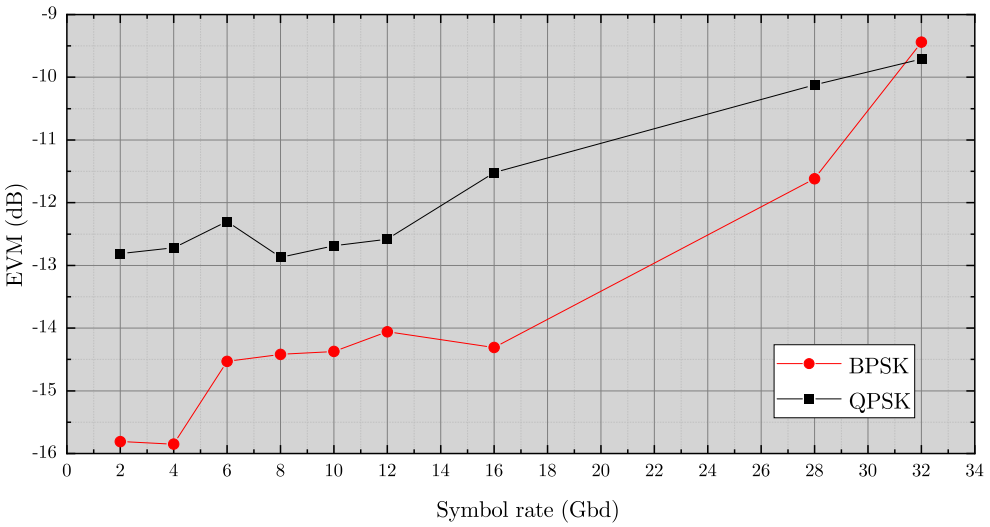

Figure 3.9: EVM versus symbol rate for different modulation formats.

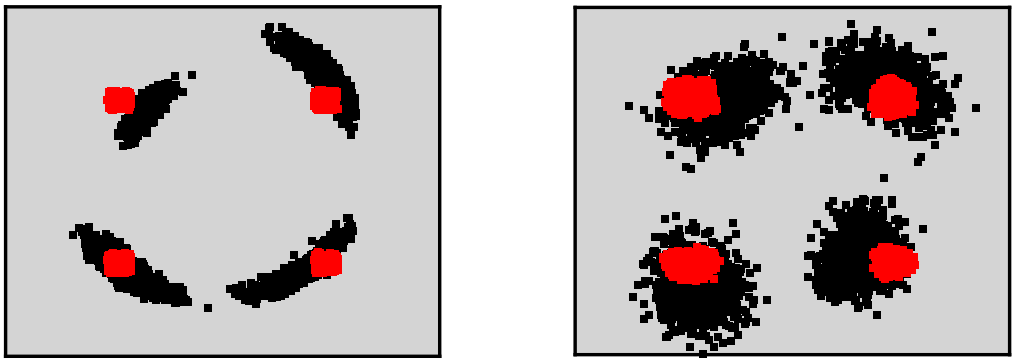

a) 2 GBd b) 28 GBd

Figure 3.10: Constellation diagrams of a QPSK signal at different symbol rates for a transmission distance of 1 m.

Fig. 3.10 shows the constellation diagrams for QPSK signals at different symbol rates. The red dots are the results of the back-to-back measurement AWG to oscilloscope. This was done in order to exclude the influence of the setup in the evaluation of the transmission quality. The black dots are the results of the wireless transmission experiment. The difference between the red and the black points gives information about the error that occurs in the link and which factor plays the critical role. For low symbol rates, 2 GBd Fig. 3.10a), the shape of the black dots, slightly arch-formed, points out that the LO phase error is the dominant factor degrading the signal. This phase error can be minimized by using a coherent setup, where the LO of both transmitter and receiver MMICs are supplied by the same source. In that way the phase of the two LOs is the same and no error occurs in the demodulation. Although the setup leads to better results in terms of phase error optimization it is not further considered in this experiment since it is only applicable in laboratory environment.

The average phase error can be calculated from the constellation diagram, considering the ideal phase of the demodulated signal. In the case of a QPSK signal, Fig. 3.10, this phase is 0.785 rad, which corresponds to 45°. For the signal in Fig. 3.10a) the average phase error is

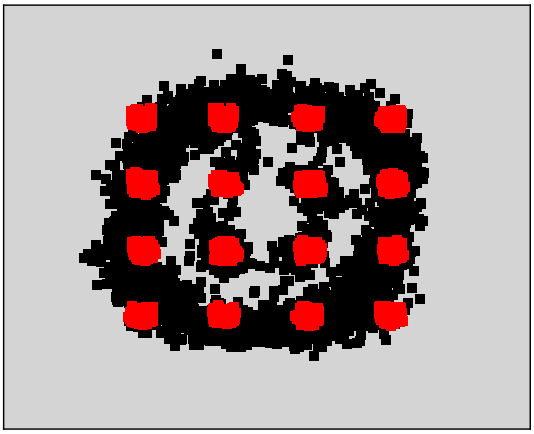

Figure 3.11: Constellation diagrams of a 16-QAM signal $2\,\mathrm{GBd}$ for a transmission distance of $1\,\mathrm{m}$.

$0.171\,\mathrm{rad}$ and for the signal in Fig. 3.10b) the phase error is calculated to be $0.200\,\mathrm{rad}$. The phase error increases with higher modulation bandwidths because the phase perturbation grows, as discussed in [AK15].

The RX and TX IQ amplitude imbalances are calculated from the module measurements by averaging over the bandwidth of the used signal. The IQ phase imbalances are mainly produced by the hybrid coupler used in the up- and down-converters. These values can be extracted from the S-parameters of the coupler measurement and are averaged over the desired bandwidth. In the case of the $2\,\mathrm{GBd}$ signal, amplitude imbalances of $0.6\,\mathrm{dB}$ and $0.8\,\mathrm{dB}$ and phase imbalances of $0.012\,\mathrm{rad}$ and $0.017\,\mathrm{rad}$ are measured for the TX and RX.

For high symbol rates, $28\,\mathrm{GBd}$ Fig. 3.10b), the constellation points smear more than in the case of the $2\,\mathrm{GBd}$ signal in Fig. 3.10a), which shows that the SNR is degrading. For symbol rates higher than $20\,\mathrm{GBd}$ at a carrier frequency of $300\,\mathrm{GHz}$ the IQ phase and amplitude imbalances are less significant, as discussed in [AK15].

Quadrature amplitude modulation formats transmit more information in each symbol interval which results in higher spectral efficiency, but higher sensitivity to noise and non-linearity. Therefore a higher data rate can be obtained than with QPSK, but the requirements for the transceiver on circuit design level are harder to meet. In this case the transmitter is operated at $-7\,\mathrm{dBm}$ IF-power, which corresponds to a $2\,\mathrm{dB}$ back off to the $1-\mathrm{dB}$ compression point. Further lowering this power is practically hard to realize because that would reduce the transmitted power and the SNR and because the AWG does not operate at such low powers. Fig. 3.11 and Fig. 3.12 show the constellation diagrams that were detected and demodulated with 16-QAM and 8-APSK at the same symbol rate, $2\,\mathrm{GBd}$. A symbol rate of $2\,\mathrm{GBd}$ for a 16-QAM and a 8-APSK signal corresponds to a data rate of $8\,\mathrm{Gbit/s}$, respectively $6\,\mathrm{Gbit/s}$. For the case of 16-QAM the signal demodulation was erroneous. As can be seen in Fig. 3.11 the 16 points of the constellation diagram are not distinct anymore. The linearity requirements of a 16-QAM signal were not met. In the case of the 8-APSK modulation, Fig. 3.12, the demodulation was successful and the points can be distinguished from one another. 8-APSK is a special modulation format where the distance in amplitude

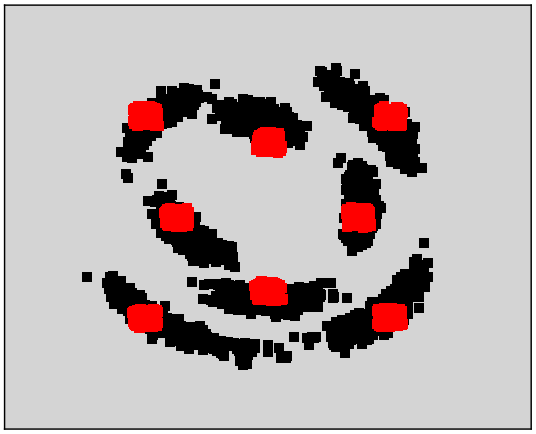

Figure 3.12: Constellation diagrams of a 8-APSK signal $2\,\mathrm{GBd}$ for a transmission distance of $1\,\mathrm{m}$.

between the points on the diagram is bigger. This allows the transmitter to work at an IF input power closer to the compression point. Accordingly, the back off for a 16-QAM needs to be much higher than for an 8-APSK modulated signal.

For a complete analysis of the transmission results a few other inquiries need to be made, like the determination of the transfer function and the measurement of the LO leakage which is a critical parameter for the direct-conversion transmission scheme.

3.2 Characterization of the analog transfer function

This section proposes a reliable method of characterizing the scattering parameters of radio links operating at terahertz frequencies. This method has been published in [4]. The complex transfer characteristics and the non-idealities of analog transmit-receive frontends with quadrature baseband channels can be evaluated. Two coherent channels of an arbitrary waveform generator, combined with filters and a frequency multiplier chain are employed to generate the phase-adjustable LO tones for the quadrature up- and down-converter. Impairments like quadrature gain and phase imbalance, port matching and group delay variation give valuable information about the performance of the terahertz wireless link. A proof-of-concept experiment is realized using the 300 GHz MMIC-based wireless link with an overall system bandwidth of 38 GHz described in the previous section. Accurate gain-frequency and phase-frequency measurements are demonstrated.

All previous works concerning THz communications present measurements of link performance in terms of data rate, EVM, bit-erorr-rate (BER) and on-chip measurements of the circuits. However, the non-idealities of the employed transmit-receive frontends and their impact on the transmission quality, apart from the obvious bandwidth limitations, are rarely discussed or evaluated. But for wideband transmission links non-idealities such as IQ imbalance, LO phase noise and group delay variation cannot be neglected anymore and result in a nonlinear effective channel [AK15]. In order to better characterize wireless links

operating at $300\,\mathrm{GHz}$ and above a method to measure the complex transfer function of the transmit-receive frontend by means of scattering parameters (SP) is elaborated. The method uses a similar approach as the channel sounding technique. Recent publication [KA16a], [KZ16] and [KA16b] report on attempts to characterize $300\,\mathrm{GHz}$ wireless channels. In comparison to the method presented in this section the goal of above mentioned publications is to measure and model propagation paths, characterizing the wireless channel under certain scenarios by using commercially available mixers. This section focuses on characterizing the $300\,\mathrm{GHz}$ analog transmit-receive frontend. Gain- and phase-imbalances, IF port matching and the group delay variation are derived from the S-parameters. In [SGS+16] and [ABM+14] results of similar IF bandwidth characterization measurements are briefly presented. While [SGS+16] presents only measurement results and gives no details or background information of the setup, [ABM+14] reports on a back-to-back measurement. The work reported in this section describes the principle of measurement and explains the key aspects of the setup and how to overcome the existing challenges. In addition, it reports on a free-space transmission, which characterizes more accurately a realistic wireless link.

The measurement technique has been validated by performing the proposed method on the wireless link operating at $300\,\mathrm{GHz}$ presented in the previous section. The link is set up using active MMICs packaged into split-block waveguide modules. The transmitter and receiver MMICs are fabricated in the $35\,\mathrm{nm}$ GaAs mHEMT technology, described in detail in the section 1.2.3 and are part of a 4 x 4 MIMO system. For simplicity reasons this section describes only measurements taken with the combination of one transmit and one receive channel and will therefore treat only a single input single output (SISO). The frequency conversion is realized by a fundamental single-balanced resistive mixer with IQ channels. To reduce LO-RF leakage a balanced design has been chosen for the mixer which suppresses the LO by destructive superposition.

Like described in section 2.5 there are two kinds of transmission schemes when considering the amount of spectrum covered by the RF signal. When the modulated sidebands are symmetrically arranged around the used carrier frequency, creating an upper side band (USB) and a lower side band (LSB) and resulting in a bandwidth of twice the IF bandwidth the transmission scheme is called double side band (DSB). In a single side band (SSB) transmission the signal is covering the same bandwidth as the applied IF signal. A SSB transmission can be generated by bandpass filtering or by using a Hartley modulator, which uses phasing to suppress the unwanted sideband or a Weaver modulator, which uses another quadrature mixer and low pass filters to remove the undesired band. As shown by [Cos57], a SSB transmission has no advantage over a DSB transmission if the phase and frequency of the local oscillator in the receiver are equal to the transmitter's.

IQ-mismatch, caused by amplitude and phase differences in the I- and Q-channel is one of the main impairments of a wireless link, degrading its performance. The influence of IQ-imbalances is discussed in detail in [WYZW13]. The proposed measurement technique shows the overall gain and phase IQ-imbalance measured between the transmitter and receiver IF ports.

Fig. 3.13 shows the setup of this measurement. The coherent setup for synchronous detection has been assured with the help of a four-channel AWG. In two channels of the AWG two single tones with a frequency of $8.244\,\mathrm{GHz}$ each and with a variable phase relation have been set as local oscillator (LO) of the transmitter and receiver, according to the following

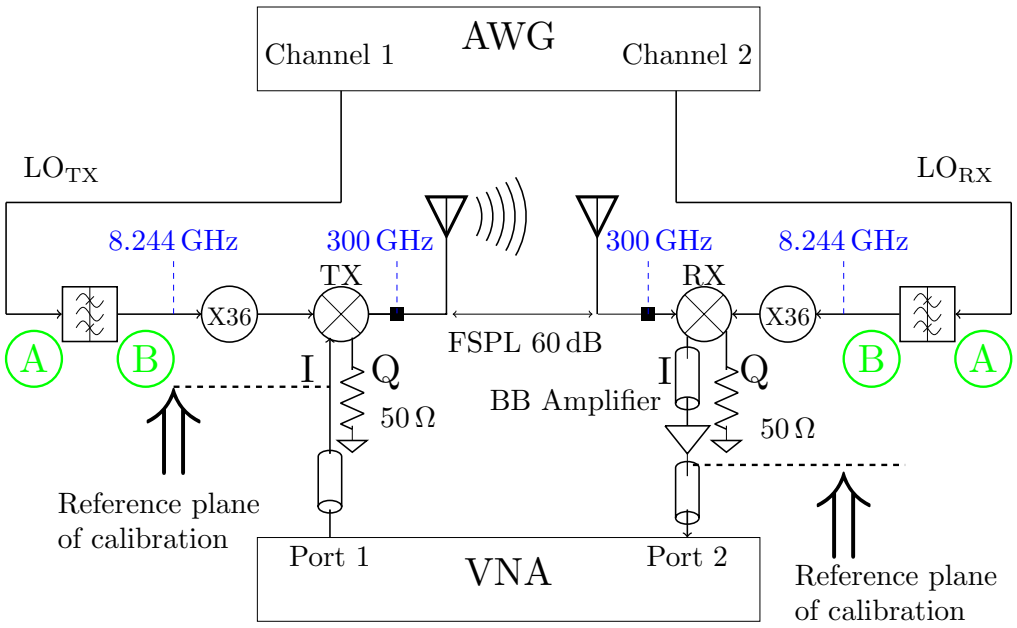

Figure 3.13: Measurement setup for the S-parameter measurements. Port 1 of the VNA is connected either to the I or the Q channel of the transmitter module, while Port 2 is connected to the I or Q channel of the receiver module.

equations:

$$u_{\mathrm{LO_{TX}}} = \mathrm{A}\cos(2\pi \mathrm{f_c} t) \tag{3.3}$$
$$u_{\mathrm{LO_{RX}}} = \mathrm{B}\cos(2\pi \mathrm{f_c} t + \Delta\phi_{\mathrm{LO}}). \tag{3.4}$$

Where A and B are the amplitudes of the single tones, $\mathrm{f_c}$ is the carrier frequency and $\Delta\phi_{\mathrm{LO}}$ is the phase set at the receiver, when the phase of the transmitter is considered to be the reference.

For simplicity reasons the link has been reduced to the components relevant for this measurement. Details about the exact structure of the analog frontend can be found in the previous section. An overall LO frequency multiplication factor of 36 is used to achieve the $300\,\mathrm{GHz}$ carrier frequency. After frequency multiplication, which is assumed to be ideal, the single tones generated by the AWG have the following form:

$$u_{\mathrm{LO_{TX}}} = \mathrm{A}\cos(2\pi \mathrm{n f_c} t) \tag{3.5}$$
$$u_{\mathrm{LO_{RX}}} = \mathrm{B}\cos(2\pi \mathrm{n f_c} t + \mathrm{n}\Delta\phi_{\mathrm{LO}}). \tag{3.6}$$

The frequency multiplier has no influence on the amplitude of the signal. The carrier frequency and the phase of the signal are multiplied with n, in this case 36. The minimal phase increment of the AWG is $0.01\,\mathrm{deg}$ which leads to a minimal phase increment of $0.36\,\mathrm{deg}$ for $\mathrm{n}\Delta\phi_{\mathrm{LO}}$.

This means the sensitivity of the LO tone to phase variation is very high. $1°$ of phase difference in the LO translates into $36°$ in the RF. The biggest challenge of this measurement was to overcome this sensitivity.

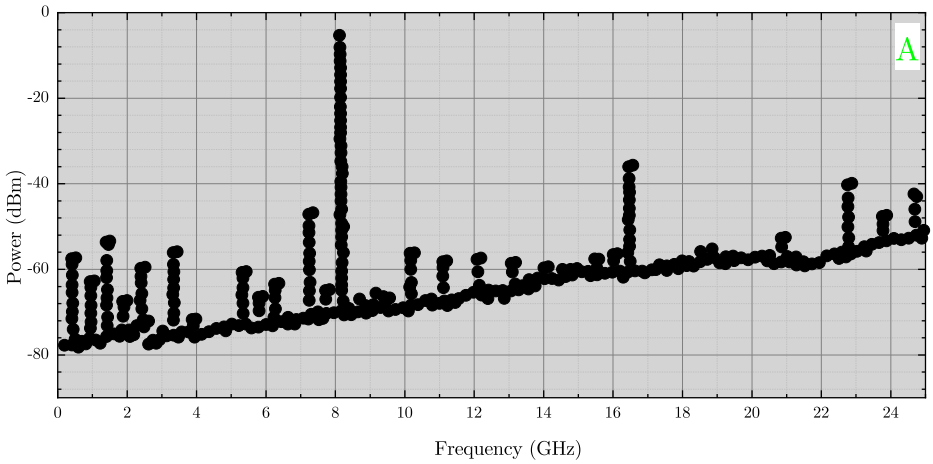

Figure 3.14: Spectrum of an AWG generated single tone.

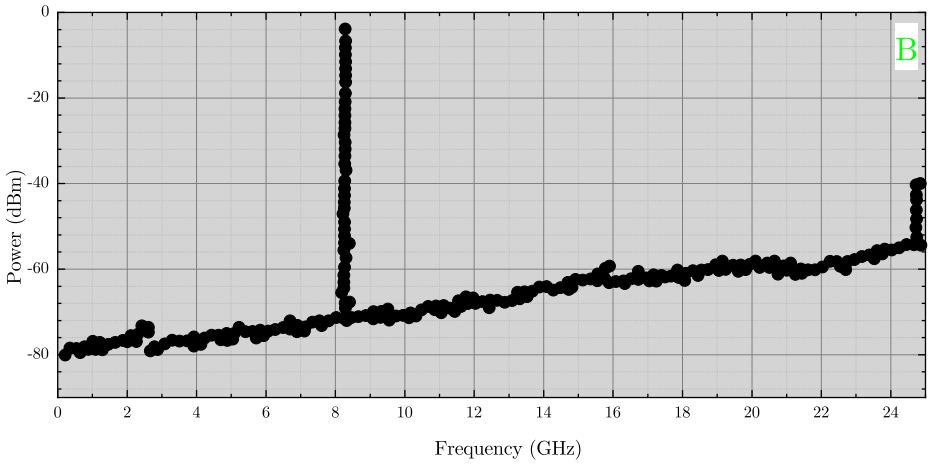

Figure 3.15: Spectrum of an AWG generated single with an external filter.

In the up-converter, if a signal $u_{\mathrm{IF}} = \mathrm{C}\cos(2\pi \mathrm{f_{IF}} \mathrm{t})$ gets multiplied with the LO in (3.5) the RF signal is:

$$u_{\mathrm{RF}} = \mathrm{D}\cos\left(2\pi\left(\mathrm{nf_c} + \mathrm{f_{IF}}\right)\mathrm{t} + \phi\prime_{\mathrm{TX}}\right) + \mathrm{D}\cos\left(2\pi(\mathrm{nf_c} - \mathrm{f_{IF}})\mathrm{t} + \phi\prime_{\mathrm{TX}}\right) \tag{3.7}$$

where D is the amplitude of the RF signal and $\phi\prime_{\mathrm{TX}}$ is the total phase shift introduced in the transmitter. The first term of the sum represents the USB and the second term is the LSB.

A vector network analyzer (VNA) is used to measure the S-parameters of the transmit-receive system. The signal will only be received on the desired channel if the phase difference between the received RF signal and the total phase delay introduced by the receiver is zero. For this purpose the I-channel of the transmitter is connected to port 1 of the VNA and the I-channel of the receiver is connected to port 2 (I to I transmission). The Q-channels are terminated with a $50\,\Omega$ load. The phase $\Delta\phi_{\mathrm{LO}}$ is set in a way that the maximum power is in the measured channel, thus compensating for the total phase delay introduced in the up- and down-converter. The work reported in [ABM+14], which shows a similar experiment uses a single tone generator, a power divider and an analog phase shifter for phase adjustment. The AWG used for this work, a Keysight M8195A with $20\,\mathrm{GHz}$ analog bandwidth and $64\,\mathrm{GSa/s}$

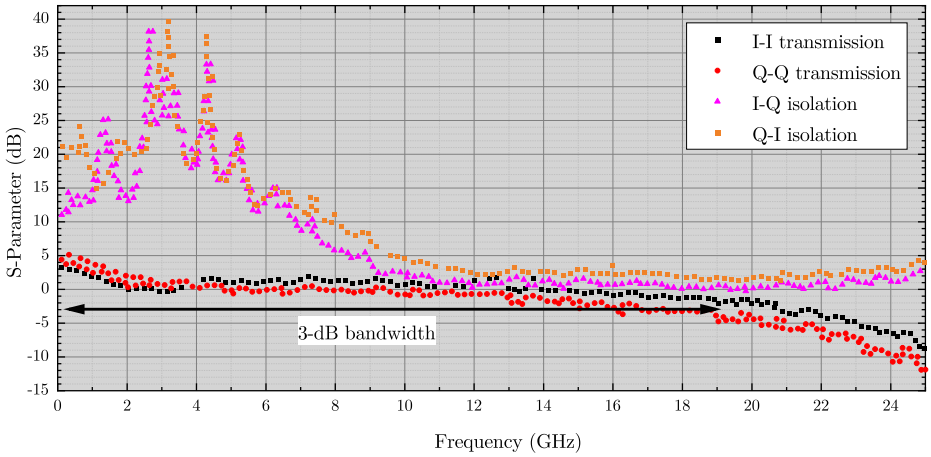

Figure 3.16: Measurement results of the transfer function characteristics, when the transmission is done from I channel to I channel or from Q channel to Q channel.

sample rate allows to digitally adjust the phase with an increment of $0.01\,\mathrm{degree}$. Optimizing for maximum power in the desired transmission channel by varying the phase in the receiver takes into account all phase differences that occur along the system. The disadvantage of the AWG in comparison to a synthesizer is the poor spectral quality of the signal, due to the finite resolution of the AWG's digital to analog converter.

To overcome this issue bandpass filters are used, to suppress the unwanted harmonics generated by the AWG which can cause intermodulation products. Fig. 3.14 and Fig. 3.15 show the spectral purity difference between a signal before and after the filter. The filter enhances the in-band spurious tone suppression from $-45\,\mathrm{dBc}$ to $-65\,\mathrm{dBc}$.

For this experiment a baseband amplifier was used to amplify the received signal to a value well beyond the noise floor of the VNA. The reference plane starts at the baseband amplifier output. Therefore, this component is not included in the calibration (Fig. 3.13). The measurement was performed over a link distance of $7.5\,\mathrm{cm}$, which was chosen according to the optimal received power of the receiver. To chose the correct distance, a link budget and a sensitivity analysis need to be made. Details about wireless link sensitivity analysis can be found in the previous section 3.1.

Information about the overall link bandwidth and complex transfer function can be gained from the transmission measurements, shown in Fig. 3.16. In comparison to single chip measurements, this experiment shows the overall frequency response of the system and the effective bandwidth limitation. The characteristics shown in Fig. 3.16 for the I-I and Q-Q transmission represent the linear transfer gain, when both the transmitter and the receiver are operated in linear regime. The validity of linear operation was verified by applying varying port power levels during the S-parameter test. An optimal power of $-40\,\mathrm{dBm}$ at receiver input and a total conversion gain of $30\,\mathrm{dB}$ lead to an output power of $-10\,\mathrm{dBm}$. Since the transmitted IF power at the transmitter input is $-10\,\mathrm{dBm}$ an overall gain (S21) of $0\,\mathrm{dB}$ is expected and achieved. The presented link shows a 3-dB-IF-bandwidth of $19\,\mathrm{GHz}$, which corresponds to an overall RF bandwidth of $38\,\mathrm{GHz}$.

The S21 parameters measured during an I to Q transmission when the phase was set for maximum power transmission from the I-channel of the transmitter to the I-channel of the receiver, represent the I-Q isolation (Fig. 3.16). The isolation for both I-Q and Q-I

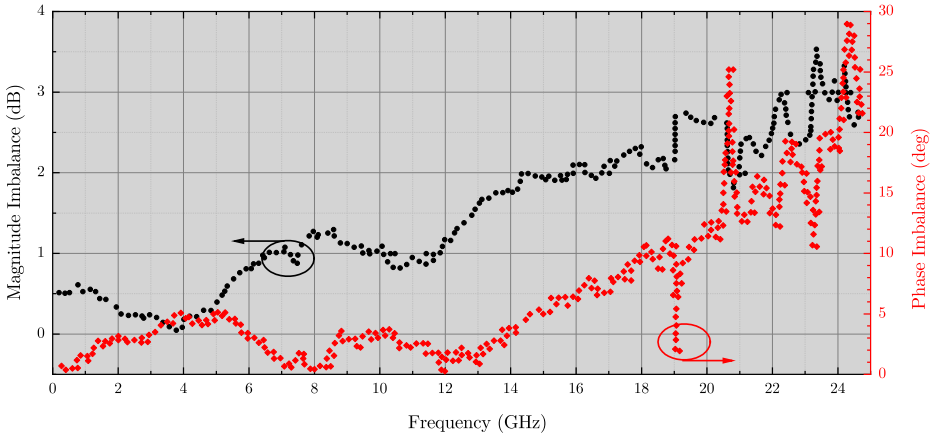

Figure 3.17: Magnitude and phase imbalance calculated from the transfer function characteristics.

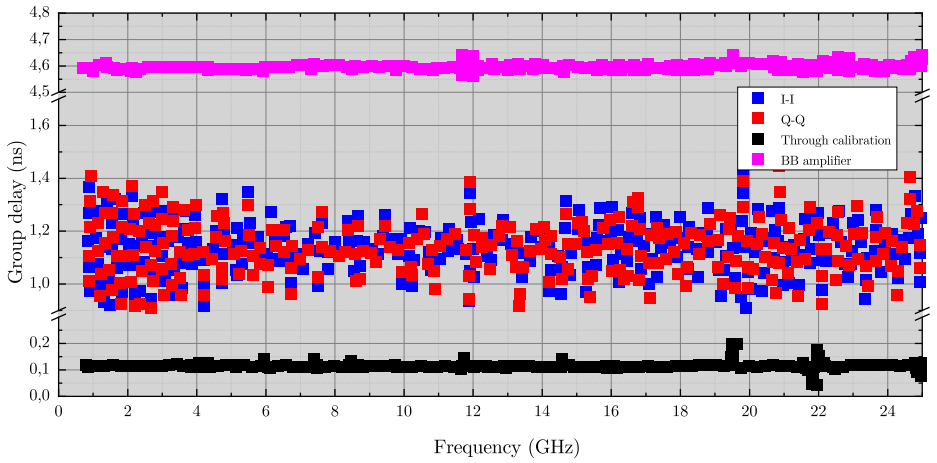

Figure 3.18: Group delay of the I to I and Q to Q transmission, the measurement equipment and the baseband (BB) amplifier and cables.

transmissions decreases with frequency. This shows that the phase offset for maximum I to I transmission is also frequency dependent and cannot compensate the phase difference in the transmit-receive system over the complete bandwidth.

The difference between the transmission on I- and the transmission on Q-channel represents the IQ-imbalance and can be seen in Fig. 3.17. For lower frequencies, where $\Delta\phi_{\mathrm{LO}}$ ensures a coherent detection the magnitude and phase imbalance are low. For frequencies above $16\,\mathrm{GHz}$ the imbalances increase substantially, which will result in an important EVM degradation, decreasing the performance of the link ([AK15]). For the mentioned bandwidth of $19\,\mathrm{GHz}$ the magnitude and phase imbalance stay under $2\,\mathrm{dB}$ and $8°$, respectively.

The phase information of the transmission is used to calculate the group delay, which is the time needed for the signal to travel through the analog frontend. Since the reference plane begins at the baseband amplifier, the influence of this component has been considered for group delay calculation, by first measuring the SP of the baseband amplifier and connecting cables and de-embeding them from the overall measurement results. To determine the group delay variation for the I to I and for the Q to Q transmission the group delay value of the baseband amplifier was measured and subtracted from the overall measured value. The

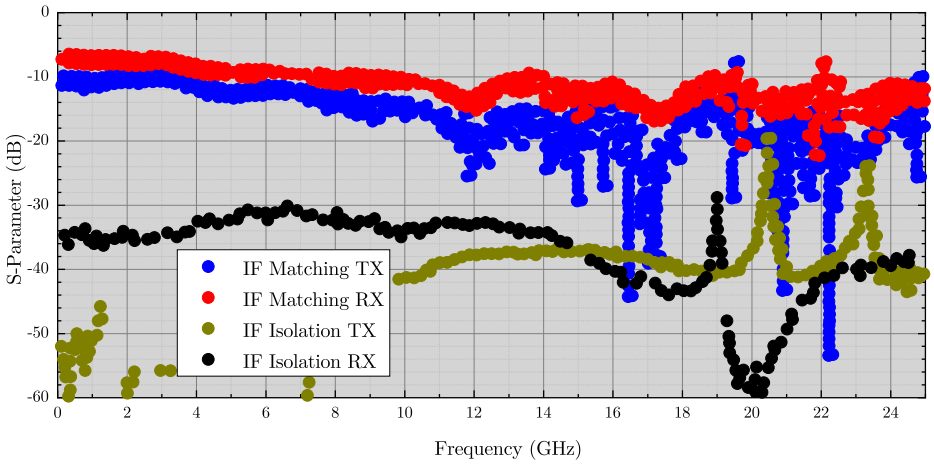

Figure 3.19: Measurement results of IF port matching and isolation.

results of this measurement can be seen in Fig. 3.18. For a better graphical representation of the results, the y-axis was interrupted. The group delay of the transmission, drawn in the middle of the diagram, is lower than $1.5\,\mathrm{ns}$ over the complete bandwidth and has a maximum ripple of $0.7\,\mathrm{ns}$. The calibration accuracy is derived from a group delay measurement of a Through standard, which shows an absolute group delay of $0.1\,\mathrm{ns}$ and a group delay ripple of $0.1\,\mathrm{ns}$. The baseband amplifier introduces the highest absolute group delay of $4.6\,\mathrm{ns}$.

Port matching and port isolation for the transmitter and the receiver can be measured with the proposed method and these results can be seen in Fig. 3.19. To obtain the isolation the VNA ports were connected to the I- and Q-ports of the same module. The measured S21 represents in this case the isolation, which lies, for both TX and RX, higher than $30\,\mathrm{dB}$ for the complete bandwidth. S11, obtained from the measurement of the transfer function is found to be lower than $-10\,\mathrm{dB}$ and indicates the port matching of the TX. For the reflection parameter of the RX an I to I transmission without the baseband amplifiers has been measured and the return loss, S22, has been recorded. The RX port reflection is lower than $-8\,\mathrm{dB}$ over the complete bandwidth.

This section presents a measurement method, that characterizes wireless links operating at terahertz frequencies and helps explain the limitations in data transmission experiments. Non-idealities like gain and phase imbalance, port matching, isolation and group delay variations can be measured with this method. Measurement results gained from this experiment can be compared with simulations and a complete analysis of wireless links can be made.

3.3 Influence of the LO isolation on the performance of the link

The following section presents the measurement and analysis of local oscillator isolation in the previously presented analog frontend at the carrier frequency of 300 GHz. This method has been partially published in [5] and in [6]. The transmit-receive wireless system uses a single-balanced resistive mixer with in-phase and quadrature channels that provides a very good isolation of the local oscillator. The dependency of the isolation on the baseband input is presented. The isolation obtained when a signal is transmitted only on the in-phase channel

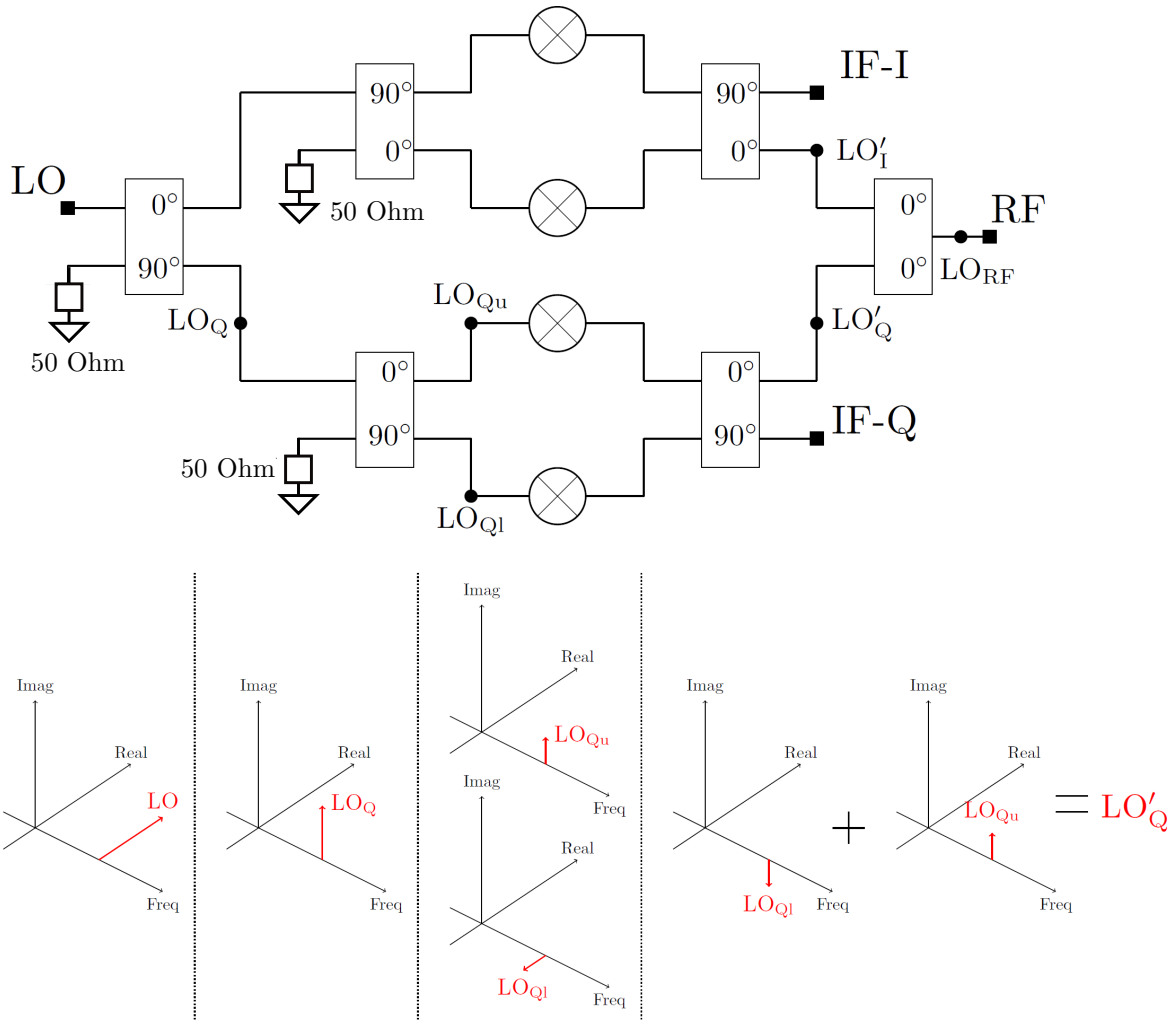

Figure 3.20: Architecture of the frequency up-converter and LO suppression mechanism in the Q path.

is higher than in the case of the signal transmitted on the quadrature channel. The section presents the measurement method and a theoretical analysis which confirms the experimental observations.

The continuous increase in the demand of high data rates across the most important wireless scenarios has been the motivation for many research groups to find a system that provides a combination of high data rate and distance capability. With the desire of analyzing the non-idealities of the employed transmit-receive frontends and their impact on the transmission quality, a method of measuring the isolation of the LO at RF frequencies in the low terahertz region is elaborated and presented in this chapter.

Fig. 3.20 shows the architecture of the frequency up-converter. A first $90°$ tandem coupler is used to create two paths with a phase shift of $90°$. Those two paths form the I and the Q channel. Two other tandem couplers, in both I and Q paths, are responsible for a total path phase shift of $180°$, which is the reason for the LO suppression. This behavior is described in detail in Fig. 3.20. We choose a 3D frequency domain representation for a better understanding of the phase relationship of the signals. Considering Euler's identity

$$\cos(\omega t) = \frac{e^{j\omega t}}{2} + \frac{e^{-j\omega t}}{2} \tag{3.8}$$

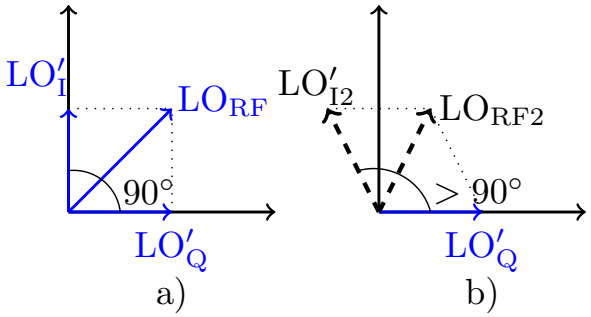

Figure 3.21: The total LO leakage of the link, $\mathrm{LO}_{\mathrm{RF}}$, is the vector sum of the leakage of the I path, LO_{I}, and the Q path, LO_{Q}. When the phase difference of between the paths is bigger than $90°$, b), the absolute value of the resulting leakage is smaller.

and neglecting the negative frequency, we can represent the LO signal in frequency domain as a phasor in the real complex plane. A phase shift of $90°$ means a rotation of the original phasor along the frequency axis and it is equivalent to a multiplication with the complex number j. The LO is pictured after each coupler for the Q path of the mixer. Given the LO signal with any given amplitude A and a frequency ω_{LO}, the LO of the upper path becomes $\mathrm{LO}_{\mathrm{Qu}} = \mathrm{A}\sin(\omega_{\mathrm{LO}}t + 90°)$ and the LO of the lower path as $\mathrm{LO}_{\mathrm{Ql}} = \mathrm{A}\sin(\omega_{\mathrm{LO}}t + 270°)$. Adding $\mathrm{LO}_{\mathrm{Ql}}$ and $\mathrm{LO}_{\mathrm{Qu}}$ under ideal conditions results in a suppressed LO signal before the RF power combiner.

Any variation from the ideal phase shift of the couplers will lead to an LO leakage. If we define $\mathrm{LO}'_{\mathrm{I}}$ and $\mathrm{LO}'_{\mathrm{Q}}$ as the LO leakage resulting from the I and Q paths the total LO leakage, $\mathrm{LO}_{\mathrm{RF}}$, will be the vector addition of the last two. Since the mixer is symmetrical the phase difference between $\mathrm{LO}'_{\mathrm{I}}$ and $\mathrm{LO}'_{\mathrm{Q}}$ will be defined by the phase difference of the first coupler, ideally $90°$. This situation is described by Fig. 3.21a). Assuming the coupler has a deviation from the ideal phase value higher than $90°$ we obtain the situation pictured in Fig. 3.21b). Between the leakage on I path and on Q path there is a phase difference bigger than $90°$. The vector addition of $\mathrm{LO}'_{\mathrm{I2}}$ and $\mathrm{LO}'_{\mathrm{Q}}$ will result in a total LO leakage, $\mathrm{LO}_{\mathrm{RF2}}$. The magnitude of $\mathrm{LO}_{\mathrm{RF2}}$ is smaller than $\mathrm{LO}_{\mathrm{RF}}$.

A particularity of this mixer is the extraction of the IF signal from the isolated but DC-coupled ports of the tandem couplers. The IF frequency range used for this mixer goes up to $30\,\mathrm{GHz}$. At these low frequencies the isolated port (port number 4 in Fig. 3.20) shows a good transmission to the coupled port (number 2) and is isolated versus the through port (number 1) of the coupler. The IF signal gets multiplied with the LO signal only in the lower mixer branch. The mixer in the upper path receives no IF signal.

Fig. 3.22 shows the setup of the measurement with the relevant components for this study. Section 3.1 describes the wireless system and its components. The LO is generated with a commercial synthesizer at a frequency of $8.244\,\mathrm{GHz}$ for the transmitter and at a frequency of $8.216\,\mathrm{GHz}$ for the receiver. Considering an overall frequency multiplication factor of 36, LO frequency of the transmitter becomes $296.7\,\mathrm{GHz}$ and the LO of the receiver $295.7\,\mathrm{GHz}$. By setting an offset between the LO frequencies we are able to measure leaked LO from the transmitter in the receiver baseband at $1\,\mathrm{GHz}$ with the help of a commercial spectrum analyzer. Due to this particular measurement setup and the impossibility to measure the power levels directly in front and behind the mixer the LO isolation can be defined as the difference between the measured output power at $1\,\mathrm{GHz}$ and the LO input power, in front of

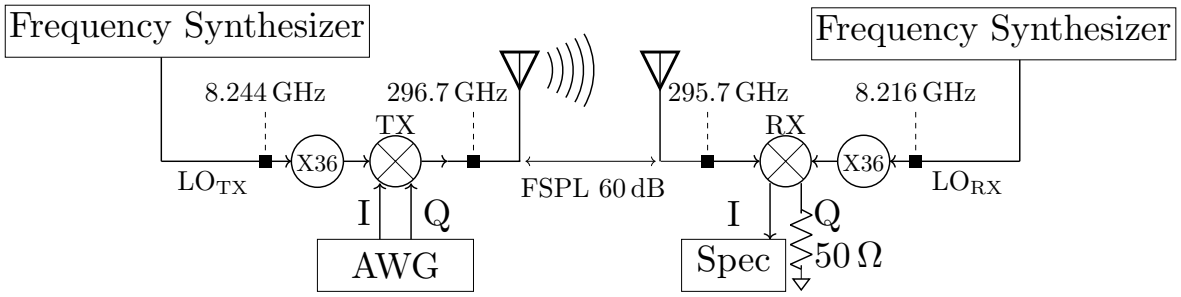

Figure 3.22: Measurement setup for the LO isolation measurements.

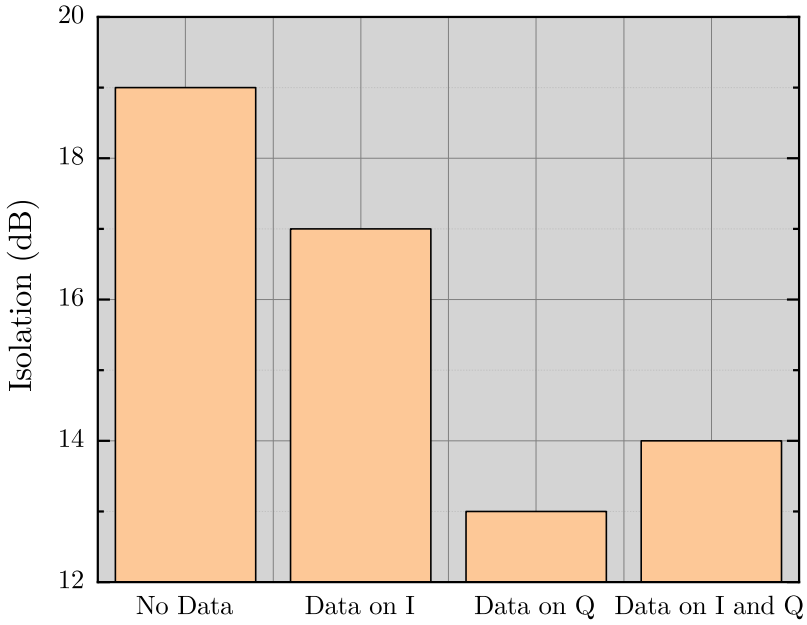

Figure 3.23: LO isolation under different scenarios.

the frequency multiplier, which was fixed to $-4\,\mathrm{dBm}$ for optimal performance. The I and Q signals are created by an AWG. The measurement was performed over a link distance of $7.5\,\mathrm{cm}$, which corresponds to a FSPL of $60\,\mathrm{dB}$. This distance was chosen according to the optimal input power of the receiver. To choose the correct distance, a link budget and a sensitivity analysis need to be made. Details about wireless link sensitivity analysis can be found in section 3.1.

The investigate of the LO isolation is realized by applying different baseband signals at the transmitter. In the first scenario the isolation when there is no IF signal applied is measured. In the second and third scenario a data signal (BPSK with a symbol rate of $4\,\mathrm{GBd}$) only on the I or the Q channel of the mixer is applied and in the last scenario both I and Q signals (QPSK with a symbol rate of $4\,\mathrm{GBd}$) are sent. As described in section 3.3 the LO leakage is dependent on the couplers used in the I and Q paths as well as the first LO coupler.

The results of the measured LO isolation under the different scenarios can be seen in Fig. 3.23. The isolation has different values for different usage of the IF ports. The highest LO isolation occurs for no IF signals. The second best result is obtained when data is applied only on the I channel, while in the case of data on the Q channel the isolation is $4\,\mathrm{dB}$ lower. When data is applied on both I and Q channels the isolation lies at $14\,\mathrm{dB}$.

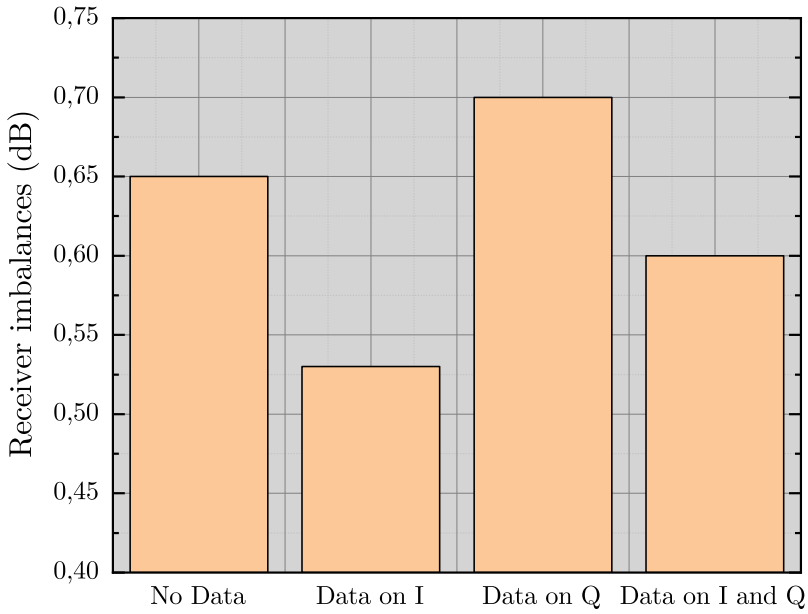

Figure 3.24: Receiver imbalances measured for different baseband signals.

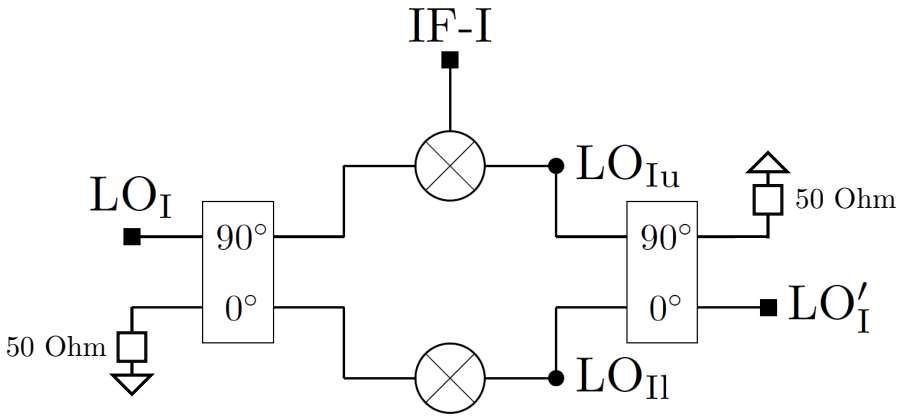

Figure 3.25: I path of the IQ mixer between the first 90° coupler and the power combiner.

The $1\,\mathrm{GHz}$ difference between the transmitter and receiver LO offers the possibility to measure the leakage in the receiver baseband. The measurement on the receiver I and Q channels allows the calculation of the receiver imbalances, defined as the difference between the value of the data signal measured on the I channel and the value measured on the Q channel, plotted in Fig. 3.24. While the isolation difference varies up to $5\,\mathrm{dB}$, the receiver imbalances vary only up to $0.2\,\mathrm{dB}$ for the different scenarios. As in the isolation measurement, the receiver imbalances when the data signal is only sent on the Q channel are the biggest, $0.7\,\mathrm{dB}$. The smallest receiver imbalance is reached by sending signals on the I channel, $0.54\,\mathrm{dB}$. A similar value is obtained by sending data on both channels.

Both non-idealities measured with this method, LO isolation and receiver IQ-imbalance, influence the transmission quality, degrading the EVM. Further investigation of the LO isolation mechanism requires the measurement of the LO signal at the points $\mathrm{LO_I}$, $\mathrm{LO_Q}$, $\mathrm{LO'_I}$ and $\mathrm{LO'_Q}$ in Fig. 3.20. Because these measurements are not possible with this architecture a circuit simulation with ideal and measured couplers is presented.

Fig. 3.25 shows the architecture of the I path of the IQ mixer, between the first $90°$ coupler and the power combiner. Under ideal conditions and no IF signal the phase difference between $\mathrm{LO_{Iu}}$ and $\mathrm{LO_{Il}}$ should be $180°$ and the signals can be described as:

$$\mathrm{LO_{Iu}} = \mathrm{A}\cos(\omega_{\mathrm{LO}}t + 90°) \tag{3.9}$$

$$\mathrm{LO_{Il}} = \mathrm{A}\cos(\omega_{\mathrm{LO}}t). \tag{3.10}$$

After the second $90°$ coupler the LO signal is

$$\mathrm{LO_{I}} = \mathrm{A}\cos(\omega_{\mathrm{LO}}t + 180°). \tag{3.11}$$

The $180°$ difference between the two paths is reached and the LO is suppressed. An applied IF signal introduces a phase offset, ϕ_{offset}, during the mixing process. In this case $\mathrm{LO_{Iu}}$ can be described as:

$$\mathrm{LO_{Iu}} = \mathrm{A}\cos(\omega_{\mathrm{LO}}t + 90° + \phi_{\mathrm{offset}}). \tag{3.12}$$

Since no IF is applied on the lower path $\mathrm{LO_{Il}}$ will remain the same as in (3.10) and $\mathrm{LO_{I}}$ will be

$$\mathrm{LO'_{I}} = \mathrm{A}\cos(\omega_{\mathrm{LO}}t + 180° + \phi_{\mathrm{offset}}) \tag{3.13}$$

which leads to a finite LO isolation value.

Therefore the difference in isolation values between applying data and not applying a signal on the IF ports is caused by the usage of only one mixer in each path, like described in Fig. 3.25. If the second mixer was receiving an IF signal, it would introduce the same ϕ_{offset} as the first mixer and this phase difference would be eliminated after the last $90°$ coupler.

Another important discovery of the measurement is that the isolation differs depending on which channel, I or Q, is used.

Fig. 3.26 shows the simplified architecture of an IQ mixer. The path described in Fig. 3.25 is replaced by a simple mixer symbol. In an ideal IQ mixer the phase difference, $\Delta\phi$, between $\mathrm{LO'_{I}}$ and $\mathrm{LO'_{Q}}$ is $90°$:

$$\Delta\phi = \phi_{\mathrm{LO'_{Q}}} - \phi_{\mathrm{LO'_{I}}} = 90° \tag{3.14}$$

Considering the case of a transmission only on I channel and the ϕ_{offset} introduced in the I path the phases $\phi_{\mathrm{LO'_{Q}}}$ and $\phi_{\mathrm{LO'_{I}}}$ become:

$$\phi_{\mathrm{LO'_{Q}}} = 90° \tag{3.15}$$

$$\phi_{\mathrm{LO'_{I}}} = \phi_{\mathrm{offset}}. \tag{3.16}$$

The difference of the two phases is therefore:

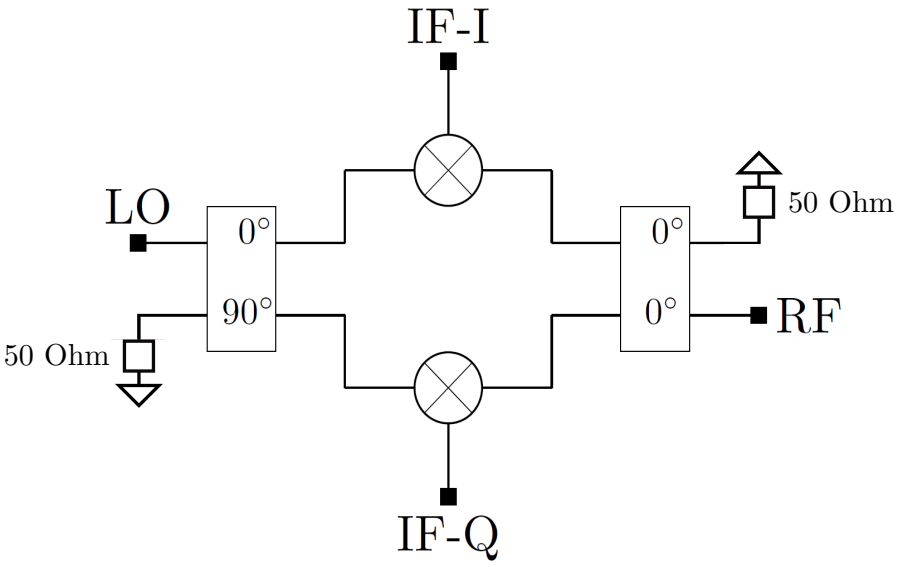

Figure 3.26: Architecture of an IQ mixer.

$$\Delta\phi = 90° - \phi_{\text{offset}} \tag{3.17}$$

For a transmission only on Q channel the relations are:

$$\phi_{\text{LO}'_{\text{Q}}} = 90° + \phi_{\text{offset}} \tag{3.18}$$

$$\phi_{\text{LO}'_{\text{I}}} = 0° \tag{3.19}$$

and the overall phase difference is accordingly:

$$\Delta\phi = 90° + \phi_{\text{offset}}. \tag{3.20}$$

The difference between usage of the I channel and usage of the Q channel can be seen in equations (3.17) and (3.20). For a phase bigger than $90°$ the magnitude of the LO will be higher than for a phase phase lower than $90°$, as shown in Fig. 3.21. As a consequence the LO isolation when the data is sent on the I channel will be higher than when data is sent only on the Q channel, which confirms the measurement in Fig. 3.23.

The value of ϕ_{offset} and isolation imbalance is strongly dependent on the state of operation of the mixer, linear or saturated with respect to LO power, and on the power of the IF signal. If the power of the LO signal is high enough for the mixer to go into saturation, ϕ_{offset} will be low. The power of the IF signal also influences the isolation. As soon as the IF power exceeds the 1-dB compression point the isolation imbalance increases considerably. Therefore, it is advised to operate the mixer in its optimum bias point, where the LO signal is saturated and the IF signal is in linear region.

Different LO isolation results depending on the used IF signals will have an impact on the link transmission performance and should be taken into consideration. This section presents

the LO isolation measurement of the $300\,\mathrm{GHz}$ wireless link from 3.1. The architecture of the IQ frequency up-converter and the LO suppression theory have been explained. The measurements have shown that the isolation is dependent on the applied IF signal and the used channels. This work helps determine the optimal mixer architecture and operation as well as analyse the observed performance imperfections during the design and measurement phases of mixers.

3.4 Conclusion

This chapter presents a complete electronic transmit-receive front-end operating at the center frequency of $300\,\mathrm{GHz}$. Due to the high available bandwidth, the direct-conversion approach is chosen as the transmission scheme. The highest data rate achieved is $64\,\mathrm{Gbps}$. The overall low linearity does not allow the transmission of complex modulated formats like 16-QAM. With careful design improvements and considerations of the analyis of the LO isolation the performance of the link could increase considerably. This $300\,\mathrm{GHz}$ wireless link is a first step towards indoor wireless communication in the low THz range and towards the integration in applications like smart offices or data proximity showers.

4 Wireless Transmission Employing a Photonic Transmitter and an Active Electronic Receiver based on the Direct-Conversion Approach

The previous chapter presented an all active electronic link. This means both transmitter and receiver are based on an active transistor technology. Another popular choice for THz communication is the employment of photonics-based transmitters. This will be the focus of the following chapter: a $300\,\mathrm{GHz}$ wireless link composed of a photonic uni-traveling-carrier diode transmitter and an active electronic receiver based on a MMIC in the same technology as the system in the previous chapter, the $35\,\mathrm{nm}$ InGaAs mHEMT. The results of this wireless transmission and the content of this chapter have been published in [7]. The data transmission reaches $100\,\mathrm{Gbps}$ over a distance of $15\,\mathrm{m}$. Complex modulation formats, like 32-QAM and 64-QAM are successfully transmitted up to a symbol rate of $8\,\mathrm{GBd}$. The system presents not only high linearity but is also capable of transmitting high symbol rates, up to $40\,\mathrm{GBd}$. To the best of the author's knowledge, this represents the highest ever reported transmission bandwidth as well as the highest spectral density symbol rate product for transmissions in the low terahertz band.

4.1 Photonic transmitter

The photonics-based transmitter is composed of an UTC-PD. This device makes use of a semitransparent top contact for front-side illumination of the GaAs-based photodiode with a $1.55\,\mu\mathrm{m}$ wavelength and is described in [LPB+17]. The DC photo response of the UTC-PD with $3\,\mu\mathrm{m}$ diameter is $0.1\,\mathrm{A/W}$. The photodiode is directly connected using a ground-signal-ground (GSG) coplanar access with $50\,\mu\mathrm{m}$ signal/ground separation. The output of the probe is waveguide-coupled. A waveguide antenna is used to out-couple the signal into the free-space and a lens is used to collimate the beam. The $300\,\mathrm{GHz}$ carrier is generated by photomixing two laser lines, where the quality of the laser lines directly impacts the quality of the THz carrier. The optical lines are at $193.4\,\mathrm{THz}$ and $193.1\,\mathrm{THz}$, hence a wavelength separation of $2.4\,\mathrm{nm}$ which results in a $300\,\mathrm{GHz}$ beat frequency. The first laser is amplitude/phase-modulated by an IQ Mach-Zehnder modulator using a Lithium Niobate technology. This enables modulation formats up to 64-QAM and a large signal bandwidth up to the 3-dB bandwidth of the modulator, which is $25\,\mathrm{GHz}$. After the combination of the modulated optical signal, a second optical tone is added, to feed the input of an erbium-doped fiber amplifier (EDFA). The amplified optical signal is then injected into the photomixer.

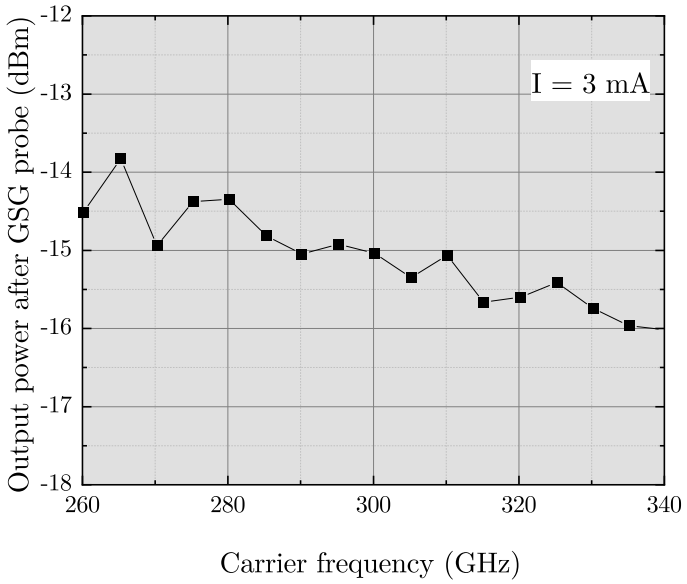

Figure 4.1: Frequency evolution of generated power at UTC-PD output, connected to the GSG probe. The power level is measured at waveguide output, for $3\,\mathrm{mA}$ photo current inside the UTC-PD. The photodiode bias is $-1\,\mathrm{V}$.

Initial characterization of the photonics-based transmitter is done using continuous wave signals in the optical domain. The frequency response as well as the linearity are determined. Fig. 4.1 shows the output power of the photodiode in the $300\,\mathrm{GHz}$ range with a current level of $3\,\mathrm{mA}$. As can be seen, a broadband behavior is obtained, with a roll-off due to the UTC-PD and probe effect. A 3-dB RF bandwidth of over $80\,\mathrm{GHz}$ centered around $300\,\mathrm{GHz}$ was obtained, compatible with very high baud-rate modulation.

Fig. 4.2 presents the linear behavior of the photonics transmitter at a carrier frequency of $300\,\mathrm{GHz}$. The red curve shows the measured power at the waveguide (WR3.4) output after GSG probe, which is the actual power radiated in free space using a horn antenna. The black curve shows the UTC-PD power taking into account the probe losses.

The probe used for the power measurements in Fig. 4.1 and Fig. 4.2 has typically 3 dB loss in the range 220-325 GHz, from 2.5 dB in the beginning of the band, and 3.5 dB at the end around 330 GHz. The power measurement is done using a commercially available power-meter, which is directly connected to the waveguide output of the probe. During this measurement only two optical lines where feeding the UTC-PD to enable a THz frequency signal at the output of the photodiode, therefore no spurious signal was present in the photodiode output. The correction in Fig. 4.2 is done with the probe loss at the 300 GHz frequency.

The bandwidth of the photomixer is determined by the probe used for the out-coupling of the 300 GHz signal. The photomixer is using an optical design that increases the sensitivity of the photodiode and enables an efficient THz power generation with respect to the photocurrent inside the UTC-PD. Comparing with a commercially available packaged UTC-PD [WFM+08], where the power level is 0.54 mW for 20 mA, the photodiode used in this work generates 0.75 mW for only 9.8 mA current, meaning a reduction by a factor of 2 [LPB+17]. This design is aiming to increase the life-time of the UTC-PD by an operation with limited current.

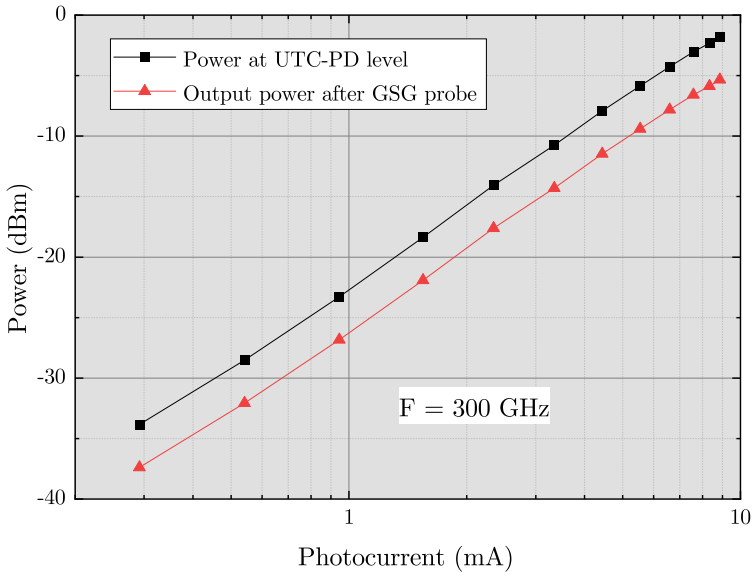

Figure 4.2: Linearity of generated power at UTC-PD output for a bias of $-1\,\mathrm{V}$. Red curve: GSG probe output, black: power at UTC-PD output (wafer level). A linear behavior of the UTC-PD is obtained up to approximately $8\,\mathrm{mA}$. In the data communication experiments, a $4\,\mathrm{dB}$ margin (back-off) is taken for linear operation of the UTC. This corresponds to a photocurrent smaller than $5\,\mathrm{mA}$ as in the photomixing process, the generated power is proportional to the square of the photocurrent inside the photodiode.

4.2 Electronic receiver

The electronic receiver is based on a MMIC fabricated using the $35\,\mathrm{nm}$ mHEMT by Fraunhofer IAF described in detail in section 1.2.3. This technology is best suited for fabricating THz receivers due to its excellent low noise properties and very high transit frequency f_t above $500\,\mathrm{GHz}$ and f_max above $1\,\mathrm{THz}$.

The receiver integrates a frequency multiplier by three, a buffer amplifier, a fundamental passive IQ mixer and a three-stage low-noise amplifier. Fig. 4.3 shows the schematic of the receiver. The single stages of the circuit have been described in detail in [TLW+17] and [KDR+15]. The integrated receiver is assembled in a waveguide split-block module as described in section 3.1. The LO input lies at 100 GHz and has a WR10 waveguide interface. The RF interface is provided by a WR3 waveguide. The transition between MMIC and waveguide is realized by a quartz substrate. The IF signals are provided by V-connectors and a liquid polymer substrate. The 100 GHz LO frequency is provided by a separate frequency multiplier module, which has an input at $8.33\,\mathrm{GHz}$. This signal is provided by an electrical synthesizer. Fig. 4.4 shows the measurement of the conversion gain and noise figure versus the RF frequency. The average conversion gain of the receiver lies at $6.5\,\mathrm{dB}$ from 270 to $325\,\mathrm{GHz}$. The measured room temperature noise figure lies at an average of $8.6\,\mathrm{dB}$ [TLW+17]. With the help of the sensitivity measurement described in more detail in section 3.1 the optimal input power of the receiver is determined at $-41\,\mathrm{dBm}$. Therefore, the power that reaches the receiver should lie in this range and the transmitting distance and gain of the antennas have to be chosen accordingly.

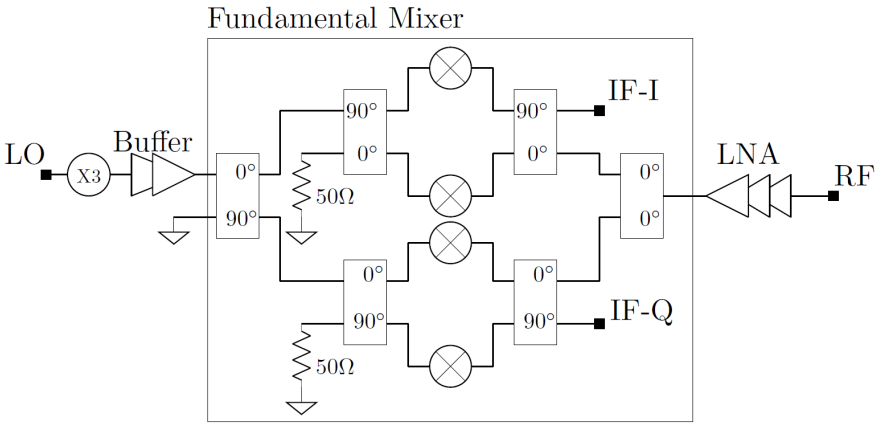

Figure 4.3: Schematic of the active electronic receiver integrating a frequency multiplier by three, a buffer amplifier, a fundamental passive IQ mixer and a three-stage LNA.

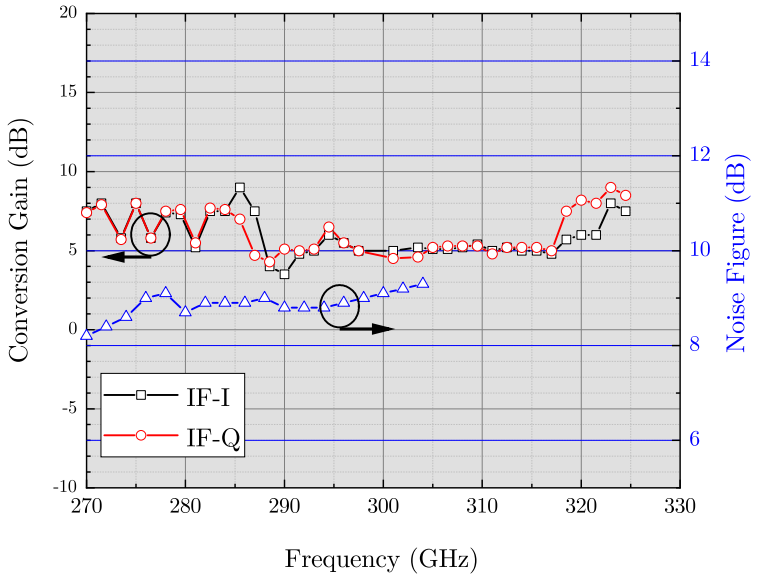

Figure 4.4: Measured conversion gain and noise figure over the RF frequency for the 300 GHz active receiver.

4.3 Digital signal processing

The transmitted signal is generated by an AWG with $8\,\mathrm{bit}$ resolution, $25\,\mathrm{GHz}$ analog bandwidth per channel and a maximum sampling rate of $65\,\mathrm{GSa/s}$. The complex IQ data signal is numerically generated as follows: a PRBS with a length of $2^{15}-1$ is converted to an integer sequence and mapped over a QAM constellation. The resulting complex sequence is up-sampled to match the AWG sampling rate range and filtered using a raised-cosine digital filter with different roll-off factors α. In comparison to rectangular pulses, which have a theoretically infinitely broadband spectrum and will influence other frequency bands, raised cosine pulse shaping offers a low adjacent channel interference.

At the receiver side a real time oscilloscope with $80\,\mathrm{GSa/s}$, an analog bandwidth of $32\,\mathrm{GHz}$ and $8\,\mathrm{bit}$ vertical resolution captures the I- and Q-signals from the receiver. Since the transmitter and the receiver do not share the same local oscillator signal source and no hardware carrier recovery is used, the setup is incoherent. A vector signal analyzer software

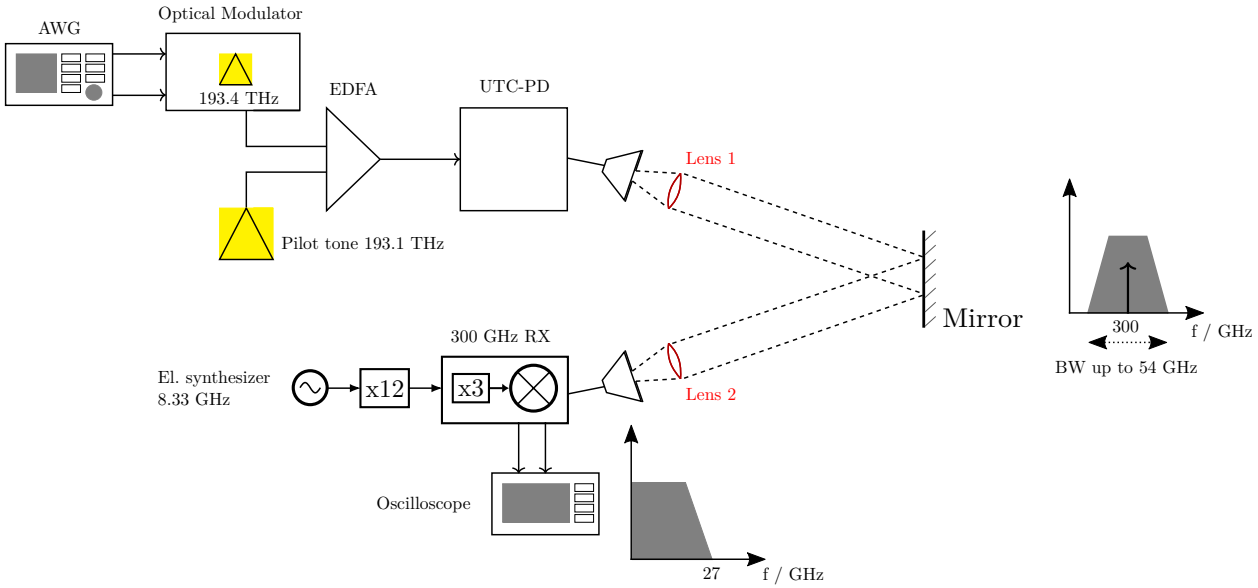

Figure 4.5: Schematic of the wireless link setup. A mirror is placed between the UTC-PD transmitter and receiver, doubling the transmitting distance. A brief spectrum of the RF signal as well as of the incoming IF signal is presented.

analyzes the incoming signal and performs the carrier recovery and the frequency equalization to compensate for the frequency and phase drift along the link. The digital equalization tool of the software has been applied to all the results shown in this section. The performance of the link is analyzed in terms of EVM.

4.4 Setup of the wireless links

Fig. 4.5 shows the schematic setup of the data transmission. The signal is radiated into free space and transmitted over a distance of $15\,\mathrm{m}$. For this purpose a mirror is placed at half the distance. This provides a convenient placement of the receiver next to the transmitter. A system of two standard horn antennas and two collimating polytetrafluoroethylene (PTFE) lenses are used to align the quasi-optical link between TX and RX. The lenses have a 100 mm diameter and a 200 mm focal length. The receiving system is composed of two modules: the $300\,\mathrm{GHz}$ receiver module and the multiplier by twelve module, which provides the $100\,\mathrm{GHz}$ LO signal necessary for the receiver. An electronic synthesizer provides the $8.33\,\mathrm{GHz}$ LO input signal. Fig. 4.6 shows photographs of the UTC-PD photomixer and of the $300\,\mathrm{GHz}$ electronic receiver.

To determine the transmission distance the following equation has been used:

$$\begin{aligned} \mathrm{FSPL} &= \mathrm{P_{out,TX}} + 2 \cdot \mathrm{G_A} - \mathrm{P_{rf,in}} \\ &= -8\,\mathrm{dBm} + 2 \cdot \mathrm{G_A} - (-41\,\mathrm{dBm}) \end{aligned} \tag{4.1}$$

The antenna system consists of three elements: two horn antennas, two PTFE lenses and one mirror. The output power $P_{out,TX}$ is dependent on the used modulation format and symbol rate transmitted, follows the curve shown in Fig. 4.2 and varies between -12 and - 8 dBm. For 16-QAM modulation a photocurrent of $5.2\,\mathrm{mA}$ was noted, which corresponds to an output power of -8 dBm. The optimal receiver input power $P_{rf,in}$ lies at around $-41\,\mathrm{dBm}$. This

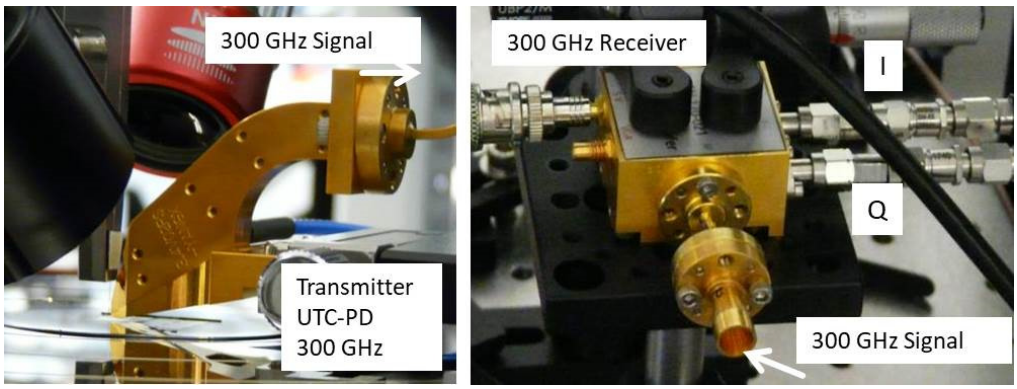

Figure 4.6: Photographs of the UTC-PD transmitter and electronic receiver with horn antenna and I/Q connections.

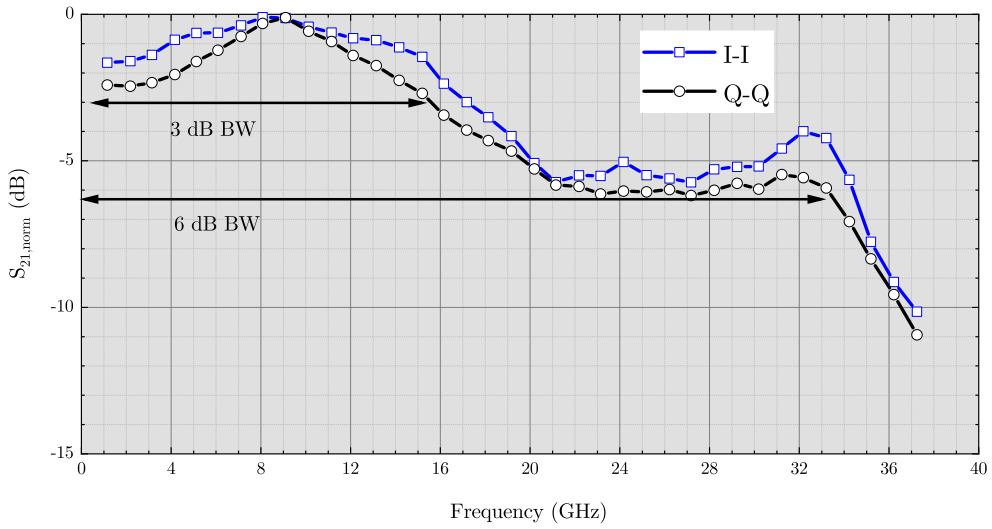

Figure 4.7: Measurement results of the transfer function characteristics, when the transmission is done from the I-channel to the I-channel or from Q-channel to Q-channel.

value was measured for a distance of $15\,\mathrm{m}$, which corresponds to a FSPL value of $105.5\,\mathrm{dB}$. This leads to an overall antenna system gain of:

$$\begin{aligned} 2 \cdot \mathrm{G_A} &= \mathrm{FSPL} - \mathrm{P_{out,TX}} + \mathrm{P_{rf,in}} \\ &= 105.5\,\mathrm{dB} - (-8\,\mathrm{dBm}) + (-41\,\mathrm{dBm}) \\ &= 72.5\,\mathrm{dB} \end{aligned} \tag{4.2}$$

To characterize the $300\,\mathrm{GHz}$ analog transmit-receive wireless system in terms of bandwidth and gain imbalance, the measurement of the complex transfer function of the system was conducted as it is described in detail in section 3.2. For this purpose, a VNA measures the S-parameters of the transmit-receive system. The setup of the measurement is similar to the one shown in Fig 4.5, with the only difference that the AWG and the oscilloscope are replaced by the VNA. The signal originating from the first port of the VNA, connected to the I-channel of the optical modulator is up-converted by the UTC-PD and transmitted over the air to the electronic receiver, down-converted and received on the I-channel, which is connected to the second port of the VNA. The Q-channels are terminated with $50\,\Omega$ loads.

The same measurement is conducted by connecting the ports of the VNA to the Q-channels of the modulator and of the receiver.

Since the setup is incoherent, a phase shifter is placed after the electronic synthesizer and adjusted in a way that the maximum power is in the measured channel and therefore compensating for the total phase delay introduced in the up- and down-converter.

In comparison to on-chip measurements, this measurement shows the overall frequency response of the system and the effective bandwidth limitation. The characteristics shown in Fig. 4.7 for the I-I and Q-Q transmission represent the linear transfer gain, when both the transmitter and the receiver are operated in their linear region. The transmission parameter S_{21} is normalized to its highest value for a better representation of the bandwidth limitation. While the 3 dB IF bandwidth lies at $16\,\mathrm{GHz}$, the 6 dB bandwidth exceeds $30\,\mathrm{GHz}$, which results in an RF bandwidth of over $60\,\mathrm{GHz}$.

4.5 100 Gbps wireless data transmission

After the measurement of the analog transfer function of the transmit-receive system, data transmission experiments have been carried out. Signals with different modulation formats, symbol rates and digital filtering were transmitted over the distance of $15\,\mathrm{m}$ and the quality of the transmission has been analyzed.

Fig. 4.8 and Fig. 4.9 show the constellation diagrams and the power spectra of 16-QAM modulated signals with increasing symbol rates. The black dots in the constellation diagrams represent the results of the demodulation of a reference signal. Prior to the $300\,\mathrm{GHz}$ wireless data experiment, signals with different modulation formats and symbol rates were measured by connecting the signal coming from the optical modulator directly to the oscilloscope. Therefore, the black dots and the resulting EVM are the best possible result and represent the reference signal.

Fig. 4.8 (a) shows the results for a symbol rate of $4\,\mathrm{GBd}$, resulting in $16\,\mathrm{Gbps}$. For this low data rate the constellation diagram is very clear and the EVM deterioration in comparison to the reference signal is below $5\,\%$. An increase in bandwidth and symbol rate leads to a decrease in the frequency response of the overall system demonstrated by the frequency dependency of the $\mathrm{S}_{21,\mathrm{norm}}$ transmission parameter presented in Fig. 4.7. For a symbol rate of $12.5\,\mathrm{GBd}$ shown in Fig. 4.8 (b), the EVM deterioration lies slightly above $5\,\%$. The bandwidth occupied by the $12.5\,\mathrm{GBd}$ 16-QAM modulated signal is within the 3-dB bandwidth of the system presented in Fig. 4.7.

Although the absolute EVM value of the measured $20\,\mathrm{GBd}$ signal, Fig. 4.9 (a), is above $12\,\%$ the EVM deterioration is similar to the previous cases, around $5\,\%$. The occupied IF-bandwidth of $15\,\mathrm{GHz}$ matches the 3-dB bandwidth of the $300\,\mathrm{GHz}$ wireless system. For the signal that achieved the highest data rate, Fig. 4.9 (b), the EVM deterioration is above $10\,\%$. This non-linear increase points to a surpassing of the 3-dB bandwidth and to increasing effects of impairments like LO isolation. For an AWGN channel, the SNR limit for 16-QAM modulation and a BER smaller than $4 \cdot 10^{-3}$, which can be reduced to 10^{-15} using forward error correction codes [COM10] is $13.4\,\mathrm{dB}$. The $25\,\mathrm{GBd}$ signal reaches an SNR of $12.4\,\mathrm{dB}$ and is therefore below this limit and could not be successfully demodulated. All the other signals, $20\,\mathrm{GBd}$, $12.5\,\mathrm{GBd}$ and $4\,\mathrm{GBd}$, have an SNR of $15.5\,\mathrm{dB}$, $17.2\,\mathrm{dB}$ and $20\,\mathrm{dB}$ and represent successful transmissions.

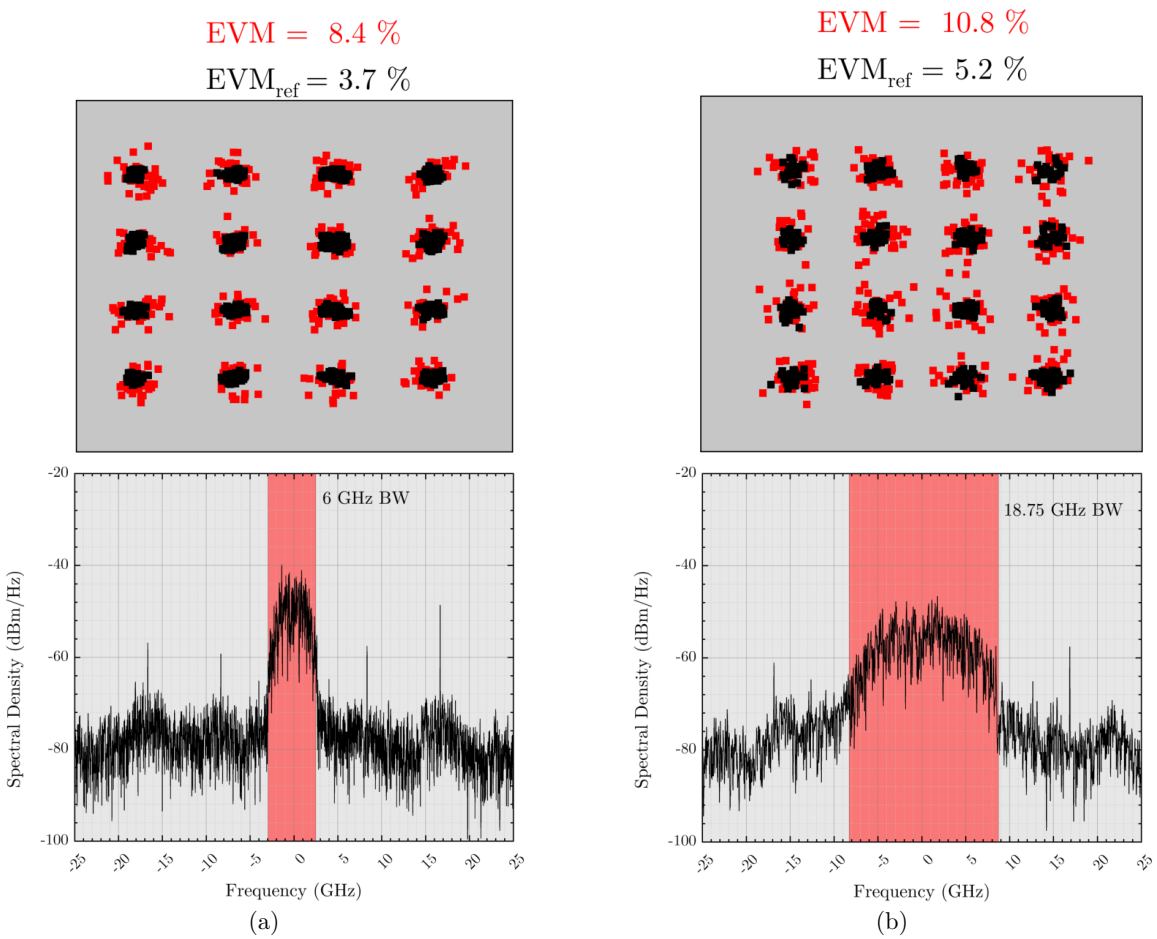

Figure 4.8: Constellation diagrams and the corresponding spectral densities of 16-QAM modulated signals with increasing symbol and data rates. (a) $4\,\mathrm{GBd}$, $16\,\mathrm{Gbps}$. (b) $12.5\,\mathrm{GBd}$, $50\,\mathrm{Gbps}$. The black dots represent the results of a reference signal measured by connecting the signal coming from the optical modulator directly to the oscilloscope and the red dots represent the results of the actual signal transmitted over $15\,\mathrm{m}$ using the setup in Fig. 4.5.

An impairment that negatively influences the transmission of the $25\,\mathrm{dB}$ signal is the LO to IF isolation, which can be graphically observed in the spectra in Fig. 4.8 at $16.66\,\mathrm{GHz}$. The spectral lines at $8.33\,\mathrm{GHz}$, $16.66\,\mathrm{GHz}$ and their negative correspondents are parasitic spurious tones of undesired harmonics. The mechanical interface between the multiplier module and the $300\,\mathrm{GHz}$ receiver is a WR-10 waveguide. This means that only harmonics above the lower cutoff frequency of the WR10 waveguide with an order higher than 8 ($\mathrm{X8} = 8 \cdot 8.33\,\mathrm{GHz} = 66.64\,\mathrm{GHz}$) can propagate. Considering the buffer amplifier's limited bandwidth, which acts as a filter for most undesired harmonics, only a few combinations remain plausible for the cause of the leakage. Fig. 4.10 shows the spectral density of the leaked signal, when the RF signal is turned off. Therefore, only the leakage of the LO in the receiver can be observed. The rest of the measurement setup remains unchanged, the demodulation occurs using both I and Q outputs, hence the possibility to plot also the negative part of the spectrum. The mixing of the 39th harmonic (X39), the leakage of the 13th harmonic coming from the multiplier module multiplied by three in the receiver, and the 40th harmonic (X40), an undesired 4th harmonic of the 10th harmonic coming from the multiplier module cause a first spurious tone at $8.33\,\mathrm{GHz}$. The highest leakage, at $16.66\,\mathrm{GHz}$, is caused by the mixing

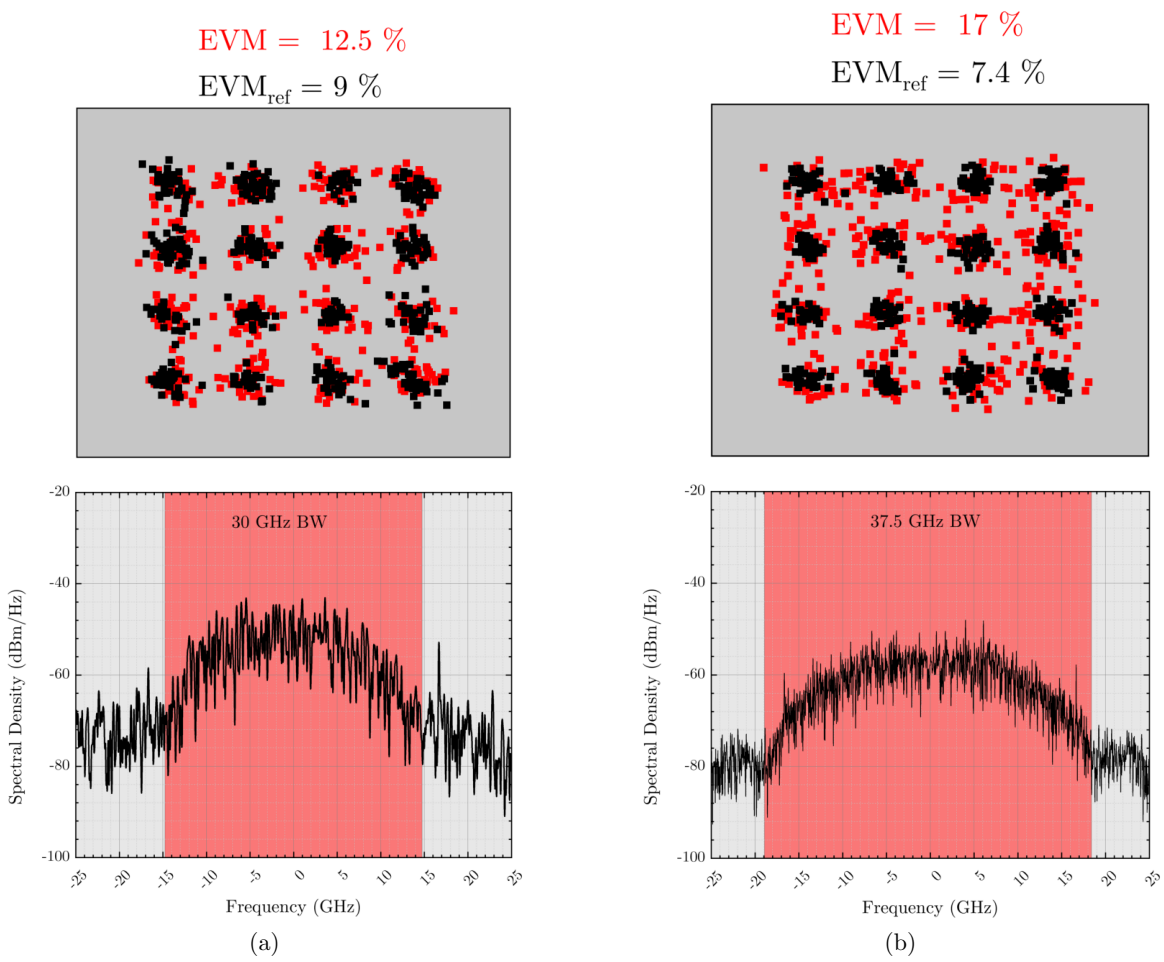

Figure 4.9: Constellation diagrams and the corresponding spectral densities of 16-QAM modulated signals with increasing symbol and data rates. (a) $20\,\mathrm{GBd}$, $80\,\mathrm{Gbps}$. (b) $25\,\mathrm{GBd}$, $100\,\mathrm{Gbps}$. The black dots represent the results of a reference signal measured by connecting the signal coming from the optical modulator directly to the oscilloscope and the red dots represent the results of the actual signal transmitted over $15\,\mathrm{m}$ using the setup in Fig. 4.5.

of the 36th harmonic (X36) at $300\,\mathrm{GHz}$ and the 34th harmonic (X34). X34 is an undesired 2nd harmonic of the 17th harmonic (X17) coming from the multiplier by twelve module. A less likely possibility is the mixing of the 40th harmonic (X40) with the 42nd harmonic (X42), which at $349.86\,\mathrm{GHz}$ is strongly filtered out by the buffer amplifier and can most probably not cause such a high leakage.

The asymmetry between the positive and the negative part of the spectrum has its origin in the particularity of the fundamental mixer, shown in Fig. 4.3. The IF signal is measured at the isolated port of the last $90°$ coupler and not, as usual, directly at the IF mixer output. In addition, only one of the mixer paths in the I- and one in the Q-channel is used. Despite this, the non-linear mixing products of both paths are added in the coupler, thus producing a different phase shift. The leakage measured on I and Q are demodulated in the VSA software, which leads to the asymmetry in the spectrum.

While for the first three 16-QAM transmissions in Fig. 4.8 (a) to Fig. 4.9 (a) the LO leakage is outside the bandwidth of the signal, depicted by the gray area, in the last case, Fig. 4.9 (b) the peak is inside the desired signal, which leads to an EVM deterioration. To avoid this and

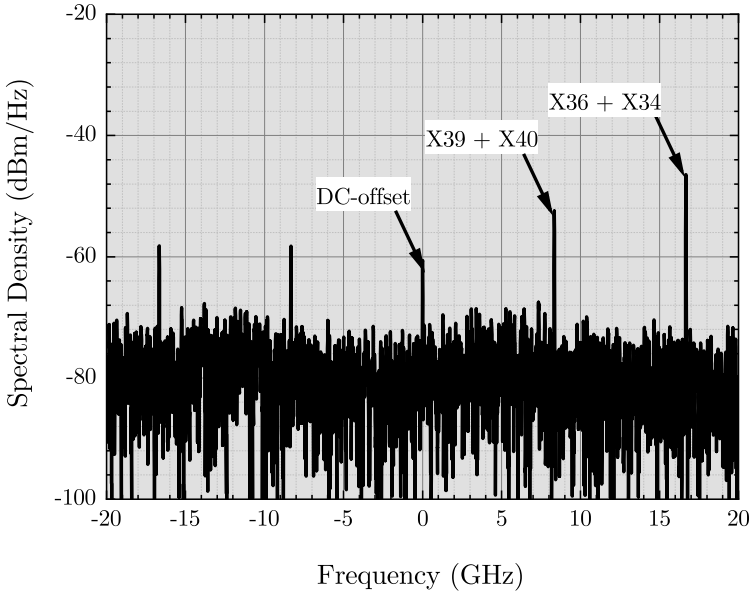

Figure 4.10: Power spectrum measured without an RF signal, showing the LO leakage in the receiver.

to improve the quality of the transmission, a narrower digital filter is used, with a roll-off factor of 0.35 instead of 0.5, which reduces the bandwidth by $4.25\,\mathrm{GHz}$. Additionally, the IF signal is modulated using an intermediate frequency generated in the AWG, so that the signal is centered around $-3\,\mathrm{GHz}$.

Fig. 4.11 shows the comparison of the power spectra between a $25\,\mathrm{GBd}$ 16-QAM modulated signal with a bandwidth of $37.5\,\mathrm{GHz}$ represented in the dotted black curve, and one with a bandwidth of $33.75\,\mathrm{GHz}$ centered around $-3\,\mathrm{GHz}$ represented in the solid red curve. The signal level of the more narrow-band signal is higher than the one of the more broadband signal. In the case of the narrow-band signal the LO leakage is outside the signal bandwidth. All these lead to an EVM improvement of more than $4\,\%$. The final absolute EVM value is therefore $13\,\%$, which is above the 16-QAM limit for BER smaller than $4 \cdot 10^{-3}$. Thus, $100\,\mathrm{Gbps}$ wireless transmission has been successfully proven. Comparing the bandwidth achieved for this very high data rate with the frequency response of the overall system, the conclusion can be derived that for 16-QAM modulation the 3-dB bandwidth is the limit for a successful transmission.

In this wireless link the influence of spurious derive from three non-linear components: the frequency multiplier-by-twelve in the first stand-alone multiplier module, the frequency multiplier-by-three, integrated on the receiver chip and finally, the down-converter also integrated on the receiver chip. The design of each stage needs to take into account the impact of spurious on the final performance of the link. In the case presented in Fig. 4.11 with the black dotted line the suppression of an in-band spurious of less than $10\,\mathrm{dBc}$ is reached, which leads to an unsuccessful transmission. Shifting the signal band is one solution, which did not involve new hardware. Another solution which would lead to a higher improvement in the performance of the link can be achieved by an optimized design of the receiver MMIC or the usage of a spurious-free LO source at $100\,\mathrm{GHz}$.

A 16-QAM $4\,\mathrm{GBd}$ signal is transmitted using the changes described above: a signal centered around a given non-zero IF frequency and a filter with a roll-off factor of 0.35.

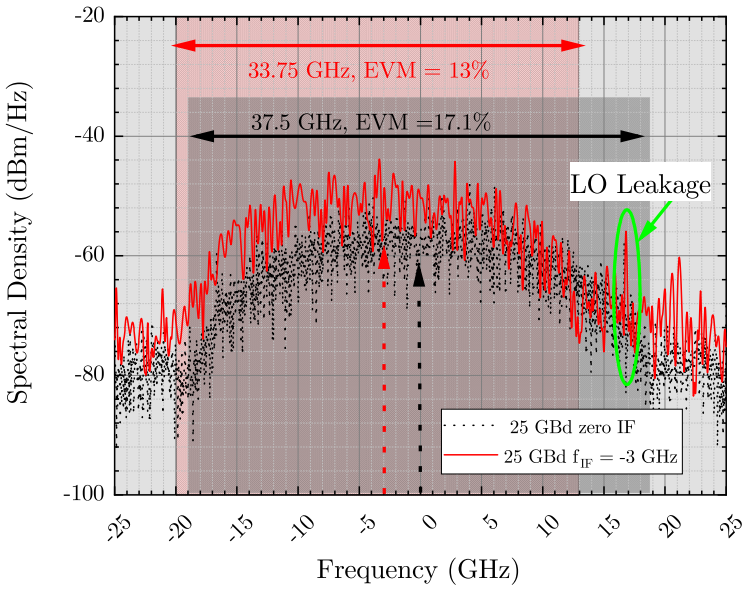

Figure 4.11: Comparison between power spectrum of a $25\,\mathrm{GBd}$ $16-\mathrm{QAM}$ modulated signal with different bandwidths and center frequencies.

Fig. 4.12 shows the constellation diagram of this new transmission in green and the comparison to the reference signal in black and the zero IF signal in red. Compared to the signal in Fig. 4.8(a) the results of this new transmission show an improvement in EVM of $31\,\%$, leading to an absolute EVM value of $5.8\,\%$ and an improvement in SNR of $14.4\,\%$, leading to an absolute SNR value of $22.08\,\mathrm{dB}$.

4.6 Transmission of complex modulation formats

In order to show the potential of the presented wireless link for future high data rate applications, signals using complex modulation formats were transmitted over the air. Data-hungry applications like kiosk-downloading, data-centers and smart offices use either a very broadband signal modulated with simple modulation formats or they aggregate multiple channels, each with a narrow bandwidth, but with complex modulation formats.

Fig. 4.13 and Fig. 4.14 show the constellation diagrams and the corresponding spectral densities of successfully transmitted signals with higher order modulation formats which achieved the highest data rate. For 64-QAM, a signal with a symbol rate of $5\,\mathrm{GBd}$, filtered using a root-raised cosine filter with a roll-off factor of 0.35 and centered around a non-zero intermediate frequency achieves an absolute SNR value of $21.4\,\mathrm{dB}$. For an AWGN channel, this value is above the limit for 64-QAM and BER smaller than $4 \cdot 10^{-3}$, which lies at $17.8\,\mathrm{dB}$. Hence, the transmission of 64-QAM, $5\,\mathrm{GBd}$ is successfully demodulated. Compared to the reference signal, the EVM value deteriorates by slightly more than $2\,\%$, which is comparable to the deterioration for 16-QAM modulation at similar symbol rates shown in Fig. 4.8(a). Due to the high linearity requirements of this modulation format, this is the highest data rate achieved with 64-QAM. Looking at the measurement of the transfer function in Fig. 4.7 we observe that the frequency response is flat until $3\,\mathrm{GHz}$, which coincides with the IF bandwidth limit for 64-QAM. Also, at $4\,\mathrm{GHz}$, there is a peak in the IQ-imbalance curve.

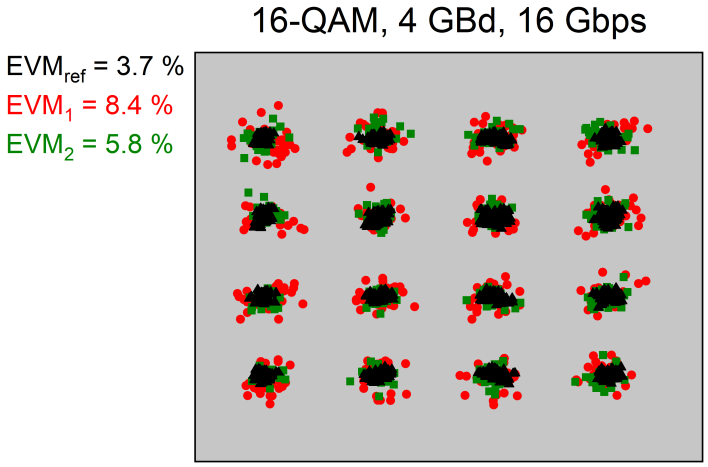

Figure 4.12: Graphic representation of the EVM improvement due to LO leakage reduction and shifting of the transmission center frequency. The black dots represent the reference signal, the red dots are the original transmitted 16-QAM signal and green the improved transmission.

A lower IQ-amplitude imbalance, a flatter frequency response of the system and a higher isolation of the LO leakage can help increase the transmitting bandwidth and thus, improve the highest possible data rate for complex modulation formats.

Another important aspect is that the distance between transmitter and receiver is kept constant during all the transmission experiments. The optimal input receiving power was determined and set for 16-QAM. To optimize the 64-QAM transmission a dynamic change in distance and transmitting output power is needed. Due to constraints of the mechanical indoor setup the transmitting distance could not be changed.

For the 32-QAM modulation format a bandwidth of up to $10.8\,\mathrm{GHz}$ is successfully transmitted. The results of this transmission are presented in Fig. 4.14. An EVM value of around $7\,\%$ and an EVM deterioration of $2.5\,\%$ are achieved. The fact that a higher bandwidth than in the case of 64-QAM was reached and the transfer function characteristic points out that for 32-QAM a 1 to $2\,\mathrm{dB}$ deviation from a perfectly flat frequency response and an IQ imbalance of up to $1\,\mathrm{dB}$ are acceptable.

4.7 Transmission of signals with high bandwidth

Using simple modulation formats, like BPSK and QPSK, the limits of the wireless system in terms of bandwidth can be tested. This approach, transmitting very broadband signals in one channel, is a viable alternative to systems using multi-channels and complex modulation formats and has been adopted in most previous works.

The $300\,\mathrm{GHz}$ wireless link presented in this section successfully transmitted and received signals with RF bandwidth up to $54\,\mathrm{GHz}$ using QPSK modulation format. Fig. 4.15 shows the dependency between EVM deterioration and signal bandwidth. The EVM deterioration is the difference between the measured EVM for the actual signal and the EVM value of the reference signal.

The $54\,\mathrm{GHz}$ RF bandwidth was achieved with a signal with a symbol rate of $40\,\mathrm{GBd}$. The absolute value of the SNR is $10.9\,\mathrm{dB}$, which is slightly above the successful demodulation

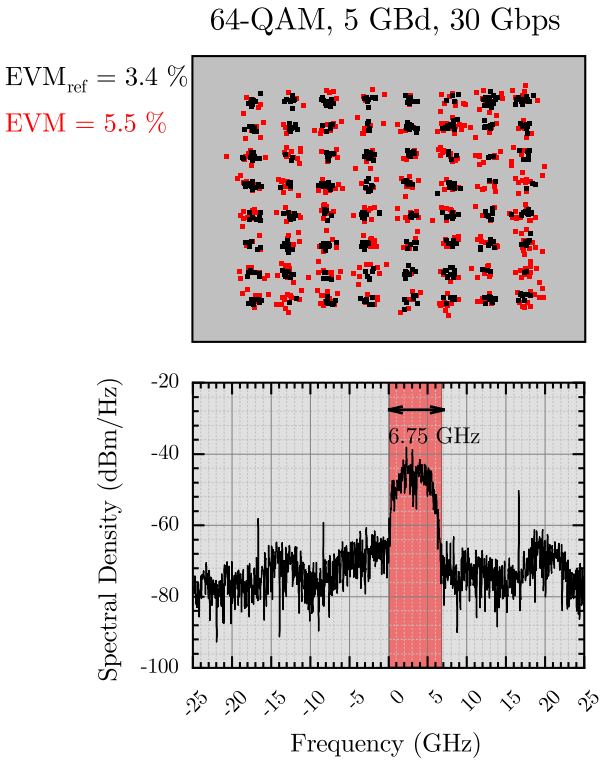

Figure 4.13: Constellation diagram and the corresponding spectral density of a 64-QAM modulated signal with a symbol rate of $5\,\mathrm{GBd}$ and bandwidth of $6.75\,\mathrm{GHz}$ achieving a data rate of $30\,\mathrm{Gbps}$.

limit for QPSK and AWGN channel, SNR of $9.6\,\mathrm{dB}$. While for a signal with $20\,\mathrm{GBd}$ symbol rate and $30\,\mathrm{GHz}$ of bandwidth, the EVM value differs just by $3\,\%$ from the reference, signals with bandwidths above $45\,\mathrm{GHz}$ show a substantial deterioration of almost $10\,\%$ at $54\,\mathrm{GHz}$. The frequency response of the system measured and presented in Fig. 4.7 shows that between $24\,\mathrm{GHz}$ and $33\,\mathrm{GHz}$ IF frequency the $6\,\mathrm{dB}$ bandwidth limit is reached. The successfully transmitted QPSK signal occupies $27\,\mathrm{GHz}$ of IF bandwidth. This means that for QPSK modulation format the digital equalization tool can compensate up to a limit of $6\,\mathrm{dB}$ from the frequency response of the system. Other limiting factors are the IQ phase and amplitude imbalances, which can be observed in the constellation diagrams, where the spread of the red points worsens with increasing bandwidth.

The transmission of high data rates at $300\,\mathrm{GHz}$ is influenced by a manifold of factors like modulation format, bandwidth, SNR and other non-idealities introduced by the front end. While higher order modulation formats offer a high spectral density they have higher requirements with respect to SNR, IQ imbalances and flatness of the transfer function characteristic. Less complex modulation formats, like BPSK and QPSK, can be successfully transmitted over a higher bandwidth, like proven in this experiment. Although the absolute highest data rate was achieved with 16-QAM, the ability of the link to transmit a $54\,\mathrm{GHz}$ signal shows the potential of the combination of photonic transmitter and electronic receiver for usage in future application that require data rates above $200\,\mathrm{Gbps}$. These high data rates will only be used by combining the advantage of a high spectral density signal over multiple channels, which require a very high total bandwidth.

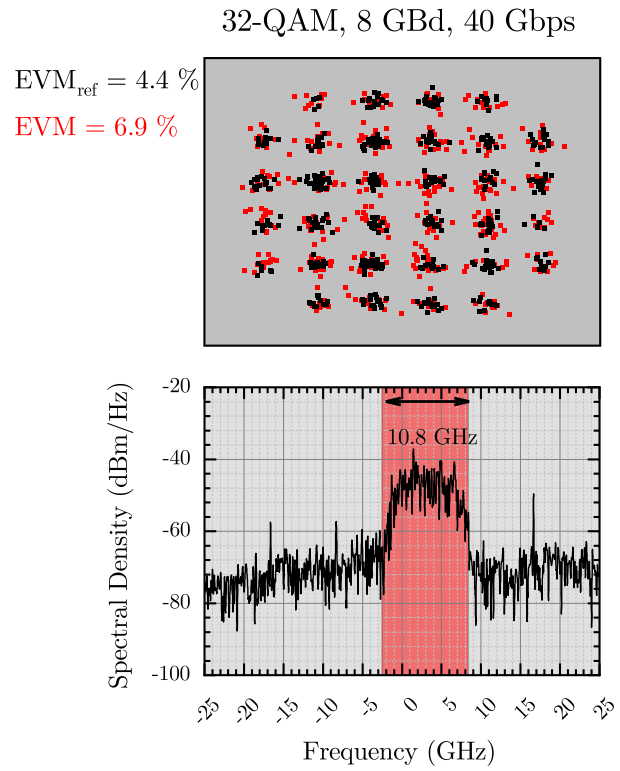

Figure 4.14: Constellation diagram and the corresponding spectral density of a 32-QAM modulated signal with a symbol rate of $8\,\mathrm{GBd}$ and bandwidth of $10.8\,\mathrm{GHz}$ achieving a data rate of $40\,\mathrm{Gbps}$.

4.8 Comparison to state-of-the-art

Wireless systems operating in the low THz region can be implemented based either on fully electronic, fully photonic or mixed electronic-photonic technologies. The latter approach is today the most promising way forward since it allows to combine the unique advantages of both domains, namely the low receiver noise, high transmit power and high functional integration density of electronics-based THz TRX, with the high spectral purity and high quality phase and frequency control of photonics-based TRX [NC15], [DSB+14]. A summary of the state of the art of successful data transmissions, in terms of data rate versus link distance, is presented in Fig. 4.16. This work is highlighted in a circle.

Data transmissions are classified depending on the used technology. The first category is based on photonic generation of high speed THz signals. The progress in fiber optics has positively influenced the development of wireless links using photonics-based transmitters [DSB+14]. At very high carrier frequencies of 300 and $425\,\mathrm{GHz}$, not only very high data rates of up to 128 Gbps can be achieved [CLZ+18], [JPO+18], but also a high distance, up to 40 meters for a transmission of 100 Gbps [KLDA+13].

There has also been notable progress in the millimeterwave links using the electronic approach, where both the transmitter and the receiver are generated electronically. A recent publication [RGHP19b] reports on a transceiver using a SiGe HBT, which has been successfully used in a data transmission and has reached a data rate of 100 Gbps, at a center frequency of 230 GHz and a transmitting distance of $1\,\mathrm{m}$. This data rate is the highest reported in a

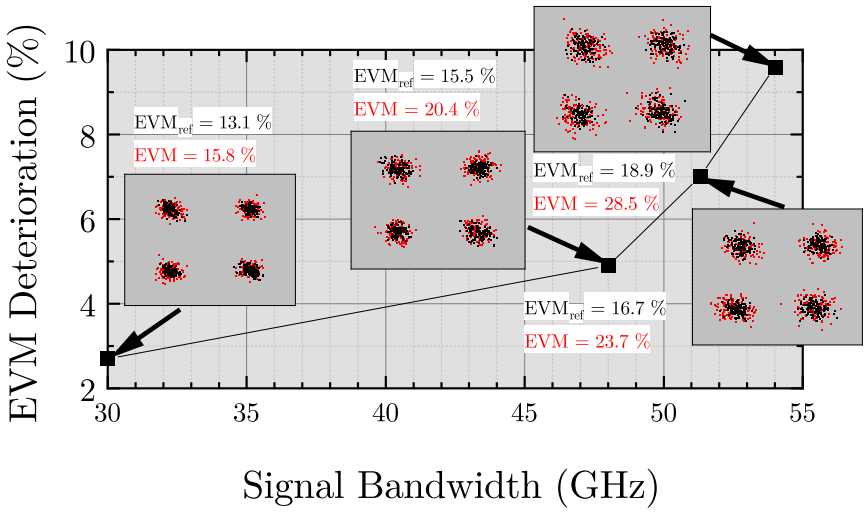

Figure 4.15: EVM deterioration and constellation diagrams for QPSK modulated signals with increasing symbol rates and bandwidth.

silicon-based technology. [HTK+18] presents a 40 nm CMOS transceiver which achieves data rates around $20\,\mathrm{Gbps}$ over small distances, $10\,\mathrm{cm}$.

Other technologies capable of realizing transceivers that operate above 200 GHz are the III-V compound semiconductor technologies: InP and InGaAs. [HFA+18] reports on a 100 Gbps $2.22\,\mathrm{m}$ data transmission using a $80\,\mathrm{nm}$ InP HEMT transceiver. An impressive distance with a corresponding high data rate has been reported in [KBM+15]. A transmission over $850\,\mathrm{m}$ was successfully conducted using QPSK modulation and a symbol rate of $32\,\mathrm{GBd}$, which leads to a data rate of $64\,\mathrm{Gbps}$. In [BMA+14] a transmission over $40\,\mathrm{m}$ with a data rate of $96\,\mathrm{Gbps}$ is reported.

The work presented here achieves the highest data rate considering the center frequency and the transmission range. This shows the advantages arising by the combination of photonic transmitter and active electronic receiver technologies: on the one hand the intrinsic high available bandwidth of the photonic source and the compatibility to the existing fiber-optic networks and on the other hand the low noise and the on-chip quadrature channel capabilities of active electronics.

Table 5.1 gives a summary of the most important parameters for the state of the art wireless data transmissions realized using different technologies. Next to data rate, distance and center frequency of operation, the used modulation format and the signal bandwidth are important parameters to asses the performance of a wireless link and to evaluate its potential for future usage in communication networks. Applications that could benefit from THz communication will either use multi-carrier configuration, where each channel has a limited bandwidth and therefore a higher modulation format is required, or they could take advantage of the immense bandwidth available in the $300\,\mathrm{GHz}$ band and use modulation formats with lower spectral efficiency, reducing the linearity requirements of the transceiver. From the state-of-the-art transmission links presented in Fig. 4.16, none except this work reports on the usage of modulation formats with a spectral density higher than five. [RGHP18] shows a 32-QAM transmission at $230\,\mathrm{GHz}$, which achieves a data rate of $90\,\mathrm{Gbps}$, using a signal bandwidth of $15\,\mathrm{GHz}$. If a publication did not mention the signal bandwidth the symbol rate has been used in the comparison in Table 4.1. While most works use signal bandwidths

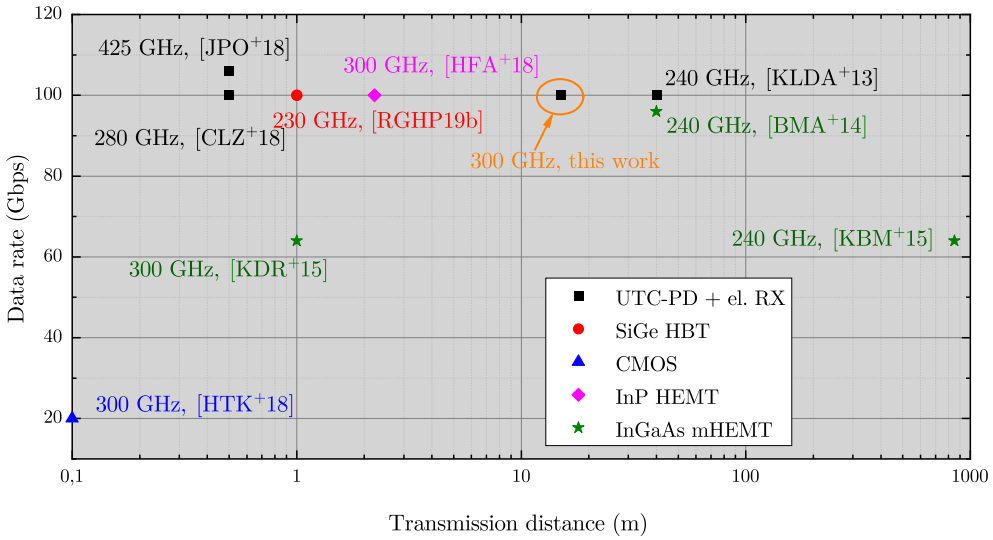

Figure 4.16: State of the art wireless transmissions realized by systems operating at frequencies above 200 GHz.

of around 35 GHz, the transmission presented in this work achieves the highest reported bandwidth of 54 GHz.

4.9 Conclusion

This chapter presents a 15 m wireless link operating at a center frequency of 300 GHz. The link combines two different technologies, a photonic transmitter and an electronic active receiver, and reaches data rates of up to 100 Gbps. Compared to other works, this is the highest data rate achieved for this frequency and range. In addition to a high data rate, the link shows a great potential in usage of a multi-channel approach for future wireless applications. Complex modulation formats like 32-QAM and 64-QAM are successfully transmitted for bandwidths of up to 10 GHz. The transmission bandwidth of the system exceeds 54 GHz, this being the highest ever reported transmission bandwidth.

The transmission scheme used for this link is the direct-conversion scheme. In comparison to the wireless link with the same transmission type presented in the previous chapter 3 the data rate is improved from 64 to 100 Gbps. Another important improvement is the linearity. Due to a better transmitter linearity complex modulation formats can be successfully transmitted and demodulated using the link presented in this chapter.

Table 4.1: State of the art wireless links above 200 GHz using different technologies.

Reference	Technology	Frequency	Highest Data Rate	Distance	Highest Modulation Format	Highest Signal Bandwidth
[KLDA+13]	UTC-PD + 35 nm InGaAs mHEMT	300 GHz	100 Gbps	40 m	16-QAM	34 GHz
[CLZ+18]	UTC-PD + passive electronic mixer	280 GHz	100 Gbps	50 cm	16-QAM	36 GHz
[JPO+18]	UTC-PD + passive electronic mixer	425 GHz	128 Gbps	50 cm	16-QAM	32 GBd
[RGHP19b]	130-nm SiGe BiCMOS	230 GHz	100 Gbps	1 m	16-QAM	28 GHz
[RGHP18]	130-nm SiGe BiCMOS	230 GHz	90 Gbps	1 m	32-QAM	15 GHz
[HTK+18]	40 nm Si-CMOS	300 GHz	20 Gbps	10 cm	16-QAM	5 GBd
[HFA+18]	80 nm InP-HEMT	300 GHz	100 Gbps	2.22 m	16-QAM	35 GHz
[BMA+14]	35 nm InGaAs mHEMT	240 GHz	96 Gbps	40 m	8-PSK	32 GHz
[KBM+15]	35 nm InGaAs mHEMT	240 GHz	64 Gbps	850 m	8-PSK	32 GHz
This work	**UTC-PD + 35 nm InGaAs mHEMT**	**300 GHz**	**100 Gbps**	**15 m**	**64-QAM**	**54 GHz**

5 An Active Electronic Receiver for the Direct-Conversion Approach

The link presented in the previous chapter has proven the high potential of the direct-conversion approach for THz wireless communication systems. The $100\,\mathrm{Gbps}$ achieved with a photonic transmitter and an active electronic receiver show that this system can provide the necessary data rate for future applications like front-and back-hauling, data centers, smart offices and homes. In order to improve the performance of this system even further this chapter presents a highly broadband quadrature down-converter with a center frequency of 300 GHz and a low-noise amplifier (LNA) with a bandwidth of 80 GHz, which was published in [8]. The operation frequency between 235 GHz and 315 GHz enables the usage in future wireless high data rate applications. The submillimeterwave MMICs are realized using the 35 nm mHEMT technology based on InAlAs/InGaAs presented in section 1.2.3. The down-converter integrates a frequency multiplier by four, a buffer amplifier and a passive fundamental I/Q mixer and reaches a conversion gain of -15 dB and an RF bandwidth of 60 GHz. The low-noise amplifier has an average gain of 26 dB over the 3 dB bandwidth. A total conversion gain of the receiver of 11 dB is therefore reached by combining the down-converter and the LNA.

As shown in the previous chapter, a very promising approach is the combination of photonics and active electronics. To overcome some of the limitations of this wireless transmission and to reach data rates well beyond $100\,\mathrm{Gbps}$ and higher distances a new $300\,\mathrm{GHz}$ receiver needs to be designed. In combination with an optimized photonic transmitter the goal of supplying ultra-high data rates to future communication links is one step closer.

5.1 Quadrature 300 GHz down converter

The $300\,\mathrm{GHz}$ quadrature down-converter integrates a frequency multiplier by four, a buffer amplifier and a fundamental mixer. The LO input frequency is $75\,\mathrm{GHz}$. At lower frequencies, the LO generation with commercially available sources is easier and more efficient than at $300\,\mathrm{GHz}$. In addition, considering the module integration of the down-converter bond wires and waveguide-to-chip transitions at $75\,\mathrm{GHz}$ have lower losses than in the H-band. With the help of the frequency multiplier an LO at the input of the down-converter of $300\,\mathrm{GHz}$ is reached.

The characterization of the MMICs is done in an on-wafer testing environment using a power meter at the output and a signal source with extensions at the input. The measurement setup was calibrated to the probe tip of the microwave probes.

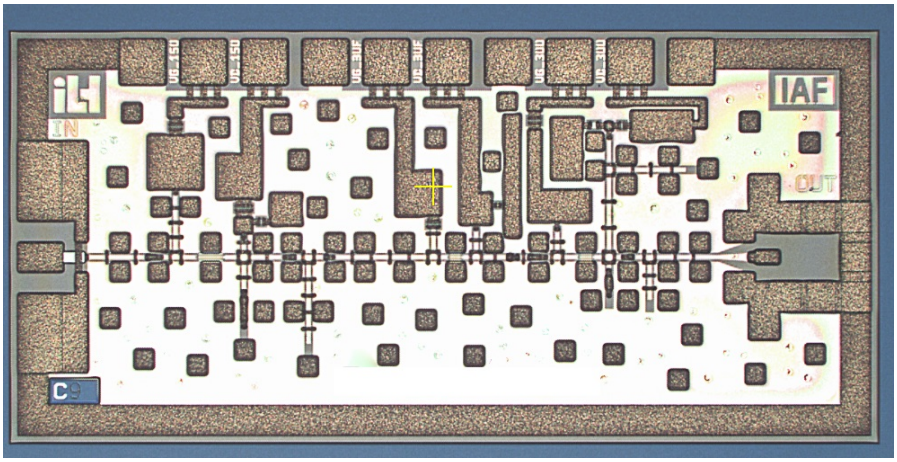

Figure 5.1: Chip photograph of the frequency multiplier by four with an input frequency of $75\,\mathrm{GHz}$ and an output frequency of $300\,\mathrm{GHz}$. The size of the chip is 0.75 x $1.5\,\mathrm{mm}^2$.

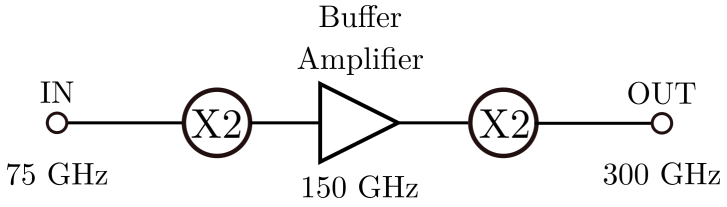

Figure 5.2: Schematic of the multiplier by four.

5.1.1 Frequency multiplier

Fig. 5.1 shows the chip photograph of the frequency multiplier by four as a stand-alone circuit. Including the RF and DC pads the chip has an overall size of 0.75 x $1.5\,\mathrm{mm}^2$. The length of the active chip area is barely over $1\,\mathrm{mm}$. Fig. 5.2 shows the schematic of the multiplier by four which is composed of two multipliers by two. An amplifier stage between the multipliers by two is required to provide the necessary input power for the second multiplication stage. Each multiplier by two is composed of one transistor with two fingers, an input matching network and an output matching network, which is in the same time a filter for unwanted harmonics. The devices are biased at the threshold voltage for class B operation mode, which corresponds to a gate voltage of $-0.3\,\mathrm{V}$ in order to generate the required second harmonic. The output signal in the case of class B operation is the positive half of a sine wave. The Fourier transformation of this output signal leads to a spectrum rich in even order harmonics. The advantage of this type of multiplier is that the desired even order harmonics appear in the output spectrum at low input powers. Fig. 5.3 shows the output power dependency of the input power for different frequencies. A constant difference between simulation and measurement of around 3 dB can be observed for all frequencies. The multiplier by four has a saturation input power of $2\,\mathrm{dBm}$. In comparison similar $300\,\mathrm{GHz}$ multipliers with a factor of three used for wireless communication need an input power around $8\,\mathrm{dBm}$ to saturate [GWL+18]. The DC power consumption of the multiplier lies at $61.3\,\mathrm{mW}$.

Fig. 5.4 shows the frequency dependency of the multiplier by four for two different input powers, $4\,\mathrm{dBm}$ and $8\,\mathrm{dBm}$ for both measurement and simulation. As in Fig. 5.3, a constant difference of 3 dB appears between simulation and measurement. As the multiplier is already in saturation, there is no notable difference between the measurement of the two different

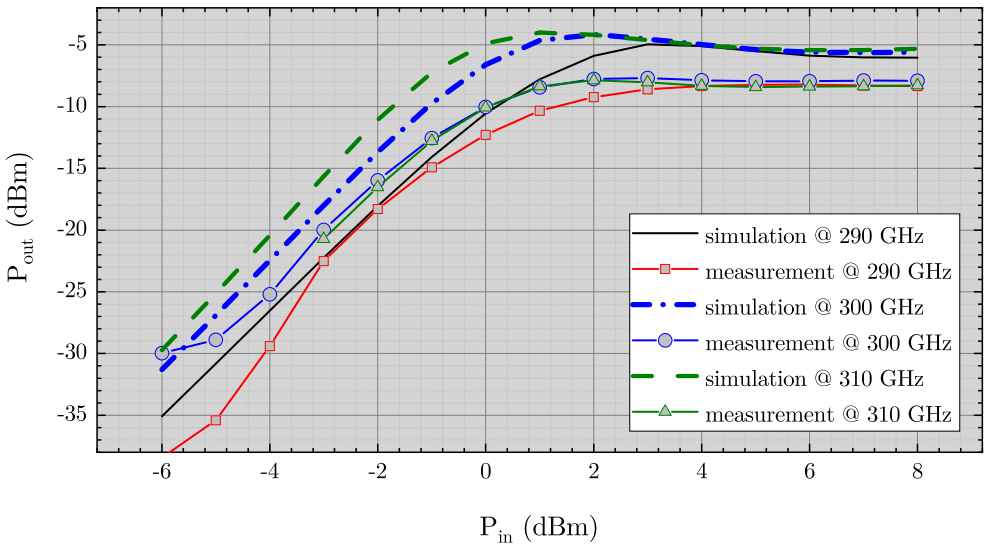

Figure 5.3: Comparison between simulation and measurement for the output power versus input power in the multiplier by four.

input powers. A 3-dB bandwidth of around $50\,\mathrm{GHz}$ is reached. This represents a relative bandwidth of over $16\,\%$.

5.1.2 Buffer amplifier

One of the biggest challenges of THz communication is the limited available output power. Currently, the state-of-the art RF power reported for $300\,\mathrm{GHz}$ solid state amplifiers is around $13\,\mathrm{dBm}$ [KJK+15]. To provide the resistive mixer with the necessary LO power for saturation, $6\,\mathrm{dBm}$, a powerful buffer amplifier is needed.

Fig. 5.5 shows the chip photograph of the 300 GHz buffer amplifier MMIC with a chip size of 0.75 x $2\,\mathrm{mm}^2$. The amplifier has five gain stages. The first stage contains one common source transistor. The second and third stage contain two parallel transistors and the fourth and last stage contain four parallel transistors. All the details about the design of the amplifier are presented in [STL+19a].

The amplifier has a 3-dB bandwidth spanning from 278 to $335\,\mathrm{GHz}$ and a maximum gain of $23\,\mathrm{dB}$. These values are reached for a drain voltage of $0.8\,\mathrm{V}$ and a total current of $144\,\mathrm{mA}$, leading to a DC power consumption of $115\,\mathrm{mW}$. The power measurement reveals that the amplifier has a saturation output power of $8\,\mathrm{dBm}$, for an input power of $-4\,\mathrm{dBm}$. Fig. 5.6 shows the output power dependency on the frequency for different input powers. Measurements are available only for -4 and $-13\,\mathrm{dBm}$. The expected input power for the buffer amplifier is according to Fig. 5.4 at $-8\,\mathrm{dBm}$. For this value a simulation was conducted. At $300\,\mathrm{GHz}$ the simulated output power is above $7\,\mathrm{dBm}$. $1\,\mathrm{dB}$ margin is calculated as being the difference between measurement and simulation. Therefore, an LO input power of $6\,\mathrm{dBm}$ is expected at mixer input.

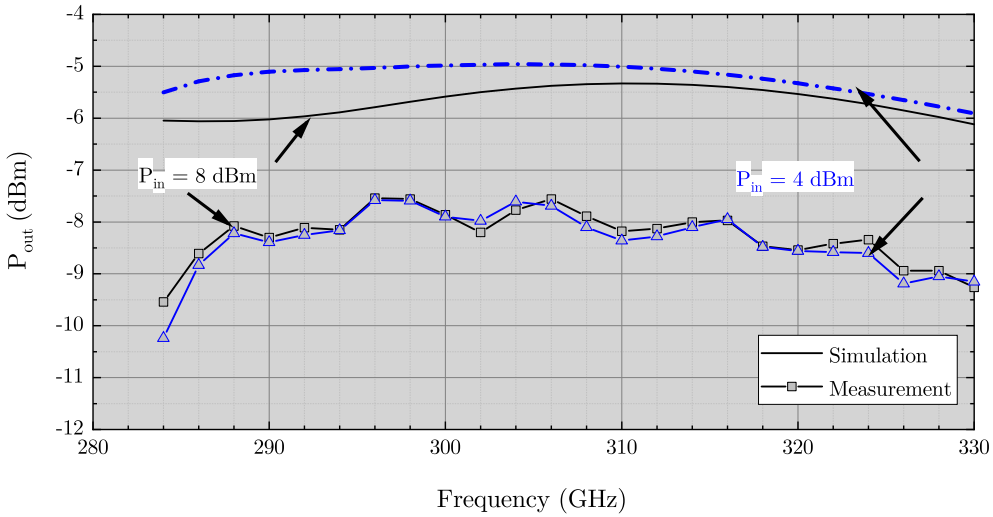

Figure 5.4: Comparison between simulation and measurement for the output power versus frequency in the multiplier by four.

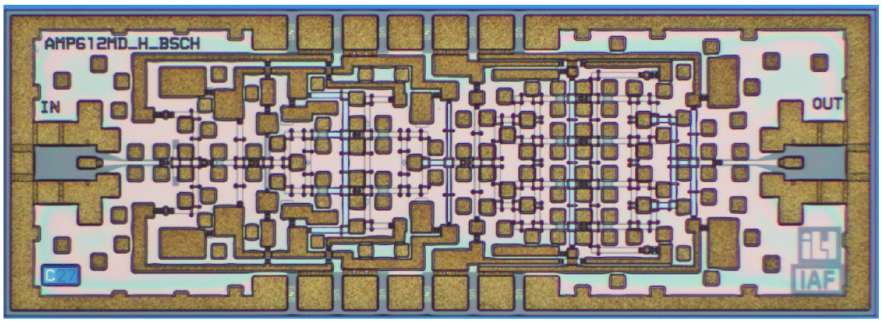

Figure 5.5: Chip photograph of the 300 GHz buffer amplifier MMIC. The size of the chip is 0.75 x 2 mm^2 [STL+19a].

5.1.3 Down-converter

The core of the down-converter chip is a single balanced fundamental resistive mixer with in-phase (I) and quadrature (Q) channels. The balancing is realized with a total of five $90°$ tandem X couplers and one 3-dB Wilkinson power divider. Since the LO power needed to saturate the mixer is above $5\,\mathrm{dBm}$, no stand-alone measurements of the mixer can be presented, but only of the integrated receiver. Each mixer cell is composed of one transistor with two fingers and a total gate width of $16\,\mu\mathrm{m}$. Both, the LO and RF input ports are broadband matched around $300\,\mathrm{GHz}$. The $180°$ difference in the LO signal reaching the tandem couplers after the Wilkinson divider leads to a destructive interference and therefore to a suppression of the LO in the RF signal. The IF channels are DC-coupled to allow for zero-IF down-conversion.

Fig. 5.7 shows the schematic and Fig. 5.8 the chip photograph of the integrated down-converter. The chip size is 1 x 3.5 mm^2. The overall power consumption of the chip is $178\,\mathrm{mW}$, which is mainly due to the buffer amplifier, which consumes $115\,\mathrm{mW}$ alone. The LO signal for the measurement of the integrated down-converter is provided using a commercial WR-10 source module followed by a power amplifier. The IF signal is generated using a commercial signal generator for frequencies up to 30 GHz and applied alternatively to the

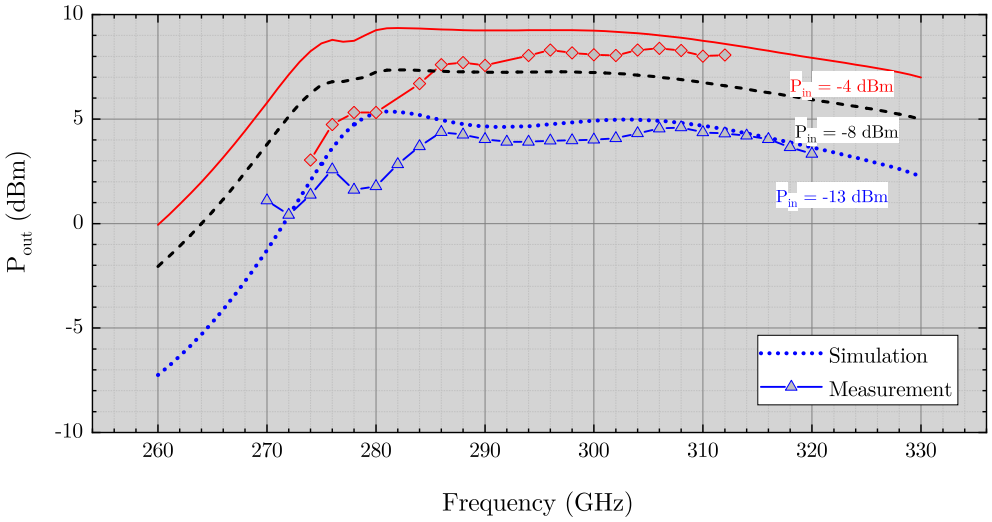

Figure 5.6: Simulated and on-wafer measured output power in dependency of frequency and input power for the buffer amplifier.

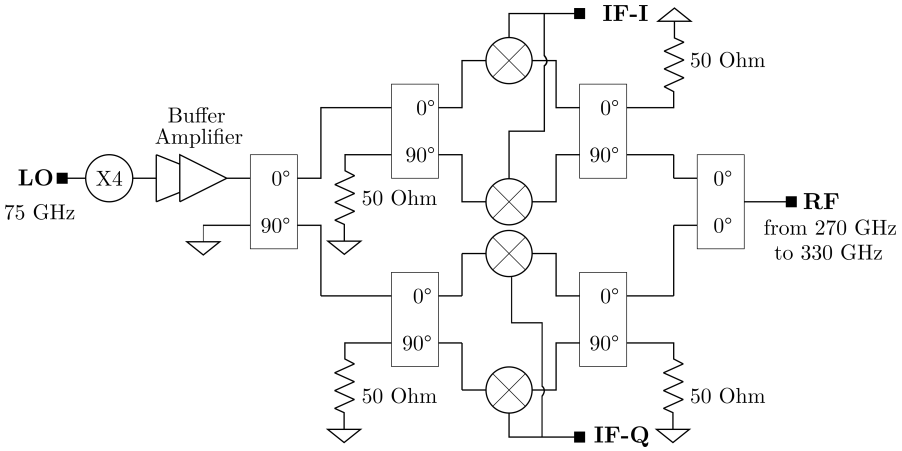

Figure 5.7: Schematic of the active electronic down-converter integrating a frequency multiplier by four, a buffer amplifier and a fundamental passive IQ mixer.

I-channel and the Q-channel, while the other is terminated with a $50\,\Omega$ load. Fig. 5.9 shows the measurement of the down-converter's conversion gain versus LO input power, for an LO input frequency of $75\,\mathrm{GHz}$, an RF input frequency of $301\,\mathrm{GHz}$ and an RF power of $-35\,\mathrm{dBm}$. The chip reaches a conversion gain of $-15\,\mathrm{dB}$ and saturates starting with $-2\,\mathrm{dBm}$ LO input power. The difference between simulation and measurement is only $1\,\mathrm{dB}$. It can be observed that the down-converter saturates even earlier than simulated. The measured IQ amplitude imbalance is lower than $0.5\,\mathrm{dB}$. The IQ phase imbalance is simulated to be at a maximum of $5°$ for the entire RF frequency range.

Fig. 5.10 shows the measurement of the 300 GHz down-converter's gain versus RF input frequency and the comparison to simulation. For this measurement the LO signal remains constant at a frequency of $75\,\mathrm{GHz}$ and a power of $2\,\mathrm{dBm}$ and the power of the RF signal is set to $-35\,\mathrm{dBm}$. The measured 3-dB bandwidth is above $40\,\mathrm{GHz}$ and the 6-dB bandwidth is $60\,\mathrm{GHz}$, from 270 to $330\,\mathrm{GHz}$. Data transmissions using similar receivers [KDR+15], show that the 6-dB bandwidth is the limit for data transmission using simple modulation formats

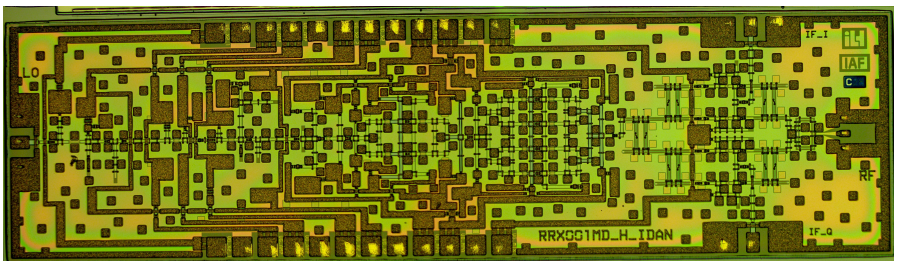

Figure 5.8: Chip photograph of the 300 GHz down-converter MMIC. The size of the chip is 1 x 3.5 mm^2.

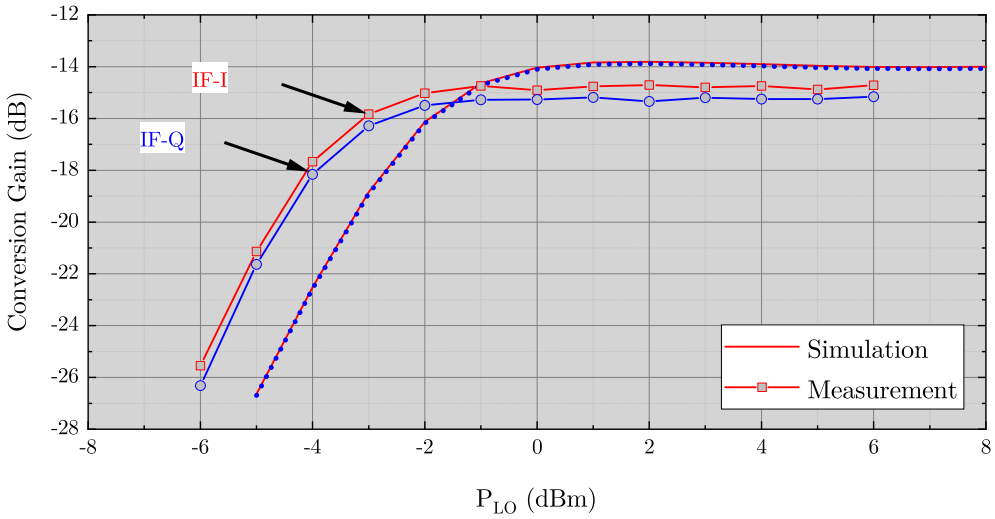

Figure 5.9: Comparison between measurement and simulation of the 300 GHz down-converter's conversion gain versus LO input power for an LO input frequency of 75 GHz, an RF input frequency of 301 GHz and an RF power of $-35\,\mathrm{dBm}$.

like quadrature phase shift keying (QPSK). The measurement fits well to the simulation, the difference is at a maximum of $1.5\,\mathrm{dB}$, in the 3-dB bandwidth.

Fig. 5.11 shows the linearity of the down-converter. The 1-dB compression point lies in measurement at an input power of $-15\,\mathrm{dBm}$, while in simulation the compression begins above $0\,\mathrm{dBm}$. This is due to an optimistic prediction of the large signal models.

5.2 Low-noise amplifier

To reduce the noise and make the down-converter suitable for THz communication a low noise amplifier was designed using the same $35\,\mathrm{nm}$ mHEMT technology. For this purpose a cascade of three cascode stages and impedance matching blocks was used to achieve a high gain-bandwidth product in combination with low noise.

Fig. 5.12 shows the chip photograph of the three-stage LNA, with a size of 0.5 x 1.75 mm^2. Fig. 5.13 shows the schematic of one of the three amplification stages. The other two stages have an identical structure. The cell consists of a cascode stage with two transistors, the first in common source (CS) configuration with a gate width of 2 x 9 µm and the second in common gate (CG) configuration with a gate width of 2 x 13 µm. The input is at the gate of the CS transistor and the output at the drain of the CG transistor. DC-biasing at the gate

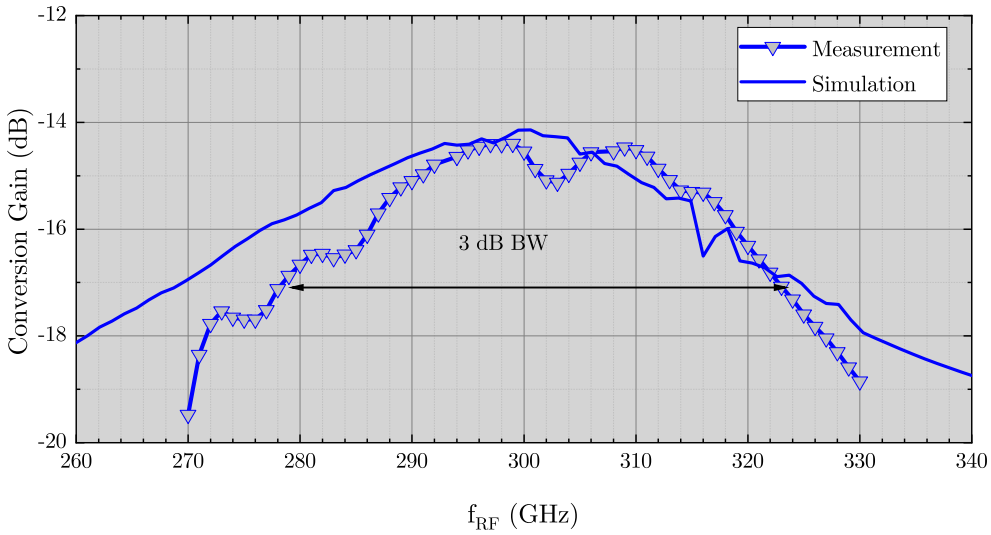

Figure 5.10: Comparison between measurement and simulation of the 300 GHz down-converter's gain versus RF input frequency for an LO input frequency of $75\,\mathrm{GHz}$, an LO input power of $2\,\mathrm{dBm}$ and an RF power of $-35\,\mathrm{dBm}$.

of the CS transistor $\mathrm{VG, CS}$, at the gate of the CG transistor $\mathrm{VG, CG}$ and at the drain of the CG transistor $\mathrm{VD, CG}$ must be provided in order for the cell to amplify.

The matching network at the input (IMN) matches the intrinsic impedance of the CS transistor to the $50\,\Omega$ system impedance and, at the same time, provides the DC-bias. The network is designed in a symmetric way in order to avoid instabilities. It consists of a series capacitor which functions as a DC-block and can be found only in the first stage, ground coplanar waveguide (GCPW) - based transmission lines used for impedance transformation, an X-junction that connects the symmetrical biasing paths and an additional transmission line to connect the transistor gate. The biasing path consists of a transmission line, a resistor for stability and capacitors used for both stability and biasing.

The interstage matching network (ISMN) is placed between the two transistors and consists of a transmission line. The biasing network at the gate of the CG transistor is also part of the ISMN, as it has a large influence on the interstage matching and stability. The biasing structure consists of capacitors and a resistor used for both stability and connection to the bond pads.

The output matching network (OMN) consists of a transmission line that connects the drain of the CG transistor to an X-junction where the symmetric biasing paths connect. The biasing network is similar to the one previously described for the IMN. The signal path continues with a transmission line to the output and in the final stage a DC-blocking capacitor.

On-wafer S-parameter measurements were performed and the results are shown in Fig. 7.14. A 3-dB bandwidth of $80\,\mathrm{GHz}$, between $235\,\mathrm{GHz}$ and $315\,\mathrm{GHz}$ is reached. The gain measurement is in good accordance with the simulation. An average gain of $26\,\mathrm{dB}$ over the 3-dB bandwidth and a maximum of $27.5\,\mathrm{dB}$ at $305\,\mathrm{GHz}$ is achieved. The input and output matching are below $-2\,\mathrm{dB}$ over the whole frequency of interest, as can be seen from the S_{11} and S_{22} plots.

The simulated noise figure (NF) is lower than $7\,\mathrm{dB}$ in the frequency band of interest. Comparing the noise figure curve with that of the simulated minimum noise figure ($\mathrm{NF_{min}}$),

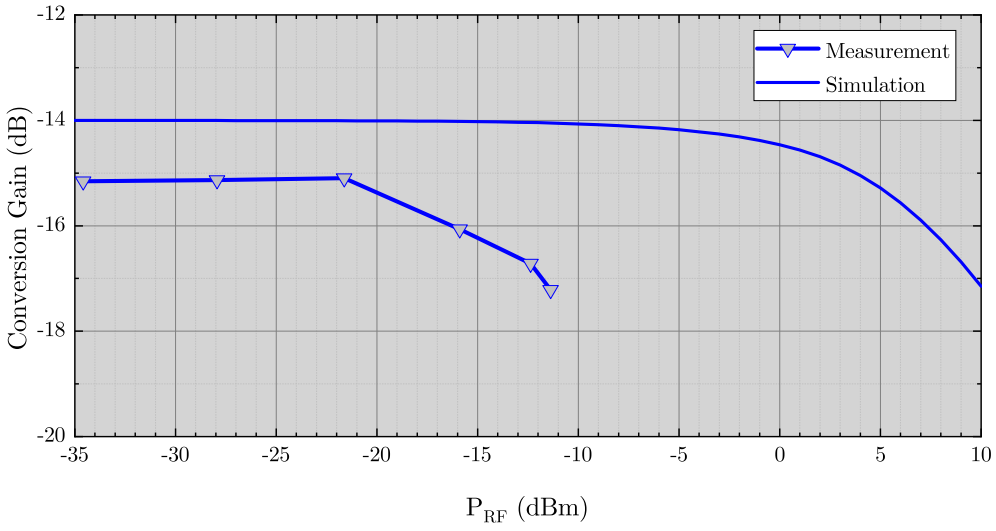

Figure 5.11: Comparison between measurement and simulation of the 300 GHz down-converter's gain versus RF input power for an LO input frequency of $75\,\mathrm{GHz}$, an LO input power of $2\,\mathrm{dBm}$ and an RF frequency of $301\,\mathrm{GHz}$.

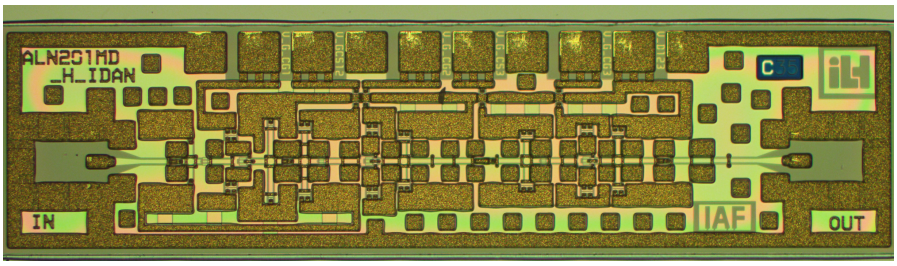

Figure 5.12: Chip photograph of the 300 GHz 3 stage LNA. The size of the chip is 0.5 x 1.75 mm^2.

it can be seen that good noise matching is achieved over a wide range. Due to the lack of available noise sources for on-wafer noise measurements around 300 GHz, the noise figure was not measured. Packaged LNAs built in the same technology in the same frequency range [TLW+17] achieve very good noise performance, an average noise figure of $6.5\,\mathrm{dB}$ around $300\,\mathrm{GHz}$.

Fig. 5.15 shows the comparison between measurements and simulation for the power measurement of the three stage LNA. The scalar power measurement is performed with a bias setting of $\mathrm{VG,CS} = 0.1\,\mathrm{V}$, $\mathrm{VG,CG} = 0.995\,\mathrm{V}$ and $\mathrm{VD,CG} = 1.8\,\mathrm{V}$. For this bias point the current density of the transistors is the same as in the small signal measurement $400\,\mathrm{mA}\cdot\mathrm{mm}^{-1}$. The total DC power consumption is $57\,\mathrm{mW}$. The $1\,\mathrm{dB}$ compression point is measured to be at $-26\,\mathrm{dBm}$ when referred to the input and $-1\,\mathrm{dBm}$ when referred to the output. This measurement is in good accordance with the simulation, especially in the low power region. Differences start to appear above $-20\,\mathrm{dBm}$ input power. A maximum of $1.5\,\mathrm{dB}$ of deviation between simulation and measurement can be observed at an input power of $-17\,\mathrm{dBm}$.

For wireless high data rate communication systems operating at frequencies above $200\,\mathrm{GHz}$ very low output powers are available. This means that highly directive antennas need to compensate for the free space path loss. Even considering the high gain offered by these antennas the input power at the receiver is below $-30\,\mathrm{dBm}$, typical $-40\,\mathrm{dBm}$. At this input

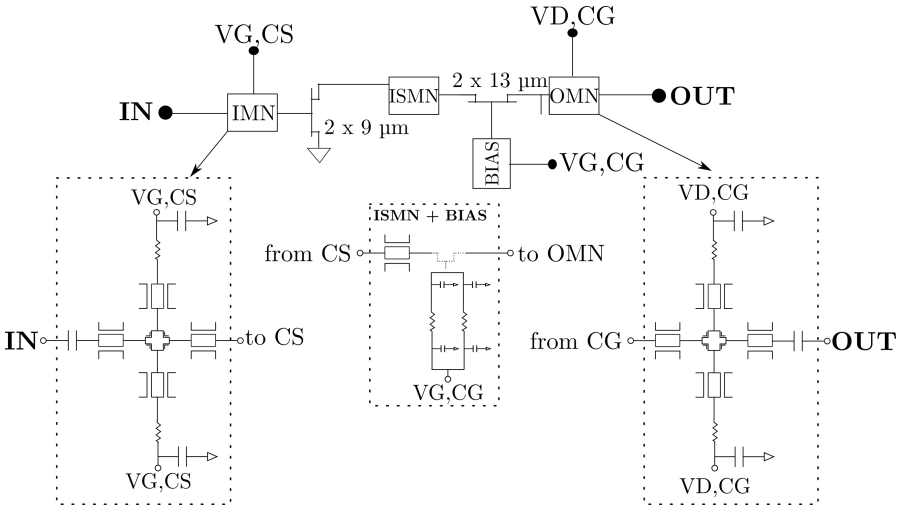

Figure 5.13: Schematic of one amplification stage in the low noise amplifier.

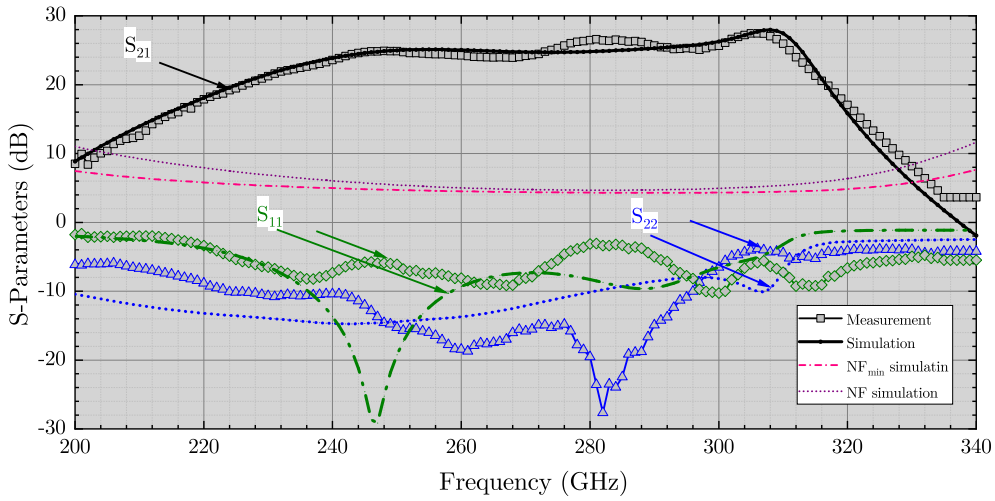

Figure 5.14: Measured and simulated S-parameters of the 300 GHz three stage LNA.

power the LNA has a considerable back-off from the $1\,\mathrm{dB}$ compression point, more than $10\,\mathrm{dB}$, which enables the transmission of complex modulation formats.

5.3 300 GHz receiver

The presented down-converter and LNA can be combined in a two-chip module to form a $300\,\mathrm{GHz}$ receiver. An RF frequency of operation between $270\,\mathrm{GHz}$ and $315\,\mathrm{GHz}$ and an average conversion gain of around $7\,\mathrm{dB}$ can be estimated on module level, considering typical packaging losses caused by the wire bonds between down-converter and LNA as well as the MMIC-to-waveguide transitions.

The 1-dB compression point of the stand-alone down-converter lies in measurement at an input power of $-15\,\mathrm{dBm}$. Combined with the linearity curve of the LNA presented in Fig. 5.15 a maximum input power of $-40\,\mathrm{dBm}$ is expected for linear operation.

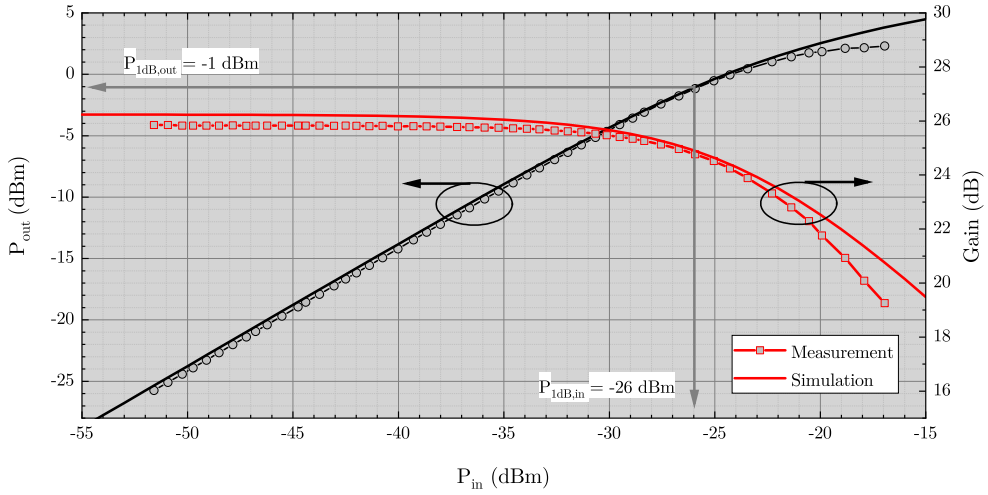

Figure 5.15: Measured and simulated power measurement of the three stage LNA at a frequency of 300 GHz with $\mathrm{VG,CS} = 0.1\,\mathrm{V}$, $\mathrm{VG,CG} = 0.995\,\mathrm{V}$ and $\mathrm{VD,CG} = 1.8\,\mathrm{V}$.

Table 5.1 shows a comparison of this estimated receiver performance with state-of-the-art receivers realized with different technologies. Among the Si-based technologies, the receiver presented in [RGHP19b] achieves the highest data rate of $100\,\mathrm{Gbps}$ using a SiGe bipolar complementary metal-oxide-semiconductor transistor. The center frequency of $230\,\mathrm{GHz}$ of this transmission is lower than the other state-of-the art transmissions in other technologies. A conversion gain of $8\,\mathrm{dB}$ is achieved due to IF amplification. The conversion gain of the $230\,\mathrm{GHz}$ receiver is not mentioned. Using another Si-based technology, a Si-CMOS transistor, the work presented in [HTK+18] shows an $300\,\mathrm{GHz}$ LNA-less receiver with a bandwidth of $27\,\mathrm{GHz}$, which enables a transmission data rate of $32\,\mathrm{Gbps}$. Due to the absence of a pre-amplifier both the conversion gain and the noise figure have a lower value than the other receivers, $-19.5\,\mathrm{dB}$ and $27\,\mathrm{dB}$, respectively.

Two III-V technologies have shown good results in producing circuits that can operate at $300\,\mathrm{GHz}$. The first one is based on a InP-HEMT. Using the all-electronic transceiver presented in [HFA+18] $100\,\mathrm{Gbps}$ were achieved over a distance of $2.22\,\mathrm{m}$. The receiver used in this transmission has a conversion gain of around $-1\,\mathrm{dB}$ calculated from the given conversion loss of the mixer and the gain of the integrated LNA. The second III-V based technology is the one used in this work and in the receiver presented in [TLW+17] which shows the best performance among all the other receivers: an RF bandwidth above $50\,\mathrm{GHz}$, a conversion gain without IF amplification of $6.5\,\mathrm{dB}$ and a noise figure of $8.6\,\mathrm{dB}$.

For a better performance of the receiver presented in this work the frequency dependence of the LNA can be optimized so that the overall RF bandwidth of the receiver improves by more than $10\,\mathrm{GHz}$.

5.4 Conclusion

This chapter presents a receiver fabricated in a $35\,\mathrm{nm}$ mHEMT technology consisting of two chips: a 300 GHz down-converter and a 300 GHz LNA. The down-converter integrates a frequency multiplier so that the LO input frequency lies at $75\,\mathrm{GHz}$. The receiver shows excellent high frequency performance in terms of bandwidth, $45\,\mathrm{GHz}$, and conversion gain,

$7\,\mathrm{dB}$, and is therefore a promising candidate for future wireless high data rate communication systems.

The transmission scheme chosen for this receiver is the direct-conversion approach. Combined with a similar photonic transmitter as presented in chapter 4 a THz wireless link could achieved which has the potential of reaching higher data rates and better linearity than in the previous chapter. The actual performance assessment of such a link is not part of this thesis, as it is an on-going research work, which is still to be published.

Table 5.1: State of the art active electronic receiver operating around 300 GHz using different technologies.

Reference	Technology	RF Frequency Range	Bandwidth	Conversion Gain	Noise Figure
[RGHP19b]	130-nm SiGe BiCMOS	215 GHz - 245 GHz	30 GHz	$8\,\mathrm{dB}$[1]	14 dB
[HTK+18]	40 nm Si-CMOS	270 GHz - 320 GHz	27 GHz	-19.5 dB	27 dB
[HFA+18]	80 nm InP-HEMT	273 GHz - 302 GHz	29 GHz	-1 dB	n.a.
[TLW+17]	35 nm InGaAs mHEMT	270 GHz - 325 GHz	55 GHz	6.5 dB	8.6 dB
This work[2]	35 nm InGaAs mHEMT	270 GHz - 315 GHz	45 GHz	7 dB	$7.5\,\mathrm{dB}$[3]

[1] including IF amplification [2] chip set consisting of a down-converter and an LNA (estimated performance) [3] theoretical value, calculated from the simulated noise figure

6 Wireless Transmission based on the Superheterodyne Approach

The reasons why research on the field of millimeterwave wireless communication has been very intense in the last two decades, investigating new paradigms for achieving the ambitious goal of $100\,\mathrm{Gbps}$, have been analyzed in detail in the chapter 1. Efforts made towards a new standard IEEE 802.15.3d show the potential of the subterahertz frequency band as a possible candidate to support ultra-broadband applications [IEE17]. This standard allocates the frequency band from 252 to $325\,\mathrm{GHz}$ to future wireless communication networks, such as backhauling, fronthauling, last-mile access, ad-hoc networks for big events or in dense urban areas, smart offices and data centers and is the worldwide first wireless communication standard operating at $300\,\mathrm{GHz}$. Furthermore, 8 different channel bandwidths between 2.16 to $69.12\,\mathrm{GHz}$ are defined.

Among all these application, one of the most promising is front- and backhauling. At the moment the connection of access cells to the internet is done by optical fiber. The future exponential growth of individual data rates means that the access cells have to be smaller and appear more frequent. The increasing number of cells will cause additional costs of optical fiber, which is already extremely high in an urban environment. Furthermore, in some remote areas, optical fiber is impossible to use. Therefore, wireless point-to-point high data rate communication operating at frequencies above $200\,\mathrm{GHz}$ offers a viable alternative. Up to now, terahertz communication systems have been using the direct-conversion approach, as analyzed in detail in the previous chapters. The success of this approach is owed to their transmitters and receivers and accordingly to their high standard technology and partly to the availability of very fast baseband system. All these links involve the usage of fast digital processing equipment both in signal generation, e.g. AWG, as well as at the receiving end, e.g. real-time oscilloscopes. With this kind of equipment PRBS with different lengths can be generated, received and post-processed, hence the high data rate. However, this is not based on real time transmission of actual user data. In this chapter the usage of another transmission concept for THz communication is analyzed: the superheterodyne transmission scheme. The results presented here are partially published in [DDH$^+$20], [10], [11] and [12]. The work presented in this chapter was carried out in the frame of ThoR (https://thorproject.eu/), a project that received funding from Horizon 2020, the European Union's Framework Programme for Research and Innovation, under grant agreement No. 814523. ThoR has also recieved funding from the National Institute of Information and Communications Technology in Japan (NICT).

Fig. 6.1 shows the superheterodyne concept, which is very common at lower frequencies, but was never used before in combination with IF frequencies above a couple of GHz. The credit for this original idea goes to Prof. Dr.-Ing. Ingmar Kallfass, the supervisor of this thesis and was first mentioned in the ThoR project proposal. In a superheterodyne system a modulator is used to modulate an intermediate frequency LO_1 with the information carrying

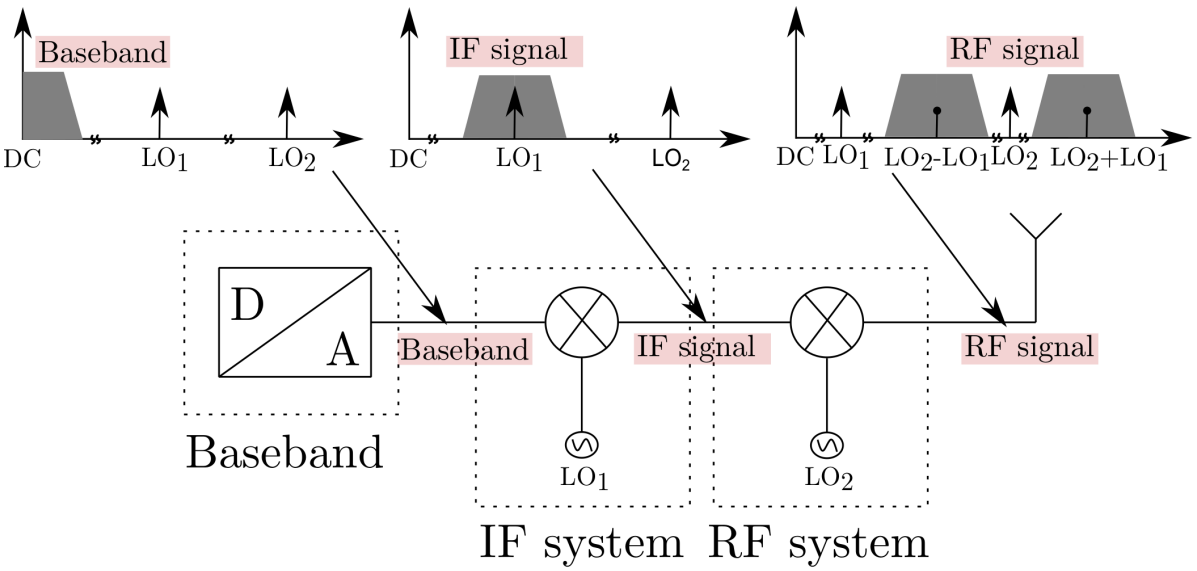

Figure 6.1: Simplified schematic of a double-sideband transmission in a superheterodyne system.

signal coming from the baseband. The resulting IF signal is then fed into a second mixing stage, up-converting the signal to the conveying RF range by mixing it with a carrier signal LO_2. At lower frequencies, since the gap between the USB and LSB is low, a series of highly selective filters are necessary to suppress unwanted image signals in the RF spectrum. This is not the case at frequencies in the millimeterwave range, where the gap between the center frequencies of the two sidebands is intrinsically high.

In order to transmit real-time data and to bring terahertz communications a step closer to real scenario application the costly analog-to-digital and digital-to-analog converters from the direct-conversion transmissions need to be replaced by accessible modems. Thanks to the progress in 5G communication systems, modems based on the IEEE 802.15.3e-2017 [IEE17] and on the ETSI EN 302 217 standard [ETS16] are already commercially available in the V- and E-Band. Combining multiple channels with a narrow bandwidth using complex modulation formats and up-converting them in the $300\,\mathrm{GHz}$ band would lead to the full usage of the regions available bandwidth, hence achieving $100\,\mathrm{Gbps}$ with real-time data.

Using these components as IF system for a $300\,\mathrm{GHz}$ superheterodyne wireless transport link would enable a feasible solution for front- and back-haul in future networks. Fig. 6.2 shows a possible combination of 5G technologies and terahertz communication links integrated in a live network. The future exponential growth of individual data rates means that the access cells have to be smaller and appear more frequent. The increasing number of cells will cause additional costs of optical fiber, which is already extremely high in an urban environment. Employing the solution pictured in Fig. 6.2 would provide the required capacity for this application but requires a super-heterodyne architecture and can not be realized with already available RF frontends like presented in [HFA+18],[LDY+19].

The usage of such a superheterodyne system involves the parallelization of different IF channels. Combined in the RF this leads to a high data rate, needed for this kind of application. According to the new $300\,\mathrm{GHz}$ standard the bandwidth of each channel is $2.16\,\mathrm{GHz}$, or a multiple of $2.16\,\mathrm{GHz}$. Due to the relatively low bandwidth complex modulation formats are

a must for high data rates. To sum up, following requirements can be defined for a $300\,\mathrm{GHz}$ transmitter and receiver that can be employed in a superheterodyne system:

- an IF frequency range between 60 and $86\,\mathrm{GHz}$
- an RF frequency range between 285 and $315\,\mathrm{GHz}$
- minimum linearity requirements: 64-QAM, under channel aggregation

Furthermore, a spectral pure LO source is desired for a good performance of the link.

Since no frontend that achieves the above mentioned specifications is available yet, this chapter focuses on the proof of concept for the superheterodyne transmission in the $300\,\mathrm{GHz}$ range. For this purpose, an existing RF frontend similar to the one presented in chapter 3 is used. This frontend has been designed for zero-IF transmission and shows good performance in this range. The results of the wireless transmission using the predecessor frontend are presented in section 3.1.

Two possibilities of realizing the superheterodyne architecture are analyzed. The usage of an AWG which provides the intermediate frequency by applying a carrier offset to the desired data validates the concept and the potential of the system. The second possibility uses commercially available mixers, which work as direct up- and down-converters, to generate the IF input and output for the $300\,\mathrm{GHz}$ transmitter and receiver. The second option, although realized with far from ideal components, shows the compatibility of the $300\,\mathrm{GHz}$ RF system to low-cost IF and models better the application case portrayed above. Key impairments of data transmissions, like linearity and phase noise, are depicted and described in detail.

6.1 System analysis

A superheterodyne link like proposed in Fig. 6.1 can be partitioned in three important components: the RF system, the IF system and the baseband.

RF system

The RF system consists of the $300\,\mathrm{GHz}$ transmitter and receiver based on monolithic millimeterwave integrated circuit (MMIC) packaged in split-block waveguide modules with a WR-3 output at the RF port and a WR-12 at the local oscillator (LO) input. The packaging technique is developed by Fraunhofer IAF. The MMICs have been described in detail in section 3.1 and are fabricated in a $35\,\mathrm{nm}$ mHEMT InGaAs technology with a $f_{\max}$ above

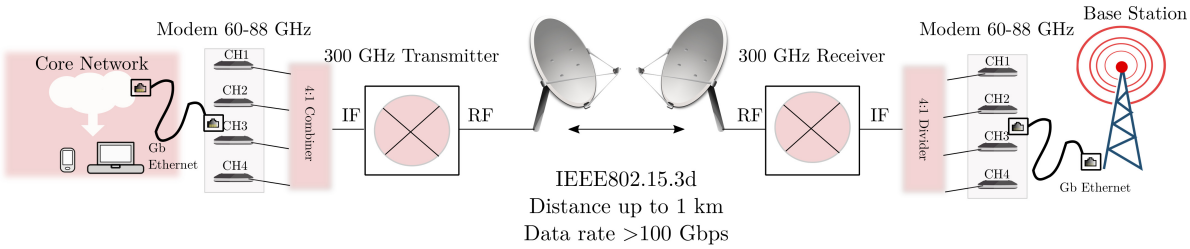

Figure 6.2: Proposed solution for the integration in a live network of a $300\,\mathrm{GHz}$ wireless link.

$1\,\mathrm{THz}$ and a maximum transit frequency of above $500\,\mathrm{GHz}$ [LTM+08]. All details about the MMICs and the packaging technology are presented in chapter 3.

A very important aspect is the $100\,\mathrm{GHz}$ LO input signal. This is generated by a separate waveguide multiplier module with a multiplication factor of twelve. The frequency multiplier as a stand-alone circuit has been published in [LJW+15]. It was shown in [AK15] that the LO noise floor is one of the most critical parameters influencing the quality of data transmission. Especially, for communication links where wide band signals are transmitted, the phase noise floor at high offset frequencies from the carrier, also known as white LO noise, shows a much more significant impact on the systems performance than the effects introduced by the near carrier phase noise. In [CKG+18] a new model of LO noise is presented, which defines the white LO noise as being the combination of phase (angular phase error) and amplitude noise. This is of importance, because the SNR of a frequency-converted signal degrades with increasing LO noise floor.

The LO source for the $300\,\mathrm{GHz}$ transmitter and receiver is provided by a commercially available signal source, an Agilent N5183B MXG, at $8.33\,\mathrm{GHz}$. Fig. 6.3 shows the measurement of the LO phase noise at the input of the multiplier module. Phase noise measurements are difficult to perform at the frequencies used at the input of the RF transmitter and receiver. Since no matching measurement equipment was available, the LO phase noise is calculated by adding $20\log(\mathrm{n})$, where n is the multiplication factor, in this case 12. According to [WTZ+11], which presents the phase noise curve of a similar multiplier-by-twelve module realized using the same technology, the difference between the measured value and the theoretical one is very small in the range of $2\,\mathrm{dB}$. A theoretical calculated phase noise curve of the $300\,\mathrm{GHz}$ LO signal is also plotted in Fig. 6.3. When assuming, that the amount of spectrum which is disturbed by the near carrier phase noise, commonly ranging up to a 10 MHz, is negligibly small compared to the overall modulation bandwidth in the range of several GHz, a white LO noise floor of around $-100\,\mathrm{dBc/Hz}$ can be taken into account. As predicted in [AK15] the influence of the carrier phase noise is expected to be significant. Thus, it would be desirable to generate the carrier signal in a different way. One solution would be to use a signal generated by an optical source. This topic will be discussed in more detail in chapter 6.7.

IF system

Two possibilities of realizing the IF system are employed. The first uses the option available in the AWG of generating an IF signal centered around a certain carrier frequency. $10\,\mathrm{GHz}$ is most appropriate as carrier frequency to take advantage of the full analog bandwidth of the AWG of $20\,\mathrm{GHz}$. The RF signal contains both side bands, since no filtering is applied. Like shown in Fig. 6.4 the USB is centered around $310\,\mathrm{GHz}$ and the LSB around $290\,\mathrm{GHz}$. The gap between the sidebands determines another limit for the maximum transmission bandwidth, which is $20\,\mathrm{GHz}$. For higher transmission bandwidths, the AWG analog limit is exceeded and an overlap between the USB and LSB occurs. Both facts will lead to a significant degradation of the transmission quality.

The second IF system involves the usage of commercially available mixers, which work as direct up- and down-converters, to generate the IF input and output. They have an IF frequency of operation between $7.5\,\mathrm{GHz}$ and $20\,\mathrm{GHz}$ with a baseband frequency range up to $7.5\,\mathrm{GHz}$ [Min]. Although this range covers the frequency bands X, Ku and K they will be, for simplicity, referred to as X-band mixers. For an LO frequency of $10\,\mathrm{GHz}$, the resulting IF

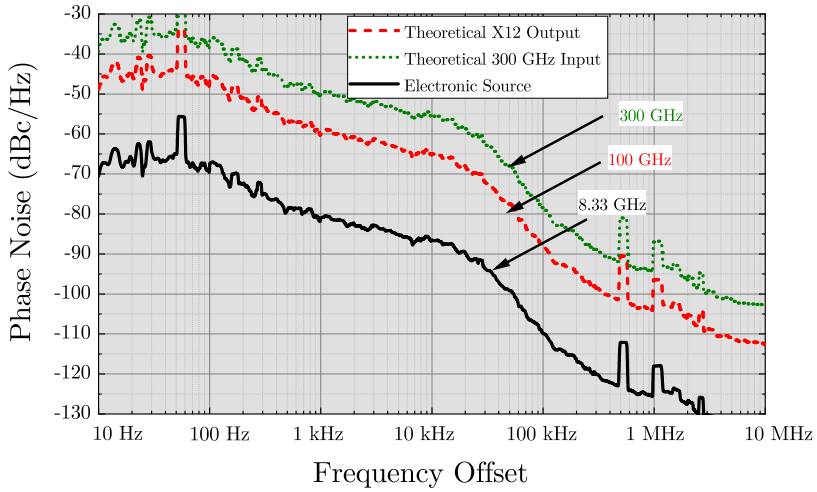

Figure 6.3: Phase-noise of the measured LO source at $8.33\,\mathrm{GHz}$ and of the theoretical calculated LO input at 100 and at $300\,\mathrm{GHz}$.

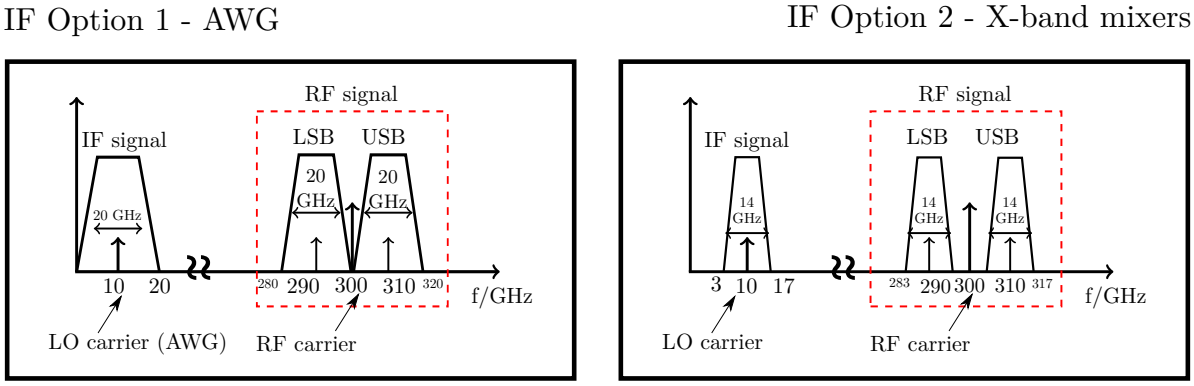

Figure 6.4: Overview of IF and RF spectra for the two possibilities of realizing the superheterodyne system: using the AWG on the left and the X-band mixers on the right.

signal will have a bandwidth up to $14\,\mathrm{GHz}$. Fig. 6.4 shows the IF and RF spectra for this second IF system. The bandwidth limitation of the mixers leads to a frequency gap of $6\,\mathrm{GHz}$ between USB and LSB.

Baseband

The transmitted signal is generated by an AWG with $8\,\mathrm{bit}$ resolution, $20\,\mathrm{GHz}$ analog bandwidth per channel and a maximum sampling rate of $65\,\mathrm{GSa/s}$. The complex in-phase and quadrature (I/Q) data signal is numerically generated as follows: a PRBS with a length of $2^{15}-1$ is converted to an integer sequence and mapped over a QAM constellation. The resulting complex sequence is up-sampled to match the AWG sampling rate range and filtered using a raised-cosine digital filter with different roll-off factors α. In comparison to rectangular pulses, which have a theoretically infinitely broadband spectrum and will influence other frequency bands, raised cosine pulse shaping offers a low adjacent channel interference. The bandwidth (BW) of a broadband signal transmitted in a double sideband transmission can be calculated using the following equation:

$$\mathrm{BW} = \mathrm{R_s}(1+\alpha) \tag{6.1}$$

where $\mathrm{R_s}$ is the symbol rate.

At the receiver side a real time oscilloscope with $60\,\mathrm{GSa/s}$, an analog bandwidth of $20\,\mathrm{GHz}$ and $8\,\mathrm{bit}$ vertical resolution captures the I- and Q-signals from the receiver, in recordings with a length of $500\,\mu\mathrm{s}$. A vector signal analyzer software analyzes the incoming signal, subdivided in 2000 packages, each containing 4096 symbols and performs the carrier recovery and the frequency equalization to compensate for the frequency and phase drift along the link. The digital equalization tool of the software has been applied to all the results shown in this chapter.

The performance of the link is analyzed in terms of measured root mean square EVM. This figure of merit has been chosen at the detriment of BER. BER can be measured using bit error testers (BERT), which can generate, transmit and receive digital signals and compare the received signal with the transmitted ones to identify errors. The disadvantage of such equipment is its inability to perform carrier recovery in an incoherent system. This is only possible when the transmitter and receiver share the same LO signal. Furthermore, BER provides only limited insight into the origin of signal distortions causing the errors. Amplitude and phase imbalances, DC offset, phase noise have a particular signature in the constellation diagram and are reflected in the measured EVM [Geo04].

In the literature many works can be found that investigate a dependency between EVM and BER. A certain probability of error, P_b and accordingly a certain BER can be associated with the ratio of bit energy to noise power density, which is dependent on the SNR. This dependency also takes into account the used modulation format and digital filter [Div15], [SRI06]. In [COM10] it is shown that forward error correction codes (FEC) can be further applied to reduce the BER limit, hence the limit for successful transmission is $\mathrm{BER} < 4\cdot10^{-3}$.

A transmission is considered successful when the probability of a bit error is smaller than $4\cdot10^{-3}$, which can be reduced to 10^{-15} using forward error correction codes [COM10]. The probability of error, P_b is dependent on the ratio of bit energy to noise power density, $E_\mathrm{b}/\mathrm{n_0}$, where E_b is the energy received during each bit interval, and n_0 is the power spectral density of the noise on the channel following the dependency

$$P_\mathrm{b} = \frac{1}{2}\mathrm{erfc}\left(\sqrt{\frac{E_\mathrm{b}}{n_0}}\right). \tag{6.2}$$

Hence, a certain $E_\mathrm{b}/\mathrm{n_0}$ can be associated to a BER of $4\cdot10^{-3}$, considering coherent demodulation and an AWGN channel. $E_\mathrm{b}/\mathrm{n_0}$ can be converted to the SNR by

$$E_\mathrm{b}/\mathrm{n_0} = \mathrm{SNR} - k_\mathrm{roll-off,mod}, \tag{6.3}$$

where $k_\mathrm{roll-off,mod}$ is a correction factor that takes into account the used modulation format and digital filter [Div15], [SRI06]. SNR is, like the EVM, obtained from the measurement devices. Table 6.1 shows the EVM limits for successful transmissions when all of the above considerations are made.

Table 6.1: Limits for successful transmissions based on measured SNR and theoretical $E_\mathrm{b}/\mathrm{n}_0$.

Modulation format	$k_{\mathrm{roll-off,mod}}$	SNR in dB	EVM in %
QPSK	3.01	11.5	26.5
16-QAM	6.02	16.9	15.2
64-QAM	7.78	23.3	6.8

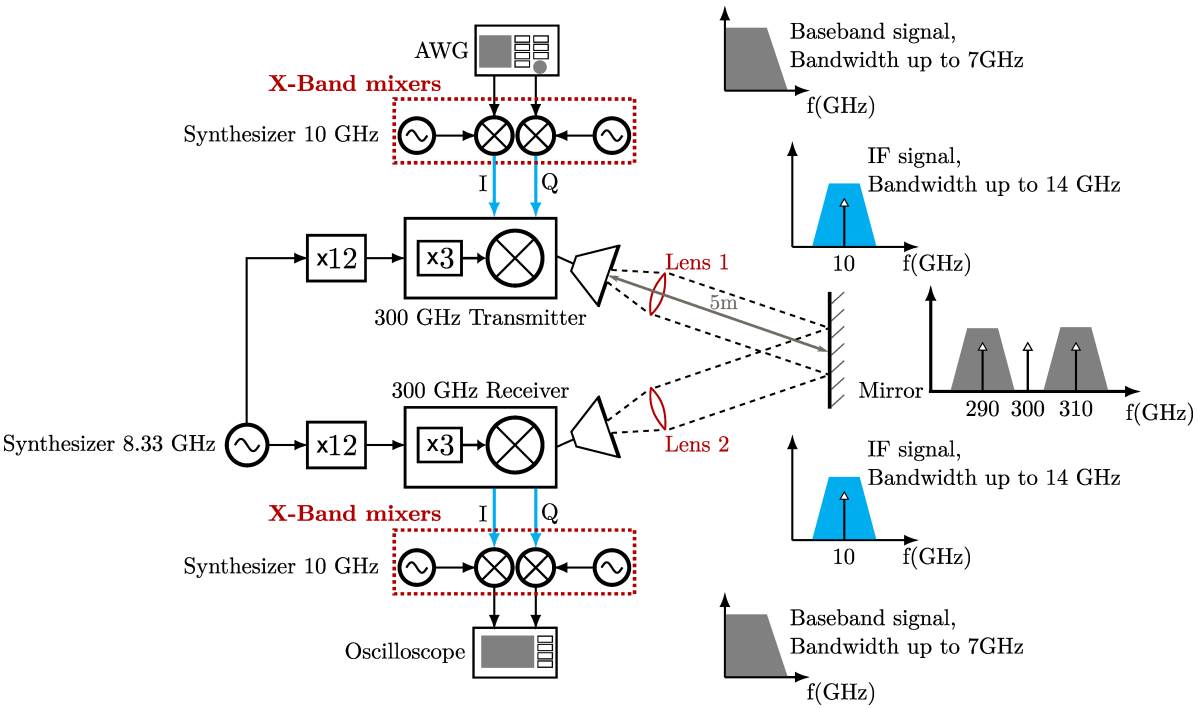

Figure 6.5: Setup of the wireless $300\,\mathrm{GHz}$ link in superheterodyne configuration with a transmission distance of $10\,\mathrm{m}$. The system is composed of the RF circuitry: the $300\,\mathrm{GHz}$ transmitter and receiver including LO generation and the baseband circuitry the X-band mixers, with their respective LO path, for the generation of the intermediate frequency and the digital-to-analog and analog-to-digital converters.

6.2 Setup of the wireless links

Combining all the previously described components a wireless data transmission experiment is carried out. Fig. 6.5 shows the schematic of the measurement setup.

The transmitter consists of a frequency multiplier by three, a buffer amplifier, a fundamental up-converter and a power amplifier as a final stage. It achieves a saturated output power of $-5\,\mathrm{dBm}$ and $20\,\mathrm{GHz}$ of IF bandwidth. The receiver integrates a low-noise amplifier, a down-converter and the same LO path as the transmitter. The receiver module achieves an average conversion gain of $6.5\,\mathrm{dB}$, has an RF frequency of operation between 270 and $325\,\mathrm{GHz}$ and an average noise figure of $8.6\,\mathrm{dB}$ [TLW+17].

The $100\,\mathrm{GHz}$ LO signal is generated by a separate waveguide multiplier module with a multiplication factor of twelve. The same electrical synthesizer provides the input signal at $8.33\,\mathrm{GHz}$ to both transmitter and receiver, thus the setup is coherent.

The X-Band mixers used to generate the IF signal have an LO of $10\,\mathrm{GHz}$ and can cover frequencies of up to $7\,\mathrm{GHz}$ at their baseband port. This results in an IF signal centered

around $10\,\mathrm{GHz}$ with a bandwidth of up to $14\,\mathrm{GHz}$, like represented in Fig. 6.5 in the IF spectrum in blue.

Two antenna systems are employed depending on the desired transmission distance. For a short range, up to 1 meter, two horn antennas each with a gain of $22\,\mathrm{dBi}$ are used. In addition, a variable attenuator is placed between the receiver and the antenna. This allows the setting of an optimal input power independent of distance and path loss. To overcome even higher distances and to prove that the system is suitable for indoor applications like smart offices, additional collimating dielectric lenses are added in front of the horn antennas to compensate for the additional free space path loss. The second systems uses two horn antennas with $25\,\mathrm{dBi}$ gain and two $100\,\mathrm{mm}$ teflon lenses leading to a total estimated gain of around 38 dBi on each side, which are used to transmit the signal over a distance of $10\,\mathrm{m}$. The transmission is obtained with a reflection on a mirror placed at $5\,\mathrm{m}$ distance from the emission/detection modules.

6.3 Linearity characterization

Linearity is a key issue in the success of ultra-fast wireless links in the low terahertz range. In the following section this will be examined for both RF and IF systems.

RF frontend

The $300\,\mathrm{GHz}$ transmitter and receiver system presented in the previous section are measured in a scenario they were designed for, when the baseband is directly up- and down-converted in and from the RF range.

The transmitter module is characterized by measuring the power at the RF output using a VDI Erickson PM5B power meter. An LO input power of $0\,\mathrm{dBm}$ at the frequency multiplier input is sufficient to drive the up-converter in saturation. Different signals are fed at the IF input using the AWG and the IF power is swept.

Fig. 6.6 shows the measurement results of the transmitter output power. The maximum and minimum input powers are determined by the limits of the AWG. However, the range between -19 and $-2\,\mathrm{dBm}$ is sufficient to determine the linear region of the transmitter. The power meter calculates the results of this measurement by integrating over the whole spectrum. A WR-3 waveguide is used with a recommended frequency range between 220 and $335\,\mathrm{GHz}$. No prediction about possible adjacent channels resulting from undesired mixing products can be gained from this measurement. It cannot be clearly stated, alone from this measurement, that the achieved transmitted power is only in the frequency band of interest, centered around $300\,\mathrm{GHz}$ and with different bandwidths. Unfortunately, no spectrum analyzer capable of measuring in the $300\,\mathrm{GHz}$ band was available. Therefore, a theoretical consideration is needed.

Table 6.2 shows the desired LO carrier and possible LO harmonics after the multiplier module (multiplication factor of twelve) and after the integrated multiplier by three. A similar multiplier module as the one used in this work is presented in [WTZ+11]. There it is shown that all harmonics are suppressed with a minimum of $35\,\mathrm{dBc}$, with the lowest suppression measured for the 10th and 14th harmonic (X10 and X14). In addition, the buffer amplifier integrated on the MMIC acts like a bandpass filter further suppressing all signals outside

Table 6.2: Desired LO carrier and possible LO harmonics at up-converter input.

Harmonic at multiplier output	Frequency at multiplier output in GHz	Harmonic at up-converter input	Frequency at up-converter input in GHz
X10	83.33	X30	249.99
X11	91.63	X33	274.89
X12	83.33	X36	300
X13	108.29	X39	324.87
X14	116.62	X42	349.86

the band 270 to $330\,\mathrm{GHz}$. This means that only the harmonics 11, 12 or 13 can reach the up-converter and they show a very good suppression in the multiplier module. Furthermore, thanks to the balanced design of the mixer, a good LO to RF isolation ensures that the amplitude of the $300\,\mathrm{GHz}$ carrier is well below that of the RF signal. This demonstrates that the power measured and plotted in Fig. 6.6 is the power level of the desired signal centered around $300\,\mathrm{GHz}$.

The first important observation is that the transmitted output power is not only dependent on the input power, as expected, but also on the modulation format and symbol rate. The output power decreases slightly with increasing symbol rate. This effect can be observed for both modulation formats, QPSK and 16-QAM, but it is higher for the more simple one, QPSK, and is a direct consequence of the RF transmitter's frequency dependency. The conversion gain of the TX is not constant over the IF frequency, the 3 dB IF bandwidth of the TX lies at around $10\,\mathrm{GHz}$. With increasing bandwidth the conversion gain decreases, which leads to a decrease of output power for increasing symbol rates in Fig. 6.6.

The second important observation concerns the saturated output power, which is higher for QPSK than for 16-QAM. A constant difference of $2\,\mathrm{dB}$ is noted between the same symbol rate and different modulation formats, like shown in Fig. 6.7. The measurement is realized with a power meter, hence the resulting values represent the average power. Therefore, this result is in good accordance with the theory presented in [MO98]. For root raised-cosine filtering with a roll-off factor of 0.35 the difference between the peak-to-average power ratio of QPSK and 16-QAM is around $2\,\mathrm{dB}$.

Finally, it can be concluded that although modulation format and symbol rate have an influence on the transmitted output power the measured curves follow the same trajectory, which means that the input related 1 dB compression point remains the same. For all measured symbol rates and modulation formats it lies at $-8\,\mathrm{dBm}$.

Using the $300\,\mathrm{GHz}$ transmitter, receiver and a zero-IF setup, like presented in chapter 3, broadband signals are transmitted over the air. Complex modulation formats up to 32-QAM are successfully transmitted up to a symbol rate of $8\,\mathrm{GBd}$. Fig. 6.8 shows the constellation diagram for an $8\,\mathrm{GBd}$ 32-QAM modulated signal measured in a zero-IF configuration. This proves that the RF frontend used for the superheterodyne system presented in this section is highly linear.

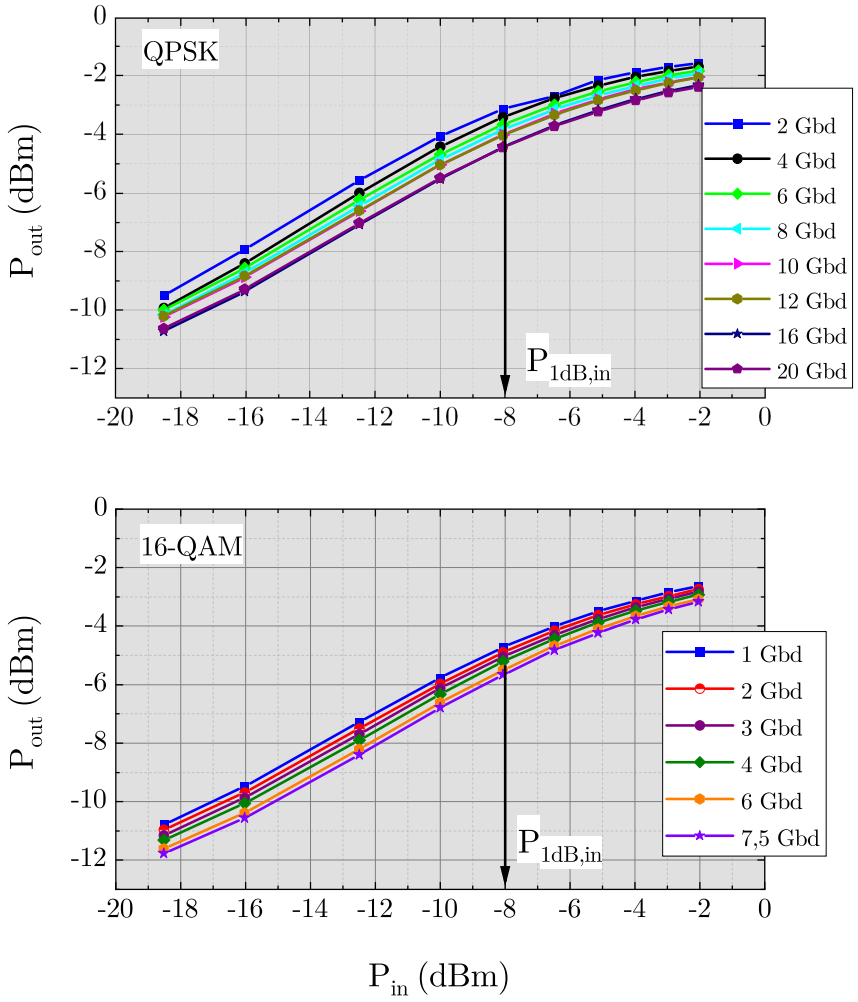

Figure 6.6: Measured transmitter output power in dependency of the IF input power for QPSK (upper graph) and 16-QAM (lower graph) modulation formats and different symbol rates.

External mixers and AWG

The X-band mixers, which form one option for the IF system in the final superheterodyne experiment, need to be tested and their linearity analyzed. Since the IF output lies in the range between 7.5 and $20\,\mathrm{GHz}$, their IF spectrum can be measured more easily than in the case of the RF components. For this purpose a spectrum analyzer is connected at the IF output of the X-band up-converter. The LO signal is provided by a commercially available synthesizer and has a frequency of $10\,\mathrm{GHz}$ and an input power of $5\,\mathrm{dBm}$. At the baseband port a broadband signal with different modulation formats and symbol rates is applied. Fig. 6.9 shows the measured spectra of two IF signals, both modulated using 16-QAM. The one plotted using the solid black line has a symbol rate of $3\,\mathrm{GBd}$ and occupies a bandwidth of $4\,\mathrm{GHz}$ and the second one, plotted using the dashed red line has a symbol rate of $6\,\mathrm{GBd}$ and occupies a bandwidth of $8\,\mathrm{GHz}$. The poor isolation of the second LO harmonic at $20\,\mathrm{GHz}$ is visible for both measurements. An undesired non-linear mixing product can be observed in the spectrum of the $6\,\mathrm{GBd}$ signal in the low frequency range, below $5\,\mathrm{GHz}$.

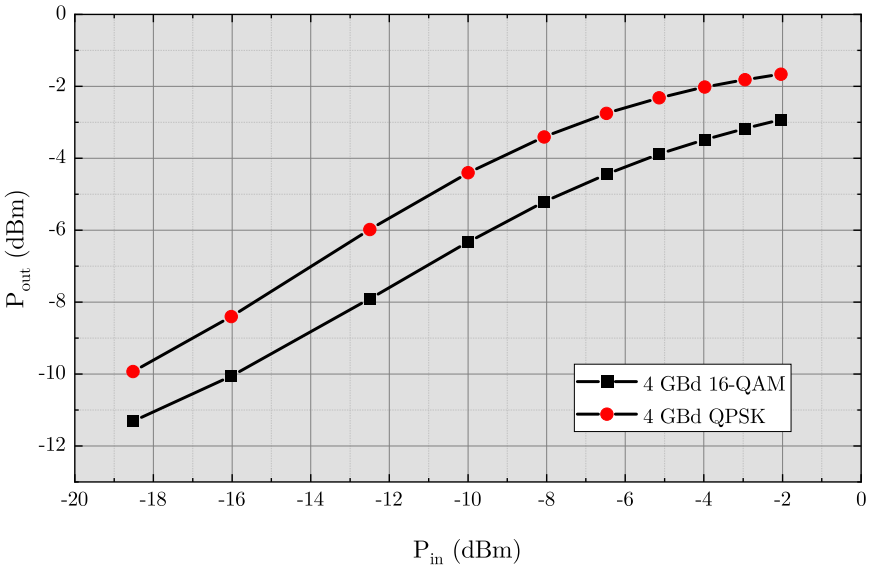

Figure 6.7: Comparison between measured output power when the symbol rate of the IF signal is kept constant and the modulation format is being varied.

To characterize the X-band mixers a back-to-back transmission measurement is conducted. The IF output of the up-converter mixer is directly connected to the IF input of the down-converter mixer. The LO signal is provided coherently from the same source and it has a frequency of $10\,\mathrm{GHz}$ and an input power of $5\,\mathrm{dBm}$. The baseband input signal is generated in the AWG. The output baseband signal is captured by an oscilloscope, like described in section 6.1. Different modulation formats and symbol rates are transmitted in this back-to-back configuration. 16-QAM is the most complex modulation format which was successfully transmitted using this configuration. Symbol rates up to $9\,\mathrm{GBd}$, corresponding to a transmission bandwidth of around $12\,\mathrm{GHz}$ are achieved. This exceeds the baseband bandwidth of the mixer indicated in the datasheet [Min]. Efforts to transmit 32-QAM show that this modulation format is possible if only the up-converter X-band mixers are used. The resulting IF signal is directly fed to the oscilloscope and demodulated using the signal processing software. In conclusion, the superheterodyne link which uses this IF system is expected to transmit modulation formats up to 16-QAM.

To determine the full potential of the superheterodyne concept, the IF signal can be generated in the AWG using an internal carrier frequency. This IF signal has, due to the usage of this equipment, a high spectral purity and can cover bandwidths up to $20\,\mathrm{GHz}$. Fig 6.10 shows the comparison between the measured IF signals using both IF system options. In dotted blue the spectrum generated in the AWG and in solid black the spectrum at RF output of the X-band mixers is plotted. The baseband signal is in both cases the same using 16-QAM modulation and a symbol rate of $3\,\mathrm{GBd}$. A similar input power at the IF of the RF transmitter is crucial for a good and fair comparison between the two IF systems. Hence, the input power at the baseband is chosen in order for the output power of the IF signal to have a similar value. This can be observed in Fig. 6.10.

When using the AWG no linearity constraints can be derived from the IF system.

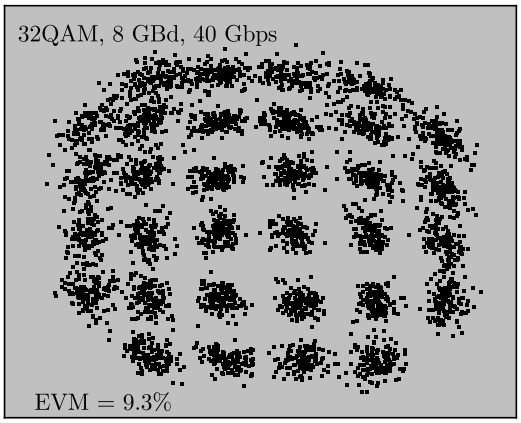

Figure 6.8: Measured constellation diagram for a 32-QAM modulated signal with a symbol rate of $8\,\mathrm{GBd}$ measured in a zero-IF configuration.

6.4 Short range wireless data transmission

For the first data transmissions a distance of half a meter is chosen between the transmitter and the receiver. To have more control over the RF input power at the receiver a waveguide variable attenuator is placed between horn antenna and receiver module. To determine the optimal power a sensitivity analysis like described in chapter 3 needs to be carried out. For this purpose the AWG and the oscilloscope are connected directly to the IF ports of the transmitter and receiver. The RF input power is varied with the help of the variable attenuator and different modulation formats and symbol rates are transmitted. The transmission is evaluated in terms of EVM, measured in % and plotted versus the input power. The power at the output of the attenuator, which corresponds to the input power at the receiver, is measured with a powermeter.

Fig. 6.11 shows the receiver's sensitivity dependency on the used modulation format. The symbol rate is kept constant at $1\,\mathrm{GBd}$. The more complex the modulation format, the lower the threshold in % for a successful transmission.

For $1\,\mathrm{GBd}$ symbol rate and for the modulation formats 16-QAM and 32-QAM the region with minimal EVM stretches over a wide range of input power, from around -38 to over $-50\,\mathrm{dBm}$. For the more complex modulation format of 64-QAM represented in the green line with diamond symbols the range of optimal input power is narrower going only up to $-45\,\mathrm{dBm}$. As a conclusion, the optimal input power range for all used modulation formats lies between -38 and $-45\,\mathrm{dBm}$, for a symbol rate of $1\,\mathrm{GBd}$.

The sensitivity curve is not only dependent on the modulation format but also on the data rate. Fig. 6.12 shows this dependency for two symbol rates $1\,\mathrm{GBd}$ and $4\,\mathrm{GBd}$ and 16-QAM modulation format. The probability of error is proportional to the data rate, which explains why the EVM value increases as the symbol rate increases. In addition, it can be observed in Fig. 6.12 that the optimal input power range decreases with increasing symbol rate. The marked area below the curves, where the EVM is at its minimum ranges for the $4\,\mathrm{GBd}$ signal from -40 to over $-45\,\mathrm{dBm}$. An input power of around $-40\,\mathrm{dBm}$ seems to be the best compromise for all modulation formats and low and high symbol rates. The optimum setup of the RF receiving power is the prerequisite for the best possible transmission results.

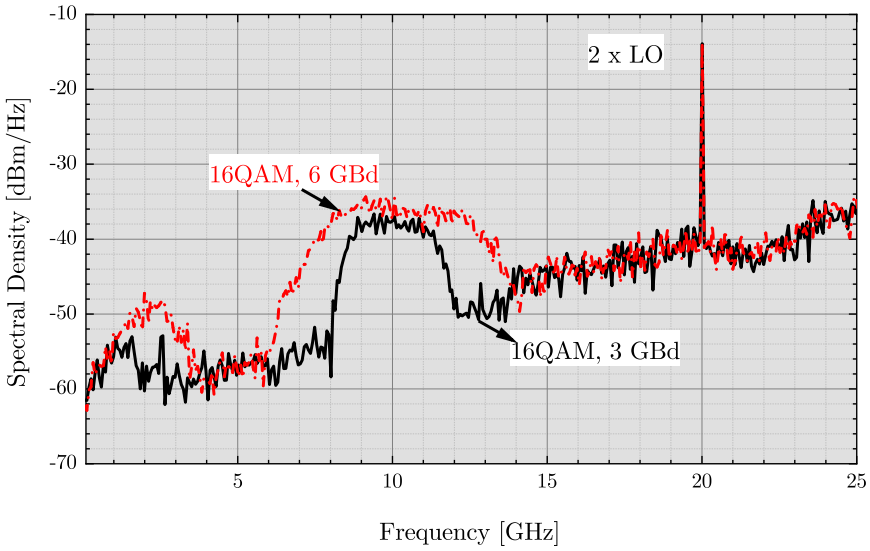

Figure 6.9: Measured spectrum of the IF signal generated with the external X-band mixer. The baseband signal is 16-QAM modulated and has symbol rates of $3\,\mathrm{GBd}$ and $6\,\mathrm{GBd}$.

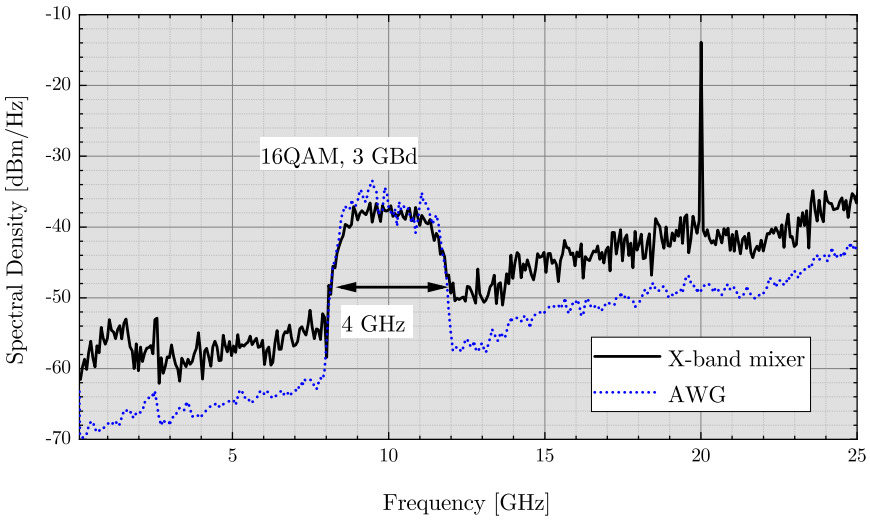

Figure 6.10: Comparison between measured IF spectrum generated with both available options: with the external mixers and with the AWG. The baseband signal is 16-QAM modulated and has a symbol rate of $3\,\mathrm{GBd}$.

The next step in the correct analysis of transmission results is the measurement of the transfer characteristic for the overall wireless link. Initially, the response of the transmitted signal through the X-band mixers is measured. For this purpose, the four X-band mixers are connected in a back-to-back configuration, the I X-band transmitter mixer is directly connected to the I-receiver mixer and the same applies for the Q path. A network analyzer is used to measure the scattering parameters from the transmitter to the receiver. The S_{21} parameter is then normalized to its maximum value and plotted versus the frequency. In Fig. 6.13, the black dash-dot line shows the results of this measurement. The $6\,\mathrm{dB}$ IF bandwidth is around $7\,\mathrm{GHz}$, which corresponds well to the IF bandwidth mentioned in the data sheets of $7.5\,\mathrm{GHz}$ [Min]. The difference between the transmission on the I-channels and

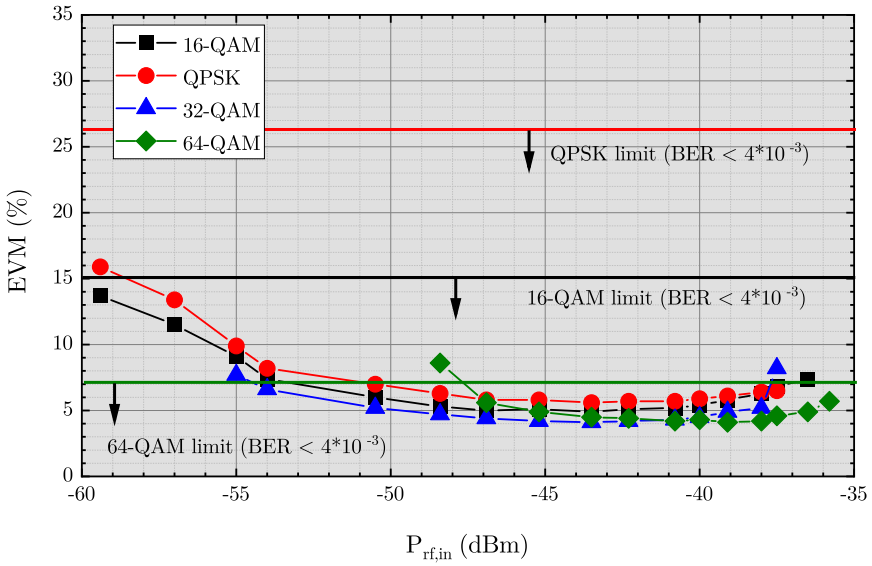

Figure 6.11: Sensitivity curves of the 300 GHz receiver for different modulation formats and signals with a symbol rate of 1 GBd.

on the Q-channels represents the IQ amplitude imbalance of the system which is plotted on the upper y-axis. The value of the imbalance remains below 1 dB for the IF bandwidth of the transmission and increases considerably after the upper frequency of 7 GHz.

In Fig. 6.13, the red dotted line represents the transfer characteristic of the 300 GHz transmit-receive system, when the baseband signal is generated directly in the AWG with no frequency offset. The zero-IF system has a 6 dB bandwidth of 20 GHz, with an IQ amplitude imbalance of below 1 dB over the IF bandwidth. Therefore, it is well suited to validate the proof of concept for the superheterodyne system. According to this transfer characteristic the best choice for the intermediate frequency is around 10 GHz, which represents the best compromise between low imbalances, good transfer behavior between transmitter and receiver and achievable data rates using the X-band mixers. Another reason why 10 GHz is a suitable IF frequency is the spacing between the LSB and USB. A higher IF frequency would lead to a higher available gap between LSB and USB reducing the risk of overlapping, but it would come at the cost of smaller available bandwidth in the superheterodyne system. For example, an IF signal centered around 15 GHz with a bandwidth of 20 GHz would have a corner frequency of the USB at 325 GHz. Like previously mentioned, the 6 dB bandwidth of the zero-IF transmission lies slightly above 20 GHz. This translates into an RF signal with an upper corner frequency of around 320 GHz. Hence, the transmission of the above mentioned IF signal would not be possible in a superheterodyne system.

The transfer characteristic of the final superheterodyne system as pictured in Fig. 6.5 is presented in Fig. 6.13 by the blue solid line. These results correspond well with the measurement of the X-band mixers in back-to-back configuration. The IF bandwidth is the same as in the case of the dash-dot line, 8 GHz. Also the two characteristics follow similar curves, therefore the system is limited by the X-band mixers.

Data transmission experiments using different modulation formats and symbol rates have been carried out and the quality of the transmission has been analyzed. Fig. 6.14 summarizes the results for 16-QAM and 32-QAM modulation formats and symbol rates up to 15 GBd.

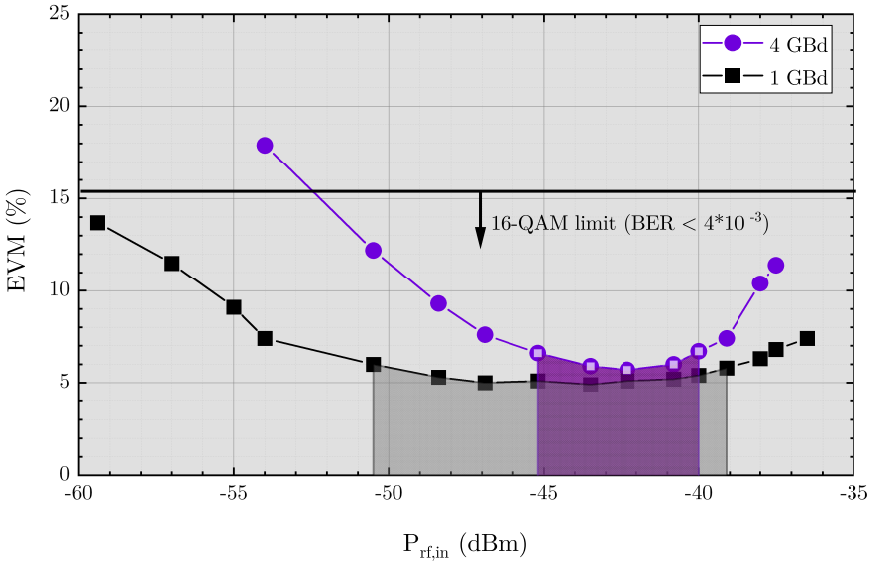

Figure 6.12: Sensitivity curves of the $300\,\mathrm{GHz}$ receiver for increasing symbol rates for 16-QAM modulation format.

The used digital filter was a raised cosine with a roll-off factor of 0.35 and it was kept constant for all transmissions.

Fig. 6.14 shows the performance comparison of different configuration of the wireless link for two modulation formats: 16-QAM and 32-QAM. First back-to-back transmissions from the AWG to the oscilloscope were made. These represent the reference measurement of the used equipment and are plotted in all three graphs using the pink line with pentagon symbols. Another reference measurement in back-to-back configuration is the one of the X-band mixers, which is represented by the green line with diamond symbols. For the $300\,\mathrm{GHz}$ link four scenarios are considered. The first uses a zero-IF approach and is plotted using the red line with round symbols. The last three scenarios use a superheterodyne approach under different conditions. The black line with the square symbols shows the results when the AWG is generating the data centered around an IF frequency of $10\,\mathrm{GHz}$. In this case the oscilloscope and the post-processing software down-convert the IF signal to the baseband. The orange line with the star symbols shows the results of the transmission where the baseband signal generated in the AWG is up-converted to an IF frequency by the X-band mixers. The down-conversion to baseband is done by the oscilloscope and the post-processing software like in the previous case. The last case represents the superheterodyne transmission using X-band mixers both on transmitter and receiver side and is plotted in the blue line with triangle symbols.

For all scenarios the EVM is degrading with increasing symbol rate due to the bandwidth limitations presented in Fig. 6.13. Besides the two reference measurements, the equipment calibration and the back-to-back transmission of the X-band mixers, the best performance is achieved using the superheterodyne architecture when the IF is generated in the AWG. For 16-QAM modulation a symbol rate of $15\,\mathrm{GBd}$ corresponding to a data rate of $60\,\mathrm{Gbps}$ and to a bandwidth of around $20\,\mathrm{GHz}$ is reached. On the one hand, this is the maximum achievable data rate due to the bandwidth limitations of the $300\,\mathrm{GHz}$ link. Fig. 6.13 shows that the zero-IF system represented with the red dotted curve has a $6\,\mathrm{dB}$ bandwidth of

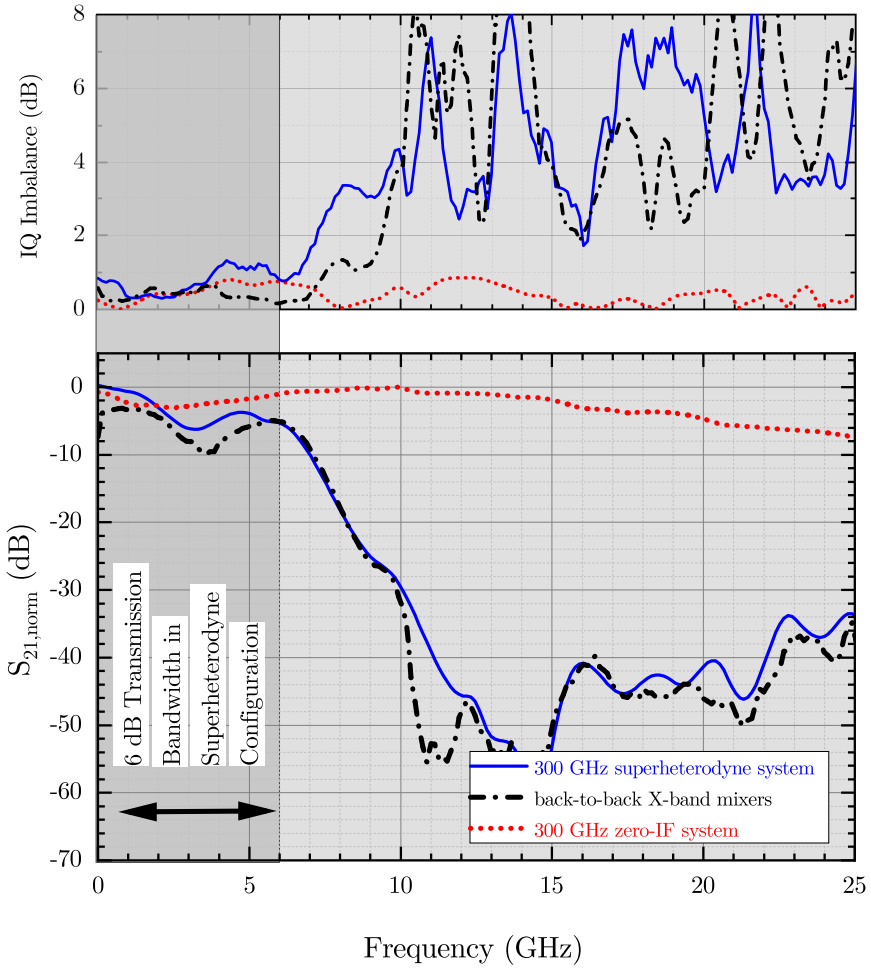

Figure 6.13: Transfer function and amplitude imbalances of the transmission system for different scenarios: in black dash-dot line the back-to-back measurement of the X-band mixers, in red dotted line the zero-IF 300 GHz system and in blue solid line the superheterodyne 300 GHz system, when the IF is provided by the X-band mixers.

around $20\,\mathrm{GHz}$. On the other hand, the analog bandwidth of the measurement equipment is also $20\,\mathrm{GHz}$. In addition, this bandwidth of $20\,\mathrm{GHz}$ is the limit for a transmission without an overlap between LSB and USB. Fig. 6.15 shows the constellation diagrams of the highest data rate achieved with the two superheterodyne systems. For the transmission plotted on the left external mixers were used and a maximum data rate of $24\,\mathrm{Gbps}$ is achieved. The bandwidth occupied by the $6\,\mathrm{GBd}$ signal achieving this maximum data rate corresponds to the $6\,\mathrm{dB}$ bandwidth measured and plotted in Fig. 6.13. For the transmission plotted on the right, the AWG is used to generate the IF signal. In this case a maximum data rate of $60\,\mathrm{Gbps}$ can be achieved.

Another important aspect of terahertz wireless links is the possibility of transmitting higher order modulation formats. The bottom graph in Fig. 6.14 shows the results for 32-QAM modulation. The $300\,\mathrm{GHz}$ RF components exhibit a high linearity, so that the transmission of 32-QAM modulated signals is possible. This is represented by the red curve which shows the results of the zero-IF transmission. The X-band mixers on the other hand do not have the necessary linearity for complex modulated signals. The reference measurement of these

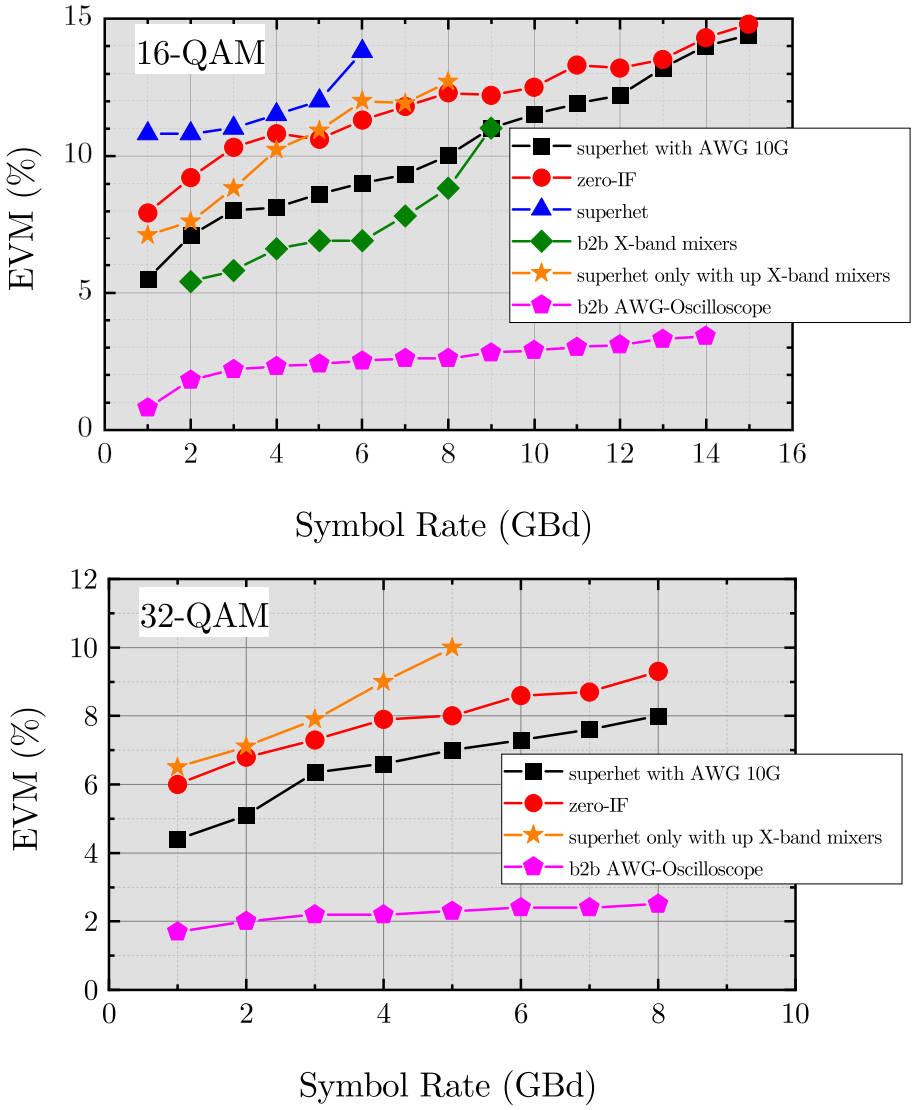

Figure 6.14: Results of the 300 GHz wireless data transmission realized using different architectures for increasing symbol rates. Two modulation formats are analyzed: 16-QAM and 32-QAM. All the transmissions show an EVM which is below the BER threshold smaller than $4 \cdot 10^{-3}$, calculated for a AWGN channel.

mixers shows that the 32-QAM transmission is not successful. The green line with diamond symbols is absent in Fig. 6.14 in the lower graph. The limiting factor is the down-converter X-band mixers. This is proven by the fact that the transmission with external mixers on the transmitter side is successful up to a symbol rate of 5 GBd. Fig. 6.14 shows this in the bottom graph in the yellow line with star symbols.

Due to the high linearity of the RF transmitter and receiver a successful transmission of 32-QAM modulated signal is realized employing the superheterodyne link which uses the AWG to generate the IF signal. Fig. 6.16 shows the constellation diagrams for the highest data rates achieved in this configuration. For 32-QAM modulation 40 Gbps are reached. 64-QAM modulation was successful up to a data rate of 12 Gbps.

To have an in-depth analyis of the performance of the superheterodyne link two important comparisons need to be discussed. The first one is the comparison between the zero-IF and

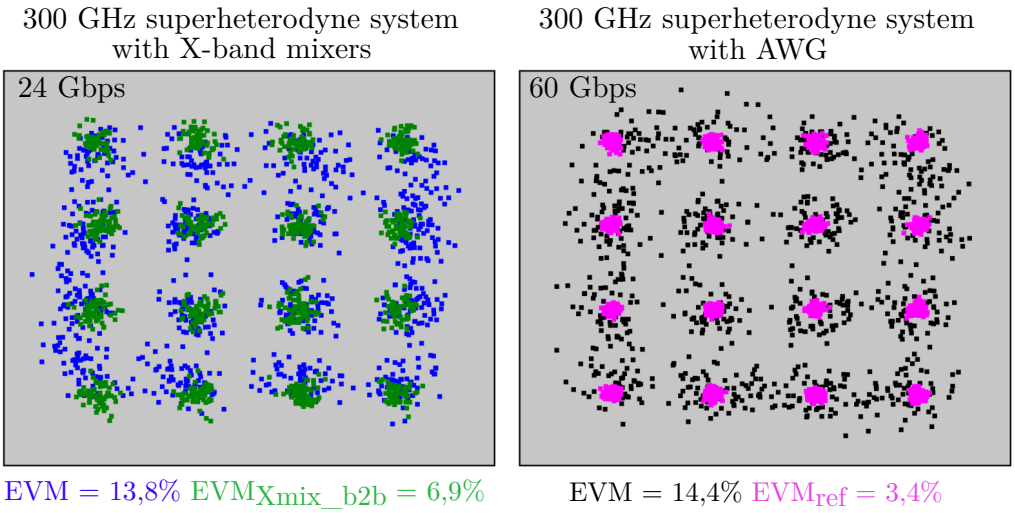

Figure 6.15: Constellation diagrams for 16-QAM modulated signals achieved using the 300 GHz superheterodyne system. For the transmission plotted on the left external mixers were used and for the transmission on the right the AWG provides the IF signal.

the superheterodyne approach using the AWG as IF generator. In the graphical representation the comparison between the red line with round symbols and the black line with square symbols. The superheterodyne approach shows better results than the zero-IF one for all modulation formats. To better visualize the reasons for this difference Fig. 6.17 shows the constellation diagrams and power spectra for a 16-QAM signal with a symbol rate of $1\,\mathrm{GBd}$ using the above mentioned approaches. For a better understanding of the transmission deterioration, in the constellation diagrams the results of the reference measurement were plotted in pink.

The transmission using the zero-IF approach is more erroneous because of impairments like DC-offset and parasitic spurious caused by the AWG at the symbol rate value, in the case pictured in Fig. 6.17 right at $1\,\mathrm{GHz}$. In addition, at zero-IF the LO frequency locking is harder to achieve. A visible impairment in the superheterodyne transmission presented in Fig. 6.17 on the left is the leakage of an unwanted mixing product at $8.33\,\mathrm{GHz}$. Another important reason for a better performance of the superheterodyne approach is the flatter frequency response of the overall system presented in Fig. 6.13 in the dotted red line. Given the bandwidth of $1.35\,\mathrm{GHz}$ of this case, the ripple of the S_{21} parameter for signal with a center frequency of $10\,\mathrm{GHz}$ is smaller than $0.3\,\mathrm{dB}$. For a signal centered around DC the same ripple exceeds $1.5\,\mathrm{dB}$.

With increasing symbol rates the EVM difference between the zero-IF and the superheterodyne approach becomes smaller. This is caused by the surpass of the 3-dB bandwidth of the system. If a signal centered around $10\,\mathrm{GHz}$ with a bandwidth of $13.5\,\mathrm{GHz}$ is considered, the upper frequency of $16.75\,\mathrm{GHz}$ is above the 3-dB bandwidth limit, which lies at $16\,\mathrm{GHz}$. For 32-QAM only symbol rates of up to $8\,\mathrm{GBd}$ lead to successful transmissions and the difference between zero-IF and superheterodyne approach remains approximately constant.

The second important comparison is the one between different superheterodyne scenarios. In this case the reference measurement is, next to the one of the equipment AWG-Oscilloscope, the measurement of the X-band mixers in back-to-back configuration. Due to the bandwidth limitation of the commercial mixers only symbol rates of up to $9\,\mathrm{GBd}$ can be transmitted

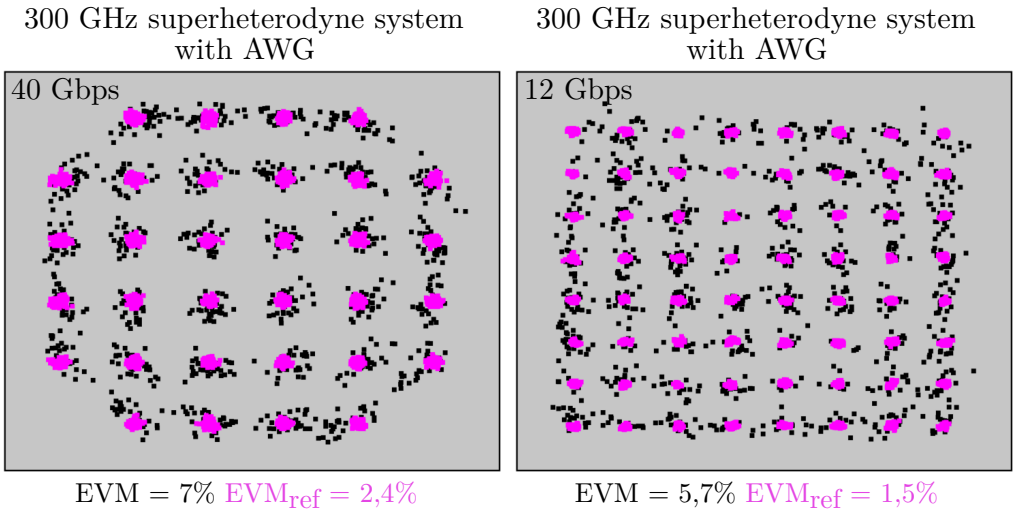

Figure 6.16: Constellation diagrams for higher order modulated signals achieved using the 300 GHz superheterodyne system with the AWG.

using 16-QAM modulation [Min]. For 32-QAM no successful transmission was achieved. To determine why, transmissions with X-band mixers only on the transmitter side are conducted. The fact that these transmissions were possible up to a symbol rate of $5\,\mathrm{GBd}$ shows that impairments of the X-band down-converters represent the limitation factor for the back-to-back X-band mixers transmission in the case of 32-QAM modulation.

For 16-QAM modulated signals the difference between the superheterodyne system in blue and the reference measurement in green is around $5\,\%$. The degradation is due to the influences of the $300\,\mathrm{GHz}$ transmitter and receiver and their impairments: IQ amplitude and phase imbalances and leakage of unwanted spurious tones.

Fig. 6.18 shows the comparison of transmission results of the $300\,\mathrm{GHz}$ superheterodyne link in different configurations: in blue, in the middle, the superheterodyne link using the X-band mixers and in orange, on the right superheterodyne link using X-band mixers only on the transmitter side. In addition, the measurements of the reference signal of the X-band mixers in back-to-back configuration are plotted in green on the left. For this comparison a 16-QAM signal with a symbol rate of $4\,\mathrm{GBd}$ was transmitted. In all three cases the results of the back-to-back transmission from AWG to Oscilloscope has been additionally plotted in the constellation diagram.

A strong interference and degradation cause represents the LO leakage of the X-band down-converters. The signal at $10\,\mathrm{GHz}$ is present in the green and in the blue curve, but not in the orange one. The leakage of the second harmonic of the X-band up-convert LO can be observed at $20\,\mathrm{GHz}$ in the left graph. In addition, other undesired spurious tones resulting from the mixing in the $300\,\mathrm{GHz}$ transmitter and receiver corrupt the signal and degrade the EVM for the superheterodyne link in blue. The fact that the orange spectrum on the right presents only one spurious tone at $16.66\,\mathrm{GHz}$ shows that the X-band down-converters are the limiting factor of the transmission.

Despite the fact that the X-band mixers are not designed for terahertz communication application and do not meet the requirements necessary for transmitting data rates in the range of $100\,\mathrm{Gbps}$, data transmissions using the superheterodyne concept were successful up to a data rate of $24\,\mathrm{Gbps}$. Another impediment is that the used $300\,\mathrm{GHz}$ transmit-receive

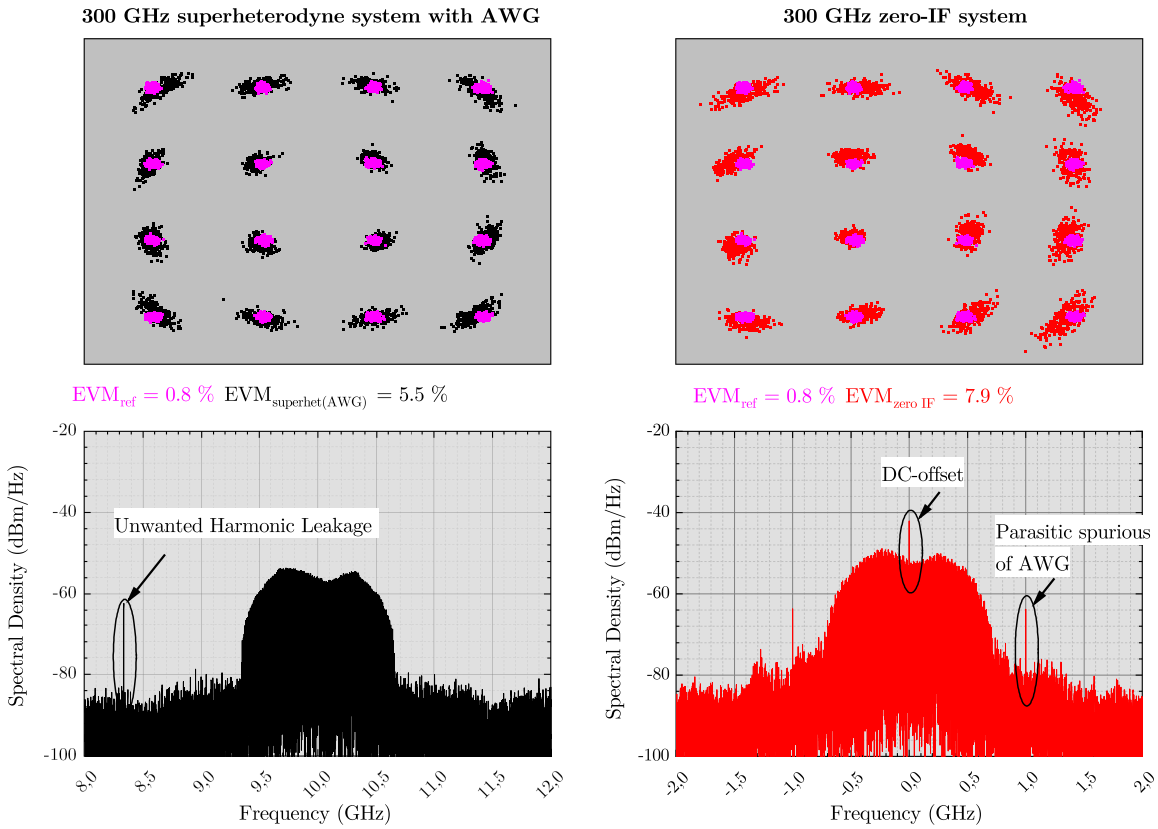

Figure 6.17: Constellation diagrams and power spectras for a 16-QAM signal with a symbol rate of $1\,\mathrm{GBd}$ using zero-IF configuration (right) and a superheterodyne configuration, where the superheterodyne has been realized using an AWG (left).

system was designed mainly for zero-IF configuration. Considering this, the maximum data rate of $60\,\mathrm{Gbps}$ achieved with the AWG shows the potential of this concept.

6.5 10 meter wireless transmission

To validate the concept also for longer distances and prove its suitability for future indoor wireless applications data transmissions over a distance of $10\,\mathrm{m}$ are conducted. The superheterodyne architecture is realized for these transmissions with the AWG, which generated the IF signal centered around a carrier of $10\,\mathrm{GHz}$.

Prior to the $10\,\mathrm{m}$ experiment, measurements in back-to-back configuration with a variable attenuator placed between the $300\,\mathrm{GHz}$ transmitter and receiver are conducted. As in the case of the longer distance transmission the superheterodyne concept is realized using the AWG and an IF centered around $10\,\mathrm{GHz}$. The variable attenuator is set for an optimal RF input power of $-40\,\mathrm{dBm}$ into the receiver. The same input power reaches the receiver also in the other two transmission cases: $0.5\,\mathrm{m}$ and $10\,\mathrm{m}$.

Data transmissions using signals modulated with QPSK, 16-QAM and 32-QAM are conducted and compared to the $0.5\,\mathrm{m}$ low distance transmission as well as to the back-to-back configuration. Fig. 6.19 shows the results of this comparison. The three transmissions show very similar performances, which was expected due to same RF input power at the

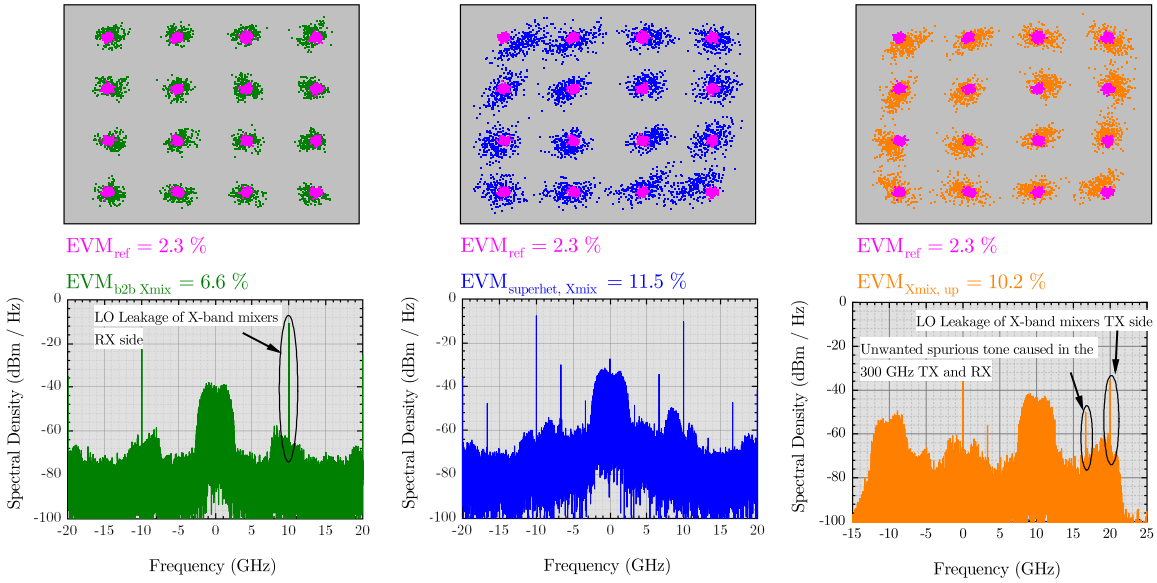

Figure 6.18: Constellation diagrams and power spectras for a signal with a symbol rate of $4\,\mathrm{GBd}$, modulated with 16-QAM using the X-band mixer link in back-to-back configuration (left), a superheterodyne configuration, where the superheterodyne architecture has been realized using the X band mixers (center) and a superheterodyne configuration, where the superheterodyne architecture has been realized using the the X band mixers only on the transmitter side (right).

receiver. The highest data rate of $56\,\mathrm{Gbps}$ is achieved for the transmission distance of $10\,\mathrm{m}$ with 16-QAM. Successful transmissions were realized also with more complex modulation formats like 32-QAM. For this case the highest data rate achieved is $30\,\mathrm{Gbps}$.

The successful $10\,\mathrm{m}$ experiment shows that additional FSPL can be easily compensated by an antenna system with enough gain and therefore the superheterodyne architecture is a promising concept for future indoor and outdoor wireless links.

6.6 Multichannel transmission

The potential of the superheterodyne concept unfolds under multichannel transmission, also called channel aggregation using frequency-domain multiplexing (FDM). The new IEEE standard for $100\,\mathrm{Gbps}$ wireless point-to-point links [IEE17] defines channels with a bandwidth of $2.16\,\mathrm{GHz}$ to be aggregated in the low THz range between 252 and $325\,\mathrm{GHz}$. Based on this standard, multichannel transmissions using the system presented in Fig. 6.5 were conducted. The signals were generated with the help of the AWG. For this experiment two channels were aggregated, each with a bandwidth of $2.16\,\mathrm{GHz}$. Different modulation formats and digital filters were applied.

Fig. 6.20 shows the constellation diagrams and power spectrum of an 32-QAM modulated IF signal. The two center frequencies of the channels at 10 and $12.16\,\mathrm{GHz}$ are close to the center frequency of the single carrier experiments. A channel data rate of $8\,\mathrm{Gbps}$ is achieved. The performance of the second channel, centered around $12.16\,\mathrm{GHz}$ is slightly better than that of the first channel, the EVM value reaches $7\,\%$ in comparison to $7.4\,\%$ on the first channel. Compared to the experiment presented in Fig. 6.14, the performance of

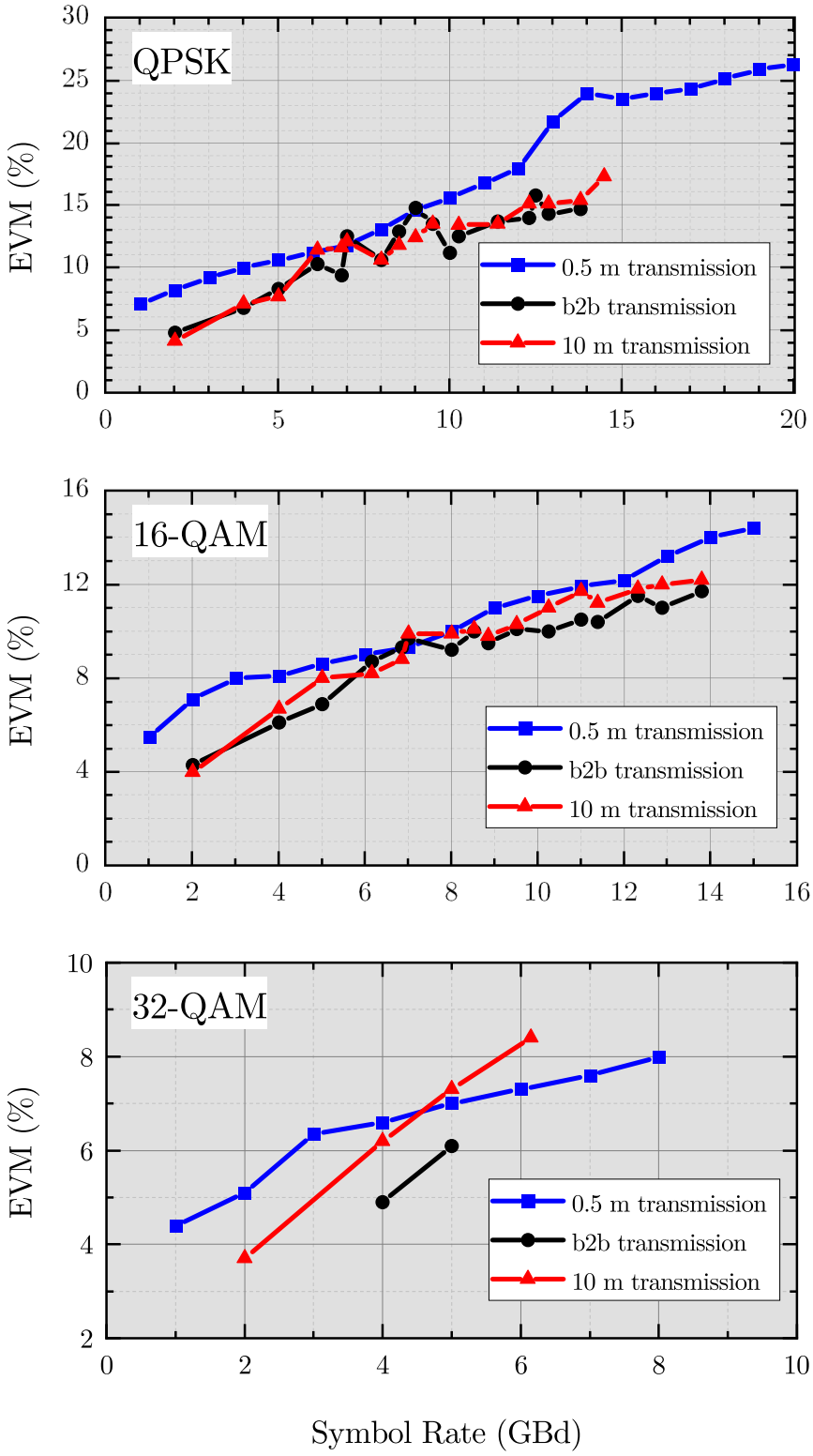

Figure 6.19: Comparison of 300 GHz wireless data transmission results over different distances. Three modulation formats are analyzed: QPSK, 16-QAM and 32-QAM.

the transmission has deteriorated. The EVM increases from around 4.2 % to 7.4 %. This deterioration is caused by the interference with the second channel.

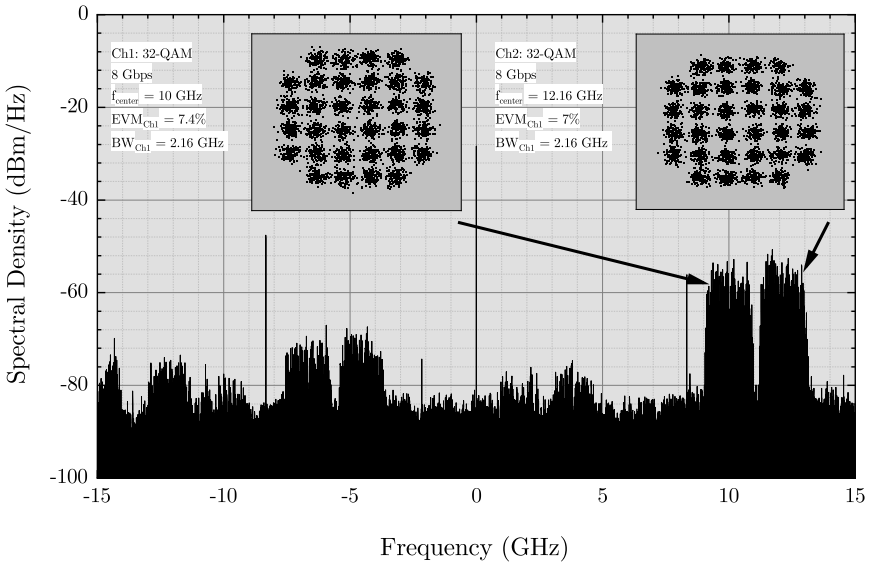

Figure 6.20: Successful transmission of a multi carrier 32-QAM modulated signal in a superheterodyne $300\,\mathrm{GHz}$ wireless link. On each channel a data rate of $9.6\,\mathrm{Gbps}$ and an overall aggregated data rate of $19.2\,\mathrm{Gbps}$ is achieved.

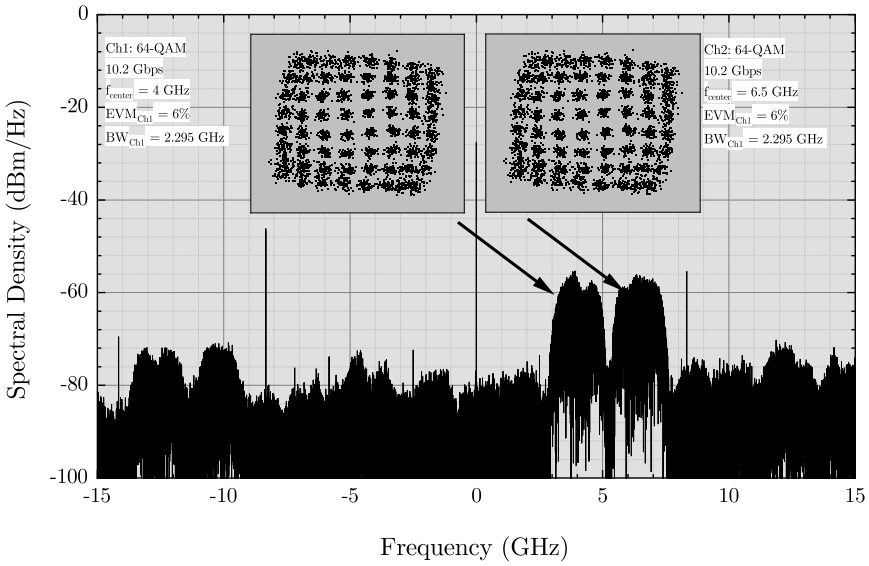

Figure 6.21: Successful transmission of a multi carrier 64-QAM modulated signal in a superheterodyne $300\,\mathrm{GHz}$ wireless link. On each channel a data rate of $10.2\,\mathrm{Gbps}$ and an overall aggregated data rate of $20.4\,\mathrm{Gbps}$ is achieved.

Fig. 6.21 shows the constellation diagrams and power spectrum of an IF signal, that achieved the highest channel data rate. The chosen modulation format is 64-QAM, the symbol rate is $1.7\,\mathrm{GBd}$ and the digital filter has a roll-off factor of 0.35, which leads to a bandwidth of $2.295\,\mathrm{GHz}$. The first channel is centered around $4\,\mathrm{GHz}$ and the second one is centered around $6.5\,\mathrm{GHz}$. The data rate transmitted on each channel reaches $10.2\,\mathrm{Gbps}$. The two channels perform similar, they both have an EVM of $6\,\%$.

The focus of the multichannel transmission was the compatibility to the new IEEE standard, which foresees channel bandwidths of around $2\,\mathrm{GHz}$. A comparison to the single carrier

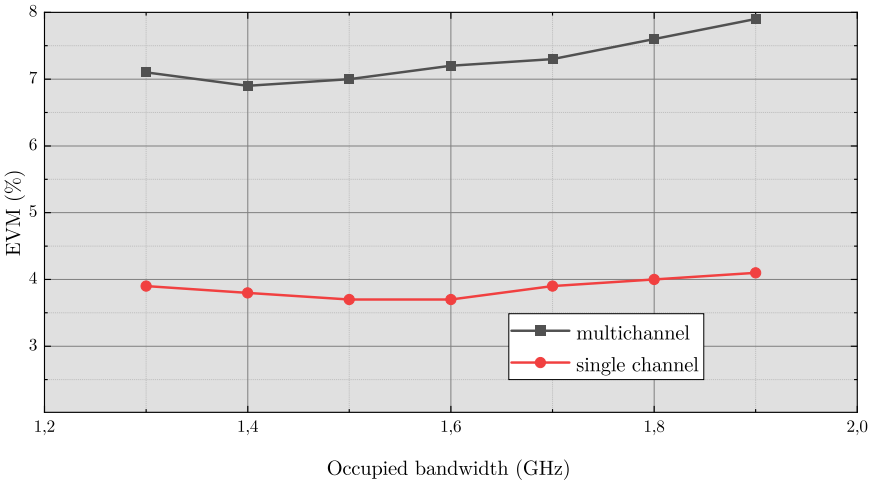

Figure 6.22: Performance comparison between single channel and multi channel transmission for a QPSK modulated signal with a symbol rate of $1\,\mathrm{GBd}$ and an increasing roll-off factor of the filter.

experiment shows the impact of channel aggregation on the linearity of the system. Fig. 6.16 shows that a data rate of $12\,\mathrm{Gbps}$ can be achieved with 64-QAM modulation when only one channel is transmitted. In the multichannel experiment this data rate is reduced to $10.2\,\mathrm{Gbps}$ due to a higher peak to average power ratio. To achieve the same data rate as in the single carrier transmission a higher back-off from the 1- dB compression point is required. This, however, leads to a lower SNR. Therefore, it can be stated, that a high linearity of the transceiver is one of the crucial issues for this type of transmission.

Fig. 6.22 shows the influence of a multi-carrier signal on the performance of the link. For this measurement the transmitted bandwidth is varied with the help of the digital filter used in the transmission. The symbol rate and the modulation format are kept constant to $1\,\mathrm{GBd}$ and QPSK. A relatively homogeneous difference between the performance of the multichannel and of the single channel transmission of around $3\,\%$ is observed, which means that inter-channel interference negatively affects the quality of the link. This effect can also be observed in Fig. 6.23, which shows the EVM in dependency of the frequency spacing between the two transmitted channels. When the gap is small, in the order of magnitude of around $250\,\mathrm{MHz}$ the EVM of each channel reaches $8\,\%$. By increasing the spacing to $750\,\mathrm{MHz}$ the performance improves by $1\,\%$.

The successful transmission of aggregated channels, compatible to the new IEEE standard, with such high data rates shows the potential of the presented wireless link for future high data rate applications. Furthermore, the used complex modulation format, 64-QAM, is another promising factor for reaching high data rates with terahertz communication links.

6.7 Influence of the frequency source

All of the above-mentioned results were achieved using an electronic LO source at $8.33\,\mathrm{GHz}$. Due to the necessary multiplication factor of 36 and considering the important aspects gained from the work presented in [AK15] and in [CKG+18] this method is not considered ideal. The influence of the white LO noise is expected to be significant. One solution would be to use a signal generated by combining two optical signals onto a UTC-PD so that the differential

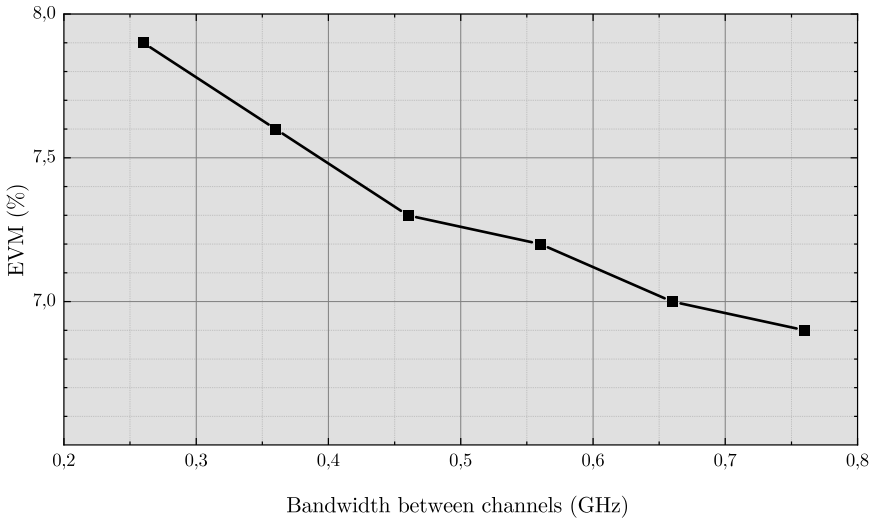

Figure 6.23: Deterioration of wireless link performance due to interferences in a multichannel transmission.

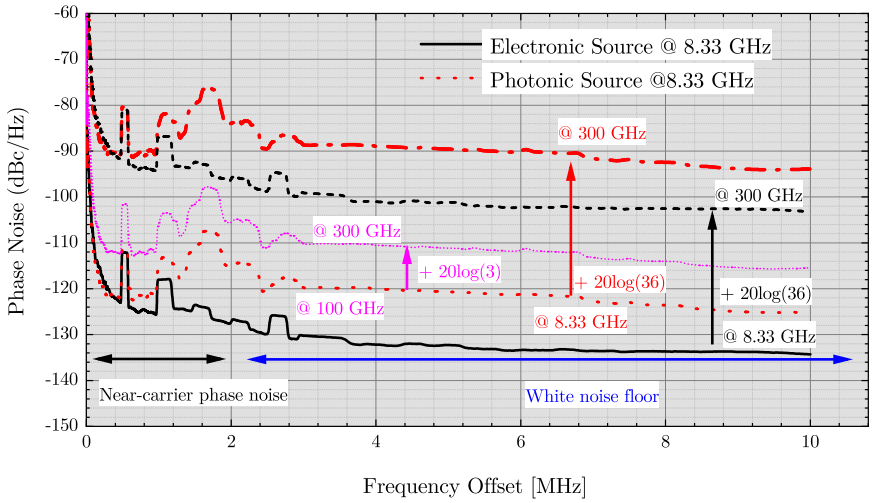

Figure 6.24: Comparison between measured phase noise of the electronic and photonic source at $8.33\,\mathrm{GHz}$ and calculated phase noise curves at $300\,\mathrm{GHz}$.

mixing product is the desired frequency signal. A good trade-off would be to generate an LO in the W-band and keep the last multiplication stage integrated in the RF components, like presented in this work.

Since such an optical test bench was not available for the testing of the superheterodyne link one initial scheme to generate the photonic LO at $8.33\,\mathrm{GHz}$ was tested. It is composed of an electrical signal that drives an optical modulator to generate an amplitude modulation, further detected by a photodiode. Then this signal is amplified to reach the required LO level of the RF transmitter and receiver. Fig. 6.24 shows the comparison between the measured phase noise of the electronic source represented in solid black line and the phase noise of the photonic source represented in dotted red line, both at $8.33\,\mathrm{GHz}$. The white noise floor of the photonic LO source is around $10\,\mathrm{dB}$ higher than the electronic one. The phase noise of the $300\,\mathrm{GHz}$ carrier is calculated adding a factor of $20\log(36)$ as explained in chapter 6.1 and plotted in the dashed black curve and in the red dot dash curve respectively.

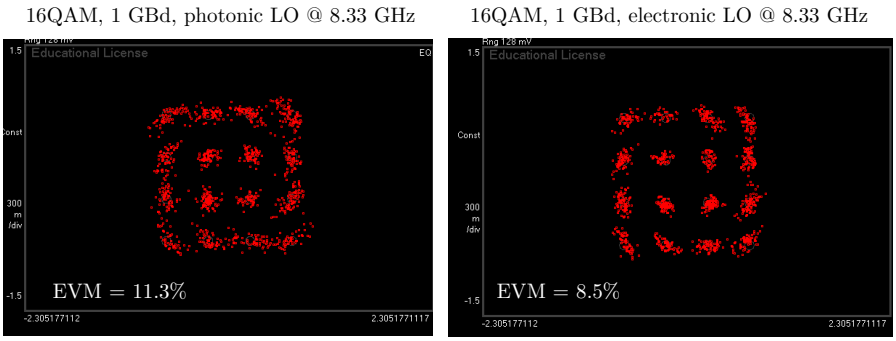

Figure 6.25: Measured constellation diagrams representing 16-QAM modulated signals with a symbol rate of $1\,\mathrm{GBd}$ using an electronic LO source on the right and a photonic LO on the left.

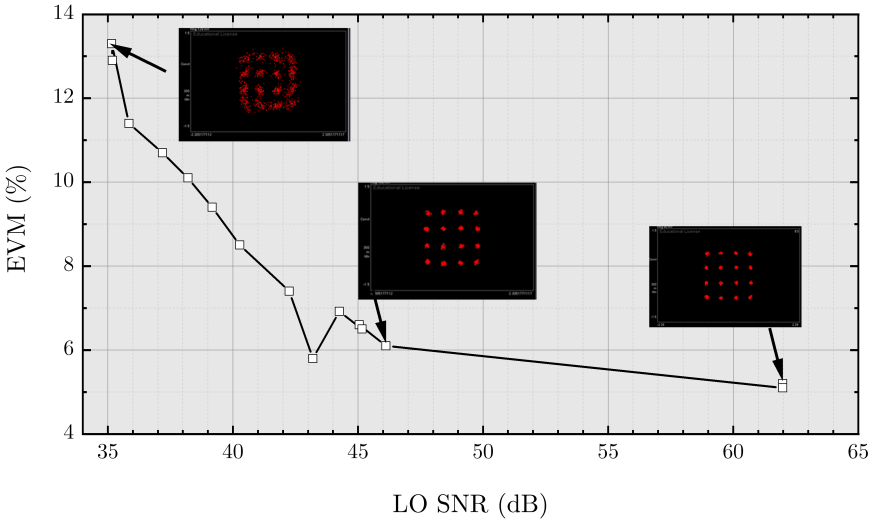

Figure 6.26: EVM evolution under degradation of the SNR of the LO. The transmitted signal is modulated using 16-QAM and has a symbol rate of $1\,\mathrm{GBd}$.

Further investigation have shown that not only the phase noise of the photonic LO was different, but also the SNR of the LO carrier. A measurement using a spectrum analyzer has revealed that the SNR of the photonic LO is $40\,\mathrm{dB}$, in comparison to the SNR of the electronic LO which has a value of $60\,\mathrm{dB}$. To have a fair comparison between the two measurements, noise was artificially added to the setup using an electronic LO, until the same SNR value was achieved. For this purpose pure thermal noise coming from a wideband amplifier without any input was added to the LO signal. An electrical attenuator was placed after the amplified noise to adjust the SNR of the LO signal. The available range is between 30 and $65\,\mathrm{dB}$. Fig. 6.25 shows the comparison between two constellation diagrams both representing 16-QAM modulated signals with a symbol rate of $1\,\mathrm{GBd}$. The diagram on the left hand side was achieved using the photonic LO source and has an EVM of $11.3\,\%$, while the diagram on the right achieved an EVM of $8.5\,\%$ using an electronic LO source. A degradation of more than $2\,\%$ is caused by phase errors due to a higher white noise floor of the photonic LO source.

Fig. 6.26 shows the evolution of EVM when the SNR of the electronic LO is varied. It is shown in this measurement, that not only the phase noise alone has an significant impact on the performance of a wireless link, but also the SNR of the frequency carrier.

A possible solution of improving the white noise floor at $300\,\mathrm{GHz}$ would be to generate the LO using the photonic test bench at $100\,\mathrm{GHz}$. This would reduce the overall white noise floor by $15\,\mathrm{dB}$ in comparison to the noise floor using the electronic LO source and frequency multipliers. This is shown in Fig. 6.24 in the dotted magenta curve, which is calculated by the addition of the factor $20\log(3)$ to the noise curve of the measured photonic LO.

Two important guidelines for the design of the frequency source for future terahertz links can be derived from this measurement. First of all, the SNR of the LO source has to be taken into account and a value of $60\,\mathrm{dB}$ is recommended. Second of all, a photonic source in the W-Band is preferred to one at lower frequencies due to the influence of white noise floor on broadband transmissions.

6.8 Comparison to state of the art

There are two options of realizing terahertz communication. The first implies the usage of a very broad bandwidth with a low bandwidth efficiency. For example at a center frequency of $300\,\mathrm{GHz}$, a bandwidth of over $50\,\mathrm{GHz}$ is available. Thus, to achieve a data rate of $100\,\mathrm{Gbps}$ only $2\,\mathrm{b/s/Hz}$ are necessary. The second option implies the usage of aggregated channels each with a small bandwidth and a high bandwidth efficiency.

Up to now mostly the first option has been the focus of research for many groups. Table 6.3 shows a summary of high-data-rate wireless links using different technologies. The terahertz signal can be generated either using photonic components like UTC-PD and positive-intrinsic-negative photodiodes (PIN-PD) or active electronics using different technologies either Silicon or $\mathrm{III}-\mathrm{V}$ compound semiconductor based. [CLZ+18], [JPO+18], [KLDA+13] and [CNE+19] use a combination of a photonic transmitter and an electronic receiver, which is either active or passive, and achieve data rates of $100\,\mathrm{Gbps}$ or above. [HFA+18] uses an all-electronic approach and an $80\,\mathrm{nm}$ InP high electron mobility transistor (HEMT) technology and also achieves $100\,\mathrm{Gbps}$. [LDY+19] and [HTK+18] report on Si CMOS integrated transmitters and receivers and on data transmissions using these transceivers. The results are state of the art for this technology with low maximum of oscillation frequencies. In [LDY+19] $80\,\mathrm{Gbps}$ over a distance of $3\,\mathrm{cm}$ are achieved.

Most of the above mentioned publications use a very broadband signal to achieve data rates of around $100\,\mathrm{Gbps}$, hence take advantage of the first option of realizing terahertz communication. The only exceptions are the work presented in [HFA+18], in [LDY+19] and this work. While [HFA+18] and [LDY+19] show only measurement results of the high data rate transmission experiment and do not consider the reasons of the architecture choice, this work gives an in-depth analysis of different configurations of a terahertz link presenting advantages and disadvantages of each.

6.9 Conclusion

This chapter reports on a $300\,\mathrm{GHz}$ superheterodyne system, that reaches a maximum data rate of $60\,\mathrm{Gbps}$ and can cover distances up to $10\,\mathrm{m}$. Two possibilities of realizing the superheterodyne architecture are analyzed: with commercial, easily accessible mixers and with an AWG. A comparison to zero-IF configuration shows the advantages of the superheterodyne

architecture. The EVM is improved for all modulation formats. The link shows compatibility to low-cost existing baseband solutions and to the new IEEE frequency standard for ultra-fast communication networks. Channel aggregation is proven feasible, by the successful transmission of complex modulated signals up to 64-QAM. Since the transmission of complex modulation formats is of vital importance for ultra-high data rate under channel aggregation a linearity analysis of the RF and IF components and of the final superheterodyne link is presented. The influence of phase noise on the quality of the transmission is experimentally examined. For this purpose, a comparison between an electronic source and a photonics-based one is realized. The importance of both white noise floor and SNR of the carrier frequency is demonstrated. For future wireless links operating in the low terahertz range an LO source in the W-band with a low phase noise is recommended. A channel data rate of $10.2\,\mathrm{Gbps}$ is reached. Although a redesign of the $300\,\mathrm{GHz}$ transmitter and receiver needs to be made so that the circuits are particularly designed for superheterodyne configuration with an IF frequency of $70\,\mathrm{GHz}$, this experiment validates the applicability of terahertz communication. The mentioned redesign is the focus of the next chapter.

Table 6.3: State of the art wireless links above 200 GHz using different technologies.

Reference	Technology	Architecture	Center Frequency	Data Rate	Distance	Modulation Format
[KLDA+13]	UTC-PD + 35 nm InGaAs mHEMT	zero-IF	300 GHz	100 Gbps	40 m	16-QAM
[CLZ+18]	UTC-PD + passiv electronic mixer	zero-IF	280 GHz	100 Gbps	50 cm	16-QAM
[JPO+18]	UTC-PD + passiv electronic mixer	zero-IF	425 GHz	106 Gbps	50 cm	16-QAM
[RGHP19b]	130 -nm SiGe BiCMOS	zero-IF	230 GHz	100 Gbps	1 m	16-QAM
[RGHP18]	130 -nm SiGe BiCMOS	zero-IF	230 GHz	90 Gbps	1 m	32-QAM
[CNE+19]	PIN-PD + active electronic receiver	zero-IF	300 GHz	128 Gbps	50 cm	16-QAM
[LDY+19]	40 nm Si-CMOS	superheterodyne	265 GHz	80 Gbps	3 cm	16-QAM
[HFA+18]	80 nm InP-HEMT	superheterodyne	300 GHz	100 Gbps	2.22 m	16-QAM
[BMA+14]	35 nm InGaAs mHEMT	zero-IF	240 GHz	96 Gbps	40 m	8-PSK
[KBM+15]	35 nm InGaAs mHEMT	zero-IF	240 GHz	64 Gbps	850 m	8-PSK
This work	35 nm InGaAs mHEMT	superheterodyne	300 GHz	60 Gbps	0.5 m	16-QAM
This work	35 nm InGaAs mHEMT	superheterodyne	300 GHz	56 Gbps	10 m	16-QAM
This work	35 nm InGaAs mHEMT	superheterodyne	300 GHz	12 Gbps	0.5 m	64-QAM

7 A Transmit Receive Chipset for the Superheterodyne Approach

As the previous chapter the work presented in this section has been carried out in the frame of the EU-funded project ThoR (https://thorproject.eu/).

The last portion of a communication network, the link between an edge cell and the core network, is realized at the moment by either wired or wireless links. The wired solutions are fast but very expensive and often impossible to deploy in remote areas. Employing the solution described and pictured in the previous chapter 6 in Fig. 6.2 would provide the required capacity for this application. This system is based on a superheterodyne architecture and consists of two important components: the modem which provides the IF and the RF frontend. The modem communicates with the core network via Ethernet cable and realizes the first up-conversion to the frequency range between 60 and $88\,\mathrm{GHz}$. According to the IEEE 802.15.3e-2017 standard [IEE17] each modem channel can occupy up to $2.16\,\mathrm{GHz}$ of bandwidth. The IF can aggregate signals coming from one or more channels. The second up-conversion is realized by the $300\,\mathrm{GHz}$ transmitter. The RF signal is transmitted with data rates exceeding $100\,\mathrm{Gbps}$ using an antenna system over a variable distance up to $1\,\mathrm{km}$ to the base station where the $300\,\mathrm{GHz}$ RX and the modem down-convert the baseband signal.

The work presented in the previous chapter concentrates on the proof of concept for the proposed superheterodyne architecture and uses an existing RF frontend designed for zero-IF transmission. In this chapter a superheterodyne $300\,\mathrm{GHz}$ transmit receive chipset is presented, with an IF operation range between 75 to $95\,\mathrm{GHz}$, compatible with the new frequency standard, which would enable the first integration of a THz communication link in a live front- and back-haul network. The $300\,\mathrm{GHz}$ transmitter and receiver are based on MMICs realized in the $35\,\mathrm{nm}$ gate-length InAlAs/InGaAs mHEMT technology presented in chapter 1.2.3. The MMICs can be packaged into compact waveguide modules, similar to the ones presented in chapter 3. To enhance the maximum transmission distance different power amplifier modules can be connected after the $300\,\mathrm{GHz}$ transmitter like the one presented in [JTL+20].

With the significant progress of 5G technologies the availability of an IF system does not represent a problem anymore. Wireless links in the V- and E-Band can be commercially purchased, e.g. [Sik]. Although 5G access networks extended the frequency spectrum above $6\,\mathrm{GHz}$, where wireless transport links are currently operated, these products alone cannot support the beyond 5G requirements in large scale network deployment. In combination with a $300\,\mathrm{GHz}$ frontend like presented in this chapter the ultra-high data rate demand can be satisfied.

Fundamental frequency converter Subharmonic frequency converter

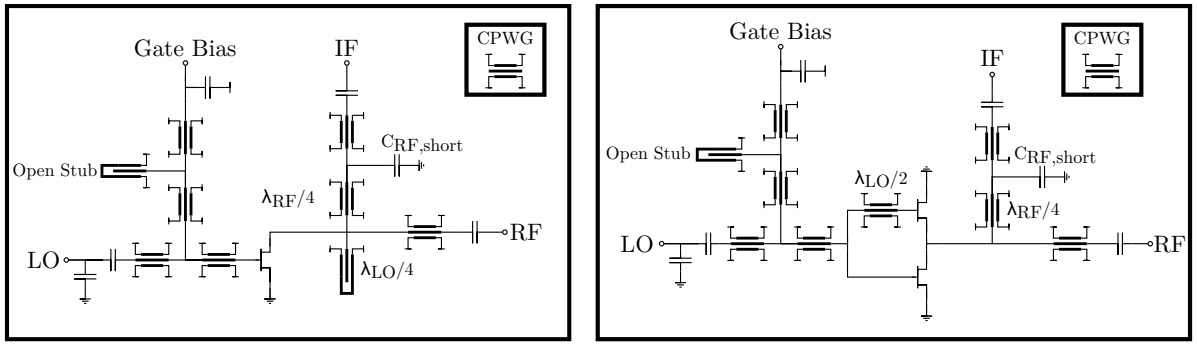

Figure 7.1: Schematics of the designed frequency converters: on the right-hand side the subharmonic one and on the left-hand side the fundamental one.

7.1 Choice of mixer architecture

Since the main applications for the designed MMIC are wireless communication systems, the frontend will integrate for sure a frequency converter. As core of the transmitter and receiver MMIC this component has a big influence on the topology of the whole transmitter and receiver chip. Due to its high linearity, high robustness against impairments and due to its simple design only resistive mixer topologies are taken into account. Two architectures can be taken into consideration for integration into the superheterodyne RF system: fundamental and subharmonic architectures.

A fundamental frequency converter has a simple structure and presents a low design risk. The well-known disadvantages of this architecture are the high necessary LO input power and the low LO to RF isolation. Balancing the same fundamental mixer would on the one hand significantly reduce the LO leakage (resulting in better LO to RF isolation), but on the other hand increase the complexity of the circuit and the necessary LO input power even further.

A subharmonic approach would lead to a much lower LO frequency. Thus, the available LO input power is easier to achieve. A disadvantage of this architecture is the high conversion loss which reflects in the lower RF power and implies extra amplification in the RF at around $300\,\mathrm{GHz}$.

In order to decide which architecture is best suited for the proposed solution one fundamental and one subharmonic frequency up-converter are designed and fabricated as stand-alone components in the frame of a student master's thesis [Hau] and further optimized in the frame of this thesis. Fig. 7.1 shows the simplified schematics of these two circuits. The fundamental frequency converter uses one mixer cell based on one common source transistor. In comparison, the subharmonic mixer uses two transistors and a quarter-wavelength delay line. The odd-order harmonics interfere destructively at the drain, while the even-order harmonics interfere constructively. The LO ports of both converters are broadband matched by using grounded coplanar transmission lines and open stubs. The gate DC supply is provided via a biasing network based on transmission lines and a capacitor which decouples the high frequency LO signal from the DC source. The IF matching network is also composed of capacitors and transmission lines. In the fundamental topology, the LO signal needs to be filtered in the RF path using an open stub with a length of lambda-quarter. The RF signal is decoupled from the IF signal also using lambda-quarter stubs and a decoupling capacitor.

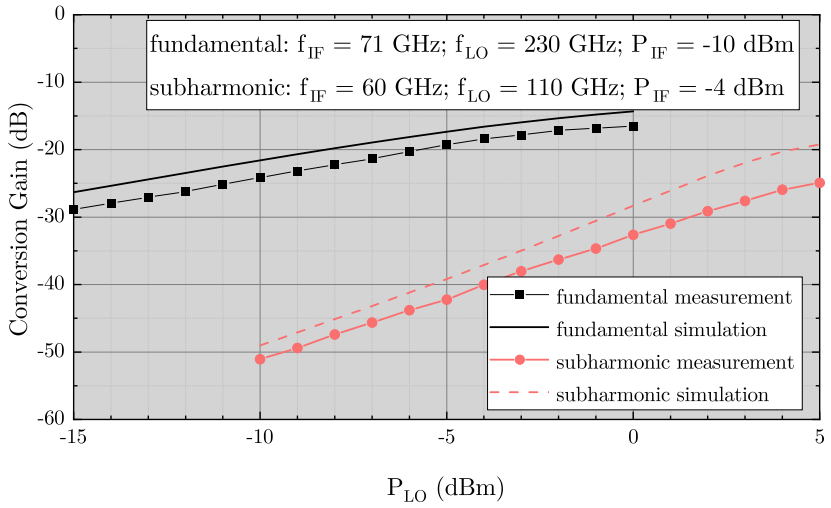

Figure 7.2: Comparison of conversion gain versus LO input power for the subharmonic and the fundamental mixer.

These chips are measured in an on-chip environment. A maximum LO input power of $5\,\mathrm{dBm}$ for the subharmonic frequency converter and of $0\,\mathrm{dBm}$ for the fundamental topology can be provided. Fig. 7.2 shows the results of the conversion gain measurement versus LO input power and the comparison to simulation for both the fundamental and the subharmonic converter. These curves show the necessary input power so that the mixers are driven into saturation. As expected better gain conversion values are reached for the fundamental topology. Due to the fact that the maximum LO input power is $0\,\mathrm{dBm}$ at an input frequency of $230\,\mathrm{GHz}$, saturation cannot be reached for the fundamental converter. Nonetheless, the tendency is obvious: a constant conversion gain difference of $8\,\mathrm{dB}$ can be observed. The highest conversion gain of the fundamental mixer is $-15\,\mathrm{dB}$, while the maximum conversion gain for the subharmonic one is $-25\,\mathrm{dB}$. The simulation matches in both cases well with the measurement, a small constant difference below $2\,\mathrm{dB}$ can be observed between the measurement and simulation curves. For further measurements LO input powers of $0\,\mathrm{dBm}$ for the fundamental case and $5\,\mathrm{dBm}$ for the subharmonic case are used.

Fig. 7.3 shows the IF frequency dependency for the two designed frequency converters. The maximum measured frequency is limited by the setup to $73\,\mathrm{GHz}$. Once again around $8\,\mathrm{dB}$ difference can be observed between the measurements of the fundamental and the subharmonic architectures.The average conversion gain of the subharmonic mixer lies at around $-24\,\mathrm{dB}$, while the one of the fundamental converter is at around $-16\,\mathrm{dB}$. A relatively constant $5\,\mathrm{dB}$ difference between measurement and simulation can be observed for the subharmonic converter. For the fundamental approach the difference amounts to around $4\,\mathrm{dB}$ at $50\,\mathrm{GHz}$, continuing to reduce with increasing IF frequency. At $70\,\mathrm{GHz}$ the measurement is only $2\,\mathrm{dB}$ lower than the simulation. Both fundamental and subharmonic frequency converters show a wideband IF frequency dependency.

A high linearity is a key requirement for reaching the goals of the system presented in Fig. 6.2. The results of the linearity measurement are given in Fig. 7.4. The output power $\mathrm{P_{RF}}$ is plotted versus the IF input power $\mathrm{P_{IF}}$. Here, the first observation is that the measurement of the fundamental converter matches better the simulation, than the subharmonic one. In

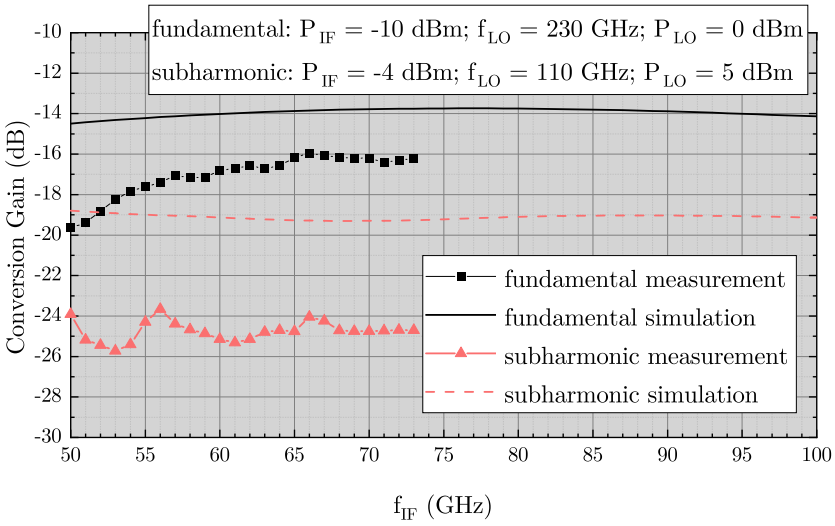

Figure 7.3: Comparison of conversion gain versus IF input frequency for the subharmonic and the fundamental mixer.

linear operation a difference of 3-dB can be observed for the subharmonic architecture, while for the fundamental one only $2\,\mathrm{dB}$ can be observed. Furthermore, around $10\,\mathrm{dB}$ of difference between the measured 1-dB output-referred compression points can be detected. For the fundamental approach $\mathrm{P}_{\mathrm{1dB,out}}$ lies at around $-18\,\mathrm{dB}$, while for the subharmonic approach $-28\,\mathrm{dB}$ were measured.

In conclusion, the theoretical advantages of the fundamental approach have been confirmed by measurements. Although the measurement setup limited the LO input power to $0\,\mathrm{dBm}$, which means that the mixer does not reach saturation, a higher conversion gain has been measured for the fundamental converter. An $8\,\mathrm{dB}$ better conversion gain in comparison to the subharmonic architecture would reduce the complexity and the requirements of the following power amplifier stage. Furthermore, a higher 1-dB output-referredcompression point, makes the fundamental architecture more suitable for transmitting more complex modulation formats, hence reaching a higher absolute data rate.

The biggest disadvantage of the fundamental approach, the high necessary LO input power can be overcome by an appropriate choice of the LO path consisting of frequency multiplier and buffer amplifier. The integration of a multiplier enables a lower LO input frequency, which can be provided either electronically by a commercially available source or by a photonic LO, based on the generation of a dual wavelength optical signal. The advantage of the latter approach is that the generated signal is free from unwanted spurious frequencies, like in the case of a low frequency electronic source, below $20\,\mathrm{GHz}$, which is further multiplied in electronic components [7].

To achieve system flexibility a multiplier with a high bandwidth is targeted. Furthermore, a high output power is necessary to drive the mixer in saturation. This helps to cope with fluctuations in the LO power level and improves the EVM which is vital to transmit complex modulation formats like 32- and 64-QAM and high data rates. This presents a challenge for the subsequent amplifier stage. To lower the requirements for the amplifier stage a high output power of the multiplier is desired. Finally, while generating harmonics of a fundamental signal also unwanted frequencies will be produced. These unwanted frequencies can lead to

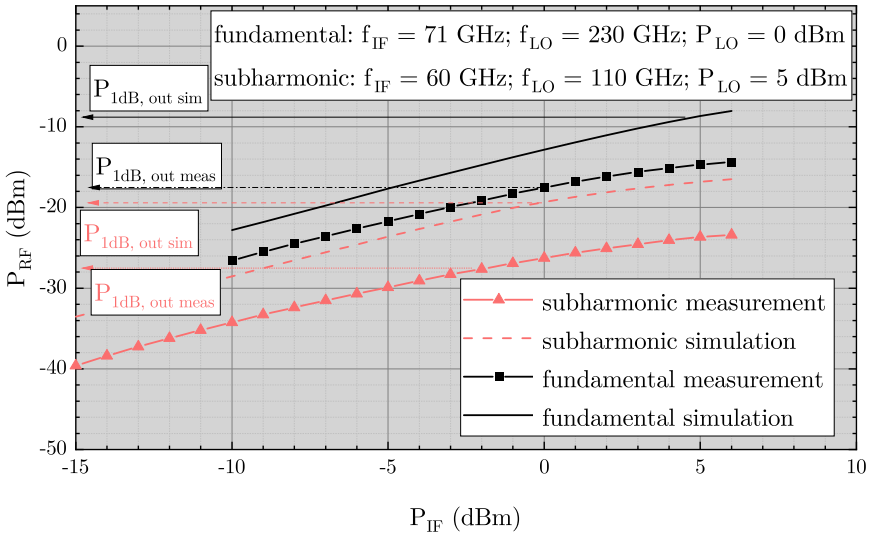

Figure 7.4: Comparison of conversion gain over the IF input power for the subharmonic and the fundamental mixer.

saturation or desensitization of the succeeding stage as well as to intermodulation products interfering with the desired data. To cope with the above challenges, the appropriate multiplier architecture must be chosen. The first property that has to be set is the multiplication factor. Typically, a factor of 2 or 3 is used in single stage frequency multipliers, due to high conversion losses at higher multiplication factors. A multiplication factor of 3 results in input frequencies in V-Band (40 to $75\,\mathrm{GHz}$). This is very convenient because of a good availability of off-the-shelf components. Additionally it is easier to generate a high input power for the multiplier in V-band rather than W-band (75 to $110\,\mathrm{GHz}$) and higher.

7.2 MMIC components

Given the established architecture of the frequency converter and the multiplication factor of the integrated multiplier the schematic of the $300\,\mathrm{GHz}$ transmitter and receiver can be determined. Fig. 7.5 shows the chip photographs and the simplified schematic of the transmitter and receiver MMIC. In the following sections each circuit component will be analyzed in detail.

7.2.1 Frequency multiplier

The frequency multiplier by three is based on the work presented in [GMLK18] and operates in class-A mode, so a drain current density of around $482\,\mathrm{mA/mm}$ is chosen. With a large input signal ideally the transistor will be driven in saturation in both the negative and the positive half-wave generating a trapezoidal output waveform. In frequency domain this leads to a spectrum rich in odd-order harmonics. Fig. 7.6 shows the schematic of the multiplier by three. All transmission lines (TL) in the circuit are implemented as CPWG. The transistor is in common source configuration and has two gate fingers each with a width of $28\,\mu\mathrm{m}$. The series capacitors C1 at the input and C2 at the output act as a DC-block. TL1 up to TL3, together with C1 represent the input matching networks. The output matching network,

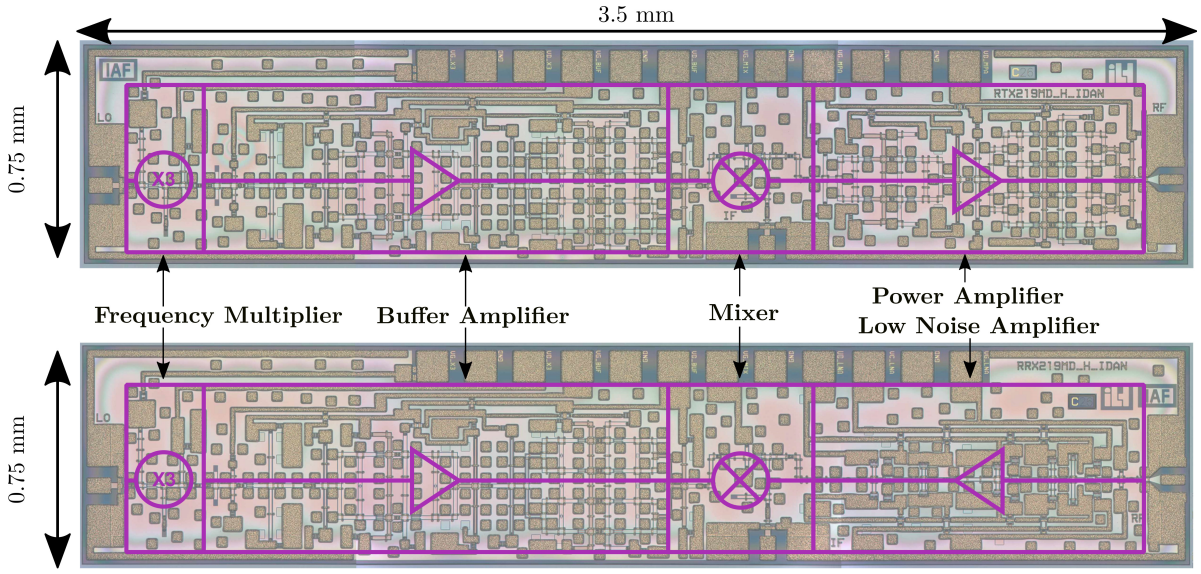

Figure 7.5: Chip photographs of the fabricated transmitter and receiver MMIC. Both chips have the same dimensions: 3.5 mm width and 0.75 mm height.

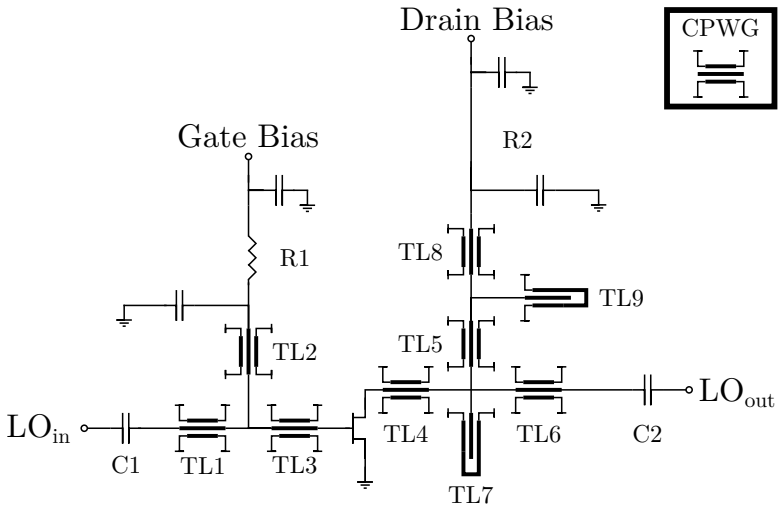

Figure 7.6: Simplified schematic of the designed frequency multiplier by three.

which is at the same time a filter for the second and fourth harmonic consists of TL4 up to TL9 and C2. The parallel capacitors in the biasing networks act as RF-blocks. The resistor R1 is introduced to ensure in- and out-of-band stability.

Fig. 7.7 shows the results of the on-wafer measurement of the output power versus input power and the comparison to simulation for the stand-alone multiplier by three. This measurement was conducted for different input frequencies, which lead to different output frequencies. The LO frequencies of interest are: 216, 220.5 and 226.5 GHz. The measurement shows that the output power curve is constant for different input frequencies and that an input power between 0 and 2 dBm is needed for the multiplier to reach a saturated output power. Compared to simulations, there is a good agreement for low input powers. The difference increases constantly with increasing power, reaching around $5\,\mathrm{dB}$ at $6\,\mathrm{dBm}$ input power. The maximum output power delivered to the buffer amplifier stage is $-5\,\mathrm{dBm}$.

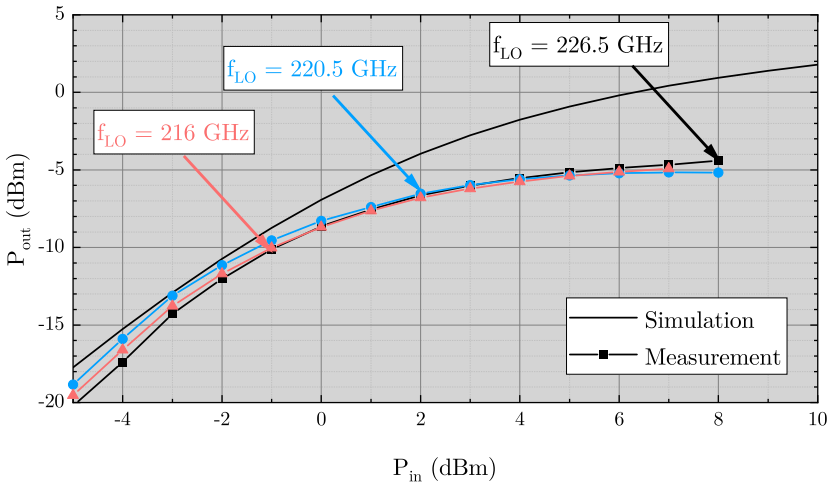

Figure 7.7: Measurement results of the output power versus input power and comparison to simulation for the stand-alone multiplier by three.

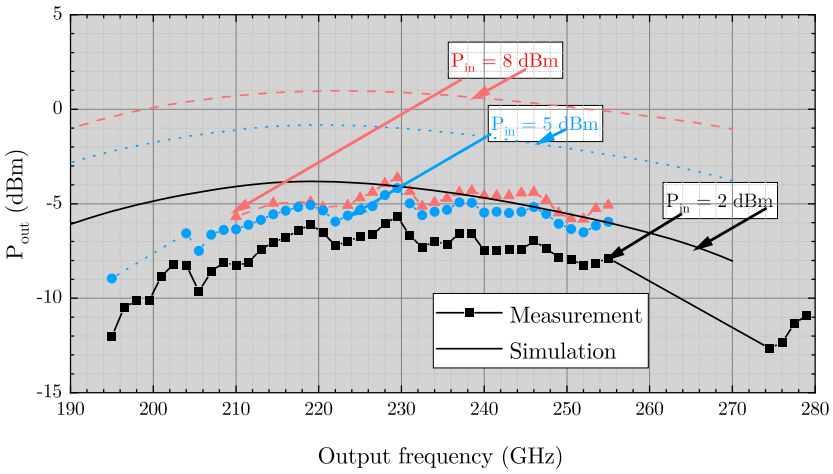

Figure 7.8: Measurement results of the output power versus frequency and comparison to simulation for the stand-alone multiplier by three.

Fig. 7.8 shows the measurement results of the output power versus frequency and comparison to simulation for the stand-alone multiplier by three. The input power varies between 2, 5 and $8\,\mathrm{dBm}$. The multiplier shows a wide band of output frequency spanning from around 200 to above $250\,\mathrm{GHz}$ for all measured input powers. The difference between measurement and simulation grows with increasing input power, as expected from the measurement plotted on Fig. 7.7. Starting from 4 dBm input power the multiplier saturates, while in simulation the saturation is not reached until 10 dBm.

7.2.2 Buffer and power amplifier

The buffer amplifier is needed to provide enough LO input power for the up- and down-converter. The buffer amplifier is adapted from the work presented in [STL+19a] and consists of five gain stages with four parallel transistors in the last two stages. Fig. 7.9 shows the

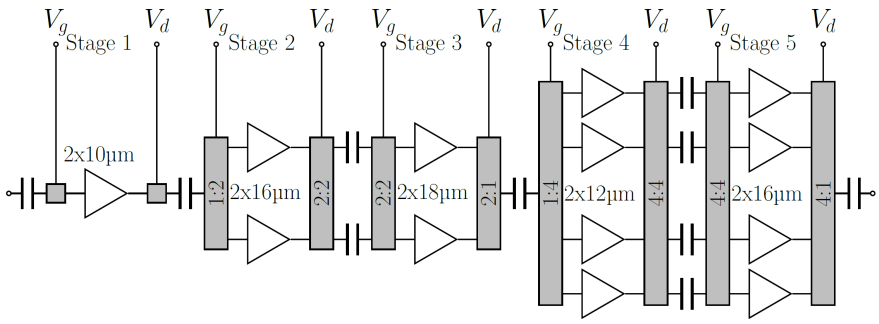

Figure 7.9: Simplified schematic of the designed buffer amplifier [STL+19a].

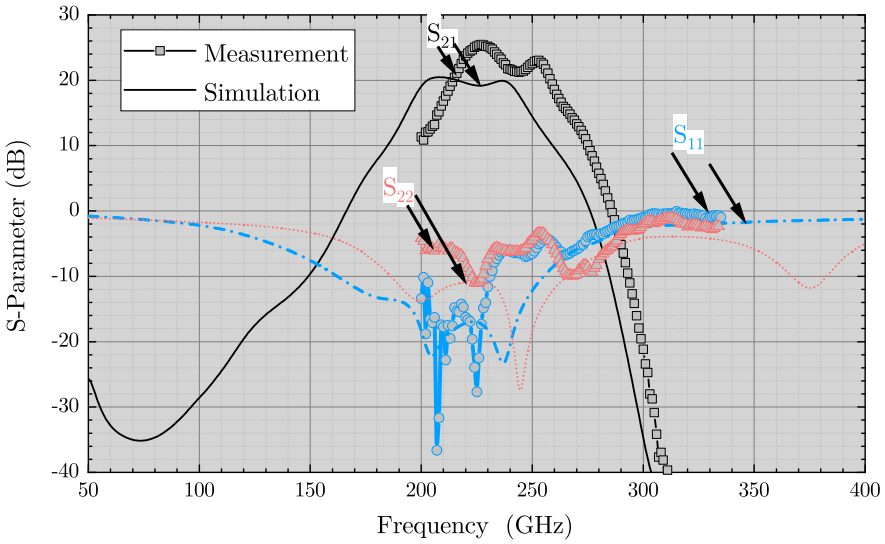

Figure 7.10: Small-signal measurement results of the buffer amplifier in the superheterodyne circuits.

simplified schematic of this buffer amplifier. All transistors are in common-source configuration and operating in class A mode. The gate widths were chosen in a way to avoid compression in the first stages. The amplifier input is a single stage followed by two times two parallel transistor stages. The last two stages are each four parallel transistors to increase the output power. Compact power combiners and dividers are used in order to parallelize the branches and to save space in comparison to standard Wilkinson combiners. Between the stages two, three, four and five there are interstage matching networks which also provide the DC-biasing. For input and output matching, transmission lines and series capacitors are used. All biasing networks are included in the matching and consist of an RF shorted stub line followed by a metal insulator metal (MIM) capacitor to ground. Series resistors are placed in the gate biasing to improve the stability and to suppress low frequency oscillations. In case of in-band-oscillation a resistor with a parallel capacitance is placed in the signal path in front of the first stage gate terminal [STL+19a].

Fig. 7.10 shows the measured S-parameters compared to the simulated ones. The frequency of operation of the buffer has moved to slightly higher frequencies and shows a slightly higher gain than simulated. In the frequency range between $215\,\mathrm{GHz}$ and $260\,\mathrm{GHz}$ the gain of the buffer amplifier is above 20 dB. In this frequency range the magnitudes of the measured input and output reflection parameters are below $-3\,\mathrm{dB}$.

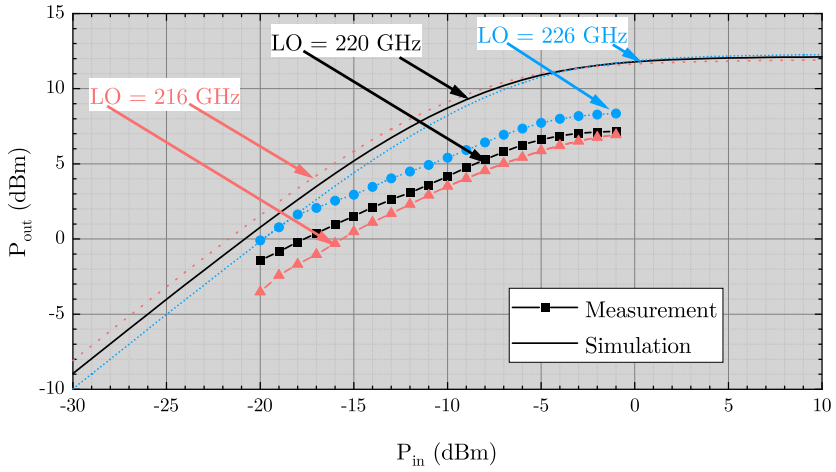

Figure 7.11: Large-signal measurement results of the buffer amplifier.

Fig. 7.11 shows the large signal measurement of the buffer for increasing input powers. The current density of the transistors is the same as in the case of the small signal measurement. This measurement is conducted for three different input frequencies: 216, 220 and $226\,\mathrm{GHz}$. The difference between measurement and simulation is dependent on the input frequency, which is confirmed also by the small-signal S-Parameter measurements. In the linear region there is good accordance, with differences below $2\,\mathrm{dB}$ for the 220 and $226\,\mathrm{GHz}$ curves. For $216\,\mathrm{GHz}$ the difference reaches $5\,\mathrm{dB}$. In the saturation region, the difference between measurement and simulation ranges between 3 and $5\,\mathrm{dB}$. Considering the power provided by the frequency multiplier of around -5 dBm, which is the input power in the buffer amplifier, an output power of above 5 dBm can be supplied to the frequency converter, independent of the LO frequency. At $226\,\mathrm{GHz}$, this power achieves $8\,\mathrm{dBm}$. Although the frequency of operation is slightly shifted to higher frequencies in comparison to simulations, the measurement shows that the buffer amplifier supplies enough power to saturate the frequency up- and down-converter for all frequencies relevant for the system.

One of the biggest challenges of data transmissions at $300\,\mathrm{GHz}$ is the low available RF power. Another crucial role in the success of the implementation of the solution pictured in Fig. 6.2 is the ability of the modules to transmit and receive complex modulated data, considerably increasing the data rate. This ability is directly reflected in the linearity. Like shown in Fig. 7.4, the 1-dB compression point of the mixer is around $-18\,\mathrm{dBm}$. This low output power requires a further amplification stage placed after the up-converter. For this component of the transmitter a similar power amplifier like the one described in detail in [STL+19b] is chosen. This component is of crucial importance not only for the achievable output power and the resulting transmission distance, but also for the transmission of complex modulation formats like 32- and 62-QAM.

To determine the optimal parameters of the power amplifier a gain partitioning analysis needs to be conducted. For this purpose two important starting points are set. Firstly the linearity of the mixer is taken into consideration. Like previously mentioned the input-related 1-dB compression point of the mixer is around $0\,\mathrm{dBm}$. Secondly, like shown in [STL+19b] the power amplifier can realistically achieve a saturated output power of around $8\,\mathrm{dBm}$ and an output referred 1-dB compression point of $3\,\mathrm{dBm}$. Fig. 7.12 graphically shows the results

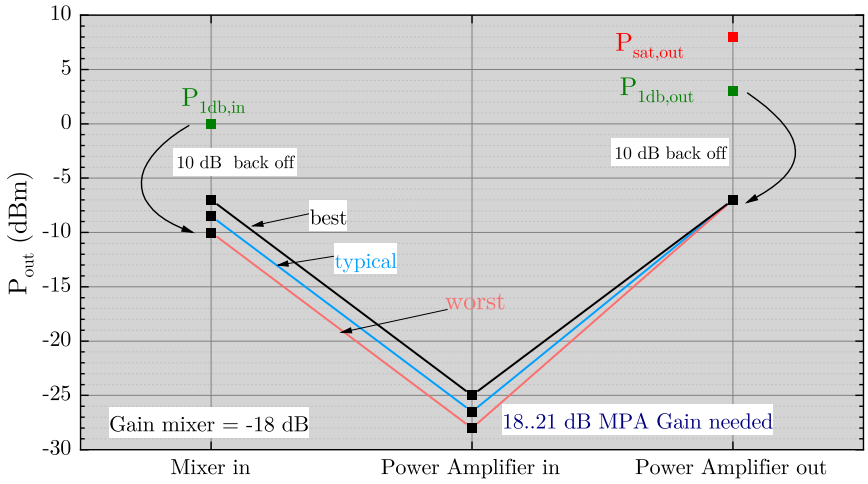

Figure 7.12: Gain partitioning for the an optimal gain of the power amplifier.

of this analysis with the two mentioned starting points. For the transmission of complex modulations a back-off from the 1-dB compression point of around $10\,\mathrm{dB}$ is necessary [7]. The $0\,\mathrm{dBm}$ represent a worst case scenario because in the measurement pictured in Fig. 7.4, the necessary LO input power is not achieved. Therefore, two other cases are considered:

- a best case, which corresponds to the simulation, where the output power is around 3 -dB higher than in the worst case
- a typical case, where the output power is around $1.5\,\mathrm{dB}$ higher than in the worst case

The gain of the mixer is $-18\,\mathrm{dB}$. This means that the power amplifier has to achieve a large signal gain between 18 and $21\,\mathrm{dB}$. To achieve this value a topology similar to the one used for the buffer amplifier in Fig. 7.9 is employed with the exception of the first amplification stage and the gate widths of the transistors. The resulting amplifier is directly integrated on the transmitter, hence no stand-alone measurement results can be presented.

In order to maximize the transmission distance for the proposed solution pictured in Fig. 6.2, further state-of-the-art solid state amplifier circuits like the ones shown in [JTL+20] can be employed in combination with the transmitter MMIC presented here. This would enable a linear output power of around $10\,\mathrm{dBm}$ at $300\,\mathrm{GHz}$.

7.2.3 Low noise amplifier

To reduce the noise and make the down-converter suitable for THz communication an LNA was designed, fabricated as a stand-alone component and measured. A similar LNA with the same requirements has been presented in detail in [8]. The amplifier consists of three cascode stages and impedance matching blocks. Fig. 7.13 shows the simplified schematic of one stage. The cell consists of a cascode stage with two transistors, the first in common source (CS) configuration and the second in common gate (CG) configuration. The input is at the gate of the CS transistor and the output at the drain of the CG transistor. DC-biasing at the gate of the CS transistor $\mathrm{V_{G,CS}}$, at the gate of the CG transistor $\mathrm{V_{G,CG}}$ and at the drain of the CG transistor $\mathrm{V_{D,CG}}$ must be provided in order for the cell to amplify.

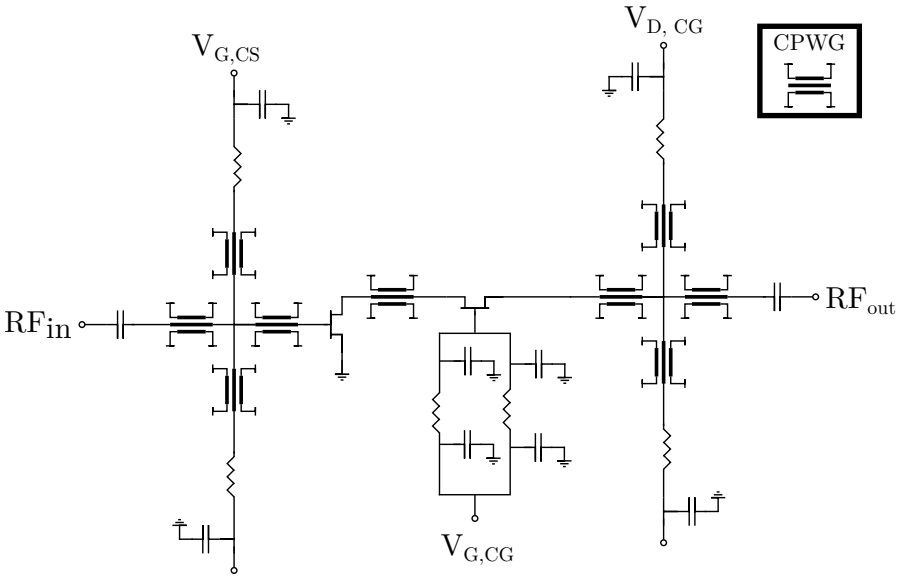

Figure 7.13: Simplified schematic of one amplification stage in the low noise amplifier.

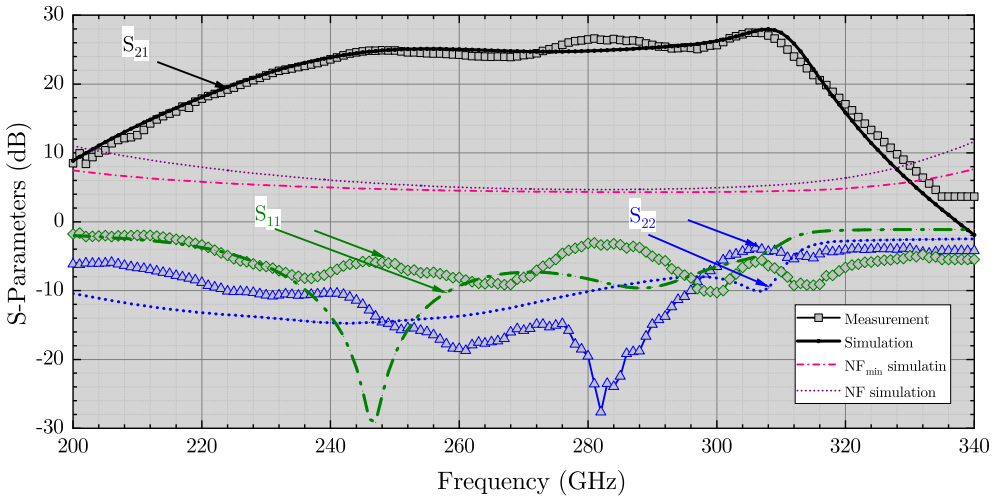

Figure 7.14: Measured and simulated S-parameters of the 300 GHz three stage LNA.

On-wafer S-parameter measurements were performed and the results plotted in Fig. 7.14 show that a 3-dB bandwidth of $80\,\mathrm{GHz}$, between $235\,\mathrm{GHz}$ and $315\,\mathrm{GHz}$ is reached. An average gain of $26\,\mathrm{dB}$ over the 3-dB bandwidth and a maximum of $27.5\,\mathrm{dB}$ at $305\,\mathrm{GHz}$ is achieved. The input and output matching are below $-2\,\mathrm{dB}$ over the whole frequency of interest. The simulated noise figure (NF) is lower than $7\,\mathrm{dB}$ in the frequency band of interest. Comparing the noise figure curve with that of the simulated minimum noise figure ($\mathrm{NF_{min}}$), it can be seen that good noise matching is achieved over a wide range. Due to the lack of available noise sources for on-wafer noise measurements around 300 GHz, the noise figure was not measured. Packaged LNAs built in the same technology in the same frequency range [TLW+17] achieve very good noise performance with an average noise figure of $6.5\,\mathrm{dB}$ around $300\,\mathrm{GHz}$.

7.3 Linearity analysis

Like previously mentioned, linearity is a key parameter for the transmission of complex modulation formats and consequently achieving ultra-high data rates with a $300\,\mathrm{GHz}$ wireless system. To assess this important parameter of the designed transceiver a gain and linearity analysis is conducted using the simulation of the integrated chips. For this simulation all components presented in the previous sections are integrated: the multiplier by three, the buffer amplifier, the mixer and the power amplifier for the transmitter and the low-noise amplifier for the receiver. The LO input power has to be high enough in order for both the transmitter and the receiver to be in linear operation. The frequencies of interest are: an IF frequency of $70\,\mathrm{GHz}$ and an LO frequency of $73.5\,\mathrm{GHz}$.

Fig. 7.15 shows the results of the linearity analysis for the transmitter. The LO frequency is $75\,\mathrm{GHz}$, the LO power is $-2\,\mathrm{dBm}$ and the chosen simulating IF frequency is $70\,\mathrm{GHz}$. The 1-dB compression point occurs at an IF input power of $1\,\mathrm{dBm}$. This value is in good accordance with the measurements of the stand-alone mixer pictured in Fig. 7.4. An output power of $4\,\mathrm{dBm}$ is achieved in the 1-dB compression point. This value confirms the optimal design of the power amplifier presented in the previous section. Operation in this compression point would mean that only less complex modulation formats can be transmitted. If we consider a $6\,\mathrm{dB}$ back-off for this point, which is a common number to be considered for transmitting modulation formats like 16-QAM, an output power of around $-1\,\mathrm{dBm}$ can be reached. For higher order modulations, 32-QAM and 64-QAM, an even higher back-off value has to be taken into account, up to 10 dB. In this case an output power of around $-5\,\mathrm{dBm}$ can be provided to the next amplifier module or antenna.

Fig. 7.16 shows the results of the gain and linearity partitioning for the $300\,\mathrm{GHz}$ receiver. The output signal is simulated at the IF port, $\mathrm{P_{IF@RXoutput}}$ and plotted versus the RF input power, $\mathrm{P_{RFin}}$, at the input of the LNA. The 1-dB compression point, $\mathrm{P_{RFin,1dB}}$, is in this case at $-21\,\mathrm{dBm}$. Considering the 10 dB back-off mentioned before, an input power of around $-30\,\mathrm{dBm}$ is reached. For the receiver to operate in linear mode, $\mathrm{P_{RFin}}$ should not be higher than this value. Since typical RF input powers for $300\,\mathrm{GHz}$ wireless links are around $-40\,\mathrm{dBm}$, the designed receiver is considered to be very linear and able of transmitting complex modulation formats, higher than 32-QAM.

7.4 Transmitter and receiver MMIC performance

Fig. 7.5 shows the chip photographs of the integrated transmitter and receiver, both with a chip size of 0.75 x $3.5\,\mathrm{mm}$. The individual stages integrated in the MMIC and presented in the previous sections are also graphically marked in the photograph. The DC power consumption of the transmitter is $357\,\mathrm{mW}$, while the receiver consumes only $281\,\mathrm{mW}$. The difference is due to the lower power consumption of the LNA in comparison to the power amplifier. The overall functionality of the MMICs is verified by on-wafer measurements conducted at Fraunhofer IAF under the guidance of their research staff. The $300\,\mathrm{GHz}$ RF input signal of the receiver is synthesized using IAFs in-house built frequency multiplier and amplifier modules. The LO signal around $70\,\mathrm{GHz}$ is generated using a commercially available frequency synthesizer with an extension module and an IAF in-house built amplifier module. The same LO source is used for both transmitter and receiver. For the receiver the IF output signal at

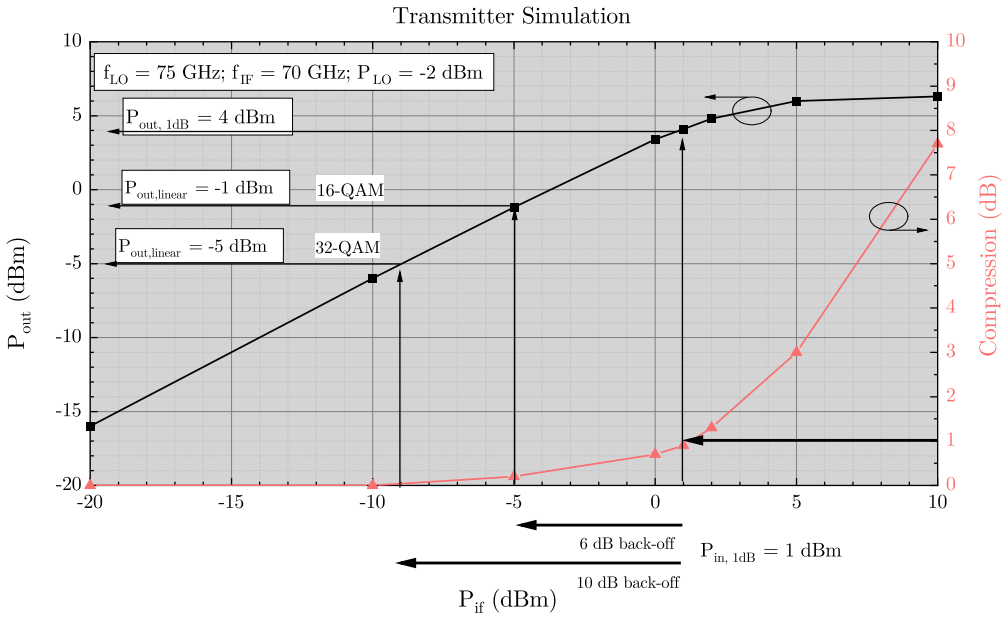

Figure 7.15: Simulation of output power versus input power for the integrated transmitter at an LO frequency of $75\,\mathrm{GHz}$, an IF frequency of $70\,\mathrm{GHz}$ and an LO input power of $-2\,\mathrm{dBm}$.

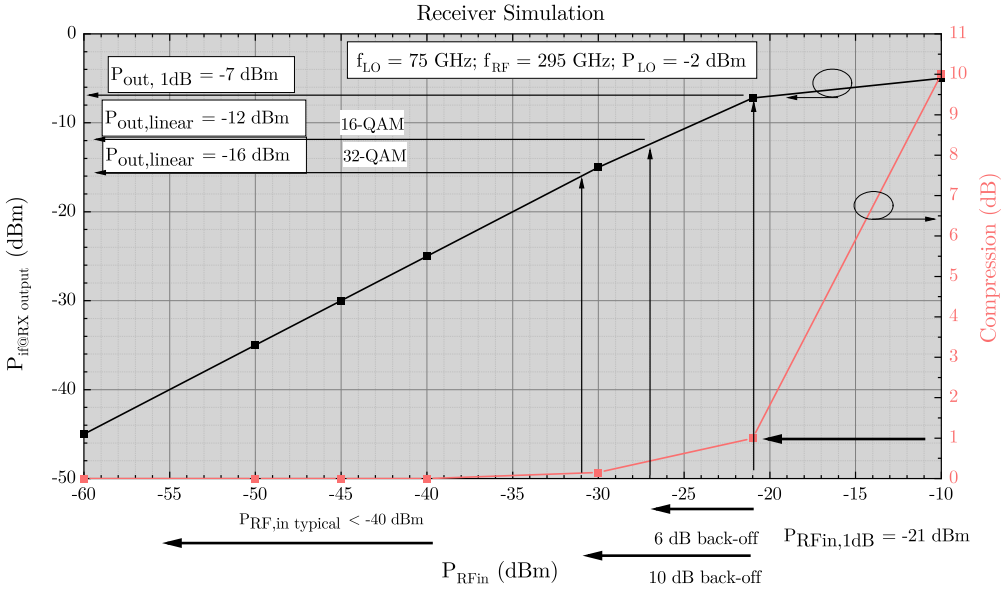

Figure 7.16: Simulation of the integrated receiver regarding linearity. For input powers below $-30\,\mathrm{dBm}$ the receiver operates in linear region and is able to transmit very complex modulation formats, higher than 32QAM.

W-band frequencies is measured using a commercially available spectrum analyzer. Due to the lower cut-off frequency of the W-band waveguide, this measurement setup is limited to IF frequencies above $65\,\mathrm{GHz}$. For the on-wafer measurement of the $300\,\mathrm{GHz}$ transmitter MMIC, the IF signal is generated using a commercially available frequency synthesizer with extension module. In this case, the IF frequency band is limited to frequencies above $70\,\mathrm{GHz}$. The $300\,\mathrm{GHz}$ output power of the transmitter MMIC is measured using a commercially available

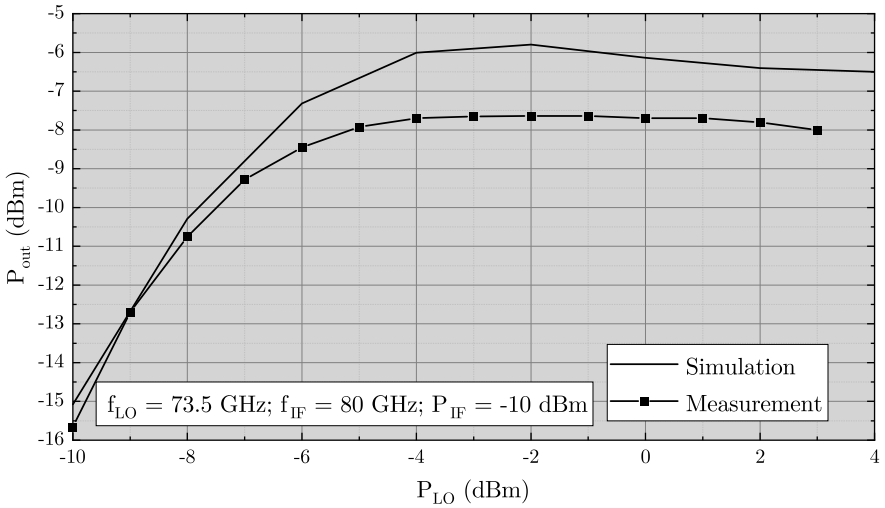

Figure 7.17: Measurement results of the transmitted output power and comparison to simulation under the variation of the LO power.

power meter. All measurements are calibrated on waveguide level and the known probe losses are deembedded.

Fig. 7.17 shows the measured output power of the transmitter, $\mathrm{P_{out}}$, versus LO input power and the comparison to the simulation. This measurement helps determine the optimal LO input power. The LO frequency is set to $73.5\,\mathrm{GHz}$, the IF frequency to $60\,\mathrm{GHz}$ and the IF power to $-10\,\mathrm{dBm}$. The value of the IF power ensures a linear operation of the transmitter. For low values of the LO power a good accordance between measurement and simulation can be observed. In saturation region, the difference increases, reaching $2\,\mathrm{dB}$ for LO input powers above $-4\,\mathrm{dBm}$. Another important observation is, that in reality the transmitter saturates earlier than in simulation. Only $-5\,\mathrm{dBm}$ are enough to saturate the transmitter.

Fig. 7.18 shows the measured output power of the transmitter, $\mathrm{P_{out}}$, versus IF input power, $\mathrm{P_{IF}}$, and the comparison to the simulation. This measurement is conducted for an LO frequency of $73.5\,\mathrm{GHz}$, an LO input power of $-2\,\mathrm{dBm}$ and an IF frequency of $75\,\mathrm{GHz}$. The $\mathrm{P_{1dB,in}}$ is measured to be at -5 dBm, while the simulated output-referred compression point lies at $2\,\mathrm{dBm}$. Hence, a difference of $5\,\mathrm{dB}$ can be observed between measurement and simulation. The difference between the simulation in Fig. 7.15 and the one in Fig. 7.18 has its roots in the slightly different LO and IF frequencies used. If we consider a 10 dB back-off from the 1-dB compression point, which would allow the transmission of complex modulation formats like 32-QAM, a distance of around 80 meters could be covered. For this link budget calculation an antenna system consisting of a transmitter and a receiver antenna with a total gain of around $90\,\mathrm{dBi}$ and only this transmitter is considered. To increase the distance even further and to achieve the goal pictured in Fig. 6.2, the usage of other power amplifier modules like the one presented in [JTL+20] is necessary.

Fig. 7.19 shows the measured output power of the transmitter, $\mathrm{P_{out}}$, versus IF frequency, $\mathrm{f_{IF}}$, and the comparison with the simulation. This measurement is conducted for an LO frequency of $73.5\,\mathrm{GHz}$, an LO input power of $-2\,\mathrm{dBm}$ and for four different IF input powers: -15, -10, -5 and $0\,\mathrm{dBm}$. The IF frequency is limited by the setup to $75\,\mathrm{GHz}$. Very good accordance between measurement and simulation can be observed for low input powers, below $-10\,\mathrm{dBm}$. For higher input powers the difference between measurement and simulation

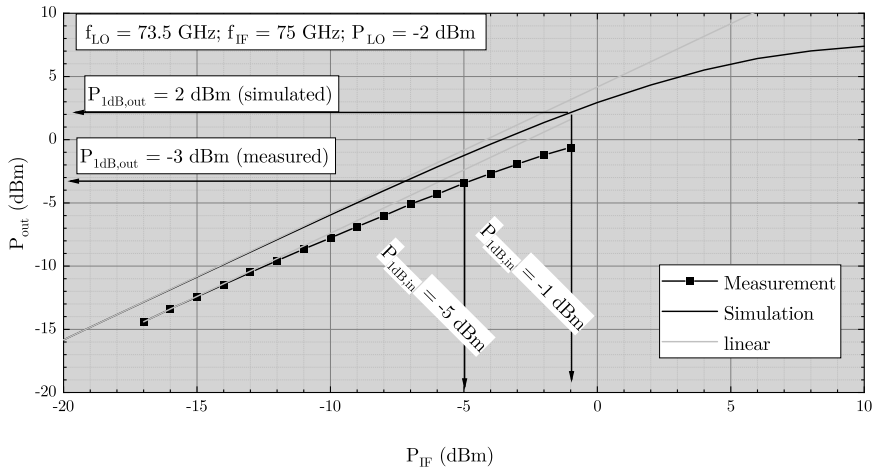

Figure 7.18: Measurement results of the transmitted output power and comparison to simulation under the variation of the IF input power.

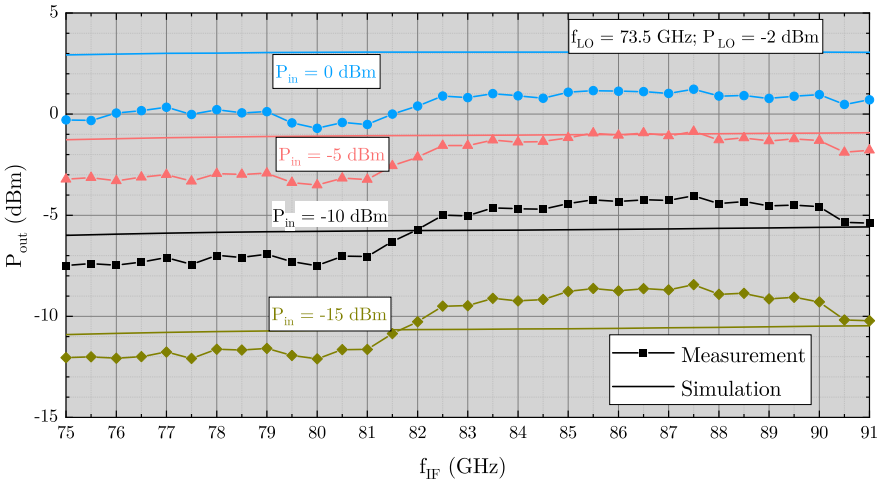

Figure 7.19: Measurement results of the transmitted output power and comparison to simulation under the variation of the IF frequency. The measurement is repeated for four different IF input powers.

increases up to around $4\,\mathrm{dB}$ for an IF input of $0\,\mathrm{dBm}$. Overall, it can be concluded that the transmitter is very broadband with over $25\,\mathrm{GHz}$ of IF bandwidth. The exact bandwidth cannot be determined since it lies outside the measurement area.

A further conducted measurement is the measurement of the output power under the variation of the LO frequency and is repeated for three different IF frequencies: 75, 80 and $85\,\mathrm{GHz}$. The LO and the IF powers are kept constant at $-2\,\mathrm{dBm}$ and $-10\,\mathrm{dBm}$ respectively. Fig. 7.20 shows the results of this measurement and the comparison to simulation. A good accordance between measurement and simulation, with a deviation below $2\,\mathrm{dB}$, occurs for LO frequencies above $73\,\mathrm{GHz}$. Hence, the optimal LO frequency range lies between 73 and $76\,\mathrm{GHz}$. This translates to a frequency range between 219 and $228\,\mathrm{GHz}$ after the frequency multiplier by three.

For the integrated receiver similar measurements were conducted. Firstly, the measurement of the conversion gain under the variation of the LO input power. Fig. 7.21 shows the results of this measurement and the comparison to simulation for an LO frequency of $73.5\,\mathrm{GHz}$,

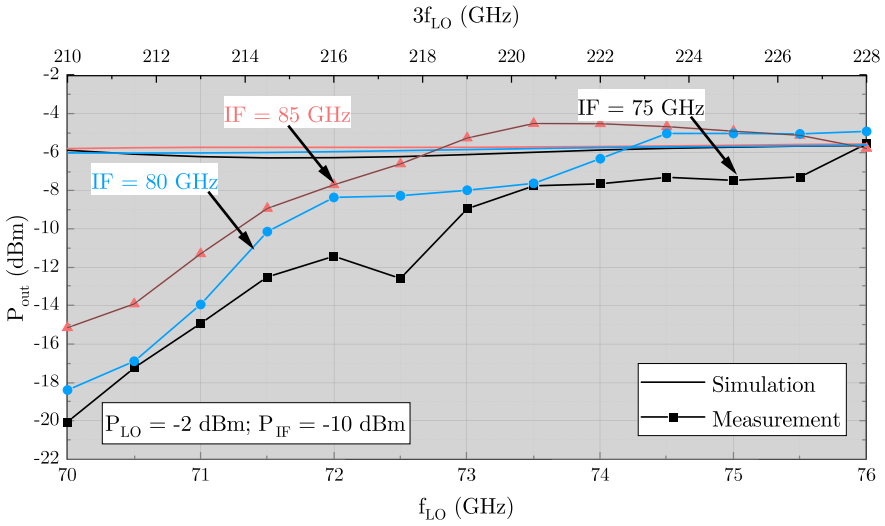

Figure 7.20: Measurement results of the transmitted output power and comparison to simulation under the variation of the LO frequency. The measurement is repeated for four different IF frequencies.

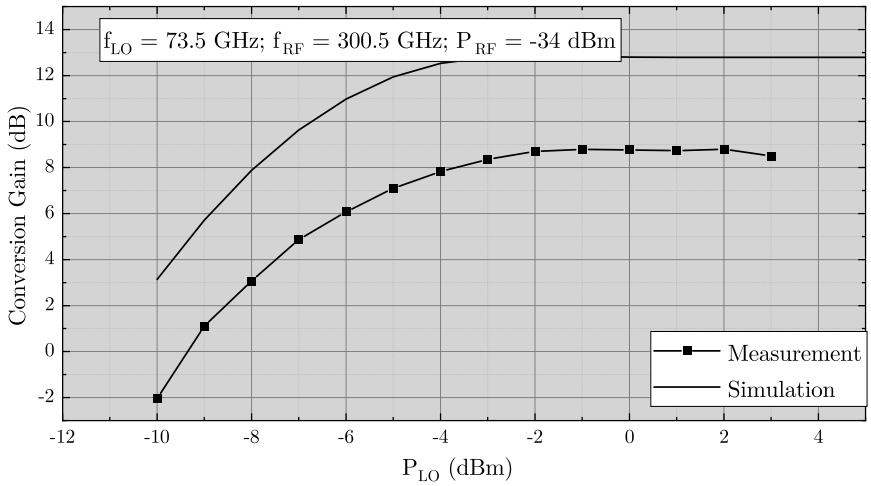

Figure 7.21: Measurement results of the conversion gain of the designed receiver and comparison to the simulation. The measurement is repeated for four different IF frequencies.

an RF frequency of $300.5\,\mathrm{GHz}$ and an input RF power of $-34\,\mathrm{dBm}$. The receiver starts to saturate at around $-2\,\mathrm{dBm}$ input power and has a saturated conversion gain of around $8\,\mathrm{dB}$ for this combination of LO and RF frequency. A constant $4\,\mathrm{dB}$ difference between measurement and simulation can be observed for the whole power range.

The bandwidth of the receiver is dependent on the used LO frequency, as can be seen in Fig. 7.22. For an LO of $72\,\mathrm{GHz}$ the 3-dB RF bandwidth lies between 288 and $303\,\mathrm{GHz}$. For an LO of around $73.5\,\mathrm{GHz}$ the the maximum conversion gain is around $11\,\mathrm{dB}$ and the 3-dB RF bandwidth is between 293 and $315\,\mathrm{GHz}$. The last measured LO frequency lies at $75.5\,\mathrm{GHz}$. The possible measurement range for this LO frequency starts at only $291.5\,\mathrm{GHz}$, limited by the measurement setup of the IF port. The 3-dB RF bandwidth corresponds in this case to almost the whole measurement range, starting at $295\,\mathrm{GHz}$. Compared to simulations, there is a good agreement, with deviations below $2\,\mathrm{dB}$, for the LO frequencies of $73.5\,\mathrm{GHz}$ and $75.5\,\mathrm{GHz}$ in the RF frequency range between 303 and $313\,\mathrm{GHz}$. Below this

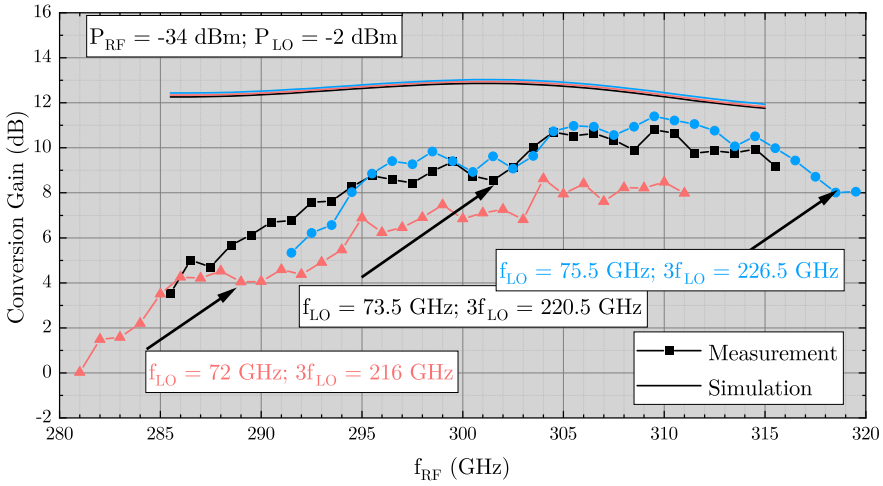

Figure 7.22: Measurement results of the conversion gain of the designed receiver and comparison to simulation under the variation of the RF frequency. The measurement is repeated for three different LO frequencies.

RF frequency band and for the LO frequency of $72\,\mathrm{GHz}$ the deviation is higher, peaking at $8\,\mathrm{dB}$ for $285\,\mathrm{GHz}$.

The linearity of the RX is plotted in Fig. 7.23. The measurement is conducted with a constant LO frequency of $75.5\,\mathrm{GHz}$, at an input power of $-2\,\mathrm{dBm}$ and three different RF frequencies: 301.5, 306.5 and $312.5\,\mathrm{GHz}$. A relatively constant deviation of around 2 to $4\,\mathrm{dB}$ can be observed between measurement and simulation. A maximum conversion gain of around $13\,\mathrm{dB}$ was simulated, while the measured conversion gain only reaches a maximum of around $9\,\mathrm{dB}$ for an RF of $301.5\,\mathrm{GHz}$ and $11\,\mathrm{dB}$ for the other two RF frequencies. The measured 1-dB compression point is 3-dB lower than the simulated one, at $-26\,\mathrm{dBm}$ RF input power.

An important measurement, which cannot be conducted on-wafer due to the lack of available sources is the measurement of the noise figure of the receiver. Considering the simulated noise figure of the LNA, the overall noise figure of the receiver can be calculated using Friis' formula and lies at $7.2\,\mathrm{dB}$. After the integration into a waveguide module, the noise figure can further degrade.

7.5 Comparison to state of the art

Table 5.1 shows the comparison to the state-of-the-art transmitter and receiver chipsets in the $300\,\mathrm{GHz}$ frequency region. For this comparison all solid-state technologies that allow operation at this frequency and the best performing chipset of the technology have been considered. A very promising technology for THz communication is the 40 nm Si-based CMOS process. [LDY+19] reports on a transceiver based on this technology which operates in the frequency range between 260 and $270\,\mathrm{GHz}$, with a good linearity and a measured noise figure of $22.9\,\mathrm{dB}$. Better noise figures offer the Si-based technologies $0.13\,\mu\mathrm{m}$ SiGe HBT and $130\,\mathrm{nm}$ SiGe BiCMOS. Transceiver and receiver chipsets operating at a center RF frequency of around $240\,\mathrm{GHz}$ using this technologies are reported in [RGHP19a] and [EMW+18]. Up to date, however, the best performance in terms of bandwidth, gain and output power of

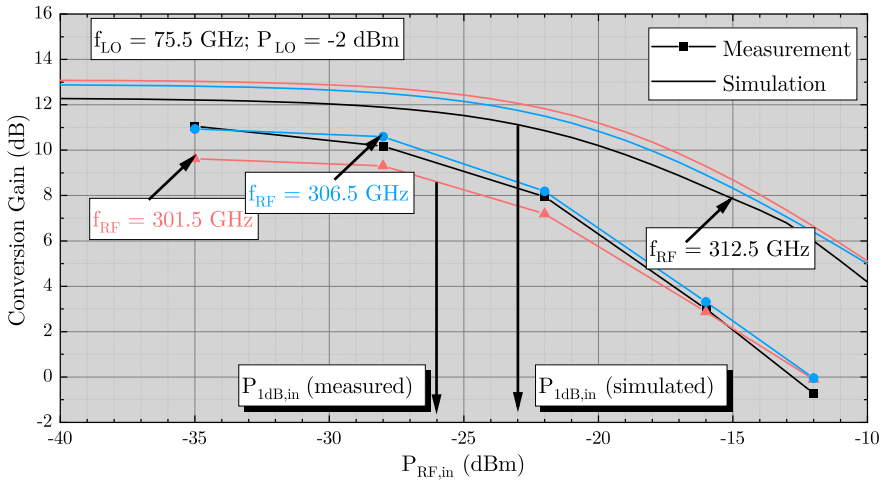

Figure 7.23: Measurement results of the conversion gain of the designed receiver and comparison to simulation under the variation of the RF input power. The measurement is repeated for three different LO frequencies.

$300\,\mathrm{GHz}$ stand-alone amplifier as well as receive and transmit circuits is enabled and has been demonstrated by III-V HEMT and HBT technologies. For the development of high-dynamic-range transmit and receive solutions at the lower THz band, the InGaAs-channel HEMT has proven to be the most suitable semiconductor device technology when requiring high gain and lowest noise figures. This is demonstrated with the $80\,\mathrm{nm}$ InP HEMT technology used in [UGS+17] as well as the underlying $35\,\mathrm{nm}$ InGaAs mHEMT technology of the chipset presented in this chapter.

The first important statement deduced from the comparison in Table 7.1 is that the MMIC chipset presented in this chapter is the only one operating with an IF input frequency above $75\,\mathrm{GHz}$, supporting a superheterodyne transmission. All the other transceivers have a zero-IF architecture, which means that the baseband signal is directly up-converted in the RF. This has been, up to now, the architecture of choice in THz communication due to a reduced complexity and component count. The superheterodyne architecture has the advantage of being easy to integrate into a network, by combing the RF system presented in this work with wireless links developed in the frame of 5G, based on the IEEE 802.15.3e-2017 [IEE17] standard.

This works exceeds the state of the art not only by architecture choice, but also by the lowest power consumption, a topic that gains more and more importance in the discussion about future networks. Although low-noise measurements cannot be conducted due to the lack of available sources, the receiver is expected to have a very low noise figure, similar to other $300\,\mathrm{GHz}$ receivers fabricated with the $35\,\mathrm{nm}$ InGaAs mHEMT technology [TLW+17]. In terms of linearity, especially important for the transmitter, measured by the output-referred 1-dB compression point, the presented transmitter MMIC is close to the state of the art. Better is only the transmitter fabricated in the same technology [KHD+15]. Furthermore, the presented MMIC chipset operates at the highest reported RF range, the 3-dB bandwidth has the upper limit above $320\,\mathrm{GHz}$.

7.6 Conclusion

This chapter presents a transmit and receive chipset fabricated in a $35\,\mathrm{nm}$ InGaAs mHEMT technology. The MMICs integrate a frequency multiplier by three, a buffer amplifier, a frequency converter and a final RF power amplifier or a first RF low-noise amplifier. The LO input frequency lies between 72 and $75.5\,\mathrm{GHz}$, the 3-dB bandwidth of the IF frequency is measured to exceed the range between 75 to $95\,\mathrm{GHz}$ and the RF frequency centers around $300\,\mathrm{GHz}$, depending on the combination of LO and IF frequency.

Based on the proposed chipset a solution for integration of the $300\,\mathrm{GHz}$ system in a future front- and back-haul network is proposed and analyzed. The superheterodyne transmission scheme allows the combination of wireless links developed in the frame of 5G, operating at frequencies above $60\,\mathrm{GHz}$, with the RF system composed of the presented transmitter and receiver. The proposed solution makes the integration of THz communication into a live application possible.

The choice of architecture for the frequency up-and down-converters is discussed in detail. The advantages of a fundamental mixer over a subharmonic one are confirmed by measurements: an $8\,\mathrm{dB}$ better conversion gain and a $10\,\mathrm{dB}$ higher 1-dB output-referred compression point. The choice of architecture for the multiplier is also presented. Furthermore, the design, the implementation and the measurements of all the MMIC components are presented in detail. The power amplifier, the last stage of the transmitter, and the low-noise amplifier, integrated in the receiver are designed according to the gain and linearity analysis conducted for the whole transmitter and receiver. This ensures that the MMICs are suited for usage in an ultra-fast communication system, where the transmission of complex modulated signals is a key requirement.

Finally, the on-wafer measurements of the integrated transmitter and receiver MMICs are presented. The chipset shows state-of-the-art high frequency performance in terms of bandwidth and linearity, and is therefore a promising candidate for future wireless high data rate communication systems in the lower THz band around $300\,\mathrm{GHz}$.

Table 7.1: Comparison of state-of-the-art transmitter and receiver chipsets with an operation frequency around $300\,\mathrm{GHz}$.

Reference	Technology	RF Frequency Range in GHz ($3\,\mathrm{dB}$ limits)	BB / IF Frequency Range in GHz	TX $\mathrm{OP}_{1\mathrm{dB}}$ in dBm	Receiver Noise Figure in dB	Power Consumption in mW
[LDY+19]	40-nm CMOS	260 - 270	0 to 20[1]	-5[2]	22.9	1790
[RGHP19a]	0.13 m SiGe HBT	216- 244	0 - 14	n.a.	14	1410
[EMW+18]	130 nm SiGe:C BiCMOS	222 - 257	0 - 17.5	-3	13.4	950
[HFA+18]	80 nm InP-HEMT	272 - 302	2 -32	-16	n.a.	n.a.
[KHD+15]	35 nm InGaAs mHEMT	270 - 314	0 to 22	-1	8.6	n.a
This work	35 nm InGaAs mHEMT	288 - 320	75 - 90	-3	7.3[1]	637

[1] according to simulation [2] estimation

8 Conclusion and Outlook

The forecast for the demand for wireless data shows that conventional technologies cannot satisfy the need of high rate transmission. This is valid especially for the data-hungry applications that are continuously evolving and that are still to be established on the market. The benefits these applications can bring to society and to the well-being of humankind sustains the search for technologies that can provide the desired data rates with a low power consumption. This thesis is part of this search, focusing on future wireless communication systems based on devices that operate in the low THz range. The quest to find a wireless system able of transmitting information with data rates above $100\,\mathrm{Gbps}$ is a troublesome one and few research groups in the world have this topic as a main focus. One of the first pioneers in this research area has been the group at the University of Stuttgart, where the work presented in this thesis was carried out.

The goal of this thesis was to examine different architectures for wireless links that operate at $300\,\mathrm{GHz}$. For this purpose two different architectures are considered: the direct-conversion and the superheterodyne approach. While the latter one is very common in radio communications below $5\,\mathrm{GHz}$ it was never employed before in the THz range. The few devices and circuits that have previously been shown operating at high frequencies used the direct-conversion approach mainly due to the huge bandwidth available in the $300\,\mathrm{GHz}$ range. Using a double-sideband transmission helps avoid complexity issues, a significant problem in superheterodyne systems. On the downside, this brings LO leakage and DC component issues. The wireless link presented in chapter 3 uses this topology and represents a perfect starting point for further comparisons to other architectures as well as to the same architecture but with a different technology for the transmitter and further optimization of the receiver. This first wireless link employs all electronic components based on MMICs realized with the III-V compound semiconductor technology described in chapter 1.2.3. A maximum data rate of $64\,\mathrm{Gbps}$ at a transmission distance of $1\,\mathrm{meter}$ and a center frequency of $300\,\mathrm{GHz}$ is reached using this link. The modulation format used for this transmission is QPSK, the transmission of more complex modulation formats was not possible with this setup. Additionally to the data transmission further impairment analysis techniques are developed employing this link: the investigation of the LO leakage and the measurement of the analog transfer function. They will be used for the performance assessment of all the other wireless links presented in this thesis. Although the system in chapter 3 is not outperforming the state of the art at the moment of writing, this work represents an important milestone in the development of THz communication for indoor applications.

Continuing with the analysis of the same architecture, the link in chapter 4 presents a wireless transmission employing a photonic transmitter and an active electronic receiver. The photonic uni-traveling-carrier diode transmitter is a popular choice for the combination of photonic and electronics technologies. This approach uses the advantages of both domains: the low receiver noise and the high functional integration density of the electronic receiver and the high spectral purity and high quality phase and frequency control of photonics-based

transmitter. This theoretical advantages are proven in practice by the transmission experiment using a pair of collimating lenses and mirrors. The transmission distance is increased in comparison to the previous experiment to $15\,\mathrm{meters}$. The data rate reaches $100\,\mathrm{Gbps}$, the transmission bandwidth exceeds $50\,\mathrm{GHz}$ and complex modulation formats up to 64-QAM are successfully transmitted. This represents a significant improvement in comparison to the previous link, showing the potential of on the one hand, the direct-conversion architecure and on the other hand the combination of photonic transmitter and electronic receiver.

Chapter 5 shows the results of an optimized receiver which can improve the performance of the wireless link even further. This receiver shows excellent high frequency performance in terms of bandwidth and conversion gain showing a promising potential for the integration in future transmission systems. Based on this receiver novel packaging methods and possibilities are the focus of further on-going research activities. The current waveguide module packaging is expensive and not a practicable solution for integration in a cost-effective application.

Using the very broadband wireless system presented in chapter 3 the idea of superheterodyne architecture can be investigated. Although the system was designed for zero-IF functionality the superheterodyne proof of concept can be realized using external, commercially available mixers and the built-in options of the used hardware, hence two different IF systems can be analyzed and compared. In both cases the IF signal is centered around $10\,\mathrm{GHz}$. This value is far from the desired one of $70\,\mathrm{GHz}$, but it is the perfect compromise for this feasibility study. Chapter 6 presents all these aspects in detail, validating for the first time the concept of superheterodyne architecture in a communication system operating at $300\,\mathrm{GHz}$. The maximum data rate reached with this setup is $60\,\mathrm{Gbps}$ at transmission distances up to $10\,\mathrm{meters}$. Given the far from ideal operation conditions this data rate represents an important achievement. The successful transmission of complex modulation formats with aggregated channels shows the potential of this link for future ultra-fast communication networks. Furthermore, the influence of phase noise on the quality of the transmission is experimentally examined. Further analyses need to be conducted to find an optimal LO source.

Finally, in chapter 7 a compact fully integrated transmitter and receiver chipset is presented. This chipset provides the technical RF solution for the superheterodyne system discussed in the previous chapter. The analog transmitter and receiver chips realized using the same III-V compound semiconductor technology are compatible with IF systems developed in the frame of 5G, with an IF operation range between 75 to $95\,\mathrm{GHz}$. Furthermore, they are compatible with the new frequency standard IEEE 802.15.3e-2017 for beyond 5G platforms. This chipset exceeds the state of the art not only by being the first superheterodyne chip in the low THz range, but also in terms of low power consumption, low noise figure and linearity.

The packaging of this chipset in waveguide modules and integration into the proposed system is still an on-going work and is not within the scope of this thesis. Nonetheless, the concept and these first measurement results promise to enable the first integration of a THz communication link in a live front- and back-haul network.

The search for the perfect THz communication system architecture does not have a simple finding. The direct-conversion approach has proven to be very effective in reaching the goal of $100\,\mathrm{Gbps}$, especially when different technologies are combined. The superheterodyne approach is a very promising candidate for network integration due to the compatibility to

existing 5G solutions. There is no doubt the two architectures will coexist and help shape the future of wireless communication at terahertz frequencies.

Bibliography

[A14] Lewis R A. A review of terahertz sources. *Journal of Physics D: Applied Physics*, 47(47):374001, aug 2014.

[ABM+14] J. Antes, F. Boes, D. Meier, T. Messinger, U. Lewark, A. Tessmann, S. Wagner, and I. Kallfass. Ultra-wideband single-balanced transmitter-MMIC for 300 GHz communication systems. In *2014 IEEE MTT-S International Microwave Symposium (IMS2014)*, pages 1–3, 2014.

[AK15] J. Antes and I. Kallfass. Performance estimation for broadband multi-gigabit millimeter- and sub-millimeter-wave wireless communication links. *IEEE Transactions on Microwave Theory and Techniques*, 63(10):3288–3299, Oct 2015.

[BAB+15] J. Bock, K. Aufinger, S. Boguth, C. Dahl, H. Knapp, W. Liebl, D. Manger, T. F. Meister, A. Pribil, J. Wursthorn, R. Lachner, B. Heinemann, H. Rucker, A. Fox, R. Barth, G. Fischer, S. Marschmeyer, D. Schmidt, A. Trusch, and C. Wipf. SiGe HBT and BiCMOS process integration optimization within the DOTSEVEN project. In *2015 IEEE Bipolar/BiCMOS Circuits and Technology Meeting - BCTM*. IEEE, oct 2015.

[BHL+14] Federico Boccardi, Robert W. Heath, Angel Lozano, Thomas L. Marzetta, and Petar Popovski. Five disruptive technology directions for 5G. *IEEE Communications Magazine*, 52(2):74–80, feb 2014.

[BMA+14] F. Boes, T. Messinger, J. Antes, D. Meier, A. Tessmann, A. Inam, and I. Kallfass. Ultra-broadband MMIC-based wireless link at 240 GHz enabled by 64GS DAC. In *2014 39th International Conference on Infrared, Millimeter, and Terahertz waves (IRMMW-THz)*, pages 1–2. IEEE, Sept 2014.

[Che04] S. Cherry. Edholm's law of bandwidth. *IEEE Spectrum*, 41(7):58–60, jul 2004.

[CKC+20] Y. Cao, V. Kumar, S. Chen, Y. Cui, S. Yoon, E. Beam, A. Xie, J. Jimenez, A. Ketterson, C. Lee, Douglas Linkhart, and Anton Geiler. Qorvo's emerging GaN technologies for mmWave applications. In *2020 IEEE/MTT-S International Microwave Symposium (IMS)*, pages 570–572. IEEE, 2020.

[CKG+18] J. Chen, D. Kuylenstierna, S. E. Gunnarsson, Z. S. He, T. Eriksson, T. Swahn, and H. Zirath. Influence of White LO Noise on Wideband Communication. *IEEE Transactions on Microwave Theory and Techniques*, 66(7):3349–3359, July 2018.

[CLR+18] Pascal Chevalier, Wolfgang Liebl, Holger Rucker, Alexis Gauthier, Dirk Manger, Bernd Heinemann, Gregory Avenier, and Josef Bock. SiGe BiCMOS current

status and future trends in Europe. In *2018 IEEE BiCMOS and Compound Semiconductor Integrated Circuits and Technology Symposium (BCICTS)*. IEEE, 10 2018.

[CLZ+18] V. K. Chinni, P. Latzel, M. Zegaoui, C. Coinon, X. Wallart, E. Peytavit, J. F. Lampin, K. Engenhardt, P. Szriftgiser, M. Zaknoune, and G. Ducournau. Single-channel 100 Gbps transmission using IIIV UTCPDs for future IEEE 802.15.3d wireless links in the 300 GHz band. *Electronics Letters*, 54(10):638–640, 2018.

[CNE+19] C. Castro, S. Nellen, R. Elschner, I. Sackey, R. Emmerich, T. Merkle, B. Globisch, D. de Felipe, and C. Schubert. 32 GBd 16QAM Wireless Transmission in the 300 GHz Band using a PIN Diode for THz Upconversion. In *2019 Optical Fiber Communications Conference and Exhibition (OFC)*, pages 1–3. OSA, March 2019.

[COM10] F. Chang, K. Onohara, and T. Mizuochi. Forward error correction for 100 G transport networks. *IEEE Communications Magazine*, 48(3):S48–S55, March 2010.

[Cona] World Radiocommunication Conference. Radio regulations, edition of 2016.

[Conb] World Radiocommunication Conference. World radiocommunication conference 2019 (wrc-19) final acts.

[Cos57] J.P. Costas. Synchronous communications. *Communications Systems, IRE Transactions on*, 5:99–105, March 1957.

[Cou] Leon W Couch. *Digital and Analog Communication Systems*. Prentice Hall.

[DDH+20] Iulia Dan, Guillaume Ducournau, Shintaro Hisatake, Pascal Szriftgiser, Ralf-Peter Braun, and Ingmar Kallfass. A terahertz wireless communication link using a superheterodyne approach. *IEEE Transactions on Terahertz Science and Technology*, 10(1):32–43, Jan 2020.

[DENB05] C.H. Doan, S. Emami, A.M. Niknejad, and R.W. Brodersen. Millimeter-wave CMOS design. *IEEE Journal of Solid-State Circuits*, 40(1):144–155, jan 2005.

[DES+04] C.H. Doan, S. Emami, D.A. Sobel, A.M. Niknejad, and R.W. Brodersen. Design considerations for 60 GHz CMOS radios. *IEEE Communications Magazine*, 42(12):132–140, dec 2004.

[Div15] Rohde& Schwarz Broadcasting Divison. Bit Error Ratio BER as a function of SNR. Technical report, Rohde& Schwarz Broadcasting Divison, 2015.

[DSB+14] G. Ducournau, P. Szriftgiser, A. Beck, D. Baquet, F. Pavanello, E. Peytavit, M. Zaknoune, T. Akalin, and J. F. Lampin. Ultrawide-bandwidth single-channel 0.4 THz wireless link combining broadband quasi-optic photomixer and coherent detection. *IEEE Transactions on Terahertz Science and Technology*, 4(3):328–337, May 2014.

[EAS+20] Hadeel Elayan, Osama Amin, Basem Shihada, Raed M. Shubair, and Mohamed-Slim Alouini. Terahertz band: The last piece of RF spectrum puzzle for communication systems. *IEEE Open Journal of the Communications Society*, 1:1–32, 2020.

[EML+20] Mohamed Hussein Eissa, Nebojsa Maletic, Lukas Lopacinski, Andrea Malignaggi, Goran Panic, Rolf Kraemer, Gunter Fischer, and Dietmar Kissinger. Frequency interleaving IF transmitter and receiver for 240-GHz communication in SiGe:c BiCMOS. *IEEE Transactions on Microwave Theory and Techniques*, 68(1):239–251, jan 2020.

[EMW+18] M. H. Eissa, A. Malignaggi, R. Wang, M. Elkhouly, K. Schmalz, A. C. Ulusoy, and D. Kissinger. Wideband 240-GHz transmitter and receiver in BiCMOS technology with 25-Gbit/s data rate. *IEEE Journal of Solid-State Circuits*, 53(9):2532–2542, 2018.

[Eria] Ericsson. Ericsson microwave outlook. Technical report, Ericsson.

[Erib] Ericsson. Ericsson mobility report june 2020. Technical report, Ericsson.

[Eric] Ericsson. Ericsson mobility report november 2019. Technical report, Ericsson.

[ESVBB19] Magda El-Shenawee, Nagma Vohra, Tyler Bowman, and Keith Bailey. Cancer detection in excised breast tumors using THz imaging and spectroscopy. *Biomedical Spectroscopy and Imaging*, 8:1–9, Jul 2019.

[ETS16] ETSI. Etsi en 302 217-2 v3.0.8 (2016-06) Fixed Radio Systems; Characteristics and requirements for point-to-point equipment and antennas; Part 2: Digital systems operating in frequency bands from 1,3 GHz to 86 GHz; Harmonised Standard covering the essential requirements of article 3.2 of Directive 2014/53/EU. Technical report, ETSI, 2016.

[FM10] John Federici and Lothar Moeller. Review of terahertz and subterahertz wireless communications. *Journal of Applied Physics*, 107(11), jun 2010.

[FSCE17] David Fritsche, Paul Starke, Corrado Carta, and Frank Ellinger. A low-power SiGe BiCMOS 190-GHz transceiver chipset with demonstrated data rates up to 50 Gbps using on-chip antennas. *IEEE Transactions on Microwave Theory and Techniques*, 65(9):3312–3323, sep 2017.

[Geo04] A. Georgiadis. Gain, phase imbalance, and phase noise effects on error vector magnitude. *IEEE Transactions on Vehicular Technology*, 53(2):443–449, March 2004.

[GMLK18] Christopher M. Grotsch, Hermann Mabler, Arnulf Leuther, and Ingmar Kallfass. An active multiplier-by-six s-MMIC for 500 GHz. In *2018 43rd International Conference on Infrared, Millimeter, and Terahertz Waves (IRMMW-THz)*, pages 1–2. IEEE, 2018.

[Gu05] Qizeng Gu. *RF system design of transcievers for wireless communications*. Springer, 2005.

[GWL+18] C. M. Groetsch, S. Wagner, A. Leuther, D. Meier, and I. Kallfass. Ultra-broadband frequency multiplier MMICs for communication and radar applications. In *2018 13th European Microwave Integrated Circuits Conference (EuMIC)*, pages 113–116. IEEE, Sep. 2018.

[HAR10] A. S. Hussaini, R. Abd-Alhameed, and J. Rodriguez. Design of energy efficient power amplifier for 4G user terminals. In *2010 17th IEEE International Conference on Electronics, Circuits and Systems*, pages 611–614. IEEE, dec 2010.

[Hau] Simon Haussmann. Master's Thesis. Design of a mixer for a superheterodyne terahertz communication-system. Oct 2018.

[HBB+10] B. Heinemann, R. Barth, D. Bolze, J. Drews, G. G. Fischer, A. Fox, O. Fursenko, T. Grabolla, U. Haak, D. Knoll, R. Kurps, M. Lisker, S. Marschmeyer, H. Rucker, D. Schmidt, J. Schmidt, M. A. Schubert, B. Tillack, C. Wipf, D. Wolansky, and Y. Yamamoto. SiGe HBT technology with ft fmax of 300 GHz and 500 GHz and 2.0 ps CML gate delay. In *2010 International Electron Devices Meeting*. IEEE, dec 2010.

[HFA+18] H. Hamada, T. Fujimura, I. Abdo, K. Okada, H. Song, H. Sugiyama, H. Matsuzaki, and H. Nosaka. 300-GHz 100 Gbps InP-HEMT Wireless Transceiver Using a 300-GHz Fundamental Mixer. In *2018 IEEE/MTT-S International Microwave Symposium - IMS*, pages 1480–1483. IEEE, June 2018.

[HGJP19] Philipp Hillger, Janusz Grzyb, Ritesh Jain, and Ullrich R. Pfeiffer. Terahertz imaging and sensing applications with silicon-based technologies. *IEEE Transactions on Terahertz Science and Technology*, 9(1):1–19, jan 2019.

[HKM+04] A. Hirata, T. Kosugi, N. Meisl, T. Shibata, and T. Nagatsuma. High-directivity photonic emitter using photodiode module integrated with HEMT amplifier for 10-Gbit/s wireless link. *IEEE Transactions on Microwave Theory and Techniques*, 52(8):1843–1850, aug 2004.

[HKT+06] A. Hirata, T. Kosugi, H. Takahashi, R. Yamaguchi, F. Nakajima, T. Furuta, H. Ito, H. Sugahara, Y. Sato, and T. Nagatsuma. 120-GHz-band millimeter-wave photonic wireless link for 10-Gb/s data transmission. *IEEE Transactions on Microwave Theory and Techniques*, 54(5):1937–1944, may 2006.

[HKT+10] A. Hirata, T. Kosugi, H. Takahashi, J. Takeuchi, K. Murata, N. Kukutsu, Y. Kado, S. Okabe, T. Ikeda, F. Suginosita, K. Shogen, H. Nishikawa, A. Irino, T. Nakayama, and N. Sudo. 5.8-km 10-Gbps data transmission over a 120-GHz-band wireless link. In *2010 IEEE International Conference on Wireless Information Technology and Systems*. IEEE, aug 2010.

[HNT+19] H. Hamada, H. Nosaka, T. Tsutsumi, H. Sugiyama, H. Matsuzaki, H.-J. Song, G. Itami, T. Fujimura, I. Abdo, and K. Okada. Millimeter-wave InP device

technologies for ultra-high speed wireless communications toward beyond 5g. In *2019 IEEE International Electron Devices Meeting (IEDM)*. IEEE, dec 2019.

[Hou00] P.A. Houston. High-frequency heterojunction bipolar transistor device design and technology. *Electronics & Communication Engineering Journal*, 12(5):220–228, oct 2000.

[HRB+16] B. Heinemann, H. Rucker, R. Barth, F. Barwolf, J. Drews, G. G. Fischer, A. Fox, O. Fursenko, T. Grabolla, F. Herzel, J. Katzer, J. Korn, A. Kruger, P. Kulse, T. Lenke, M. Lisker, S. Marschmeyer, A. Scheit, D. Schmidt, J. Schmidt, M. A. Schubert, A. Trusch, C. Wipf, and D. Wolansky. SiGe HBT with fx/fmax of 505 GHz/720 GHz. dec 2016.

[HTI+19] Hiroshi Hamada, Takuya Tsutsumi, Go Itami, Hiroki Sugiyama, Hideaki Matsuzaki, Kenichi Okada, and Hideyuki Nosaka. 300-GHz 120-gb/s wireless transceiver with high-output-power and high-gain power amplifier based on 80-nm InP-HEMT technology. In *2019 IEEE BiCMOS and Compound semiconductor Integrated Circuits and Technology Symposium (BCICTS)*. IEEE, nov 2019.

[HTK+18] S. Hara, K. Takano, K. Katayama, R. Dong, S. Lee, I. Watanabe, N. Sekine, A. Kasamatsu, T. Yoshida, S. Amakawa, and M. Fujishima. 300-GHz CMOS Transceiver for Terahertz Wireless Communication. In *2018 Asia-Pacific Microwave Conference (APMC)*, pages 429–431. IEEE, Nov 2018.

[HTM+20] Hiroshi Hamada, Takuya Tsutsumi, Hideaki Matsuzaki, Takuya Fujimura, Ibrahim Abdo, Atsushi Shirane, Kenichi Okada, Go Itami, Ho-Jin Song, Hiroki Sugiyama, and Hideyuki Nosaka. 300-GHz-band 120-gb/s wireless front-end based on InP-HEMT PAs and mixers. *IEEE Journal of Solid-State Circuits*, pages 1–1, 2020.

[HYK+09] A. Hirata, R. Yamaguchi, T. Kosugi, H. Takahashi, K. Murata, T. Nagatsuma, N. Kukutsu, Y. Kado, N. Iai, S. Okabe, S. Kimura, H. Ikegawa, H. Nishikawa, T. Nakayama, and T. Inada. 10-Gbit/s wireless link using InP HEMT MMICs for generating 120-GHz-band millimeter-wave signal. *IEEE Transactions on Microwave Theory and Techniques*, 57(5):1102–1109, may 2009.

[IEE17] IEEE. IEEE standard for high data rate wireless multi-media networks amendment 2: 100 Gbps wireless switched point-to-point physical layer. Technical report, IEEE, 2017.

[II20] Tadao Ishibashi and Hiroshi Ito. Uni-traveling-carrier photodiodes. *Journal of Applied Physics*, 127(3):031101, jan 2020.

[IKO+15] Yu Ikeda, Seiichirou Kitagawa, Kengo Okada, Safumi Suzuki, and Masahiro Asada. Direct intensity modulation of resonant-tunneling-diode terahertz oscillator up to ∼30 GHz. *IEICE Electronics Express*, 12(3), 2015.

[Ino21] Akira Inoue. Millimeter-wave GaN devices for 5G: Massive MIMO antenna arrays for sub-6-GHz and mm-Wave bandwidth. *IEEE Microwave Magazine*, 22(5):100–110, 2021.

[ISO+08] T. Idehara, T. Saito, I. Ogawa, S. Mitsudo, Y. Tatematsu, La Agusu, H. Mori, and S. Kobayashi. Development of terahertz FU CW gyrotron series for DNP. *Applied Magnetic Resonance*, 34(34):265–275, aug 2008.

[ITU] ITU. Sharing between the radio astronomy service and active services in the frequency range 275-3000 GHz. Technical report, International Telecommunication Union (ITU) https://standards.globalspec.com/std/1404550/ITU-R REPORT RA.2189.

[JPO+18] S. Jia, X. Pang, O. Ozolins, X. Yu, H. Hu, J. Yu, P. Guan, F. Da Ros, S. Popov, G. Jacobsen, M. Galili, T. Morioka, D. Zibar, and L. K. OxenlÃ¸we. 0.4 THz Photonic-Wireless Link with 106 Gbps Single Channel Bitrate. *Journal of Lightwave Technology*, 36(2):610–616, Jan 2018.

[JTL+20] L. John, A. Tessmann, A. Leuther, P. Neininger, T. Merkle, and T. Zwick. Broadband 300-GHz Power Amplifier MMICs in InGaAs mHEMT technology. *IEEE Transactions on Terahertz Science and Technology*, 10(3):1–1, may 2020.

[KA16a] N. Khalid and O. B. Akan. Experimental throughput analysis of low-thz MIMO communication channel in 5G wireless networks. *IEEE Wireless Communications Letters*, 5(6):616–619, 2016.

[KA16b] N. Khalid and O. B. Akan. Wideband THz communication channel measurements for 5G indoor wireless networks. In *2016 IEEE International Conference on Communications (ICC)*, pages 1–6, 2016.

[KBA] A. Kral, F. Behbahani, and A.A. Abidi. RF-CMOS oscillators with switched tuning. In *Proceedings of the IEEE 1998 Custom Integrated Circuits Conference (Cat. No.98CH36143)*. IEEE, April 1998.

[KBM+15] Ingmar Kallfass, Florian Boes, Tobias Messinger, Jochen Antes, Anns Inam, Ulrich Lewark, Axel Tessmann, and Ralf Henneberger. 64 Gbps transmission over 850 m fixed wireless link at 240 GHz carrier frequency. *Journal of Infrared, Millimeter, and Terahertz Waves*, 36(2):221–233, jan 2015.

[KDR+15] I. Kallfass, I. Dan, S. Rey, P. Harati, J. Antes, A. Tessmann, S. Wagner, M. Kuri, R. Weber, H. Massler, A. Leuther, T. Merkle, and T. Kuerner. Towards MMIC-based 300 GHz Indoor Wireless Communication Systems. *IEICE Transactions on Electronics*, E98-C(12):1081–1090, Dec 2015.

[Keya] Keysight. High-performance digital products catalog Feb 2021 https://www.keysight.com/de/de/assets/7120-1099/catalogs/high-performance-digital-products-catalog.pdf.

[Keyb] Keysight. Online help pathwave vector signal analysis Feb 2021 http://rfmw.em.keysight.com/wireless/helpfiles/89600b/webhelp/89600.htm.

[KHD+15] I. Kallfass, P. Harati, I. Dan, J. Antes, F. Boes, S. Rey, T. Merkle, S. Wagner, H. Massler, A. Tessmann, and A. Leuther. MMIC chipset for 300 GHz indoor wireless communication. In *2015 IEEE International Conference on Microwaves, Communications, Antennas and Electronic Systems (COMCAS)*, pages 1–4, Nov 2015.

[KJK+15] J. Kim, S. Jeon, M. Kim, M. Urteaga, and J. Jeong. H-band power amplifier integrated circuits using 250-nm InP HBT technology. *IEEE Transactions on Terahertz Science and Technology*, 5(2):215–222, March 2015.

[KLDA+13] S. Koenig, D. Lopez-Diaz, J. Antes, F. Boes, R. Henneberger, A. Leuther, A. Tessmann, R. Schmogrow, D. Hillerkuss, R. Palmer, T. Zwick, C. Koos, W. Freude, O. Ambacher, J. Leuthold, and I. Kallfass. Wireless sub-THz communication system with high data rate. *Nature Photonics*, 7(12):977–981, oct 2013.

[KON11] Thomas Kleine-Ostmann and Tadao Nagatsuma. A review on terahertz communications research. *Journal of Infrared, Millimeter, and Terahertz Waves*, 32(2):143–171, jan 2011.

[Kra17] Rolf Kraemer. Challenges and ideas to achieve wireless 100 Gb/s transmission: A short overview of work in progress of the german research foundation (DFG) special priority program (SPP). In *IEEE EUROCON 2017 -17th International Conference on Smart Technologies*. IEEE, jul 2017.

[KZ16] S. Kim and A. Zajic. Characterization of 300-ghz wireless channel on a computer motherboard. *IEEE Transactions on Antennas and Propagation*, 64(12):5411–5423, 2016.

[LDY+19] S. Lee, R. Dong, T. Yoshida, S. Amakawa, S. Hara, A. Kasamatsu, J. Sato, and M. Fujishima. An 80 Gb/s 300 GHz-Band Single-Chip CMOS Transceiver. In *2019 IEEE International Solid- State Circuits Conference - (ISSCC)*, pages 170–172. IEEE, Feb 2019.

[LHY+19a] Sangyeop Lee, Shinsuke Hara, Takeshi Yoshida, Shuhei Amakawa, Ruibing Dong, Akifumi Kasamatsu, Junji Sato, and Minoru Fujishima. An 80-gb/s 300-GHz-band single-chip CMOS transceiver. *IEEE Journal of Solid-State Circuits*, 54(12):3577–3588, dec 2019.

[LHY+19b] Sangyeop Lee, Shinsuke Hara, Takeshi Yoshida, Shuhei Amakawa, Ruibing Dong, Akifumi Kasamatsu, Junji Sato, and Minoru Fujishima. An 80-gb/s 300-GHz-band single-chip CMOS transceiver. *IEEE Journal of Solid-State Circuits*, 54(12):3577–3588, dec 2019.

[LJW+15] U. J. Lewark, L. John, S. Wagner, A. Tessmann, A. Leuther, T. Zwick, and I. Kallfass. Ultra-broadband w-band frequency multiplier-by-twelve MMIC. In *2015 10th European Microwave Integrated Circuits Conference (EuMIC)*, pages 5–8. IEEE, 2015.

[LLW17] Guozhen Liang, Tao Liu, and Qi Jie Wang. Recent developments of terahertz quantum cascade lasers. *IEEE Journal of Selected Topics in Quantum Electronics*, 23(4):1–18, jul 2017.

[LMD+07] R. Lai, X. B. Mei, W. R. Deal, W. Yoshida, Y. M. Kim, P. H. Liu, J. Lee, J. Uyeda, V. Radisic, M. Lange, T. Gaier, L. Samoska, and A. Fung. Sub 50 nm InP HEMT device with fmax greater than 1 THz. In *2007 IEEE International Electron Devices Meeting*. IEEE, 2007.

[LPB+17] P. Latzel, F. Pavanello, M. Billet, S. Bretin, A. Beck, M. Vanwolleghem, C. Coinon, X. Wallart, E. Peytavit, G. Ducournau, M. Zaknoune, and J. Lampin. Generation of mw level in the 300-GHz band using resonant-cavity-enhanced unitraveling carrier photodiodes. *IEEE Transactions on Terahertz Science and Technology*, 7(6):800–807, Nov 2017.

[LTD+13] Arnulf Leuther, Axel Tessmann, Michael Dammann, Hermann Massler, Michael Schlechtweg, and Oliver Ambacher. 35 nm mHEMT technology for THz and ultra low noise applications. In *2013 International Conference on Indium Phosphide and Related Materials (IPRM)*. IEEE, may 2013.

[LTM+08] A. Leuther, A. Tessmann, H. Massler, R. Losch, M. Schlechtweg, M. Mikulla, and O. Ambacher. 35 nm metamorphic HEMT MMIC technology. In *Indium Phosphide and Related Materials, 2008. IPRM 2008. 20th International Conference on*, pages 1–4. IEEE, May 2008.

[LTW+12] U. J. Lewark, A. Tessmann, S. Wagner, A. Leuther, T. Zwick, and I. Kallfass. 255 to 330 GHz active frequency tripler MMIC. In *2012 Workshop on Integrated Nonlinear Microwave and Millimetre-wave Circuits*, pages 1–3. IEEE, sep 2012.

[MBN+95] K. A. McIntosh, E. R. Brown, K. B. Nichols, O. B. McMahon, W. F. DiNatale, and T. M. Lyszczarz. Terahertz photomixing with diode lasers in low-temperature-grown GaAs. *Applied Physics Letters*, 67(26):3844–3846, dec 1995.

[MHAA15] Siavash Moghadami, Fleura Hajilou, Priyanka Agrawal, and Shahab Ardalan. A 210 GHz fully-integrated OOK transceiver for short-range wireless chip-to-chip communication in 40 nm CMOS technology. *IEEE Transactions on Terahertz Science and Technology*, 5(5):737–741, sep 2015.

[Min] Minicircuits. Datasheet https://ww2.minicircuits.com/pdfs/zx05-24mh+.pdf.

[MO98] S. L. Miller and R. J. O'Dea. Peak power and bandwidth efficient linear modulation. *IEEE Transactions on Communications*, 46(12):1639–1648, Dec 1998.

[Mol10] Andreas F. Molisch Molisch. *Wireless Communications 2e*. John Wiley & Sons, 2010.

[MP05] M. Marcus and B. Pattan. Millimeter wave propagation: Spectrum management implications. *IEEE Microwave Magazine*, 6(2):54–62, jun 2005.

[NC15] Tadao Nagatsuma and Guillermo Carpintero. Recent Progress and Future Prospect of Photonics-Enabled Terahertz Communications Research. *IEICE Transactions on Electronics*, E98.C(12):1060–1070, 2015.

[NDR16] Tadao Nagatsuma, Guillaume Ducournau, and Cyril C. Renaud. Advances in terahertz communications accelerated by photonics. *Nature Photonics*, 10(6):371–379, may 2016.

[NHR+] T. Nagatsuma, A. Hirata, Y. Royter, M. Shinagawa, T. Furuta, T. Ishibashi, and H. Ito. A 120-GHz integrated photonic transmitter. In *International Topical Meeting on Microwave Photonics MWP 2000 (Cat. No.00EX430)*. IEEE.

[OHSA17] Naoto Oshima, Kazuhide Hashimoto, Safumi Suzuki, and Masahiro Asada. Terahertz wireless data transmission with frequency and polarization division multiplexing using resonant-tunneling-diode oscillators. *IEEE Transactions on Terahertz Science and Technology*, 7(5):593–598, sep 2017.

[P80] IEEE P802.3bm. 40 Gbps and 100 Gbps fiber optic task force official website http://www.ieee802.org/3/bm/.

[PAC+06] I. Post, M. Akbar, G. Curello, S. Gannavaram, W. Hafez, U. Jalan, K. Komeyli, J. Lin, N. Lindert, J. Park, J. Rizk, G. Sacks, C. Tsai, D. Yeh, P. Bai, and C.-H. Jan. A 65nm CMOS SOC technology featuring strained silicon transistors for RF applications. In *2006 International Electron Devices Meeting*. IEEE, 2006.

[PKT+12] Jung-Dong Park, Shinwon Kang, Siva V Thyagarajan, Elad Alon, and Ali M. Niknejad. A 260 GHz fully integrated CMOS transceiver for wireless chip-to-chip communication. In *2012 Symposium on VLSI Circuits (VLSIC)*. IEEE, jun 2012.

[Raz98] Behzad Razavi. *RF Microelectronics*. Prentice-Hall, Inc., USA, 1998.

[RGHP18] P. Rodriguez-Vazquez, J. Grzyb, B. Heinemann, and U. R. Pfeiffer. Performance evaluation of a 32-QAM 1-meter wireless link operating at 240 GHz with a data-rate of 90 Gbps. In *2018 Asia-Pacific Microwave Conference (APMC)*, pages 723–725. IEEE, nov 2018.

[RGHP19] P. Rodriguez-Vazquez, J. Grzyb, B. Heinemann, and U. R. Pfeiffer. A 16-QAM 100-Gbps 1-m Wireless link with an EVM of 17 percent at 230 GHz in an SiGe technology. *IEEE Microwave and Wireless Components Letters*, 29(4):297–299, April 2019.

[RHF12] H. Rucker, B. Heinemann, and A. Fox. Half-terahertz SiGe BiCMOS technology. In *2012 IEEE 12th Topical Meeting on Silicon Monolithic Integrated Circuits in RF Systems*. IEEE, jan 2012.

[RMG11] T. S. Rappaport, J. N. Murdock, and F. Gutierrez. State of the art in 60-GHz integrated circuits and systems for wireless communications. *Proceedings of the IEEE*, 99(8):1390–1436, 2011.

[RVGHP19] Pedro Rodriguez-Vazquez, Janusz Grzyb, Bernd Heineman, and Ullrich R. Pfeiffer. Optimization and performance limits of a 64-QAM wireless communication link at 220-260 GHz in a SiGe HBT technology. In *2019 IEEE Radio and Wireless Symposium (RWS)*. IEEE, jan 2019.

[RVGHP20] Pedro Rodriguez-Vazquez, Janusz Grzyb, Bernd Heinemann, and Ullrich R. Pfeiffer. A QPSK 110-gb/s polarization-diversity MIMO wireless link with a 220-255 GHz tunable LO in a SiGe HBT technology. *IEEE Transactions on Microwave Theory and Techniques*, pages 1–1, 2020.

[RVGS+18] Pedro Rodriguez-Vazquez, Janusz Grzyb, Neelanjan Sarmah, Bernd Heinemann, and Ullrich R. Pfeiffer. Towards 100 Gbps: A fully electronic 90 Gbps one meter wireless link at 230 GHz. In *2018 48th European Microwave Conference (EuMC)*. IEEE, sep 2018.

[SA11] Pavel Shumyatsky and Robert R. Alfano. Terahertz sources. *Journal of Biomedical Optics*, 16(3), 2011.

[Sae13] Daryoosh Saedkia. *Handbook of terahertz technology for imaging, sensing and communications.* Woodhead, jan 2013.

[SAM+12] H.-J. Song, K. Ajito, Y. Muramoto, A. Wakatsuki, T. Nagatsuma, and N. Kukutsu. 24 Gbps data transmission in 300 GHz band for future terahertz communications. *Electronics Letters*, 48(15):953, 2012.

[SBd+16] M. Schroter, J. Boeck, V. d'Alessandro, S. Fregonese, B. Heinemann, C. Jungemann, W. Liang, H. Kamrani, A. Mukherjee, A. Pawlak, U. Pfeiffer, N. Rinaldi, N. Sarmah, T. Zimmer, and G. Wedel. The EU DOTSEVEN project: Overview and results. In *2016 IEEE Compound Semiconductor Integrated Circuit Symposium (CSICS)*. IEEE, oct 2016.

[Sch20] James Schellnberg. Millimeter-wave GaN SSPAs: Technology to power 5G and the future. In *2020 IEEE BiCMOS and Compound Semiconductor Integrated Circuits and Technology Symposium (BCICTS)*, pages 1–7. IEEE, 2020.

[SGS+16] N. Sarmah, J. Grzyb, K. Statnikov, S. Malz, P. Rodriguez Vazquez, W. Foerster, B. Heinemann, and U. R. Pfeiffer. A fully integrated 240-GHz direct-conversion quadrature transmitter and receiver chipset in SiGe technology. *IEEE Transactions on Microwave Theory and Techniques*, 64(2):562–574, 2016.

[SHY18] Ho-Jin Song, Hiroshi Hamada, and Makoto Yaita. Prototype of KIOSK data downloading system at 300 GHz: Design, technical feasibility, and results. *IEEE Communications Magazine*, 56(6):130–136, jun 2018.

[SI10] Svilen Sabchevski and Toshitaka Idehara. Design of a compact sub-terahertz gyrotron for spectroscopic applications. *Journal of Infrared, Millimeter, and Terahertz Waves*, jun 2010.

[Sik] Siklu https://www.siklu.com/product/etherhaul-hundred-series/. *EtherHaul Hundred Series Products*.

[SJB+06] S. Sengele, H. Jiang, J. H. Booske, D. W. van der Weide, S. Limbach, A. Mashal, B. Yang, A. Marconnet, M. He, and P. Larsen. Generation of terahertz regime radiation by microfabricated folded waveguide traveling wave tubes. In *2006 IEEE International Vacuum Electronics Conference held Jointly with 2006 IEEE International Vacuum Electron Sources*, pages 421–422. IEEE, 2006.

[SL00] M.S. Shur and Jian-Qiang Lu. Terahertz sources and detectors using two-dimensional electronic fluid in high electron-mobility transistors. *IEEE Transactions on Microwave Theory and Techniques*, 48(4):750–756, apr 2000.

[SMA+98] K. Sano, K. Murata, T. Akeyoshi, N. Shimizu, T. Otsuji, M. Yamamoto, T. Ishibashi, and E. Sano. Ultra-fast optoelectronic circuit using resonant tunnelling diodes and uni-travelling-carrier photodiode. *Electronics Letters*, 34(2):215, 1998.

[SN11] Ho-Jin Song and Tadao Nagatsuma. Present and future of terahertz communications. *IEEE Transactions on Terahertz Science and Technology*, 1(1):256–263, sep 2011.

[SRC+16] Michael Schroter, Tommy Rosenbaum, Pascal Chevalier, Bernd Heinemann, Sorin P. Voinigescu, Ed Preisler, Josef Bock, and Anindya Mukherjee. SiGe HBT technology: Future trends and TCAD-based roadmap. volume 105, pages 1068–1086. Institute of Electrical and Electronics Engineers (IEEE), 1 2016.

[SRI06] Rishad Ahmed Shaik, Md. Shahriar Rahman, and AHM Razibul Islam. On the Extended Relationship Among EVM, BER, and SNR as Performance Metrics. In *4th International Conference on Electrical and Computer Engineering ICECE*, 2006.

[SSH+16] Rayko Ivanov Stantchev, Baoqing Sun, Sam M. Hornett, Peter A. Hobson, Graham M. Gibson, Miles J. Padgett, and Euan Hendry. Noninvasive, near-field terahertz imaging of hidden objects using a single-pixel detector. *Science Advances*, 2(6):e1600190, jun 2016.

[SSYH15] Kaushik Sengupta, Dongjin Seo, Lita Yang, and Ali Hajimiri. Silicon integrated 280 GHz imaging chipset with 4x4 receiver array and CMOS source. *IEEE Transactions on Terahertz Science and Technology*, 5(3):427–437, may 2015.

[STL+19a] B. Schoch, A. Tessmann, A. Leuther, S. Wagner, and I. Kallfass. 260 GHz Broadband Power Amplifier MMIC. In *2019 12th German Microwave Conference (GeMiC)*, pages 232–235. IEEE, March 2019.

[STL+19b] B. Schoch, A. Tessmann, A. Leuther, S. Wagner, and I. Kallfass. 300 ghz broadband power amplifier with 508 ghz gain-bandwidth product and 8 dbm output power. In *2019 IEEE MTT-S International Microwave Symposium (IMS)*, pages 1249–1252. IEEE, June 2019.

[THTK10] J. Takeuchi, A. Hirata, H. Takahashi, and N. Kukutsu. 10-Gbit/s bi-directional and 20-Gbit/s uni-directional data transmission over a 120-GHz-band wireless

link using a finline ortho-mode transducer. In *2010 Asia-Pacific Microwave Conference*, pages 195–198, 2010.

[TKH+13] Hiroyuki Takahashi, Toshihiko Kosugi, Akihiko Hirata, Jun Takeuchi, Koichi Murata, and Naoya Kukutsu. 120-GHz-band 10-Gbit/s fully integrated wireless link using quadrature-phase-shift keying. In *2013 IEEE MTT-S International Microwave Symposium Digest (MTT)*. IEEE, jun 2013.

[TLW+17] A. Tessmann, A. Leuther, S. Wagner, H. Massler, M. Kuri, H. . Stulz, M. Zink, M. Riessle, and T. Merkle. A 300 GHz low-noise amplifier S-MMIC for use in next-generation imaging and communication applications. In *2017 IEEE MTT-S International Microwave Symposium (IMS)*, pages 760–763. IEEE, June 2017.

[UGS+17] M. Urteaga, Z. Griffith, M. Seo, J. Hacker, and M. J. W. Rodwell. InP HBT Technologies for THz integrated circuits. *Proceedings of the IEEE*, 105(6):1051–1067, June 2017.

[VTD+13] Sorin P. Voinigescu, Alexander Tomkins, Eric Dacquay, Pascal Chevalier, Juergen Hasch, Alain Chantre, and Bernard Sautreuil. A study of SiGe HBT signal sources in the 220–330-GHz range. *IEEE Journal of Solid-State Circuits*, 48(9):2011–2021, sep 2013.

[Web07] William Webb. *Wireless Communications: The Future*. John Wiley & Sons, Ltd, jan 2007.

[WFM+08] A. Wakatsuki, T. Furuta, Y. Muramoto, T. Yoshimatsu, and H. Ito. High-power and broadband sub-terahertz wave generation using a j-band photomixer module with rectangular-waveguide output port. In *2008 33rd International Conference on Infrared, Millimeter and Terahertz Waves*, pages 1–2. IEEE, Sep. 2008.

[Wil07] B Williams. Terahertz quantum-cascade lasers. *Nature Photonics*, 1(9):517–525, sep 2007.

[WS04] J. Wuerfl and M. Schlechtweg. Frontiers of III - V compounds and devices. In *GAAS 2004 conference proceedings : 12th European Gallium Arsenide and other compound semiconductors application symposium, Monday 11th Tuesday 12th October 2004*, London UK, 2004. Horizon House Publications.

[WTZ+11] R. Weber, A. Tessmann, M. Zink, M. Kuri, I. Kallfass, H. . Stulz, M. Riessle, H. Massler, T. Maier, A. Leuther, and M. Schlechtweg. A W-Band x12 Frequency Multiplier MMIC in Waveguide Package Using Quartz and Ceramic Transitions. In *2011 IEEE Compound Semiconductor Integrated Circuit Symposium (CSICS)*, pages 1–4. IEEE, Oct 2011.

[WYZW13] Z. Wang, H. Yin, W. Zhang, and G. Wei. Monobit digital receivers for QPSK: Design, performance and impact of IQ imbalances. *IEEE Transactions on Communications*, 61(8):3292–3303, August 2013.

[YJH+16] X. Yu, S. Jia, H. Hu, M. Galili, T. Morioka, P. U. Jepsen, and L. K. Oxenløwe. 160 Gbit/s photonics wireless transmission in the 300-500 GHz band. *APL Photonics*, 1(8):081301, nov 2016.

[ZRG+20] Dan-Dan Zhang, Jiao-Jiao Ren, Jian Gu, Li-Juan Li, Ji-Yang Zhang, Wei-Hua Xiong, Yi-Fan Zhong, and Tong-Yu Zhou. Nondestructive testing of bonding defects in multilayered ceramic matrix composites using THz time domain spectroscopy and imaging. *Composite Structures*, 251(251):112624, nov 2020.

List of Own Publications

[1] I. Dan, B. Schoch, G. Eren, S. Wagner, A. Leuther, and I. Kallfass, "A 300 GHz MMIC-based quadrature receiver for wireless terahertz communications," in *2017 42nd International Conference on Infrared, Millimeter, and Terahertz Waves (IRMMW-THz)*. IEEE, Aug 2017, pp. 1–2.

[2] I. Kallfass, I. Dan, S. Rey, P. Harati, J. Antes, A. Tessmann, S. Wagner, M. Kuri, R. Weber, H. Massler, A. Leuther, T. Merkle, and T. Kuerner, "Towards MMIC-based 300 GHz Indoor Wireless Communication Systems," *IEICE Transactions on Electronics*, vol. E98-C, no. 12, pp. 1081–1090, Dec 2015.

[3] I. Dan, S. Rey, T. Merkle, T. Kuerner, and I. Kallfass, "Impact of modulation type and baud rate on a 300 GHz fixed wireless link," in *2017 IEEE Radio and Wireless Symposium (RWS)*, 2017, pp. 86–89.

[4] I. Dan, E. Rosello, P. Harati, S. Dilek, I. Kallfass, and S. Shiba, "Measurement of complex transfer function of analog transmit-receive frontends for terahertz wireless communications," in *2017 47th European Microwave Conference (EuMC)*, Oct 2017, pp. 1009–1012.

[5] I. Dan, C. M. Groetsch, S. Shiba, and I. Kallfass, "Investigation of local oscillator isolation in a 300 GHz wireless link," in *2017 IEEE International Conference on Microwaves, Antennas, Communications and Electronic Systems (COMCAS)*, Nov 2017, pp. 1–5.

[6] I. Dan, C. M. Grotsch, S. Shiba, and I. Kallfass, "Considerations on local oscillator isolation in a terahertz wireless link used for future communication systems," in *2018 43rd International Conference on Infrared, Millimeter, and Terahertz Waves (IRMMW-THz)*, 2018, pp. 1–2.

[7] I. Dan, P. Szriftgiser, E. Peytavit, J.-F. Lampin, M. Zegaoui, M. Zaknoune, G. Ducournau, and I. Kallfass, "A 300-GHz wireless link employing a photonic transmitter and an active electronic receiver with a transmission bandwidth of 54 GHz," *IEEE Transactions on Terahertz Science and Technology*, vol. 10, no. 3, pp. 271–281, may 2020.

[8] I. Dan, C. M. Groetsch, B. Schoch, S. Wagner, L. John, A. Tessmann, and I. Kallfass, "A 300 GHz Quadrature Down-Converter S-MMIC for Future Terahertz Communication," in *2019 IEEE International Conference on Microwaves, Antennas, Communications and Electronic Systems (COMCAS)*, Nov 2019, pp. 1–6.

[9] I. Dan, G. Ducournau, S. Hisatake, P. Szriftgiser, R.-P. Braun, and I. Kallfass, "A terahertz wireless communication link using a superheterodyne approach," *IEEE Transactions on Terahertz Science and Technology*, vol. 10, no. 1, pp. 32–43, Jan 2020.

[10] ——, "A superheterodyne 300 GHz wireless link for ultra-fast terahertz communication systems," in *2019 49th European Microwave Conference (EuMC)*, Oct 2019, pp. 734–737.

[11] ——, "A superheterodyne 300 GHz wireless link for ultra-fast terahertz communication systems," *International Journal of Microwave and Wireless Technologies*, vol. 12, no. 7, pp. 578–587, May 2020.

[12] I. Kallfass, I. Dan, P. Szriftgiser, V. Chinni, M. Zaknoune, and G. Ducournau, "300 GHz wireless communication systems exploiting the benefits of combining photonic and electronic transceiver components," in *2019 44th International Conference on Infrared, Millimeter, and Terahertz Waves (IRMMW-THz)*, Sep 2019, pp. 1–2.

[13] I. Dan, D. Meier, S. Wagner, A. Leuther, A. Tessmann, H. Massler, and I. Kallfass, "A 300 GHz multi-stage balanced variable gain amplifier with Tandem-X couplers," in *2015 IEEE International Conference on Microwaves, Communications, Antennas and Electronic Systems (COMCAS)*, Nov 2015, pp. 1–4.

[14] I. Kallfass, P. Harati, I. Dan, J. Antes, F. Boes, S. Rey, T. Merkle, S. Wagner, H. Massler, A. Tessmann, and A. Leuther, "MMIC chipset for 300 GHz indoor wireless communication," in *2015 IEEE International Conference on Microwaves, Communications, Antennas and Electronic Systems (COMCAS)*, Nov 2015, pp. 1–4.

[15] P. Harati, E. Rosello, I. Dan, E. R. Bammidi, J. Eisenbeis, A. Tessmann, D. Schwantuschke, R. Henneberger, and I. Kallfass, "E-band downlink wireless data transmission for future satellite communication," in *2017 Topical Workshop on Internet of Space (TWIOS)*, Jan 2017, pp. 1–4.

[16] I. Kallfass, S. M. Dilek, and I. Dan, "Signal quality impairments by analog frontend non-idealities in a 300 GHz wireless link," in *2017 11th European Conference on Antennas and Propagation (EUCAP)*, 3 2017, pp. 1618–1621.

[17] I. Dan, S. Hisatake, P. Szriftgiser, R.-P. Braun, I. Kallfass, and G. Ducournau, "Towards super-heterodyne THz links pumped by photonic local oscillators," in *2019 44th International Conference on Infrared, Millimeter, and Terahertz Waves (IRMMW-THz)*, Sep 2019, pp. 1–2.

[18] C. Groetsch, I. Dan, L. John, S. Wagner, and I. Kallfass, "A compact 281-319 GHz low-power downconverter MMIC for superheterodyne communication receivers," *IEEE Transactions on Terahertz Science and Technology*, pp. 1–1, 2020.

Acknowledgments

My PhD journey had a lot of ups and downs and I would not have made it without the help of an army of people.

I can not express enough gratitude for my supervisor Prof. Dr.-Ing. Ingmar Kallfass, which has helped with every step of the work presented in this thesis. Besides hard work and a good technical guidance he showed me how to have fun and be productive at the same time. He always had an open door, which I took advantage of plenty of times. I am particularly grateful for his fast feedback on all my publications and interest in my work.

It has been an honor to meet and work with my second supervisor Prof. Dr-Ing. Thomas Kurner. He has accompanied my journey in academic research from the very beginning and his professionalism, diplomacy and excellent project management skills have set a high standard for my career. I thank him for everything he has done for me.

All circuits presented and essential for this thesis were fabricated at Fraunhofer IAF. I do not have enough words to thank the staff that fabricated and measured these circuits as well as guided me throughout this journey. Just to name a few that had a huge contribution: Dr. Axel Tessmann, Dr. Arnulf Leuther, Hermann Massler, Laurenz John and last but definitely not least Sandrine Wagner. I would not have made it without you!

The first transmission experiments I carried out and are presented here could not have been possible without the help and guidance of Sebastian Rey. Thank you Sebastian for everything I learned from you!

A very special thank you to Prof. Guillaume Ducournau and Dr. Pascal Szriftgiser. The experiments at IEMN are a pillar of this thesis and were wonderful not just for the high quality research we were able to gain. We had loads of fun and I will always think dearly of Lille.

I would like to thank all ThoR consortium partners I had the pleasure to work with. I consider myself extremely lucky to have been part of an collaborative European -Japanese project and even more to have worked with such talented engineers and scientists. This thesis benefited from the fruitful discussion I had with Dr. Bruce Napier, Dr. Petr Jurcik, Yigal Leiba, Dr. Ralf-Peter Braun and Prof. Shintaro Hisatake. I thank them all for the great memories from Japan, Germany and Israel.

Needless to say what an impact my colleagues at ILH played during my work at the university. I thank them all. The list of names is too long for this page, but please rest assured I am forever grateful for all your help, discussions and support. I am particularly happy that the paths of Dr. Stefan Monch and mine have crossed and stayed together for such a long time: from the first Bachelor's courses, to Bachelor's thesis, Master's thesis and ended up in a shared office.

Lastly, I would like to thank my parents and friends, that had to endure a lot of mood swings associated with the ups and downs mentioned in the beginning. Certainly the most wonderful thing that resulted from the work at ILH was meeting my soulmate, who believes in me more than I could possibly ever do. His constant encouragement and technical support is the reason why I was able to finish writing this thesis.